Pair instability supernovae: Evolution, explosion, nucleosynthesis

Dissertation

zur

Erlangung des Doktorgrades (Dr. rer. nat.)

der

Mathematisch-Naturwissenschaftlichen Fakultät

der

Rheinischen Friedrich-Wilhelms-Universität Bonn

vorgelegt von

Alexandra Kozyreva

aus

Moskau, Russland

Bonn 2014

Angefertigt mit Genehmigung der Mathematisch-Naturwissenschaftlichen Fakultät der Rheinischen Friedrich-Wilhelms-Universität Bonn.

1. Referent: Prof. Dr. Norbert Langer
2. Referent: Prof. Dr. Robert Izzard

Tag der Promotion: 28 April 2014
Erscheinungsjahr 2014

Abstract

Supernova explosions are among the most impressive events in the Universe. Tens of supernovae are exploding in the visible Universe each second, and at present there are a few of them discovered every day. The average peak luminosity of a supernova competes with that of entire galaxies. Supernovae are the main contributor of heavy elements, energy and momentum to the interstellar medium, and thus play a crucial role for the evolution of galaxies.

Stars with initial masses above 10 solar masses produce core-collapse supernovae at the end of their lives, which comprise about two-third of all supernovae. These events produce neutron stars or black holes as compact remnants. It has since long been predicted that very massive star, i.e., stars above 140 solar masses, undergo a dynamical collapse due to electron-positron pair creation before core oxygen ignition. The explosive ignition can then disrupt the whole star, leading to so called "pair instability supernovae" (PISNe).

Since many of them are believed to explode in the early Universe, so far there were only zero and extremely low metallicity evolutionary models computed for this particular supernovae type. The recent discovery of so called super-luminous supernovae in the local Universe revealed the need for corresponding models at higher metallicity. This thesis is based on the self-consistent evolutionary calculations of 150 $M_{\odot}$ and 250 $M_{\odot}$ models including rotation and magnetic fields from the zero-age main sequence up to the collapse due to pair creation. In this thesis, using an extended and improved nuclear reaction network, these evolutionary models are evolved through their PISN explosions. In this way, the first detailed nucleosynthetic yields of finite metallicity pair instability supernovae are produced, which allows to identify routes to constrain their number based on the elemental abundances of metal poor low mass stars in our Galaxy.

In a second step, the post-explosion expansion of the pair instability supernova ejecta is calculated with a multigroup radiation transport-hydro code in order to describe the visual display of such events. The results of these calculations enabled us to compare the models to observed supernovae. We found the appearance of our low mass PISN model to be similar to that of several observed Type II-Plateau supernovae, while our high mass model shows striking coincidence with the observations of the superluminous supernova SN 2007bi. We suggest criteria to distinguish PISNe from ordinary ones, and conclude that PISNe in the local Universe may occur more frequent than previously thought.

Dedicated to my little angel Galina Kozyreva

Contents

Contents **1**

List of Figures **6**

List of Tables **10**

1 Introduction and thesis outline **13**
1.1 Massive stars . . . 13
1.2 Evolution and final fates of massive stars . . . 18
1.2.1 10 – 100 $M_\odot$ stars . . . 18
1.2.2 100 – 260 $M_\odot$ stars . . . 24
1.2.3 260 – 5 $\times$ 10^4 $M_\odot$ stars . . . 29
1.2.4 5 $\times$ 10^4 – 10^5 $M_\odot$ stars . . . 30
1.2.5 Beyond stability . . . 31
1.3 Superluminous supernovae . . . 31
1.3.1 Nickel-powered SLSNe . . . 33
1.3.2 Interaction-powered SLSNe . . . 33
1.3.3 Magnetar-powered SLSNe . . . 34
1.4 Motivation for the thesis work . . . 35
1.5 Thesis content . . . 37

2 Nuclear networks **39**
2.1 Thermonuclear fusion in stars . . . 39
2.2 Nuclear networks for stellar evolution . . . 40
2.2.1 Nuclear networks and silicon burning . . . 41
2.2.2 Implementation of silicon burning in the Binary Evolution Code . . . 43
2.2.3 Quasi-statistical equilibrium and energy generation rate table . . . 49
2.3 Applications of the $\alpha-$chain network . . . 56
2.3.1 Helium star models . . . 56
2.3.2 Supercollapsar progenitors . . . 60

3 Explosion and nucleosynthesis of low redshift pair instability supernovae **65**
3.1 Overview . . . 65

3.2 Introduction . . . 66
3.3 Numerical method and input physics . . . 67
3.4 Results . . . 69
3.4.1 Explosion . . . 69
3.4.2 Nucleosynthesis . . . 71
3.5 Implications for chemical evolution . . . 77
3.6 Conclusions . . . 79

4 Observational properties of low redshift pair instability supernovae 89
4.1 Overview . . . 89
4.2 Introduction . . . 90
4.3 Evolutionary models and light curves modeling . . . 92
4.3.1 Description of the evolutionary models . . . 92
4.3.2 Simulation of light curves and SEDs . . . 94
4.4 Results . . . 98
4.4.1 The 150 $M_\odot$ model . . . 101
4.4.2 The 250 $M_\odot$ model . . . 103
4.5 Discussion . . . 104
4.5.1 Comparison with other theoretical PISN light curves . . . 104
4.5.2 The chemical structure during the coasting phase . . . 110
4.5.3 Comparison with observed SNe . . . 112
4.6 Conclusions . . . 117

5 Summary and concluding remarks 125
5.1 Improvement of the nuclear network . . . 125
5.2 Pair instability supernovae in the local Universe . . . 126
5.3 Observational properties of low redshift pair instability supernovae . . . 127

A Basic stellar structure equations 129

B Integration SN yields over the IMF 131
B.1 Integration over the IMF . . . 131
B.1.1 Isotopic production factor . . . 131
B.2 Elemental production factor . . . 132
B.2.1 The sum details . . . 132
B.2.2 The imprint of pair instability supernovae on the yield from one generation of stars . . . 134

Bibliography 151

Acknowledgments 153

List of publications 155

Curriculum Vitae **157**

List of Figures

1.1 Massive stars in the Orion constellation observed with the naked eye. . . . 14
1.2 Massive stars in our Galaxy and in the Large Magellanic Cloud 16
1.3 Schematic illustration of the sequence of nuclear burning stages with final onion-like chemical structure of the evolved massive star. 19
1.4 Schematic illustration of supernova light curves 21
1.5 Observed examples of light curves of core-collapse supernovae. 22
1.6 The dominant contributors to the pressure 26
1.7 Transition between two polytropes with $\gamma = 4/3$ 27
1.8 Schematic illustration of the fate of massive, very massive and supermassive stars 32

2.1 Illustration of $\alpha-$ and proton flows in the α-chain nuclear network. 47
2.2 Demonstration of the improvement of the nuclear network solver 48
2.3 Illustration of QSE for two QSE-groups of isotopes. 50
2.4 Evolution of energy generation rate during silicon burning for different initial compositions. 51
2.5 Energy generation rate during silicon burning for different initial compositions 52
2.6 Schematic flow chart of the BEC 53
2.7 Dependence of nuclear energy generation rate on electron number Y_e 54
2.8 Helium star models of solar metallicity in the Hertzsprung-Russel diagram 57
2.9 Helium star models in the central $\rho - T$ diagram. 58
2.10 Helium star models in the central $\rho - T$ diagram. Latest stages. 59
2.11 Density–temperature diagram for 15 $M_\odot$ helium star model, 25 $M_\odot$ and 40 $M_\odot$ hydrogen star models. 60
2.12 Chemical structure in the rotating 500 $M_\odot$ model at the pre-collapse stage. 61
2.13 Angular momentum distribution in the rotating 500 $M_\odot$ model 63

3.1 Evolutionary tracks of our 150 $M_\odot$ and 250 $M_\odot$ models in central density – temperature diagram. 70
3.2 The energetics of the PISN explosions for our 150 $M_\odot$ and 250 $M_\odot$ models. 80
3.3 Total energy evolution for our 1500 $M_\odot$ and 250 $M_\odot$ models. 81
3.4 The final chemical structure of our models. 82
3.5 Kippenhahn diagram for 250 $M_\odot$ PISN model. 83

3.6 Production factors of major elements from our 150 $M_\odot$and 250 $M_\odot$ PISN models with those of comparable Population III helium star models. 84
3.7 Isotopic production factors for the indicated nuclei for our 150 $M_\odot$and 250 $M_\odot$ PISN models for those of comparable Population III helium star models. 85
3.8 The total metal yields of core-collapse SN models at $Z = 0.002$ and of PISNe at $Z = 0.001$ from the one generation of stars. 86
3.9 Production factors of major elements from core-collapse SNe and from both core-collapse and PISNe 87

4.1 Density structure of the 150 $M_\odot$ and 250 $M_\odot$ PISN progenitor models at the onset of the STELLA calculations. 93
4.2 Chemical structure of the exploding 150 $M_\odot$ and 250 $M_\odot$ stars at metallicity $Z = 10^{-3}$ at the onset of the STELLA calculations. 95
4.3 Pre-supernova evolution of the stellar mass of our models due to stellar wind mass loss. 96
4.4 Bolometric and multiband (U, B, V, I, R) light curves for 150 $M_\odot$ and 250 $M_\odot$ PISNe. 97
4.5 Evolution of the composition at the receding electron-scattering photosphere for the 150 $M_\odot$ and 250 $M_\odot$ PISN models. 99
4.6 Shock breakout events for 150 $M_\odot$ and 250 $M_\odot$ PISN explosions. 100
4.7 Evolution of the effective and color temperature of 150 $M_\odot$ and 250 $M_\odot$ PISN models. 102
4.8 Bolometric luminosity for the red supergiant models 150M, R150.K, R190.D, and R250.K. 105
4.9 Photospheric velocities for the red supergiant models 150M, R150.K, R190.D, and R250.K. 106
4.10 Bolometric luminosity for the Model 250M, Model B190.D, Model B210.D, and Model B250.K. 107
4.11 Photospheric velocities for the Model 250M, Model B190.D, Model B210.D, and Model B250.K. 109
4.12 Chemical structure of ejecta of 150 $M_\odot$ and 250 $M_\odot$ PISNe at late time. . 111
4.13 Absolute V-band light curve for 150 $M_\odot$ PISN and absolute V-band magnitudes for typical and bright SNe IIP. 112
4.14 Color temperature evolution of 150 $M_\odot$ PISN and of typical SN IIP SN 1999em and NUV-bright SN 2009kf. 113
4.15 Photospheric velocity of our 150 $M_\odot$ PISN model and observed SNe IIP. . 115
4.16 Absolute bolometric light curve for our 250 $M_\odot$ PISN model and for SLSN Ic.116
4.17 Absolute bolometric light curve for our 250 $M_\odot$ PISN model and for SLSNe Ic.118
4.18 Photospheric velocity of our 250 $M_\odot$ PISN model and of several SLSN Ic. . 120

B.1 Average elemental production factor for CCSN at zero metallicity. 133

B.2 Average elemental production factor for one generation of massive and very massive stars at different metallicities. 135

List of Tables

1.1 List of the most massive stars known 15

2.1 Evolutionary timescales of the burning stages in massive stars 41
2.2 Jacobian matrix for simplified silicon burning 42
2.3 Old and new list of isotopes 43
2.4 Old list of nuclear reactions with the list of additional reactions 44
2.5 Radioactive decay 55

3.1 Properties of our PISN progenitor models and of comparable Population III helium star models 69
3.2 Total nucleosynthetic yields for selected isotopes in solar masses for our 150 $M_\odot$ and 250 $M_\odot$ models in comparison with 70 $M_\odot$ and 115 $M_\odot$ zero metallicity helium star yields. 72
3.3 Total nucleosynthetic yields in solar masses and production factors for 150 $M_\odot$ and 250 $M_\odot$ models at metallicity $Z = 0.001$. 73

4.1 Characteristics of the PISN models. 122
4.2 Shock breakout and plateau-maximum phase characteristics. 123

Chapter 1

Introduction and thesis outline

This introductory chapter schematically describes the ultimate fates of massive, very massive, and supermassive stars. Details are provided for the progenitors of pair instability supernovae and their applications to the recently discovered class of superluminous supernovae.

1.1 Massive stars

What kind of stars do we see on the sky during a clear night? The brightest stars include Sirius, Arcturus, Vega, Capella, Rigel, Procyon, Betelgeuse, Altair, Aldebaran, Pollux, and Deneb, among many others (in the northern hemisphere of the Earth) that we see with the naked eye. Their apparent magnitudes, which are a measure of their brightness[1], are -1.5, 0, 0, 0.1, 0.1, 0.3, 0.4, 0.8, 0.9, 1.1, and 1.3 mag, respectively. The corresponding absolute magnitudes, which reveal their intrinsic luminosity[2], that can be obtained considering their distances are 1.4, -0.3, 0.6, -0.5, -7, 2.6, -1.3, 2.3, -0.3, 0.7, -7.2 mag, respectively. The masses of these stars estimated from their intrinsic luminosities range from 1.5 $M_\odot$ to 19 $M_\odot$. Approximately, the mass of Sirius is 2 $M_\odot$, the mass of Arcturus is 1.5 $M_\odot$, the mass of Vega is 2 $M_\odot$, the mass of Capella is 2.5 $M_\odot$, the mass of Rigel is 18 $M_\odot$, the mass of Procyon is 1.5 $M_\odot$, the mass of Betelgeuse is 15 $M_\odot$, the mass of Altair is 1.7 $M_\odot$, the mass of Aldebaran is 2 $M_\odot$, the mass of Pollux is 2 $M_\odot$, and the mass of Deneb is 19 $M_\odot$.

[1]The apparent magnitude m is defined as $m \propto -2.5 \log_{10} F$, where F is the energy flux from the star in units [erg s^{-1} cm^{-2}]. F corresponds to the amount of energy an observer receives at the Earth per second through one square centimeter. Due to historical reasons, a higher brightness of a star corresponds to a smaller value of the magnitude. The Greek astronomer Hipparchus in the 2nd century BC divided all stars into 6 classes according to their brightness. The brightest stars were stars of the first magnitude, the faintest stars were the sixth magnitude. The apparent magnitude of the Sun is -26.7 mag.

[2]The absolute magnitude is defined as the magnitude of the star if it was located at the distance 10 parsec or 3×10^{19} cm. The absolute magnitude is defined from the apparent magnitude and the distance to the star as $M = m + 5 - 5 \log_{10} D$, where D is the distance to the star in parsec. The absolute magnitude of the Sun is 4.7 mag, which means that if the Sun was 10 parsec away from the Earth it would almost be invisible to the naked eye.

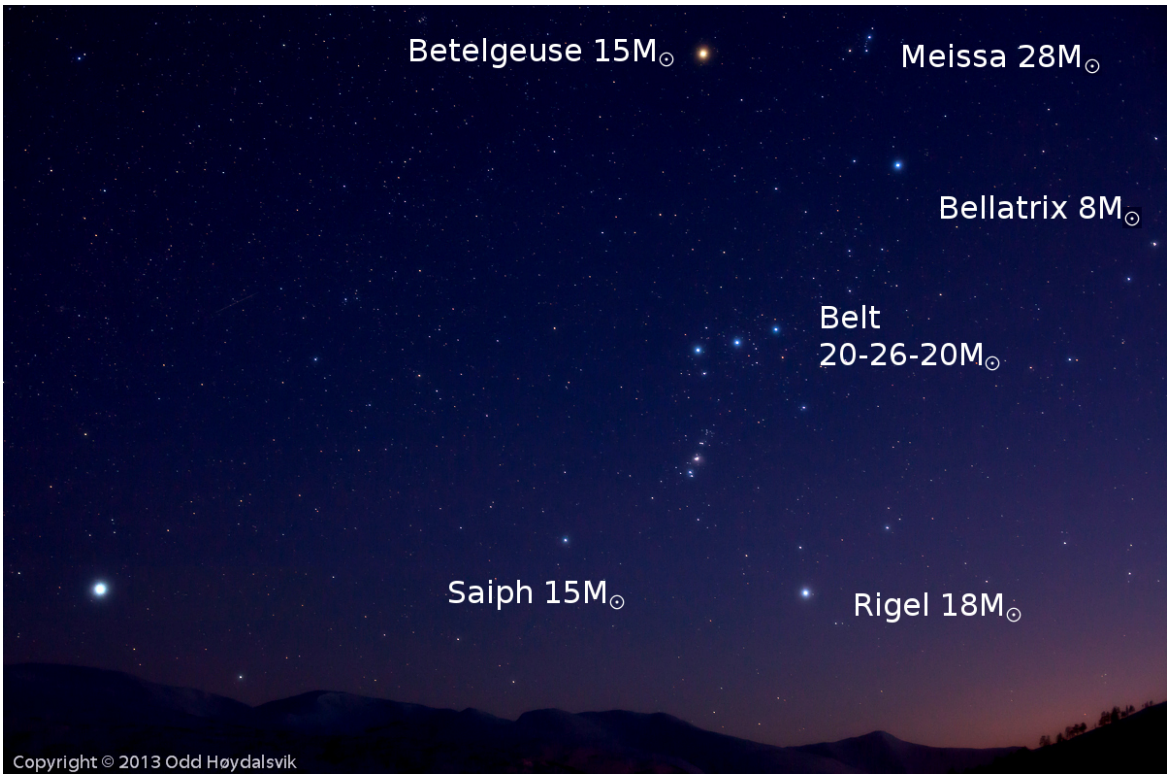

Figure 1.1: Massive stars in the Orion constellation observed with the naked eye.

In Figure 1.1 we show the well-known constellation of Orion and label the most massive stars which are easily observed with the naked eye.

The stars mentioned above are located in our Galaxy. We see many of these stars during their most long-lasting phase — core hydrogen burning. Only a few of them can be truly considered as massive stars — Rigel, Betelgeuse and Deneb. It is believed that currently hydrogen is exhausting in the cores of these stars or helium is burning there.

Do we have even more massive stars? Do they exist? The answer is "Definitely!".

More massive stars have shorter lifetimes and, therefore, are fewer in number. Moreover the absolute number of newly born massive stars is less than that of low-mass stars due to the mass spectrum of fragmented star forming clouds and the consequent initial mass function (Kolmogorov 1941; Salpeter 1955). Massive stars are usually born in dense clusters and have complex circumstellar material resulting from their strong stellar winds. Modern telescopes and observational techniques are often powerful enough to resolve individual stars in such environments. Consequently, a number of very massive stars much above 20 $M_{\odot}$ have been detected. In Table 1.1, we list the most massive stars that have been observed to date, and in Figure 1.2 we demonstrate the star clusters with the most massive stars known. A recent study by Schneider et al. (2014) indicates that the masses of the stars from the cluster R136 are reliable.

Other questions arise when talking about massive stars:

Table 1.1: The list of the most massive stars based on Davidson (1999); Walborn et al. (2004); Barniske et al. (2008); Martins et al. (2008); Schnurr et al. (2008); Crowther et al. (2010); Bestenlehner et al. (2011); Schneider et al. (2014). The numbers in parentheses following the current mass means the estimated initial mass.

Name	Current mass in $M_\odot$	Location	Reference
R136a1	265(320)	LMC	Crowther et al. (2010)
R136a2	195	LMC	Crowther et al. (2010)
R136c	175	LMC	Crowther et al. (2010)
Peony star (WR 102ka)	175 WR	MW	Barniske et al. (2008)
HD 269810	150	LMC	Walborn et al. (2004)
VFTS 682	150 WR	LMC	Bestenlehner et al. (2011)
R136a3	135	LMC	Crowther et al. (2010)
NGC 3603-B	132	MW	Schnurr et al. (2008)
Arches-F9	120 WN	MW	Martins et al. (2008)
η Carina-A	120(160)	MW	Davidson (1999)

Note: 'WR': Wolf-Rayet star, 'WN': Wolf-Rayet of type WN. 'LMC': Large Magellanic Cloud. 'MW': Milky Way.

- What is the difference between massive stars and our Sun?
- How long do they live?
- What is the final fate?

We briefly answer these questions here and in the next sections in more detail.

The Sun is a low-mass star. The life of our Sun is well known. Its age is about 5 billion years and it will continue to live its quiet life for the next 5 billion years. This corresponds to the long-lasting phase where hydrogen is transformed into helium in the depth of the Sun. The energy released from the thermonuclear reactions in the core diffuses during millions of years to the surface of the Sun. The specific solar luminosity is comparable to that of rotting leaves in autumn ($L_\odot/M_\odot \simeq 2$ erg s^{-1} g^{-1}). Note that the human body releases 10^4 times more energy per gram each second![3] During its further evolution, the solar core will converts helium into carbon and oxygen. Gravity is not large enough to provide conditions for further nuclear evolution, and after a series of helium flashes the solar core becomes a degenerate carbon-oxygen core (a so-called "white dwarf") surrounded by shed shells of the outer solar atmosphere (the so-called "planetary nebula").

The fate of more massive stars (above 10 $M_\odot$) is very different. Note that according to their higher masses the hydrogen burning phase lasts only millions of years. Their

[3]The energy generation rate of human body is 100 W if the person is in quiet state. This approximately corresponds to specific energy generation rate 10^4 erg s^{-1} g^{-1}. While doing any sports the body radiates 4×10^4 erg s^{-1} g^{-1}.

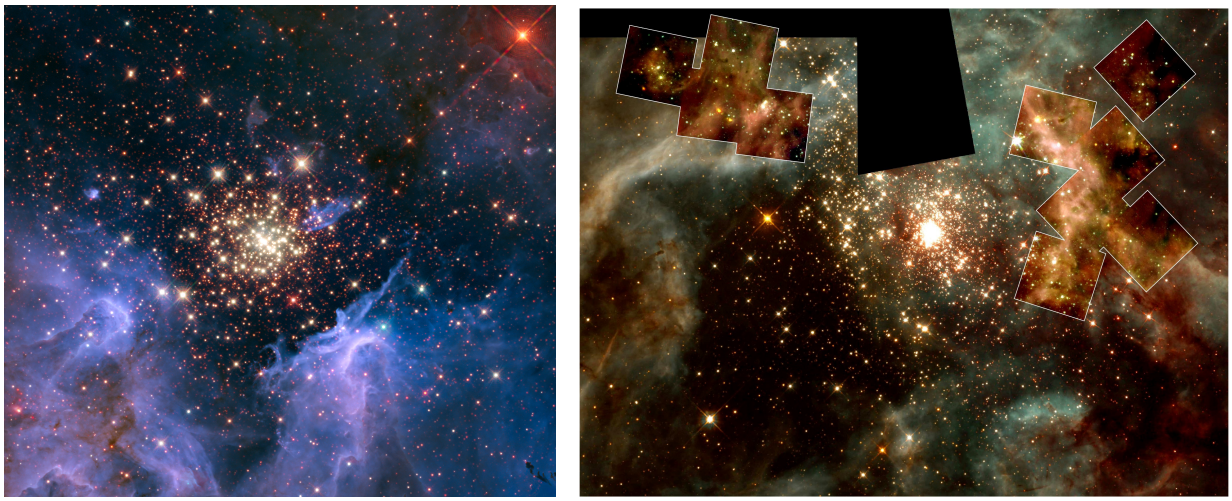

Figure 1.2: Massive stars in our Galaxy (left) and in the Large Magellanic Cloud (right).
Left: Star cluster NGC 3603 in our Galaxy which contains stars 92 $M_\odot$, 113 $M_\odot$, 120 $M_\odot$, and 132 $M_\odot$ (Schnurr et al. 2008).
Right: Tarantula nebula (or 30 Doradus star forming region) in the nearby galaxy Large Magellanic Cloud contains the star cluster R136 with stars 135 $M_\odot$, 175 $M_\odot$, 195 $M_\odot$, 265 $M_\odot$ (Crowther et al. 2010; Schneider et al. 2014).
Photos are taken from http://hubblesite.org/ and http://nssdc.gsfc.nasa.gov/.

nuclear evolution continues far beyond helium burning. The gravity of massive stars is high enough to provide thermodynamic conditions for carbon, neon and oxygen burning, which last 500 years, 5 years and 1 year, successively. Following this stage, silicon burning occurs and lasts only 1 day. During this stage the iron core is formed in the centre. As a final chord of the relatively short life of massive stars, the iron core loses its dynamical stability and collapses. The gravitational energy released during the collapse initiates a tremendous explosion and the ejection of all overlying layers. This phenomenon is called a "supernovae". The amount of energy released during a supernova explosion is compatible to the energy the Sun generates during its whole life, and the luminosity of supernova can be 10^{10} times that of the Sun or as bright as a whole galaxy.

Such powerful explosions can be seen from very large distances, where galaxies cannot be resolved into individual stars. Therefore, supernovae operate as beacons in the Universe. Discovering supernovae at large distances allows us to investigate stellar evolution in the early Universe. One can derive the value of the intrinsic luminosity of the supernova from photometric and spectroscopic observations for various types of supernovae. Knowing the intrinsic luminosity one is able to calculate the distance to the supernova, which is important for measuring the scales of the Universe.

One of the most significant aspect of supernovae consists in the impact on chemical enrichment. During the explosion, a large amount of heavy elements[4] is expelled into the

[4]Heavy elements, or metals, are those heavier than helium.

surrounding medium, increasing its metal fraction, i.e. the metallicity[5]. Many elements heavier than helium are produced during the evolution of a massive star and the supernova explosion, and are ejected with high velocities. These include carbon, oxygen, sodium, magnesium, aluminium, silicon, calcium, titanium, iron, zinc and many others. Low-mass stars cannot produce this ensemble of vital chemical elements on a short timescale because of their large evolutionary timescale. Massive stars evolve quickly and are the first contributors to the chemical evolution of the Universe. Due to the high velocities, freshly synthesized elements are effectively mixed into the interstellar matter and provide new chemical conditions for the formation of the next generations of stars.

For example, a 25 $M_\odot$ star enriches the circumstellar medium with 0.3 $M_\odot$ of carbon, several solar masses of oxygen, 0.1 $M_\odot$ of magnesium. 0.5 $M_\odot$ of silicon, 0.05 $M_\odot$ of iron. Some very massive stars above 140 $M_\odot$ are completely disrupted during their explosions and enrich the medium with more than a hundred solar masses of heavy elements (see below).

Our Sun was formed from matter that was already processed by many generations of stars. One of the strongest signature of this fact comes from the iron-group abundance in the Solar system. Iron-56 contributes 0.1% of the whole Solar system's mass, which corresponds to 6% of the Solar system's mass of species heavier than helium, and 20% of the mass of all elements beyond oxygen (Wallerstein et al. 1997). Such a high iron-56 abundance (and also those of some other iron-group isotopes) is explained by the fact that the Solar system's matter underwent in the past the condition of nuclear statistical equilibrium[6], i.e. very high temperature (above $\sim 4 \times 10^9$ K) and density (above $\sim 10^9$ g cm^{-3}). The system of isotopes in nuclear statistical equilibrium has a specific distribution of isotopes determined by their binding energies. Therefore, the dominant isotopes in equilibrium are those with the highest binding energy, i.e. the most tightly bound nuclei. The conditions of statistical equilibrium are naturally attained in an evolved massive star, namely during the pre-supernova stage, the core collapse and during the supernova explosion. Accreting white dwarfs (i.e. the evolved cores of low-mass stars) can also reach the condition of statistical equilibrium during a thermonuclear explosions (Seitenzahl et al. 2009). Together, core-collapse supernova isotopic yields and SNe Ia yields can explain the Solar system's abundances of isotopes between oxygen and iron (Timmes et al. 1995; Woosley et al. 2002; Thielemann et al. 2007).

Therefore, supernova explosions govern the chemical evolution of the entire galaxy and manage the processes of on-going star formation. In the following sections we discuss the mass dependence of these processes.

[5]Metallicity Z is defined as a mass fraction of all elements heavier than helium.

[6]Nuclear statistical equilibrium is the state of the matter when many micro-processes are governed by macro-thermodynamical characteristics (see e.g., Meyer 1994; Wallerstein et al. 1997; Meyer et al. 1998). The condition of nuclear statistical equilibrium is reached at high temperature (4×10^9 degrees) and density (10^9 g cm^{-3}). In these conditions, the distribution of species is set by values of temperature, density and the electron fraction.

1.2 Evolution and final fates of massive stars

The initial mass function of stars in the nearby Universe is relatively well known up to about 100 $M_{\odot}$. The number of stars in the range $(M, M + \Delta M)$ is proportional to M^{Γ}, where $\Gamma \simeq -2.35$ (Salpeter 1955). In the early Universe where elements heavier than lithium are absent, the number of massive stars could be significantly larger because of the lack of efficient coolants like carbon atoms and interstellar dust in star-forming regions (e.g., Bromm et al. 1999; Nakamura & Umemura 2001; Abel et al. 2002; Omukai & Palla 2003; O'Shea & Norman 2006; Ohkubo et al. 2009).

We briefly review the evolution of massive stars and their consequent final fates according to their initial masses. We focus on stars above approximately 10 $M_{\odot}$, because they are expected to end their lives as supernovae (SN, hereafter).

1.2.1 10 – 100 $M_{\odot}$ stars

The evolution of stars follows a sequence of hydrostatic burning stages in the interior. Schematically it can be written as the following sequence:

> core nuclear burning → nuclear fuel exhaustion → core contraction → core heating → core nuclear burning → and so on...

For stars in the mass range of 10 – 100 $M_{\odot}$, this sequence terminates when the core is converted into iron, which eventually collapses to form a neutron star or black hole. A large number of detailed studies are dedicated to this topic (e.g., Woosley & Weaver 1995; Chieffi et al. 1998; Heger et al. 2000; Limongi et al. 2000; Hirschi et al. 2004; Chieffi & Limongi 2013; Georgy et al. 2013).

A set of well-known nuclear reactions convert hydrogen to iron through a series of phases of hydrostatic hydrogen, helium, carbon, oxygen, neon, and silicon burning. Silicon burning in the core occurs at quasi-statistical equilibrium condition and results in the formation of iron. The schematic illustration of the sequence of nuclear burning stages (not to scale) is presented in Figure 1.3. At the end of its nuclear evolution a star has onion-like stratified chemical structure. Nuclear fusion cannot continue with iron because of its high nuclear binding energy, and the iron core continues to contract. The accompanying neutronisation of the matter due to the photo-dissociation of matter and electron captures near the center eventually leads to the dynamical instability and gravitational collapse of the core. The gravitational energy of the core is released in the form of an intense neutrino flux during the dynamical collapse. Neutrinos then interact with the surrounding matter and generate a bounce and a strong shock, which eventually results in a spectacular explosion known as core-collapse supernova (CCSN, hereafter). The gravitational collapse of the iron core ceases when its central density reaches nuclear matter density ($10^{14} - 10^{15}$ g cm^{-3}), and leaves a neutron star if the initial stellar mass does not exceed approximately 25 $M_{\odot}$.

Massive stars contribute about 75% to the total number of all exploding supernovae (Mackey et al. 2003; Smartt 2009; Arcavi et al. 2010; Li et al. 2011; Smith et al. 2011; Eldridge et al. 2013). The rest fraction of supernovae are produced by explosions of white

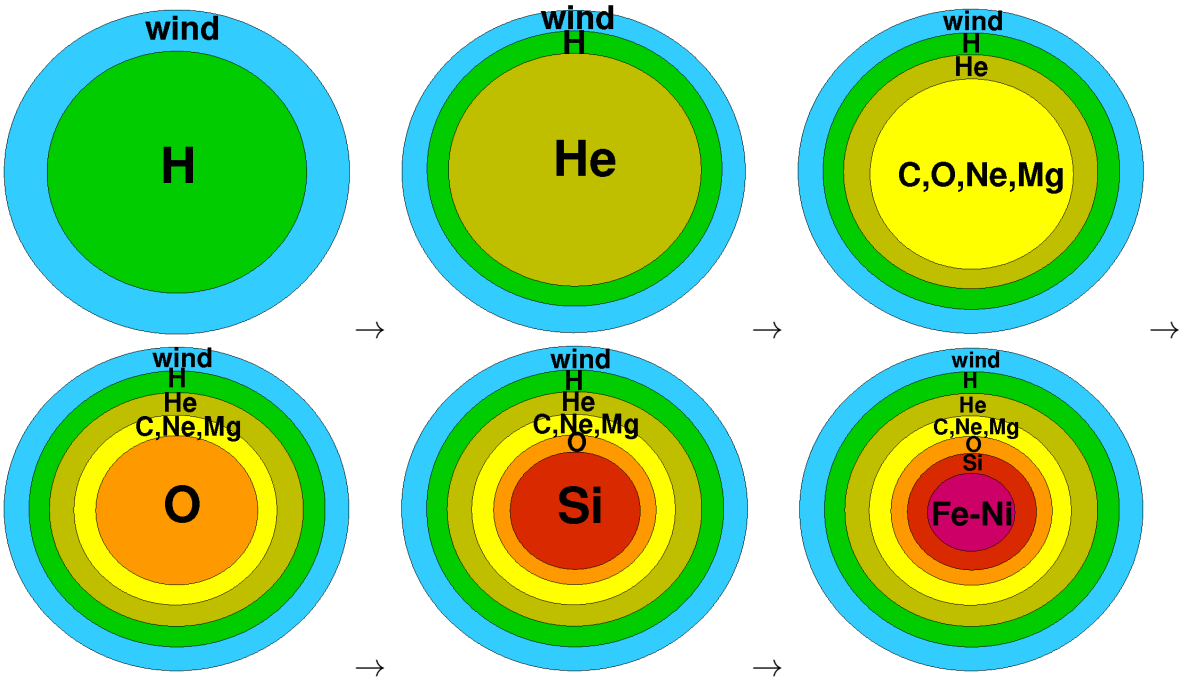

Figure 1.3: Schematic illustration of the sequence of nuclear burning stages with final onion-like chemical structure of the evolved massive star at the pre-collapse stage (not to scale).

dwarfs which are the results of evolution of low-mass stars (a few solar masses) (Arnett 1969; Nomoto et al. 1976; Nomoto 1982). A large fraction of faint core-collapse supernovae leave invisible because of strong selection effect and limited observational capabilities (Mannucci et al. 2007; Botticella et al. 2008; Young et al. 2008; Mattila et al. 2012; Gal-Yam et al. 2013).

Although it is still a matter of debate how the imploding core of the massive star provides the explosion (Janka 2012; Burrows 2013), great success has been achieved recently for low and intermediate energy explosions driven by neutrino transport (Marek & Janka 2009; Bruenn et al. 2009; Kotake et al. 2012; Kuroda et al. 2012; Müller et al. 2012; Bruenn et al. 2013). Bruenn et al. (2013) reached the time up to 2 ms after the onset of the gravitational collapse and successfully produced neutrino-driven shocks. Nevertheless, these computationally expensive numerical calculations still involve a number of unclear assumptions about the onset of the collapse and bounce itself. Moreover, there is a discrepancy between two- and three-dimensional CCSN simulations (Dolence et al. 2013; Couch 2013; Takiwaki et al. 2013). Explosions of more massive progenitors ($M > 15M_{\odot}$) appear problematic (Burrows 2013; Papish et al. 2014).

One-dimensional parametrized CCSN simulations involve assumptions about the explosion energies, mass-cuts (Utrobin 1993; Woosley & Weaver 1995). These parameters allow models to match the scatter in observational signatures and nucleosynthetic imprints (e.g., Umeda & Nomoto 2003; Heger & Woosley 2010; Moriya et al. 2010).

In the literature, it is often argued that massive stars with initial masses higher than about 25 – 30 $M_\odot$ collapse to a black hole rather than to a neutron star, without producing a bright supernova (e.g., Fryer 1999; Heger et al. 2003). This is because more massive stars have higher binding energies, which makes it more difficult to unbind the stellar envelopes. This may also depend on the size of the iron core formed in the interior of these massive stars. As discussed by Wallerstein et al. (1997) the iron core mass correlates with the ratio of the oxygen to carbon abundance at the end of helium burning, which is usually higher for a higher mass star. In particular, if the iron core mass exceeds the Tolman-Oppenheimer-Volkoff limit that is the maximum possible mass for a neutron star (Oppenheimer & Volkoff 1939; Oppenheimer & Snyder 1939), the formation of a black hole is the likely outcome. Recently Ugliano et al. (2012) investigate the question of the mass-dependence of neutron star/black-hole formation and show that stars less massive than 20 $M_\odot$ can result in black holes and stars of 20 – 40 $M_\odot$ can end their evolution with the formation of a neutron star. Hence, it is not fully understood which stars die as bright supernovae leaving neutron stars as remnants and which stars collapse into black holes with or without supernova.

Formation of the light curve and types of supernovae

The shock wave is generated in the silicon layer after the bounce of the collapsing core and strong neutrino–matter interaction. The large fraction of explosion energy is converted into kinetic and thermal energy of the shock. The first indication of the explosion is seen when the shock breaks out on the surface of the supernova progenitor. It takes hours to days for the shock to get to the surface. Approximately this time can be estimated according to the following formula:

$$t_{\rm shock} \sim \frac{R_{\rm progenitor}}{u_{\rm sound}}\,, \tag{1.1}$$

where $R_{\rm progenitor}$ is the radius of the supernova progenitor, and $u_{\rm sound}$ is the average sound speed in the envelope[7] (e.g. Falk & Arnett 1977; Shigeyama et al. 1987).

The phenomenon, called "shock breakout", can be seen as a short-lasting X-ray/ultraviolet flash, because the temperature on the shock front reaches millions of Kelvin. The duration of the flash depends on the radius of the progenitor

$$\Delta t_{\rm shock} \sim \frac{R_{\rm progenitor}}{c}\,, \tag{1.2}$$

where c is the speed of light. The duration of the shock breakout for supergiant progenitors does not exceed hours (see e.g. Ensman & Burrows 1992; Calzavara & Matzner 2004; Tolstov et al. 2013).

The envelope matter is optically thick, and the photon diffusion time exceeds thousands of years. The opacity is dominated by electron scattering. The propagating shock heats and accelerates the envelope depositing a fraction of its thermal and kinetic energy into the matter. After the shock breakout the outermost layers relaxes from the shock. The

[7]Note, that the shock wave propagates with the velocity exceeding the sound speed.

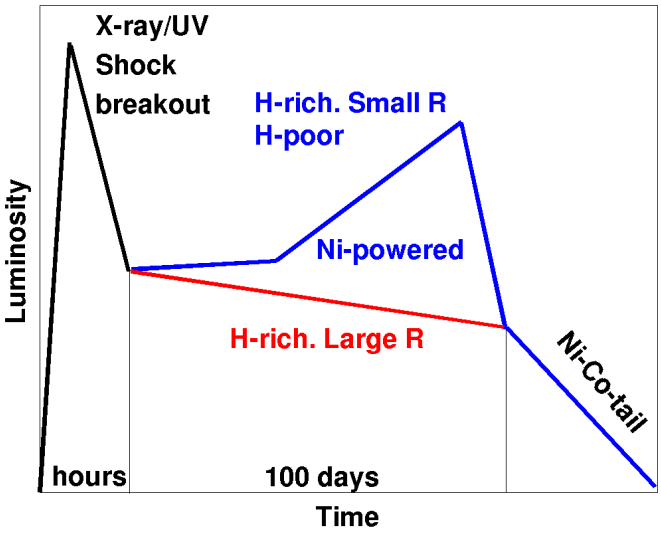

Figure 1.4: Schematic illustration of supernova light curves.

surface of $\tau \approx 1$ (i.e. photosphere front) is still located in these outermost layers at this time.

During first days the radius of the progenitor star increases tremendously (in hundreds to thousands times depending on the compactness of the progenitor). The envelope expands and adiabatically cools allowing the electrons to recombine. The recombination and cooling wave is established if the condition are fulfiled (Grasberg & Nadezhin 1976). The recombination and cooling front propagates inwards through the envelope (along decreasing mass coordinate) with the velocity greatly exceeding the sound speed. Note, that due to radial expansion the overall direction of the photospheric motion[8] is outwards. The front of recombination and cooling wave indicate the drop in electron density and electron-scattering opacity, and also represent the surface of $\tau \approx 1$.

Following the recombination and cooling wave the photosphere propagates through the diverse chemical layers. Consequently, the light curve of the supernova presents the radiation from the subsequently located layers which appears on the path of the photosphere.

The number of factors influence the characteristics of an emerging supernova light curve. Schematically the light curve of a pure supernova is illustrated in Figure 1.4. Generally, the photospheric phase follows after the shock breakout. At this time the light curve traces the front of the photosphere. The shock-deposited energy is released during the so-called plateau phase when the luminosity remains nearly constant. Hydrogen-rich extended (hundreds to thousands of solar radii) progenitors have long supernova plateau lasting about 100 days (Barbon et al. 1979). Hydrogen-rich compact (approximately ten to hundred solar radii) progenitors and those without hydrogen envelope produce light

[8]Photospheric velocity is the radial velocity of the shell where the photosphere is located.

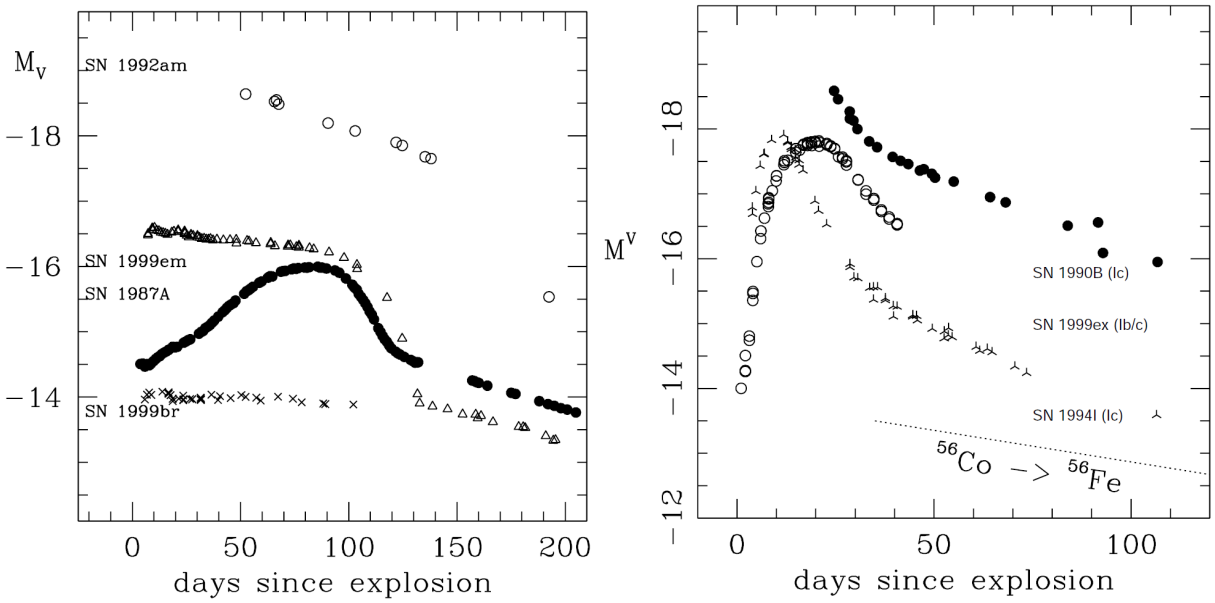

Figure 1.5: Observed examples of light curves of core-collapse supernovae.
Upper panel: Evolution of the absolute visual-band magnitude ($M_V \sim -2.5 \log F_V$, where F_V is energy flux in visual spectral band) of two SNe IIP (1999em, 1992am) and two SNe II-pec (1987A, 199br).
Bottom panel: Evolution of the absolute visual-band magnitude of a few SNe Ibc (1990B, 1999ex, 1994I). Both plots are taken from Hamuy (2003b).

curves with a prominent maximum after their explosions. The re-brightening occurs when moving inwards photosphere encounters high-energy photons synthesized in nickel-cobalt radioactive decay and diffusing outwards. One of the famous example of such light curve is the supernova exploded in 1987 in the nearby galaxy Large Magellanic Cloud (SN 1987A, see e.g., Arnett et al. 1989b; Imshennik & Nadezhin 1989).

When at later time the envelope becomes transparent then the light curve follows the instant deposition of energy synthesized in radioactive decay of nickel and cobalt[9].

Observationally, core-collapse supernovae are broadly classified into Type I and Type II, depending on the absence or the presence of hydrogen lines in their early spectra, respectively (Minkowski 1941; Shklovskii 1966).

Massive stars which retain their hydrogen envelopes produce hydrogen-rich Type II core-collapse supernovae. Not all massive stars can retain their hydrogen envelope until the end of their lives. Several factors such as metallicity, pulsations, degree of rotation, and binary interactions may determine how massive stars lose their outer layers (see e.g., Langer & El Eid 1986; Woosley et al. 1993; Heger et al. 1997). High metallicity (i.e. the mass fraction of metals in the envelope) can be either initial or increased by convective

[9]Radioactive decay of nickel and cobalt is: $^{56}\mathrm{Ni} + e^- \rightarrow {}^{56}\mathrm{Co} + \nu_e$ (half-time is about 6 days), $^{56}\mathrm{Ni} + e^- \rightarrow {}^{56}\mathrm{Fe} + \nu_e$ (half-time is about 77 days).

and rotationally-induced mixing. Convection and rotation operate as a mixer stirring underlying freshly synthesized heavy elements and overlying unburnt matter). The higher metallicity implies higher mass-loss rate (Vink et al. 2001). Pulsations serve as an additional mechanism for reducing the stellar mass (Yoon & Cantiello 2010). Being a companion of the binary system the star easily loses its mass via Roche lobe overflow (Paczyński 1971; Podsiadlowski et al. 1992). When stars lose their hydrogen envelope they produce hydrogen-poor Type I explosions.

There is a few observationally distinct supernova types. Based on the recent progress of stellar evolution theory these types are connected to certain evolution of the massive star (see e.g., Smith et al. 2011; Langer 2012). Depending on the hydrogen mass retained and the radius at the onset of the explosion the supernova can be:

- Type II plateau (SN IIP) if the progenitor has about 5 to 20 $M_\odot$ envelope polluted by hydrogen, and its radius exceeds several hundreds of solar radii (Shklovskii 1960; Grasberg et al. 1971). The main property of these supernovae is the so-called "plateau" phase in the light curve during which the luminosity remains around a constant level. The duration of the plateau phase and luminosity during this time directly depend on the radius of the progenitor, the ejected mass and explosion energy (Litvinova & Nadezhin 1985; Popov 1993);

- Type II peculiar (SN II-pec) if the progenitor retains similar mass of hydrogen-polluted envelope, but if it is more compact, i.e. its radius does not exceed hundred solar radii. The classical example is the SN 1987A with a prominent bump-like light curve;

- Type IIn ("narrow lines", SN IIn) if the progenitor is similar to the first case but explodes in dense medium (either originally dense or left by extensive mass-loss) (Moriya et al. 2011). The light curve is powered by interaction of the supernova shock and supernova ejecta with the surrounding medium causing low ejecta velocities, therefore, narrow emission lines in the spectra;

- Type II linear (SN IIL) if retained envelope mass which contains hydrogen is less than 1-2 $M_\odot$, and a star is very extended before the explosion (thousands of solar radii) (Langer 2012). It is supposed that the stars at the upper mass boundary for core-collapse supernovae loses a large fraction of their mass retaining only a shallow hydrogen layer and produce SN IIL. The signature of this type of supernovae is a linear decayed luminosity after the peak value;

- Type IIb (SN IIb) if the progenitor has lost almost the entire hydrogen atmosphere. The hydrogen lines quickly disappear from the spectra after maximum phase;

- Type Ib or Ic (SN Ib/Ic) if the progenitor has lost the entire hydrogen atmosphere (Langer 2012). The early spectra do not exhibit any hydrogen line, but have strong helium lines. According to Filippenko (1997); Turatto (2003) those supernovae which do not exhibit helium lines classified as SNe Ic (Dessart et al. 2012a). The explosion

of SN Ib/Ic originates from the bared helium core of this massive star. Most probably that the progenitor of SN Ib/Ic is a companion of a binary system and it has lost its mass while transferring it via Roche lobe overflow to the second star (Yoon et al. 2010; Eldridge et al. 2013).

Figure 1.5 demonstrates the diversity of core-collapse supernova light curves. As mentioned above, the plateau of SNe IIP is caused by the propagation of cooling and recombination wave moving from the surface into inner regions and radiating the shock-deposited energy. The bump of SNe II-pec and SNe Ibc is produced by flux of thermalized high-energy photons from radioactive nickel decay. The tails of the most supernova light curves are powered by the instant energy deposition from radioactive decay. For illustration, the dotted line in the right panel of Figure 1.5 shows the slope of nickel-to-cobalt-to-iron decay[10]. The late-time supernova luminosity directly indicates the amount of radioactive nickel-56 ejected into the envelope during the explosion. The typical amount of nickel is 0.004 – 0.1 $M_\odot$ (Patat et al. 1994). Note, that the large fraction of nickel-56 produced during the evolution and the earliest stage of the explosion collapses into neutron star.

1.2.2 100 – 260 $M_\odot$ stars

Very massive stars with initial masses of about 100 – 260 $M_\odot$ constitute the main focus of the current study. If these stars avoid heavy mass loss, they end their lives with pair instability explosions (Fowler & Hoyle 1964; Bisnovatyi-Kogan & Kazhdan 1967; Rakavy & Shaviv 1967; Barkat et al. 1967; Fraley 1968; Kippenhahn & Weigert 1990; Heger & Woosley 2002). One of the reasons for our specific interest in this class of supernovae is that their explosion mechanism is fully comprehensible and therefore easily reproduced by numerical simulations.

Similar to the stars discussed in the previous section, these very massive stars follow hydrostatic hydrogen, helium, carbon and neon burning. After core carbon exhaustion and a brief neon burning phase, they undergo a thermonuclear explosion due to the dynamical instability caused by the creation of electron-positron pairs in their oxygen cores. This can be understood as follows.

A higher mass star has a lower central density for a given central temperature, because the density ρ_c and temperature T_c in the centre of the star are bound through its mass M as

$$T_c \sim M^k \rho_c^{1/3} \quad \Rightarrow \quad \rho_c \sim \frac{T_c^3}{M^{3k}} \,. \tag{1.3}$$

The exponent k depends on the equation of state. $k = 1/6$ corresponds to the case of radiation-dominated pressure ($P = a\,T^4$). If pressure is dominated by gas pressure ($P = \mathcal{R}\rho T/\mu$), we have $k = 2/3$ (see Figure 1.6). Note that in the case of dominant ideal

[10] In case of the instant energy deposition from radioactive decay the resulting luminosity declines according to the decay rate: $L_{\rm tail} \sim M_{\rm Ni} e^{-t/\tau}$, where τ is life-time of nickel isotope.

gas pressure the density–temperature relation depends also on molecular weight:

$$\rho_c \sim \frac{T_c^3}{\mu_c^3 M^{3k}}, \tag{1.4}$$

where μ_c is the molecular weight in the centre of the star.

Assuming the polytropic star ($T \sim \rho^{1/3}$) it is easy to show that the role of radiation in the pressure depends on the mass of the star. Let us define the ratio of gas pressure to total pressure as $\beta = \frac{P_{\rm gas}}{P_{\rm total}}$. Then

$$\beta^{1/3}(1+\beta) \sim M^{2/3}, \tag{1.5}$$

where M is the mass of star. Eddington (1926), Wagoner (1969a) and Zel'dovich et al. (1981) find the following relation between β and the mass of star M.

$$1-\beta = 0.00298 \left(\frac{M}{M_\odot}\right)^2 (\mu\beta)^4, \tag{1.6}$$

where μ is the mean molecular weight (i.e. the number of atomic units per particle). If radiation contributes to the pressure equally to matter then $\beta = 1/2$ and the mass value is about 50 $M_\odot$. For higher mass stars radiation contributes stronger to the pressure and plays a significant role in their evolution. We provide an illustration from Kippenhahn & Weigert (1994) demonstrating the dominant contributor to the pressure (crystal matter, relativistic degenerate electron gas, non-relativistic degenerate electron gas, ideal gas, radiation pressure) depending on temperature and density.

During the late stages of the evolution of a very massive star, when the core undergoes carbon burning, the temperature approaches one billion Kelvin. Photons are distributed approximately according to Planck's law and some fraction of the photons in the high energy tail of the energy distribution exceed the rest-mass energy of an electron-positron pair ($m_e c^2 \sim 0.5$ MeV). These photons spontaneously produce such pairs ($2\gamma \leftrightarrows e^- e^+$).

The transition "photons $\longrightarrow$ matter" leads to a drop in the radiation pressure which compensates the gravity force and holds the hydrostatic equilibrium. Dominant radiation pressure and the emerging relativistic electrons reduces the resistance of the matter to the gravitational force (Kippenhahn & Weigert 1994). Consequently, the structural adiabatic index $\gamma = \frac{d(\ln P)}{d(\ln \rho)}$ falls below the dynamical stability threshold of 4/3, which leads to the dynamical instability in the core.

An explanation of this instability is given by Zel'dovich et al. (1981) from first principles. Firstly, we consider the idealistic situation when the pressure is dominated by radiation and matter does not contribute to the pressure. In this case the entropy is the sum of two terms responsible for matter and radiation. The final expression for the pressure is given by:

$$P = \frac{a}{3}\left(\frac{4}{3}\frac{S}{a}\right)^{4/3} \rho^{4/3}, \tag{1.7}$$

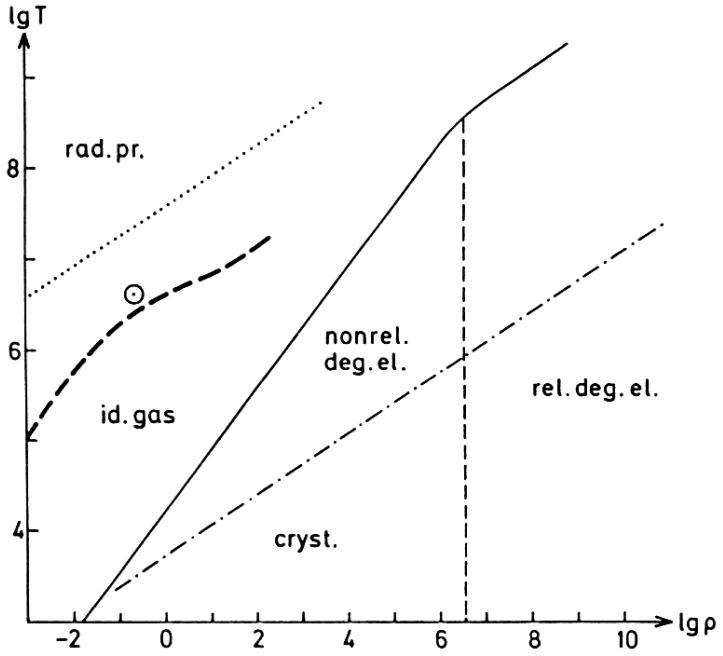

Figure 1.6: The plot from Kippenhahn & Weigert (1994) demonstrating the main contributors to the pressure in the thermodynamical phase space.

where $a = 7.56 \times 10^{-15}\,\mathrm{erg\ cm^{-3}K^{-4}}$ is the radiation constant. The corresponding line is the left-hand straight line in Figure 1.7.

Secondly, if the temperature is very high, and photon energy significantly exceeds the rest-mass energy of electron-positron pairs $kT \gg m_e c^2$, the energy density as well as the entropy is the sum of the two terms responsible for radiation and a relativistic electron-positron gas, without account for ions. In this case the pressure–density relation is given by:

$$P = A\,\frac{a}{3}\left(\frac{4}{3}\frac{S}{a}\right)^{4/3}\rho^{4/3}\,, \tag{1.8}$$

where $A \simeq 0.3$ is a numerical factor. The right-hand straight line in Figure 1.7 is responsible for this situation. Figure 1.7 illustrates that in the intermediate case between two considered states with $P \sim \rho^{4/3}$ corresponds to the transition where the adiabatic index drops below 4/3. More detailed study by Blinnikov et al. (1996) shows that the photon gas at temperature of 10^9 K begins to create pairs, and the adiabatic index sharply drops below 4/3. While exceeding temperature of 3×10^9 K, the adiabatic index becomes slightly higher than 4/3 and asymptotically approaches 4/3. Pair creation instability resembles ionisation, since a fraction of energy is spent not to increase the temperature, but to create pairs. The result should be the development of a dynamical instability and the consequent implosion because the pressure gradient is not able to compensate the gravitational attraction.

The mentioned explanation is applicable to the conditions occurring in the interior of very massive stars after carbon exhaustion. The dynamical collapse of the oxygen core

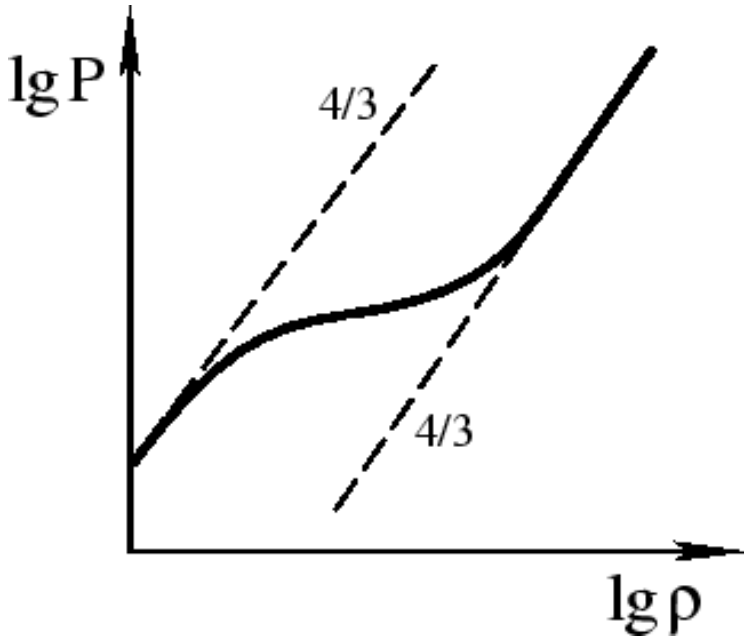

Figure 1.7: The plot from Zel'dovich et al. (1981) demonstrating the transition between two states both with the same pressure-density relation ($\gamma = 4/3$). The left-hand straight line corresponds to radiation-dominated pressure, and the right-hand straight line represents the state in which both radiation and pairs contribute to pressure.

occurs if a large fraction of the core enters the instability region ($\gamma < 4/3$). According to Kippenhahn & Weigert (1990), 40% (in mass) of the star should enter the instability region in the density – temperature – diagram. The crucial characteristic quantity for massive star evolution is the oxygen-core mass. The earliest estimates indicate a critical oxygen-core mass of about 30 $M_\odot$ for the pair creation instability (Rakavy & Shaviv 1967). The corresponding initial mass is about 65 $M_\odot$. Recent results show that this limit in terms of the initial mass is about 100 $M_\odot$ for metal free non-rotating stars (Heger & Woosley 2002).

The dynamical instability results in the collapse of the oxygen core and the consequent explosive oxygen burning when temperature exceeds 2×10^9 K. When the amount of energy produced by nuclear burning is high enough, the collapse ceases and is reversed into an explosion. Even when the amount of the released nuclear energy is less than the binding energy of the star, this can lead to the ejection of a fraction of the envelope (Woosley et al. 2007a). After such an eruption the star relaxes to hydrostatic conditions on a thermal timescale. If the remaining stellar mass is sufficiently high for pair creation the star undergoes a second pair creation episode accompanied by another eruption. This phenomena is the so-called "pulsational pair instability". This scenario may occur for stars with initial masses from 100 $M_\odot$ to 140 $M_\odot$. After several such eruptions, the star cannot undergo the pair-instability anymore, and finally collapses to a black hole.

For higher mass stars of about 140 – 260 $M_\odot$ with more massive oxygen cores, the energy

generated during explosive oxygen and explosive silicon burning is sufficient to terminate the collapse and reverse it to an explosion. The resulting thermonuclear explosion is known as the pair instability supernova (PISN, hereafter) which completely destroys the star by expelling the whole final mass into the circumstellar medium. Hence, PISNe are efficiently enriching the interstellar matter with heavy elements. We discuss the nucleosynthetic imprint of PISNe in Chapter 3.

The upper limit for this mass range (260 $M_{\odot}$) corresponds to the case when all the energy generated in the explosive burning is equal to the binding energy of the star (Bond et al. 1982, 1984). Very roughly the amount of energy generated in oxygen and silicon burning is:

$$E_{\mathrm{nucl.bind}}^{\mathrm{Oxygen}} - E_{\mathrm{nucl.bind}}^{\mathrm{Nickel}} = E_{\mathrm{bind}}\,, \tag{1.9}$$

where $E_{\mathrm{nucl.bind}}$ means the nuclear binding energy of the oxygen core (the sum of the entire nuclear energy stored in the whole ensemble of nuclei) and E_{bind} is its gravitational binding energy. However, it should be taken into account that only a fraction of oxygen in the oxygen core is burnt, and in turn a fraction of silicon is converted into iron. The estimated critical value of the oxygen core mass is 100 $M_{\odot}$ which corresponds roughly to an initial stellar mass of 200 $M_{\odot}$. More recent studies show that stars with an initial mass above 260 $M_{\odot}$ (helium core mass higher than 137 $M_{\odot}$) collapse to black holes after the pair instability phase (Heger & Woosley 2002).

A number of factors can influence the growth of the oxygen core and the above-mentioned mass range for pair instability explosions can vary accordingly. The most important consideration is chemical mixing. A variation of the convection parameters during evolutionary calculations, in particular, the degree of overshooting can strongly change the final size of the oxygen core (Langer & El Eid 1986; Meynet & Maeder 1987; Maeder & Meynet 1987). These studies show that the minimum initial mass for the star to experience the pair creation instability varies between 100 $M_{\odot}$ and 120 $M_{\odot}$. The corresponding oxygen core mass is about 64 $M_{\odot}$.

Rotationally-induced chemical mixing can also lead to an increase of the stellar core mass (Heger et al. 2000; Hirschi et al. 2004; Yoon & Langer 2005; Yoon et al. 2012a; Yusof et al. 2013). For a very high rotational velocity, even the so-called chemically homogeneous evolution can occur, which can significantly reduce the lower initial mass limit for pair instability progenitors (Yoon & Langer 2005; Yoon et al. 2012a; Chatzopoulos & Wheeler 2012). For example, a 65 $M_{\odot}$ star with an initial rotation of about 300 km/s can produce a 60 $M_{\odot}$ pair instability progenitor (Yoon et al. 2012a; Chatzopoulos & Wheeler 2012).

Additionally, rotation acts against gravity and weakens the gravitational attraction. The consequence of this is an increase of the mass limits for pair instability progenitor (Glatzel et al. 1985; Carr & Glatzel 1986).

Nickel production and the connection to SLSNe

Pair instability explosions completely disrupt very massive stars. Consequently, many tens of solar masses of newly produced heavy elements are expelled into the circumstellar medium. Depending on the progenitor mass, 30 – 60 $M_{\odot}$ of hydrogen, 50 – 80 $M_{\odot}$ of

helium, 2 $M_\odot$ of carbon, about 40 – 50 $M_\odot$ of oxygen, 10 – 25 $M_\odot$ of silicon and up to 55 $M_\odot$ of radioactive nickel (i.e., ^{56}Ni) are returned into the surroundings (Heger & Woosley 2002; Umeda & Nomoto 2002; Kozyreva et al. 2014b).

There is no other kind of supernova which enriches the interstellar medium so strongly. For example, average nucleosynthetic yields of CCSN are: hydrogen — 10 $M_\odot$, helium — 8 $M_\odot$, carbon — 0.3 $M_\odot$, oxygen — 3 $M_\odot$, silicon — 0.4 $M_\odot$, radioactive nickel — 0.2 $M_\odot$ (see e.g., Patat et al. 1994; Woosley & Weaver 1995). An ordinary Type Ia SN, which is believed to originate from a thermonuclear explosion of a carbon-oxygen white dwarf at the Chandrasekhar limit, produces no hydrogen and helium, 0.3 – 0.5 $M_\odot$ of carbon, 0.1 – 0.4 $M_\odot$ of oxygen, 0.1 $M_\odot$ of silicon and 0.5 – 0.7 $M_\odot$ of radioactive nickel (Iwamoto et al. 1999; Travaglio et al. 2004).

The most impressive case among other elemental yields is the amount of the produced radioactive nickel ^{56}Ni. Theoretical models indicate that PISNe from sufficiently massive progenitors can produce large amounts of nickel (up to 55 $M_\odot$) without any fine-tuned assumption on the explosion physics. In contrast, the largest amount of nickel produced during a typical CCSN explosion is limited to about 0.5 $M_\odot$ (Woosley & Weaver 1995; Iwamoto et al. 1998; Limongi & Chieffi 2003; Umeda & Nomoto 2008; Heger & Woosley 2010). In principle, an extreme amount of nickel of up to about 6 $M_\odot$ can be produced in a CCSN. However, that should correspond to an explosion of an unusually massive progenitor having a helium core of about 40 $M_\odot$ with an exceptionally high explosion energy of up to $\sim 10^{52}$ erg (Moriya et al. 2010).

The amount of radioactive nickel strongly affects the SN light curve and directly governs the late time luminosity. An extended mixing of nickel into the hydrogen-helium envelope enhances the luminosity during the photospheric phase for some Type II supernovae (Shigeyama & Nomoto 1990; Kasen & Woosley 2009). The peak luminosity of hydrogen-deficient Type Ibc SNe is determined by the amount of radioactive nickel (Dessart et al. 2011).

The recently discovered superluminous supernovae (SLSNe) have peak luminosities $M_V < -21$ mag ($L > 10^{44}$ erg s^{-1}) which is 2 – 3 magnitudes higher than those of usual CCSNe[11]. Some of them appear as SNe Ic[12] (Pastorello et al. 2010) having very high late time luminosities (Gal-Yam 2012b). In particular, such properties support the presence of large amounts of nickel powering the maximum and late time phases. Although there exist other possible mechanisms which could explain these properties, the pair creation mechanism remains one of the most natural ones. We discuss the application of PISNe to SLSNe in the section 1.3.

1.2.3 260 – 5×10^4 $M_\odot$ stars

Stars in this mass range follow similar evolutionary stages as those of PISN progenitors (140 – 260 $M_\odot$) in general. Because of the weak dependence of $\frac{T_c}{{\rho_c}^{1/3}} \sim M^{1/6}$ on mass

[11] Absolute discovered luminosities of CCSNe range from –14 mag to –19 mag (i.e. $10^{41} - 10^{43}$ erg s^{-1}) Hamuy (2003b); Richardson et al. (2014).

[12] SN Ic is that lacking hydrogen and helium lines in the early spectra.

(see equation 1.3) for very massive stars, the central temperature-density conditions after core carbon exhaustion are almost the same as those of stars with masses 140 – 260 $M_\odot$ (see section 1.2.2). As a result, the cores of stars of this mass range (260 $-$ 5 $\times$ 10^4 $M_\odot$) also undergo the pair creation instability after carbon exhaustion in the core. However, these stars have relatively low ratios of nuclear energy released from explosive burning to binding energy of the star. Consequently, they cannot explode despite the explosive nuclear burning due to the pair instability. The cores eventually collapse into black holes following the on-going contraction resulting from the pair instability without displaying a supernova phenomenon.

1.2.4 $5 \times 10^4 - 10^5\,M_\odot$ stars

The existence of supermassive stars of $5 \times 10^4 - 10^5\,M_\odot$ is a matter of debate even for the case of metal-free (Population III) stars (Sonoi & Umeda 2012). At the same time these supermassive objects are interesting for the feedback to the evolution of the early Universe as we explain below. Other studies, however, show no difficulties to form such a supermassive stars and indicate their stability (Wagoner 1969a; Abel et al. 2002; Hosokawa & Omukai 2009; Hosokawa et al. 2013, and references therein). Moreover, the presence of these stars may be needed to explain the abundances of metal-poor stars (see e.g., Carr et al. 1984; Abel et al. 2002; Denissenkov & Hartwick 2014).

Despite their high masses, supermassive stars do not collapse directly to black holes but explode already at the beginning of their nuclear fusion history (Bisnovatyi-Kogan 1968; Fuller et al. 1986; Whalen et al. 2013b; Chen et al. 2014).

These stars cannot have hydrostatic nuclear burning phases but undergo a brief quasi-static contraction on a Kelvin-Helmholtz timescale accompanied by rapid nuclear burning. It starts with the hot *pp*-cycle (also known as rapid proton capture, or *rp*-process) for the case of zero-metallicity but the energy generated by this cycle is not large enough to maintain the hydrostatic equilibrium of the star. The central temperature continues to increase until the 3α-reaction starts. Once some carbon and oxygen are thus produced, the hot βCNO-cycle starts to govern the evolution. The βCNO-cycle is a CNO-cycle limited by the β^+ decay lifetimes of ^{14}O and ^{15}O. If the metallicity differs from zero, hydrogen burns via the βCNO-cycle from the beginning. The energy released from this βCNO-cycle is sufficient to terminate the gravitational contraction and to explode the star as a thermonuclear supernova. Chen et al. (2014) however show that their 55500 $M_\odot$ star undergoes a static hydrogen burning during 1.7 Myr, and then following relativistic effects explodes due to explosive helium burning. The amount of energy generated during an explosion of supermassive star exceeds 10^{55} erg.

In general the presence of these supermassive progenitors is possible only at very high redshifts ($z > 10$) and it is difficult to discover the resulting supernovae. The light curves of these supernovae are very broad according to the huge ejecta mass. It would be possible for future missions to discover them during their long-lasting (up to 10 years) plateau phase shifted to infra-red wavelengths (Whalen et al. 2013b). The shock breakout event of this explosion is shifted from the ultraviolet/X-ray (usual for an average SNe-IIP shock

breakout) to the visual band, and its duration and luminosity would be similar to an average local supernova in the observer's frame. However, the luminosity of the shock breakout can be greatly weakened due to intergalactic absorption (Ride & Walker 1977; Wilms et al. 2000; Richter et al. 2008; Willingale et al. 2013). Nevertheless, by chance such a supernova can be discovered if it is gravitationally lensed (Patel et al. 2013; Nordin et al. 2014).

The result of such an explosion is the full disruption of the star. Similar to PISNe an explosion of supermassive star ejects the whole mass (about $10^5\ M_\odot$) into the circumstellar medium (Johnson et al. 2013; Whalen et al. 2013e). The bulk elements are hydrogen and helium with a fraction of CNO–elements for the case of initially metal-free stars. For the case of Population II and possibly Population I[13] the medium can also be enriched by some other isotopes like ^{7}Li, ^{13}C, ^{17}O, ^{25}Mg, ^{26}Al (Hillebrandt et al. 1987).

Even a small amount of angular momentum can strongly affect the above picture (Fowler 1966b; Fricke 1974). The centrifugal force helps nuclear energy generation to resist the gravitational contraction and reduce the general relativity effects (Fuller et al. 1986), which can hold the star in quasi-static equilibrium longer than in the case without rotation. This allows to generate somewhat more heavy elements in the interiors of supermassive stars than in the case of no-rotation, which is a subject of future study.

1.2.5 Beyond stability

The possibility of stars with masses up to $10^7\ M_\odot$ were discussed by Fowler (1966b) for the explanation of quasi-stellar objects. Readers are referred to a number of reviews dedicated to this problem for detailed explanations on the the general relativity effects which play the most important role for the stability of objects with masses greater than a few $10^5\ M_\odot$ (Fowler 1966a; Zel'dovich & Novikov 1971; Shapiro & Teukolsky 1983). Here we only want to mention that such supermassive objects reach instability before any nuclear energy is released and hence they immediately collapse to black holes on a dynamical timescale (Fuller et al. 1986).

We summarize the above-discussed fates of massive, very massive and supermassive stars in Figure 1.8. The nomenclature is according to Carr et al. (1984).

1.3 Superluminous supernovae

During the last few years a number of superluminous supernovae (SLSNe) has been discovered (Gal-Yam et al. 2009; Quimby et al. 2011; Gal-Yam 2012a; Richardson et al. 2014). Their peak luminosities in the optical band ($M_V \lesssim -21$ mag) exceed those of usual supernovae by 2 – 3 magnitudes (i.e. by a factor of 10 in luminosity). Some of them were classified as Type Ic SNe (Chomiuk et al. 2011; Inserra et al. 2013; Lunnan et al. 2013).

[13]Population I stars are those of about solar metallicity ($Z = 0.02$). Population II is an environment with a metallicity of $10^{-4} - 10^{-3}$. Population III stars are born at metal free circumstances (i.e. zero metallicity, $Z = 0$).

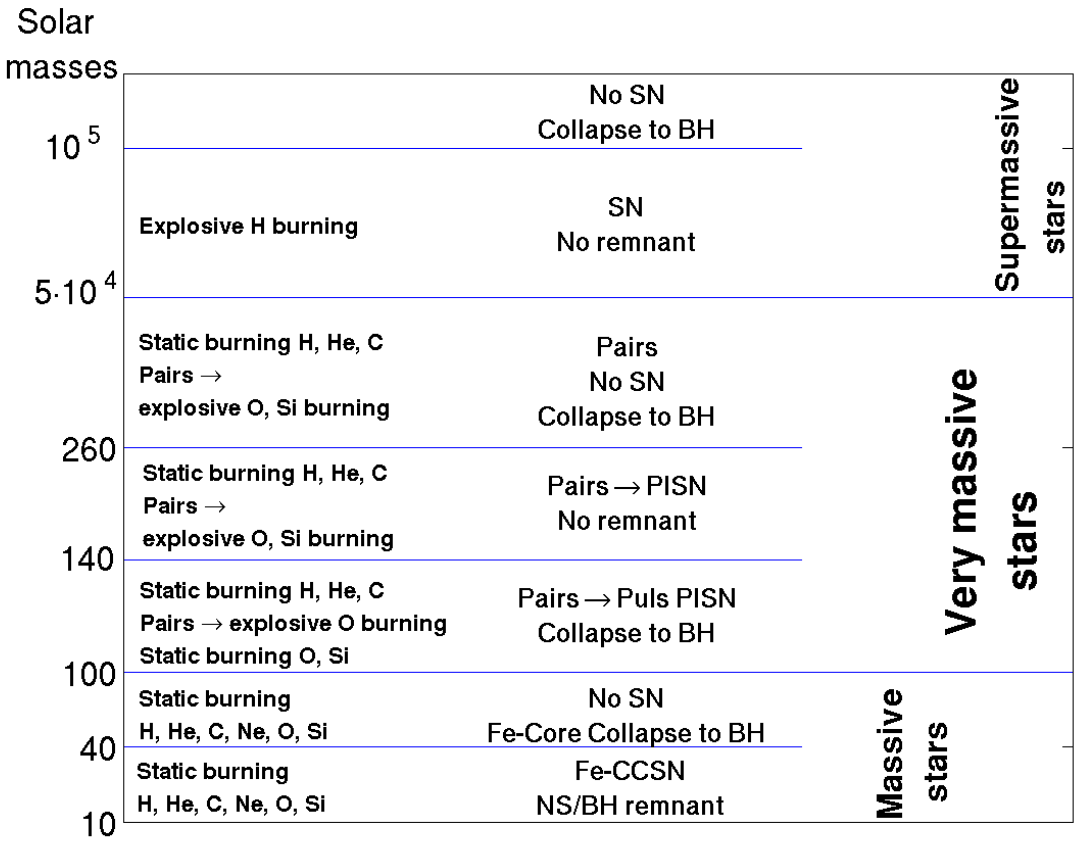

Figure 1.8: Schematic illustration of the fate of massive, very massive and supermassive stars. The labels and acronyms mean: "NS" — neutron star, "BH" — black hole, SN — supernova, "CCSN" — core-collapse supernova, "Pairs" — pair creation instability, "PISN" — pair instability supernova,"Puls PISN" — pulsational pair instability supernova.

One of the most extensively discussed supernovae of this kind is SN 2007bi (Gal-Yam et al. 2009). Some other SLSNe have very broad light curves and low photospheric velocities, and are classified as Type IIn supernovae[14].

There are three possible engines for supernovae to reach such extreme luminosities:

1. The nickel-powered mechanism,
2. The interaction-powered mechanism,
3. The magnetar-powered mechanism.

We briefly explain each of them below.

1.3.1 Nickel-powered SLSNe

It has been argued for unusually large amounts of radioactive material (namely ^{56}Ni) produced during the explosion to explain the high peak luminosities, slow declines of the light curves and spectral features of some SLSNe (see Gal-Yam 2012a, for a review). The best candidate for this subtype is SN 2007bi (Gal-Yam et al. 2009). The spectral and photometric analyses of SN 2007bi indicate that more than 3 $M_\odot$ of nickel were ejected during the explosion[15]. Ordinary core-collapse Type II and Type Ibc supernovae produce no more than about 0.5 $M_\odot$ of radioactive nickel (cf. Drout et al. 2011). Nevertheless, theoretically it is possible to produce up to about 6 $M_\odot$ of nickel from CCSN explosions but this requires an unusually high explosion energy exceeding 10^{52} erg (Moriya et al. 2010). As we discussed above, however, the most natural way to produce such a large amount of nickel to explain SN 2007bi is a PISN explosion, for which the supernova energy is not a tuning parameter. In Chapter 4 we discuss this possibility in a detailed way.

1.3.2 Interaction-powered SLSNe

If a star explodes into a relatively dense circumstellar environment, the interaction of the supernova ejecta with the circumstellar matter may result in a peculiar supernova (Chevalier 1981, 1982; Smith 2014). One of the main characteristics of such interaction supernovae is strong narrow-lined emission in the spectra (Drake et al. 2010; Quimby et al. 2011). Therefore, these supernovae are classified as Type IIn supernovae ("n" = narrow). Some of SNe IIn display high peak luminosities and appear as SLSNe. The best example is SN 2006gy (Agnoletto et al. 2009). Some of them are also accompanied by a relatively high ultraviolet luminosity, for instance SN 2009kf Botticella et al. (2010).

The powering energy comes from the collision of the supernova ejecta with the matter surrounding the supernova progenitor. In this case, instead of a typical shock breakout

[14]SNe IIn are Type II SNe with narrow hydrogen emission lines in their spectra

[15]Recently several authors pointed out that an energy input by a milliseconds magnetar can also explain the observed light curves of this supernova (Kasen & Bildsten 2010; Dessart et al. 2012b; Inserra et al. 2013), and the PISN origin of SN 2007bi is still a matter of debate.

event, the radiation-driven shock deposits energy into the surrounding matter. Their progenitors are believed to be massive stars that undergo very strong steady winds or sporadic mass eruptions due to strong pulsations prior to their explosion like Luminous Blue Variables (LBVs) (e.g., Humphreys & Davidson 1994; Vink 2012; Fadeyev 2011, 2012; Blinnikov & Sorokina 2010; Chevalier & Irwin 2011; Moriya et al. 2011; Chevalier 2012; Moriya et al. 2013).

The interaction scenario usually considers core-collapse supernova explosions at a moderate kinetic energy of 3 – 5 foe[16]. The mass of the circumstellar medium consists of 3 – 10 $M_\odot$ of dense matter. However, the case of SN 2006gy can also be explained by the interaction of the ejecta with the shells made during the pulsational pair-instability episode (Woosley et al. 2007a; so-called "pulsational pair instability supernovae" mentioned in section 1.2.2). SLSNe caused by interaction need not always appear as Type IIn. The interaction of the supernova shock with a super-extended steady wind can explain the behavior of superluminous SNe II with linearly declining light curves (SN IIL, Blinnikov & Bartunov 1993; Young et al. 2005). In this case the shock breaks out in the surrounding wind and produces a high peak optical luminosities.

In the interaction scenario, there is no need of radioactive nickel for explaining the peak luminosities of the supernovae — the amount of radioactive material could be similar to that of average CCSNe ($\sim$ 0.05 $M_\odot$). Since the maximum luminosity in interaction supernovae does not depend on the amount of radioactive nickel, such interaction models can assume an arbitrary amount of nickel. This property can be applied to supernovae with a fast decline, for instance SN 2005kj and SN 2006aa Taddia et al. (2013).

1.3.3 Magnetar-powered SLSNe

The light curves of at least some SLSNe often have a short rise time (Nicholl et al. 2013) and, therefore could not possibly involve very massive stars (Inserra et al. 2013; Nicholl et al. 2013). For those, the magnetar-driven mechanism proposed by a few studies appears promising in the frame of SLSNe (Woosley 2010; Kasen & Bildsten 2010; Dessart et al. 2012b).

It is believed that a small fraction of neutron stars are born with very strong magnetic fields (10^{14} Gauss) and rapid rotation (periods of several to ten ms) (Ferrario & Wickramasinghe 2008; Heras 2012). In the presence of such magnetars the light curve of usual core-collapse SN Ibc or SN II explosions could be changed drastically. Firstly, during the maximum phase the newly born magnetar adds a large fraction of thermalized spin-down energy into the ejecta and strongly increases the peak luminosity. The deposited energy is provided by rapid rotation. Secondly, at later times it continues to power the supernova light keeping it at a high level for a long duration after the luminosity peak. Therefore, the light curve can have a fast rise and a long-lasting tail.

The simulations involving magnetar radiation include a finite number of parameters.

[16] 1 foe $\equiv 10^{51}$ erg is an average explosion energy of core-collapse supernova. The abbreviation originates from the phrase "fifty one erg"

These are the usual ones for CCSN calculations (i.e. ejecta mass, explosion energy, mass-cut, fall-back) along with additional parameters related to the magnetar, namely, its magnetic field strength and spin period. Recent observational studies indicate that a number of superluminous SNe Ic can be best explained by magnetars (Inserra et al. 2013; Nicholl et al. 2013). Some very luminous SNe IIL and IIP can also be explained by the magnetar scenario (Kasen & Bildsten 2010; Barkov & Komissarov 2011).

1.4 Motivation for the thesis work

The interest in pair instability explosions has rapidly grown during the last several years. One of the reasons is the discovery of superluminous supernova (SLSN) in 2007 (SN 2007bi, Gal-Yam et al. 2009). The high peak luminosity of this supernova (– 21.6 mag), its long-lasting light curve and spectral estimates strongly implies a large amount of nickel produced during the explosion ($> 3\ M_{\odot}$). This is far above the average nickel amount produced in core-collapse supernovae ($0.1 - 0.2\ M_{\odot}$) and type Ia supernovae ($0.5\ M_{\odot}$). This property can be best explained by the pair instability supernova (PISN) mechanism as discussed above (Section 1.3; Heger & Woosley 2002; Umeda & Nomoto 2002; Langer 2009). Although other possibilities like very energetic core-collapse supernova explosions or magnetar-powered supernovae have also been suggested (Woosley 2010; Kasen & Bildsten 2010; Dessart et al. 2012b; Inserra et al. 2013; Nicholl et al. 2013), SN 2007bi still remains the best candidate for a PISN in the local Universe.

As discussed above, a PISN progenitor has to be very massive ($140\ M_{\odot} \lesssim M \lesssim 260\ M_{\odot}$). The existence of such very massive stars in the nearby Universe is well confirmed as mentioned in Sect. 1.1 (see also Crowther et al. 2010; Schneider et al. 2014), and their initial masses may be up to about $300\ M_{\odot}$. These very massive stars are supposed to lose mass rapidly during their entire evolution via strong stellar winds and/or episodic eruptions, given that their luminosities are close to the Eddington limit (Vink et al. 2011). The stellar wind mass loss rate is usually higher for a higher metallicity in the star because of the strong impact of metal lines on the radiation pressure at the stellar surface (e.g., Vink et al. 2001). This means that very massive stars would lose too much mass to produce a PISN with a metallicity higher than a certain limit.

Recent stellar evolution models by Langer et al. (2007) and Yusof et al. (2013) indicate that the metallicity threshold for PISN progenitors ($Z_{\rm PISN}$) can be as high as $Z = 0.006$, which is comparable to the metallicity of the Large Magellanic Cloud. Langer et al. (2007) point out that one PISN out of 1000 supernovae can occur with such a metallicity limit (i.e., $Z_{\rm PISN} \approx 0.006$). This raises the following important questions: How can we distinguish PISNe from other supernovae? Can we confirm that some of the observed superluminous supernovae like SN 2007bi have a PISN origin?

Therefore, we were motivated to calculate the realistic evolution of possible PISN progenitors, i.e. the evolution of stars with initial masses of about $140 - 260\ M_{\odot}$. So far there have been mostly successful self-consistent models at zero metallicity (El Eid et al. 1983; Heger & Woosley 2002). These models are applicable only for an environment lacking in

metals, i.e., the early Universe. It is important to note that many of the discovered SLSNe are located in galaxies with metallicities far from zero (see e.g. Young et al. 2010; Neill et al. 2011). The above-mentioned superluminous SN 2007bi exploded in a dwarf galaxy with a metallicity of about $Z_{\odot}/3$ (Young et al. 2010). This observational fact requires the computation of evolutionary models which possess a reasonable fraction of elements heavier than helium. The evolution of stars strongly depends on the fraction of metals and differs for those lacking of them.

Another reason for activating a study on PISNe in the local Universe lies in the nucleosynthetic signature of these explosions. According to theoretical predictions the progenitor star of a PISN is completely disrupted during the explosion. This should greatly affect the chemical condition in which the next generations of stars are formed. Note that these explosions might have been one of the first contributors to the enrichment of the medium with metals in the early Universe. Abundances of elements in extremely metal-poor stars in our Galaxy measured recently, however, contradict the PISN yields (Umeda & Nomoto 2003; Frebel et al. 2005). Nevertheless, the question is not fully understood yet and needs more precise methods for measuring the abundances. At the same time detailed calculations of PISN yields exist only for metal free or extremely metal poor models (Heger & Woosley 2002; Umeda & Nomoto 2002). The study by El Eid & Langer (1986) was done for the solar metallicity but gives only the approximate mass distribution of a limited number of species.

Models for PISNe at solar metallicity were computed by Langer & El Eid (1986) and El Eid & Langer (1986). However, the nuclear network used for these calculations included only a simple $\alpha-$chain network for the advanced nuclear evolution. Langer et al. (2007) and Yusof et al. (2013) presented PISN progenitor models at metallicities of 0.001 and 0.002/0.006, respectively. The calculations by Langer et al. (2007) were terminated prior to the explosive burning phase and those by Yusof et al. (2013) were done with a nuclear network limited by magnesium isotopes and the neon burning phase, and stop prior to oxygen ignition (for a description of the network see Ekström et al. 2012). Therefore, we found a lack of self-consistent detailed calculations of PISN for the local Universe.

This thesis aims to explore the consequences of local PISNe using an extensive nuclear network in the stellar evolution code for nucleosynthesis calculations, and a radiation hydrodynamics code for the supernova light-curve modelings, as a follow-up study of Langer et al. (2007). For this purpose, we chose two models with initial masses of 150 $M_{\odot}$ and 250 $M_{\odot}$ at a metallicity 0.001 from Langer et al. (2007) and calculated their evolution from core carbon exhaustion through the pair instability explosion using the last version of the Binary stellar evolution code (Yoon et al. 2010) with our newly implemented extended nuclear network (Chapter 3). Then, the shock breakout and light curve of the resulting supernovae were calculated with the radiation hydrodynamics code STELLA developed by Blinnikov (Blinnikov & Tolstov (2011), Chapter 4).

More specifically, the aims of this thesis are:

1. to follow the evolution of PISN progenitors of 150 $M_{\odot}$ and 250 $M_{\odot}$ with an initial metallicity of 0.001 throughout the explosive nuclear burning phase,

2. to provide the detailed nucleosynthesis of these PISN models and investigate the contribution of PISNe compared to core-collapse supernovae to the chemical evolution,

3. to compute the explosions of these PISNe with a radiation hydrodynamics code and to discuss the observational properties of PISNe exploding in the local Universe, and

4. to compare the simulated light curves and other photospheric characteristics of our PISNe with observed luminous and superluminous supernovae.

1.5 Thesis content

- Chapter 2. Nuclear networks.

  In Chapter 2, we briefly explain the nuclear burning stages in the interior of massive stars. For the purpose of our thesis work, we had to implement a silicon burning network into the stellar evolution code. Therefore, we describe specific details on silicon burning, and the corresponding assumptions and prescriptions adopted in the network. We discuss details about improving the nuclear network and implementation of silicon burning in the stellar evolution code. In the thesis work we extended the nuclear network up to germanium isotopes (the overall number of isotopes is 204) that involves 2134 reaction rates using the F. Timmes' public nuclear network (Timmes 1998, 1999). We also constructed an energy generation rate table for the evolutionary calculations during silicon burning, which enables stable and rapid stellar evolution calculations.

- Chapter 3. Explosion and nucleosynthesis of low redshift pair instability supernovae

  Based on the modification of the nuclear network, we computed two PISN models of 150 $M_{\odot}$ and 250 $M_{\odot}$ at a metallicity 0.001 from core carbon exhaustion until the on-going explosion. The early evolution of our models is described in Langer et al. (2007). We emphasize that these models are applicable to observed supernovae exploding in the local Universe. We present a nucleosynthesis analysis comparing the nucleosynthetic yields of our models with those of zero-metal PISN models. Additionally, we analyse the nucleosynthetic yields of one generation of stars including massive and very massive star, i.e. yields of both CCSNe and PISNe. We briefly discuss the signature of the PISN contribution to the chemical evolution of the local Universe.

- Chapter 4. Observational properties of low redshift pair instability supernovae.

  We were also motivated to compare observational properties of our PISN explosions with observed luminous and superluminous supernovae. For this purpose we mapped our evolutionary models (150 $M_{\odot}$ and 250 $M_{\odot}$) into the radiation hydrodynamics code STELLA and computed the appearance of the shock breakout events and the photospheric evolution. We compare both models with observed supernovae. We

found that our 150 $M_{\odot}$ PISN model resembles bright SNe IIP and our higher mass PISN resembles a superluminous SN Ic during its maximum phase. We conclude the chapter with a list of criteria which can help to distinguish PISNe from CCSNe.

- Chapter 5. Summary

  Chapter 5 contains the summary and the overall conclusions of this work, as well as an outlook.

Chapter 2

Nuclear networks

This chapter briefly describes the nuclear reaction networks needed for stellar evolution calculations. The improvement of the nuclear network in the evolution code used for this thesis work is explained. This mainly concerns the implementation of silicon-burning reactions that are needed for simulating pair-instability supernova explosions. The performance and application of the new networks are discussed.

2.1 Thermonuclear fusion in stars

The life of a star consists of several nuclear "burning" stages. These are the sequential phases of core thermonuclear burning of hydrogen, helium, carbon, neon, oxygen, and silicon (Bethe 1939; Fowler 1954; Burbidge et al. 1957; Wallerstein et al. 1997). Thermonuclear reactions at the stellar center cease with the formation of an iron core, since no exothermic fusion reaction can occur beyond this point.

Stars spend most of their lives (up to 90%) on processing hydrogen into helium in the core, and most of the rest on core helium burning. The advanced burning stages beyond helium burning last for a very short time compared to the main hydrogen and helium burning phases. Table 2.1 presents the various nuclear burning timescales in massive stars of 15 $M_{\odot}$ and 25 $M_{\odot}$. Due to such successive burning stages a massive star has a layered chemical structure at the end of its life.

Many massive stars are believed to end their lives in spectacular supernovae (Heger et al. 2003). By observing successive supernova spectra one can follow the photosphere of the ejecta moving inwards. The photosphere thus works as a scanner of the radial chemical stratification (Filippenko 1997; Elmhamdi et al. 2003). At early times, hydrogen Balmer lines are most prominent in hydrogen-rich type II SNe. At late times, helium, oxygen, sodium, calcium, silicon and other intermediate elements successively become visible spectroscopically. The photospheres of Type Ib SNe start being located in helium-rich layers early on and in inner shells composed of heavy elements at later times. Type Ic SNe show

firstly intermediate mass elements like silicon, and more heavy elements become visible later.

Supernova remnants provide another probe to look at the chemical structure of a star after its death. Remnants of type Ia supernovae, which originate from thermonuclear explosions of carbon-oxygen white dwarfs in close binary systems (Taam 1980; Iben & Tutukov 1984), indeed display a layered chemical structure (Lewis et al. 2003; Kosenko et al. 2010; Lopez et al. 2011). However, remnants of core-collapse explosions appear less chemically stratified. The reason for this may be that chemical mixing due to Rayleigh-Taylor instabilities occurs more efficiently in core-collapse explosions than in thermonuclear supernovae (Joggerst et al. 2009).

To correctly interpret these observations, we need to construct models of supernova progenitors with an evolutionary code that properly considers the most important isotopes and nuclear reactions for the entire evolutionary history of stars. The energy generated in nuclear reactions can heat the matter and create sufficient pressure to balance the gravitational attraction to maintain the hydrostatic equilibrium of the star. Therefore, it is important to consider all meaningful burning processes with appropriate rates that contribute to the energy balance.

Changes in the nuclear reaction rates can have a great impact on the evolution of stars. The reaction $^{12}\mathrm{C}(\alpha,\gamma)^{16}\mathrm{O}$ provides the most prominent example (Caughlan & Fowler 1988). As shown by Weaver & Woosley (1993), the chemical structure, final core masses and nucleosynthetic yields can vary significantly for different values of the multiplier to the basic value of this rate. Another example is the evolution of supermassive stars for which the maximum value of the energy generation rate of the CNO-cycle can determine whether a star explodes or collapses (Fricke 1973).

Before this thesis work, the stellar evolution code of the Bonn stellar physics group employed a nuclear network that could follow the evolution until oxygen burning (Yoon et al. 2006, 2010). Given that we are interested in pair-instability explosions that involve nuclear fusions beyond this, the nuclear network had to be revised accordingly, which is described below.

2.2 Nuclear networks for stellar evolution

To model pair-instability supernovae properly, we implemented two different nuclear networks that include silicon burning. One is a simplified network limited to 39 isotopes. This network allows to take the major isotopes including ^{4}He, ^{12}C, ^{16}O, ^{20}Ne, ^{24}Mg, ^{28}Si, ^{32}S, and ^{56}Ni into account and hence accounts for the main energy production contributors (Timmes et al. 2000). This network was constructed for a pilot study of the thesis to test the capability of the code for modeling pair-instability explosions. The second network is based on the Torch code by F. Timmes and consists of 200 isotopes (Timmes 1998). This network allows to follow the detailed nucleosynthesis during the pre-supernova evolution of massive stars, although it is computationally more expensive than the 39 isotopes network (see Chapter 3). Here we explain the technical details on this development.

Table 2.1: Evolutionary timescales of the burning stages in massive stars. Data are taken from Weaver et al. (1978); Woosley et al. (2002); Hirschi et al. (2004); Chieffi & Limongi (2013) (references 1,2,3,4 in the table respectively) together with the names of the codes that were used to produce the data. All models are at solar metallicity and non-rotating.

Burning stage	H Myr	He Myr	C kyr	Ne yr	O yr	Si	reference
Time	15 $M_\odot$						
	12.4	1.3	6.4	7	1.8	6 d	Kepler (1)
	11.1	2	2	0.7	2.6	18 d	Kepler (2)
	11.3	1.3	4	3	2.4	30 mins	Geneva (3)
	13.1	0.9	21	15.5	3.4	7.2 h	Franec (4)
Time	25 $M_\odot$						
	7.3	0.7	0.2	1.2	0.5	1.4 d	Kepler (1)
	6.7	0.8	0.5	0.9	0.4	16.8 h	Kepler (2)
	6.6	0.7	0.3	0.9	0.3	5 mins	Geneva (3)
	7.2	0.5	12	5.2	1.2	2.4 h	Franec (4)
T, K 15 $M_\odot$	3.5×10^7	1.8×10^8	8.3×10^8	1.6×10^9	1.9×10^9	3.3×10^9	Kepler (2)

2.2.1 Nuclear networks and silicon burning

Mathematically a nuclear network can be described as a system of differential equations. Each equation takes into account all reactions that contribute to the abundance change of a given isotope, and can be written as the following:

$$\frac{dY_k}{dt} = \sum_{ij} R_{ij} Y_i Y_j - \sum_i R_{ik} Y_i Y_k \,, \tag{2.1}$$

where the first term in the right-hand side is responsible for the reactions producing a given isotope k (from isotopes i and j) and the second term is responsible for the reactions destroying the isotope k. The factor R is the reaction rate which depends on individual cross sections and has a steep dependence on temperature and density (Timmes 1999).

The system can be rewritten in matrix form:

$$\dot{Y} = \mathrm{A}Y \quad . \tag{2.2}$$

In general the matrix elements of A differ by orders of magnitude because the reaction rates are non-linearly dependent on thermodynamical conditions. This property of the nuclear network matrix is called "stiffness". Another important feature is the sparseness of the matrix **A**. Solving such a system of equations is not trivial because the large scatter

Table 2.2: The Jacobian matrix for our simplified nuclear network describing silicon burning. An empty cell means a zero Jacobian element. A cell with a circle means a non-zero Jacobian element.

	H	He	C	O	Ne	Mg	Si	S	Ar	Ca	Ti	Cr	Fe	Ni
H	○	○					○	○	○	○	○	○	○	○
He	○	○	○	○	○	○	○	○	○	○	○	○	○	○
C		○	○	○										
O		○	○	○	○									
Ne		○	○	○	○	○								
Mg		○	○	○	○	○	○							
Si	○	○	○	○		○	○	○						
S	○	○		○			○	○	○					
Ar	○	○						○	○	○				
Ca	○	○							○	○	○			
Ti	○	○								○	○	○		
Cr	○	○									○	○	○	
Fe	○	○										○	○	○
Ni	○	○											○	○

of the element values should be properly considered. The solver for such a system should be an accurate implicit solver that can deal with a stiff and sparse system (Timmes et al. 2000).

In particular, silicon burning is different from carbon and oxygen burnings that involve fusion of two equal nuclei. A temperature of $\sim 4 \times 10^9$ K does not support the condition for reaction $2\,^{28}\mathrm{Si} \rightarrow {}^{56}\mathrm{Ni}$ because the kinetic energy of the silicon nuclei is not sufficient to exceed the Coulomb barrier. During the silicon burning stage the main reactions involve the α-chain isotopes that capture and release α-particles. There is also an additional set of flows including proton capture and release that plays an important role for silicon burning. This can be included into the $\alpha-$chain network implicitly. This property makes the silicon-burning network very stiff, compared to other nuclear burning processes.

To show the structure of a nuclear network, the Jacobian matrix J is often used, which is defined as $J = \frac{\partial \mathrm{A}}{\partial Y}$ (2-dimensional matrix). Its entries represent flows of the reactions involving two given isotopes (the intersection of the corresponding row and column). Table 2.2 demonstrates the Jacobian for the simplified nuclear network representing silicon burning, namely the α-chain network. Other examples of Jacobian matrices for nuclear networks including 13, 19, 47, 76, 127, 200 and 487 isotopes can be found in Timmes (1999).

2.2.2 Implementation of silicon burning in the Binary Evolution Code

In this thesis we focus on the late stages of stellar evolution. These are all burning stages beyond core hydrogen and core helium burning (Wallerstein et al. 1997; Woosley et al. 2002). So far the Binary Stellar Evolution Code (BEC) of the Bonn stellar physics group had a nuclear network including up to oxygen burning. The old version of the network is fairly comprehensible for describing core hydrogen and helium burning.

Table 2.3: The lists of isotopes for the old and revised nuclear networks in BEC. "Explicit" isotopes are explicitly involved into the reaction network. "Implicit" isotopes participate in the network implicitly. See section 2.2.2 for details.

old	new		old	new	
	explicit	implicit		explicit	implicit
${}^{1}_{0}n$	${}^{1}n$		${}^{19}_{9}$F		
${}^{1}_{1}$H	${}^{1}_{1}$H		${}^{20}_{10}$Ne	${}^{20}_{10}$Ne	
${}^{2}_{1}$H	${}^{2}_{1}$H		${}^{21}_{10}$Ne	${}^{21}_{10}$Ne	
${}^{3}_{2}$He	${}^{3}_{2}$He		${}^{22}_{10}$Ne	${}^{22}_{10}$Ne	
${}^{4}_{2}$He	${}^{4}_{2}$He		${}^{23}_{11}$Na	${}^{23}_{11}$Na	
${}^{6}_{3}$Li	${}^{6}_{3}$Li		${}^{24}_{12}$Mg	${}^{24}_{12}$Mg	
${}^{7}_{3}$Li	${}^{7}_{3}$Li		${}^{25}_{12}$Mg	${}^{25}_{12}$Mg	
${}^{7}_{4}$Be	${}^{7}_{4}$Be		${}^{26}_{12}$Mg	${}^{26}_{12}$Mg	
${}^{9}_{4}$Be	${}^{9}_{4}$Be		${}^{26}_{13}$Al		
${}^{8}_{5}$B	${}^{8}_{5}$B		${}^{27}_{13}$Al		${}^{27}_{13}$Al
${}^{10}_{5}$B	${}^{10}_{5}$B		${}^{28}_{14}$Si	${}^{28}_{14}$Si	
${}^{11}_{5}$B	${}^{11}_{5}$B		${}^{29}_{14}$Si	${}^{29}_{14}$Si	
${}^{11}_{6}$C	${}^{11}_{6}$C		${}^{30}_{14}$Si	${}^{30}_{14}$Si	${}^{31}_{15}$P
${}^{12}_{6}$C	${}^{12}_{6}$C			${}^{32}_{16}$S	${}^{35}_{17}$Cl
${}^{13}_{6}$C	${}^{13}_{6}$C			${}^{36}_{18}$Ar	${}^{39}_{19}$K
${}^{12}_{7}$N	${}^{12}_{7}$N			${}^{40}_{20}$Ca	${}^{43}_{21}$Sc
${}^{14}_{7}$N	${}^{14}_{7}$N			${}^{44}_{22}$Ti	${}^{47}_{23}$V
${}^{15}_{7}$N	${}^{15}_{7}$N			${}^{48}_{24}$Cr	${}^{51}_{25}$Mn
${}^{16}_{8}$O	${}^{16}_{8}$O			${}^{52}_{26}$Fe	${}^{55}_{27}$Co
${}^{17}_{8}$O	${}^{17}_{8}$O		${}^{56}_{26}$Fe	${}^{56}_{26}$Fe	
${}^{18}_{8}$O	${}^{18}_{8}$O			${}^{56}_{28}$Ni	

To calculate the final stages of stellar evolution and pair-instability explosions, the code should include oxygen and silicon burning. For this reason we modified the list of involved isotopes and reactions. The first step of this task was to implement a simplified network based on the network already implemented into the code. Table 2.3 shows the isotopes included in the old and new versions of the nuclear network. Table 2.4 shows the

corresponding list of nuclear reactions.

Table 2.4: Old list of nuclear reactions with the list of additional reactions used in the extended network. The old network is used for hydrogen, helium and carbon burning. The full list of reactions is suitable for complete oxygen burning and simplified silicon burning.

old list		additional	
		explicit	implicit
1	$2p(p,e^+\nu)^3_2\mathrm{He}$		
2	$^3_2\mathrm{He}(^3_2\mathrm{He},2p)\alpha$		
3	$\alpha(^3_2\mathrm{He},\gamma)^7_4\mathrm{Be}$		
4	$2\alpha(\alpha,\gamma)^{12}_6\mathrm{C}$	$^{12}_6\mathrm{C}(\gamma,\gamma)3\alpha$	
5	$^6_3\mathrm{Li}(p,\alpha)^3\mathrm{He}$		
6	$^7_3\mathrm{Li}(p,\alpha)\alpha$		
7	$^7_3\mathrm{Li}(\alpha,\gamma)^{11}_5\mathrm{B}$		
8	$^7_4\mathrm{Be}(e^-,\nu)^7_3\mathrm{Li}$		
9	$^7_4\mathrm{Be}(^3_2\mathrm{He},2p)2\alpha$		
10	$^7_4\mathrm{Be}(p,\gamma)^8_5\mathrm{B}$		
11	$^7_4\mathrm{Be}(\alpha,\gamma)^{11}_6\mathrm{C}$		
12	$^9_4\mathrm{Be}(p,\mathrm{D})2\alpha$		
13	$^9_4\mathrm{Be}(p,\alpha)^6_3\mathrm{Li}$		
14	$^8_5\mathrm{B}(e^+,\nu)2\alpha$		
15	$^8_5\mathrm{B}(\alpha,p)^{11}_6\mathrm{C}$		
16	$^8\mathrm{B}^5(\gamma,p)^7_4\mathrm{Be}$		
17	$^{10}_5\mathrm{B}(p,\alpha)^7_4\mathrm{Be}$		
18	$^{11}_5\mathrm{B}(p,\gamma)^{12}_6\mathrm{C}$		
19	$^{11}_5\mathrm{B}(p,\gamma)3\alpha$		
20	$^{11}_6\mathrm{C}(e^+,\nu)^{11}_5\mathrm{B}$		
21	$^{11}_6\mathrm{C}(p,\gamma)^{12}_7\mathrm{N}$		
22	$^{12}_6\mathrm{C}(p,\gamma)^{13}_6\mathrm{C}$		
23	$^{12}_6\mathrm{C}(n,\gamma)^{13}_6\mathrm{C}$		
24	$^{12}_6\mathrm{C}(\alpha,\gamma)^{16}_8\mathrm{O}$		
25	$^{12}_6\mathrm{C}(^{12}_6\mathrm{C},\alpha)^{20}_{10}\mathrm{Ne}$		
26	$^{12}_6\mathrm{C}(^{12}_6\mathrm{C},p)^{23}_{11}\mathrm{Na}$		
27	$^{13}_6\mathrm{C}(p,\gamma)^{14}_7\mathrm{N}$		
28	$^{13}_6\mathrm{C}(\alpha,n)^{16}_8\mathrm{O}$		
29	$^{12}_7\mathrm{N}(e^-,\nu)^{12}_6\mathrm{C}$		
30	$^{14}_7\mathrm{N}(p,\gamma)^{15}_7\mathrm{N}$		
31	$^{14}_7\mathrm{N}(\alpha,\gamma)^{18}_8\mathrm{O}$		
32	$^{15}_7\mathrm{N}(p,\alpha)^{12}_6\mathrm{C}$		
33	$^{15}_7\mathrm{N}(p,\gamma)^{16}_8\mathrm{O}$		
34	$^{15}_7\mathrm{N}(2\alpha,\gamma)^{23}_{11}\mathrm{Na}$		

continuing at the next page

	old list	additional	
		explicit	implicit
35	${}^{16}_{8}\mathrm{O}(\alpha,\gamma)^{20}_{10}\mathrm{Ne}$	${}^{16}_{8}\mathrm{O}(\gamma,\alpha)^{12}_{6}\mathrm{C}$	
36	${}^{16}_{8}\mathrm{O}({}^{12}_{6}\mathrm{C},\alpha)^{24}_{12}\mathrm{Mg}$		
37	${}^{16}_{8}\mathrm{O}({}^{16}_{8}\mathrm{O},\alpha)^{28}_{14}\mathrm{Si}$	${}^{16}_{8}\mathrm{O}({}^{16}_{8}\mathrm{O},\gamma)^{32}_{16}\mathrm{S}$	${}^{16}_{8}\mathrm{O}({}^{16}_{8}\mathrm{O},p)^{31}_{15}\mathrm{P}$
38	${}^{17}_{8}\mathrm{O}(p,\alpha)^{14}_{7}\mathrm{N}$		
39	${}^{16}_{8}\mathrm{O}(p,\gamma)^{17}_{8}\mathrm{O}$		
40	${}^{17}_{8}\mathrm{O}(p,\gamma)^{18}_{8}\mathrm{O}$		
41	${}^{17}_{8}\mathrm{O}(\alpha,n)^{20}_{10}\mathrm{Ne}$		
42	${}^{18}_{8}\mathrm{O}(p,\alpha)^{15}_{7}\mathrm{N}$		
43	${}^{18}_{8}\mathrm{O}(\alpha,\gamma)^{22}_{10}\mathrm{Ne}$		
44	${}^{20}_{10}\mathrm{Ne}(\alpha,\gamma)^{24}_{12}\mathrm{Mg}$		
45	${}^{20}_{10}\mathrm{Ne}(n,\gamma)^{21}_{10}\mathrm{Ne}$		
46	${}^{20}_{10}\mathrm{Ne}(\gamma,\alpha)^{16}_{8}\mathrm{O}$		
47	${}^{21}_{10}\mathrm{Ne}(\alpha,\gamma)^{25}_{12}\mathrm{Mg}$		
48	${}^{21}_{10}\mathrm{Ne}(\alpha,n)^{24}_{12}\mathrm{Mg}$		
49	${}^{21}_{10}\mathrm{Ne}(n,\gamma)^{22}_{10}\mathrm{Ne}$		
50	${}^{22}_{10}\mathrm{Ne}(\alpha,\gamma)^{26}_{12}\mathrm{Mg}$		
51	${}^{22}_{10}\mathrm{Ne}(\alpha,n)^{25}_{12}\mathrm{Mg}$		
52	${}^{23}_{11}\mathrm{Na}(p,\alpha)^{20}_{10}\mathrm{Ne}$		
53	${}^{23}_{11}\mathrm{Na}(p,\gamma)^{24}_{12}\mathrm{Mg}$		
54	${}^{24}_{12}\mathrm{Mg}(\alpha,\gamma)^{28}_{14}\mathrm{Si}$	${}^{24}_{12}\mathrm{Mg}(\gamma,\alpha)^{20}_{10}\mathrm{Ne}$	${}^{24}_{12}\mathrm{Mg}(\alpha,p)^{27}_{13}\mathrm{Al}(p,\gamma)^{28}_{14}\mathrm{Si}$
55	${}^{24}_{12}\mathrm{Mg}(n,\gamma)^{25}_{12}\mathrm{Mg}$		
56	${}^{25}_{12}\mathrm{Mg}(n,\gamma)^{26}_{12}\mathrm{Mg}$		
57	${}^{25}_{12}\mathrm{Mg}(\alpha,n)^{28}_{14}\mathrm{Si}$		
58	${}^{25}_{12}\mathrm{Mg}(\alpha,\gamma)^{29}_{14}\mathrm{Si}$		
59	${}^{26}_{12}\mathrm{Mg}(\alpha,n)^{29}_{14}\mathrm{Si}$		
60	${}^{26}_{12}\mathrm{Mg}(\alpha,\gamma)^{30}_{14}\mathrm{Si}$		
61	${}^{28}_{14}\mathrm{Si}(n,\gamma)^{29}_{14}\mathrm{Si}$	${}^{28}_{14}\mathrm{Si}(\gamma,\alpha)^{24}_{12}\mathrm{Mg}$ ${}^{28}_{14}\mathrm{Si}(\alpha,\gamma)^{32}_{16}\mathrm{S}$	${}^{28}_{14}\mathrm{Si}(\gamma,p)^{27}_{13}\mathrm{Al}(p,\alpha)^{24}_{12}\mathrm{Mg}$ ${}^{28}_{14}\mathrm{Si}(\alpha,p)^{31}_{15}\mathrm{P}(p,\gamma)^{32}_{16}\mathrm{S}$
62	${}^{29}_{14}\mathrm{Si}(n,\gamma)^{30}_{14}\mathrm{Si}$		
		${}^{32}_{16}\mathrm{S}(\gamma,\alpha)^{28}_{14}\mathrm{Si}$	${}^{32}_{16}\mathrm{S}(\gamma,p)^{31}_{15}\mathrm{P}(p,\alpha)^{28}_{14}\mathrm{Si}$
		${}^{32}_{16}\mathrm{S}(\alpha,\gamma)^{36}_{18}\mathrm{Ar}$	${}^{32}_{16}\mathrm{S}(\alpha,p)^{35}_{17}\mathrm{Cl}(p,\gamma)^{36}_{18}\mathrm{Ar}$
		${}^{36}_{18}\mathrm{Ar}(\gamma,\alpha)^{32}_{16}\mathrm{S}$	${}^{36}_{18}\mathrm{Ar}(\gamma,p)^{35}_{17}\mathrm{Cl}(p,\alpha)^{32}_{16}\mathrm{S}$
		${}^{36}_{18}\mathrm{Ar}(\alpha,\gamma)^{40}_{20}\mathrm{Ca}$	${}^{36}_{18}\mathrm{Ar}(\alpha,p)^{39}_{19}\mathrm{K}(p,\gamma)^{40}_{20}\mathrm{Ca}$
		${}^{40}_{20}\mathrm{Ca}(\gamma,\alpha)^{36}_{18}\mathrm{Ar}$	${}^{40}_{20}\mathrm{Ca}(\gamma,p)^{39}_{19}\mathrm{K}(p,\alpha)^{36}_{18}\mathrm{Ar}$
		${}^{40}_{20}\mathrm{Ca}(\alpha,\gamma)^{44}_{22}\mathrm{Ti}$	${}^{40}_{20}\mathrm{Ca}(\alpha,p)^{43}_{21}\mathrm{Sc}(p,\gamma)^{44}_{22}\mathrm{Ti}$
		${}^{44}_{22}\mathrm{Ti}(\gamma,\alpha)^{40}_{20}\mathrm{Ca}$	${}^{44}_{22}\mathrm{Ti}(\gamma,p)^{43}_{21}\mathrm{Sc}(p,\alpha)^{40}_{20}\mathrm{Ca}$
		${}^{44}_{22}\mathrm{Ti}(\alpha,\gamma)^{48}_{24}\mathrm{Cr}$	${}^{44}_{22}\mathrm{Ti}(\alpha,p)^{47}_{23}\mathrm{V}(p,\gamma)^{48}_{24}\mathrm{Cr}$
		${}^{48}_{24}\mathrm{Cr}(\gamma,\alpha)^{44}_{22}\mathrm{Ti}$	${}^{48}_{24}\mathrm{Cr}(\gamma,p)^{47}_{23}\mathrm{V}(p,\alpha)^{44}_{22}\mathrm{Ti}$
		${}^{48}_{24}\mathrm{Cr}(\alpha,\gamma)^{52}_{26}\mathrm{Fe}$	${}^{48}_{24}\mathrm{Cr}(\alpha,p)^{51}_{25}\mathrm{Mn}(p,\gamma)^{52}_{26}\mathrm{Fe}$
		${}^{52}_{26}\mathrm{Fe}(\gamma,\alpha)^{48}_{24}\mathrm{Cr}$	${}^{52}_{26}\mathrm{Fe}(\gamma,p)^{51}_{25}\mathrm{Mn}(p,\alpha)^{48}_{24}\mathrm{Cr}$

continuing at the next page

old list	additional	
	explicit	implicit
	${}^{52}_{26}\mathrm{Fe}(\alpha,\gamma)^{56}_{28}\mathrm{Ni}$ ${}^{56}_{28}\mathrm{Ni}(\gamma,\alpha)^{52}_{26}\mathrm{Fe}$	${}^{52}_{26}\mathrm{Fe}(\alpha,p)^{55}_{27}\mathrm{Co}(p,\gamma)^{56}_{28}\mathrm{Ni}$ ${}^{56}_{28}\mathrm{Ni}(\gamma,p)^{55}_{27}\mathrm{Co}(p,\alpha)^{52}_{26}\mathrm{Fe}$

Simplified α-chain network

Reaction rates implemented in BEC are taken from Cameron (1959a); Fowler et al. (1975); Harris et al. (1983); Filippone (1985); Caughlan et al. (1985); Filippone (1986); Caughlan & Fowler (1988). We increased the number of significant digits in reaction rate expressions where the numerical coefficients were rounded. The prescription on screening factors are based on Graboske et al. (1973).

We completed the carbon and oxygen burning network with the necessary reactions (Table 2.4). For the main carbon and oxygen burning reactions we set the following fractions on the reaction channels based on Cameron (1959a,b); Caughlan & Fowler (1988); Timmes (1998); Woosley et al. (2002):

$$\begin{aligned} {}^{12}\mathrm{C} + {}^{12}\mathrm{C} &\longrightarrow \alpha + {}^{20}\mathrm{Ne} && 1 \\ &\longrightarrow p + {}^{23}\mathrm{Na} && 0 \\ &\longrightarrow n + {}^{23}\mathrm{Mg} && 0 \end{aligned} \tag{2.3}$$

$$\begin{aligned} {}^{12}\mathrm{C} + {}^{16}\mathrm{O} &\longrightarrow \alpha + {}^{20}\mathrm{Ne} && 0.5 \\ &\longrightarrow {}^{28}\mathrm{Si} && 0.5 \\ &\longrightarrow p + {}^{27}\mathrm{Al} && 0 \end{aligned} \tag{2.4}$$

$$\begin{aligned} {}^{16}\mathrm{O} + {}^{16}\mathrm{O} &\longrightarrow \alpha + {}^{28}\mathrm{Si} && 0.56 \\ &\longrightarrow p + {}^{31}\mathrm{P} && 0.34 \\ &\longrightarrow {}^{32}\mathrm{S} && 0.1 \end{aligned} \tag{2.5}$$

We also implemented the α-chain network (shown in Figure 2 of Timmes et al. (2000)) for silicon burning. Implicit isotopes with an odd charge number (^{27}Al, ^{31}P, ^{35}Cl etc.) involved in proton flows assumed to be in nuclear equilibrium: the number of produced nuclei is compensated by the number of captured nuclei. The necessary reactions concerning proton flows are therefore treated implicitly. These isotopes are not explicitly included in isotope array and the corresponding reactions are not explicitly included in the Jacobian matrix. Instead, these proton flows are implicitly added to the main reaction rates.

As an example let's consider ^{28}Si (Figure 2.1) and the additional proton flow for this isotope. The additional term related to ^{28}Si destruction is:

$$R^{-} = -\frac{R(p,\gamma)}{R(p,\alpha) + R(p,\gamma)}\,, \tag{2.6}$$

and the additional term related to ^{28}Si production is:

$$R^{+} = \frac{R(p,\alpha)}{R(p,\alpha) + R(p,\gamma)}\,, \tag{2.7}$$

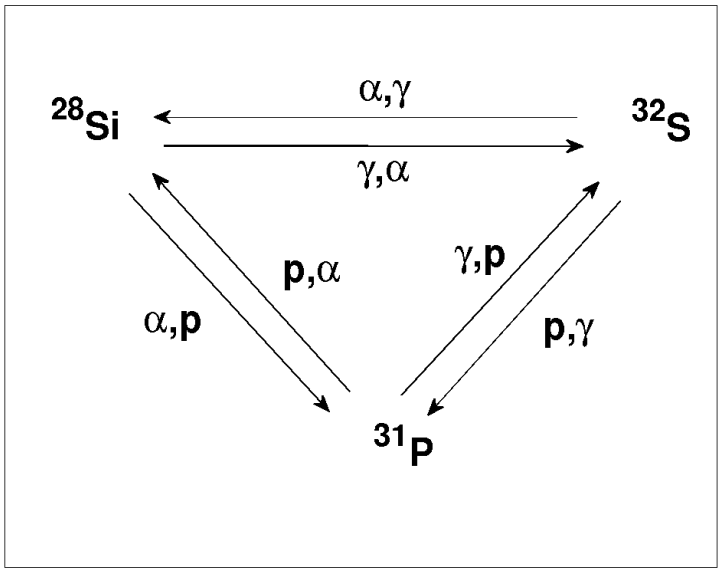

Figure 2.1: Illustration of $\alpha-$ and proton flows in the α-chain nuclear network.

where $R(p,\alpha)$ and $R(p,\gamma)$ are channels for ^{31}P destruction. Note that the ^{31}P abundance is kept constant at its equilibrium value.

Approaching NSE

After reaching the nuclear statistical equilibrium (NSE) condition at about $T \gtrsim 4.6\times10^9$ K the abundances of isotopes are calculated by F. Timmes' public NSE subroutine. Just before approaching the NSE critical temperature we made a smooth transition from the ordinary network to the NSE routine for a temperature range of $T = 4 - 4.6 \times 10^9$ K, by means of linear interpolation of the energy generation rate. This was done to avoid any discontinuity at the NSE critical condition ($T_{\rm critNSE} = 4.6 \times 10^9$ K).

Numerics

The first comparison between the isotope evolution calculated with the revised nuclear network, which involves $\alpha-$chain, and that with the Torch network of F. Timmes (Timmes 1998) showed discrepancy as demonstrated in Figure 2.2.

The inspection showed that the solver implemented in BEC for the nuclear network did not work correctly for the revised network. By default the solution was built on the linearization method described in Wagoner (1969b) which is based on the 2nd order Runge-Kutta method of solving a system of differential equations. The final sparse matrix for the derived system of algebraic equations had a specific form for which the solution was

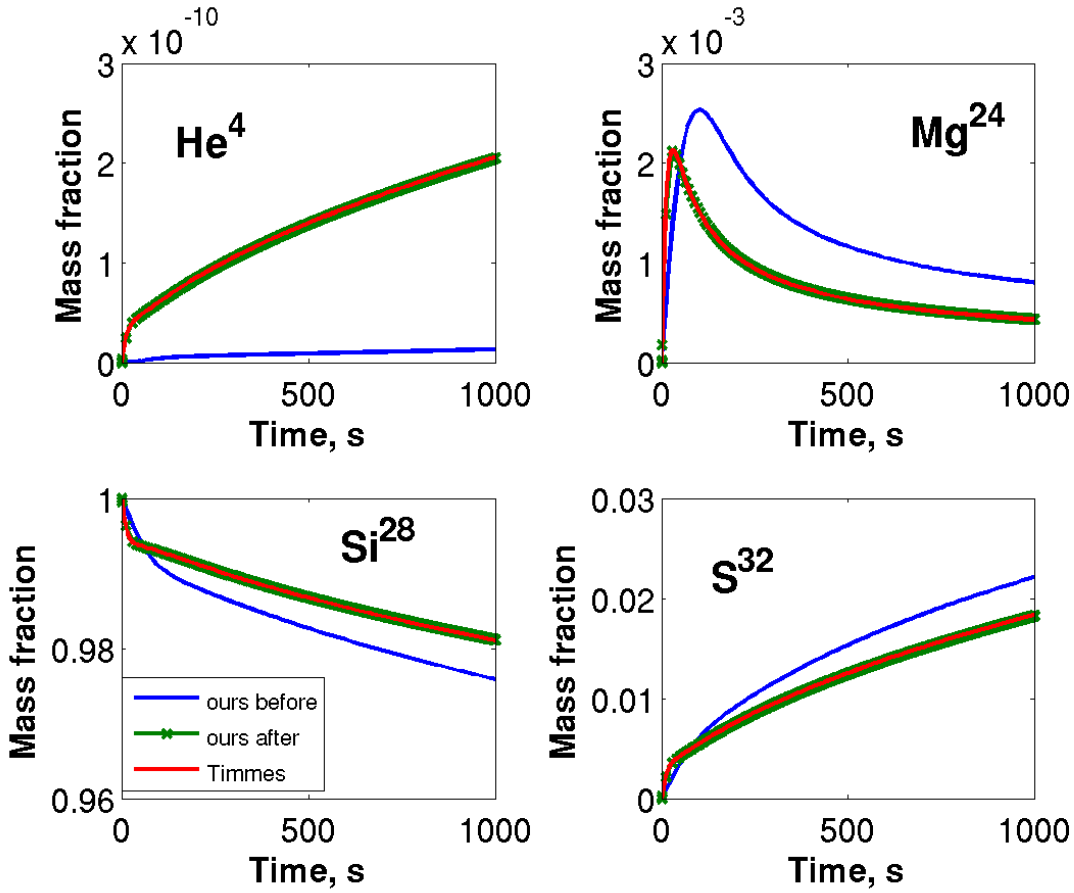

Figure 2.2: Comparison of the isotopic evolution calculated with the revised nuclear network (which involves $\alpha-$chain) and the Torch network of F. Timmes **before** (blue line) and **after** (green line) improvement of the solver. Pure silicon burning is simulated at thermodynamic conditions $T = 3 \times 10^9$ K, $\rho = 10^8$ g cm^{-3}.

obtained by the pseudo-Gaussian elimination (Prantzos et al. 1987).

Due to the changes in the set of isotopes and list of reactions, the matrix form was modified accordingly. Therefore, the solution provided by the old solver was only approximate. Using this approximation as a "predictor" we improved it by adding a "corrector" as described in McCracken & Dorn (1965). We also switched to an ordinary Gaussian elimination because the pseudo-Gaussian elimination cannot be applied with the addition of some isotopes any more. This modification finally gives the same solution as the Torch network as illustrated in Figure 2.2.

The Torch network

The simplified $\alpha-$chain network can describe the energy generation rate reasonably well for nuclear reactions that do not involve weak interactions (Timmes et al. 2000). This

network is therefore useful for certain applications like modeling super-massive stars (see Section 2.3). The energetics of PISNe can also be correctly represented with this network since the neutronization in the core of PISN progenitors is not significant enough to affect the nuclear energy generation. However, considering weak interactions is important for a study on the PISN nucleosynthesis because even a small degree of neutronization may have an interesting consequence in terms of the nucleosynthetic yields as discussed in Chapter 3.

To overcome this shortcoming, the Torch network by F. Timmes (Timmes 1998; Timmes et al. 2000) has also been implemented in BEC. This code is computationally much more expensive than the simplified $\alpha-$chain network, but includes all the necessary weak interactions that are needed to model PISN explosions. The number of isotopes in the routine can be flexibly chosen such that options from 47 to 3302 isotopes are currently available in BEC. For our PISNe models we used 200 isotopes. More details on the use of this routine for our PISN models are discussed in Chapter 3.

2.2.3 Quasi-statistical equilibrium and energy generation rate table

The nuclear energy generation is determined by the variation of the entire nuclear binding energy stored by all nuclei. The energy generation rate is therefore defined as:

$$\varepsilon = \dot{E}_{\rm bind} = \sum_i N_A m_i c^2 \dot{Y}_i \ , \tag{2.8}$$

where N_A is the Avogadro's number, Y_i and m_i the abundance and the mass of the isotope i, respectively.

The BEC code solves the stellar structure and the nuclear network separately. We found that using the above equation for the energy generation rate can cause a convergence problem with the solver of the stellar structure equations during silicon-burning because of its stiffness. Therefore, we constructed a table for the energy generation rate due to silicon burning as the following. It was suggested by a number of studies (Bodansky et al. 1968; Hix & Thielemann 1996; Hix et al. 1998; Panov et al. 2001; Hix & Meyer 2006) that it is possible to describe the isotopic evolution during silicon burning in the terms of a quasi-statistical equilibrium (QSE) (Wallerstein et al. 1997). In this case, all isotopes are roughly divided into two QSE-groups: the silicon-group and the iron-group:

$$\underbrace{\mathrm{He\,C\,O\,Ne\,Mg\,Si\,S\,Ca}}_{\mathrm{Si-group}} \Longleftrightarrow \underbrace{\mathrm{Ti\,Cr\,Fe\,Ni}}_{\mathrm{Fe-group}}, \tag{2.9}$$

with the boundary lying around titanium isotopes. In each QSE group the abundances of isotopes can be expressed by Saha-like equations ($= f_i(T, \rho, Y_e)$) and it is not necessary to solve the network inside the QSE group. Instead one should solve a couple of "bottleneck" reactions which are not in an equilibrium (Wallerstein et al. 1997). Figure 2.3 schematically illustrate the case of QSE.

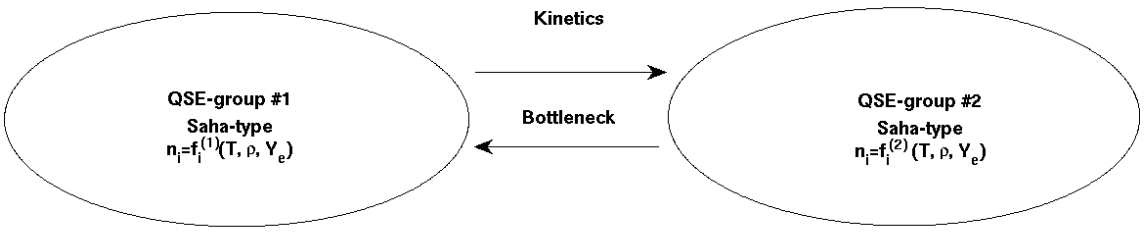

Figure 2.3: Illustration of QSE for two QSE-groups of isotopes.

The energy generation rate is therefore determined by changes in the mass fractions of the QSE-groups. This is illustrated in Figures 2.4 and 2.5. It is shown that the energy generation rate curves for different initial compositions converge very quickly after the beginning of isotopic evolution, during the first second. After one second the energy generation rate depends on the abundance of the silicon group. The detailed composition inside the silicon group does not play a significant role. This means that the nuclear energy generation rate can be tabulated for certain grid combinations of the temperature, the density, the silicon-group abundance and the electron fraction. This procedure can greatly simplify calculations and reduce the computational time (see e.g., Nomoto & Hashimoto 1988; Moll & Woosley 2013). The overall procedure for the stellar evolution calculation with this approach is illustrated in Fig. 2.6.

Let us now define the following variable:

$$X_{\mathrm{Si-group}} = \sum_{i=\mathrm{He}}^{\mathrm{Ca}} X_i \tag{2.10}$$

— the sum of mass fractions of all silicon group isotopes. The boundary of the QSE silicon group depends on the electron fraction (Y_e) and varies around calcium and titanium isotopes (Hix & Thielemann 1996). But the exact choice of the boundary is not important for the table values because of the very small mass fraction of the boundary elements.

In addition to temperature, density and mass fraction of silicon-group elements, the fourth parameter that affects the energy generation rate is the electron fraction (Y_e) as shown in Figure 2.7. Therefore, we built a 4-dimensional table for the range of $T = 2.4 \times 10^9 - 10^{10}$ K, $\rho = 10^5 - 10^{10}$ g cm^{-3}, $Y_e = 0.44 - 0.5$ and $X_{\mathrm{Si-group}} = 0 - 1$. We extended the range for the density down to $\log \rho = 5$ to make the energy table suitable for running PISN explosion models, i.e. stellar models of initial mass $150 - 250 M_\odot$. We used the Torch network with 127 isotopes for the calculations to produce the table.

The BEC code takes interpolated values of the energy generation rate from the table using a four-dimensional interpolation subroutine. A linear interpolation is applied along $\log T$ and $\log \rho$ and a second-order polynomial interpolation along $\log Y_e$ and $X_{\mathrm{Si-group}}$.

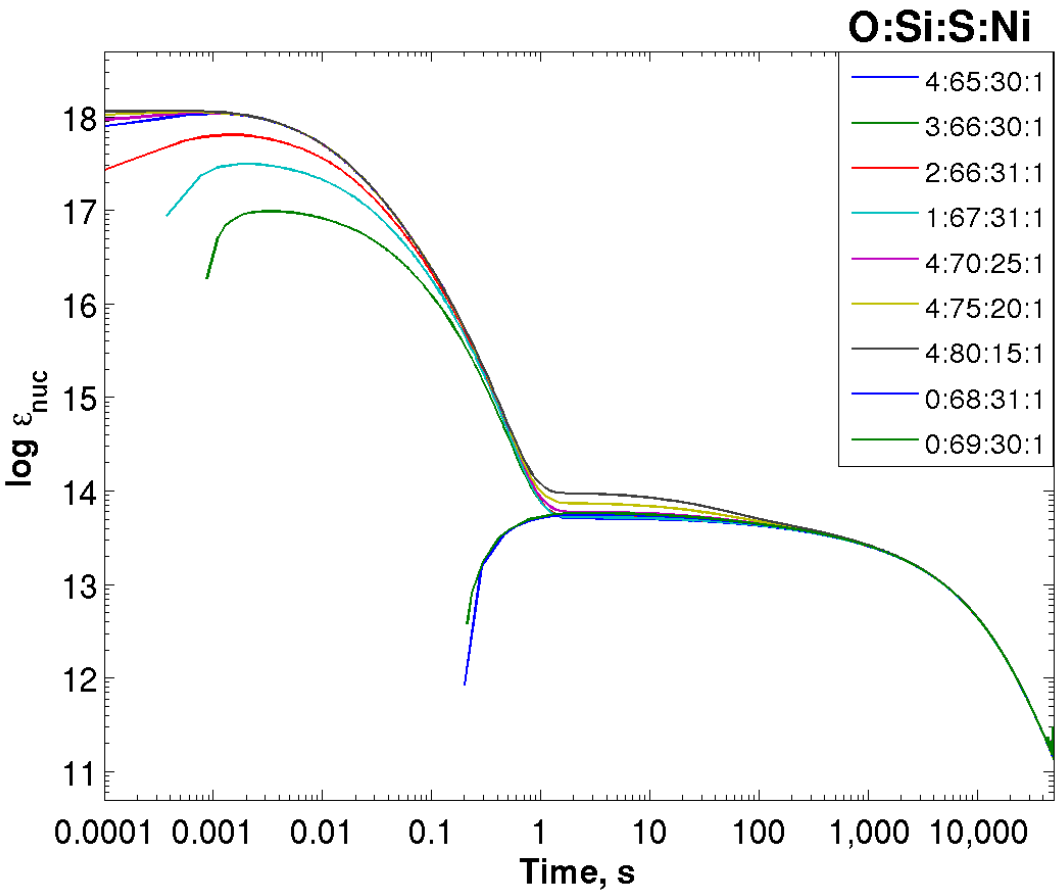

Figure 2.4: Evolution of energy generation rate during silicon burning for different initial composition. The nickel abundance is 1% for each case. Different colors correspond to different initial abundances of oxygen, silicon and sulphur. The constant thermodynamical conditions are $T = 3.5 \times 10^9$ K, $\rho = 10^8$ g cm^{-3}.

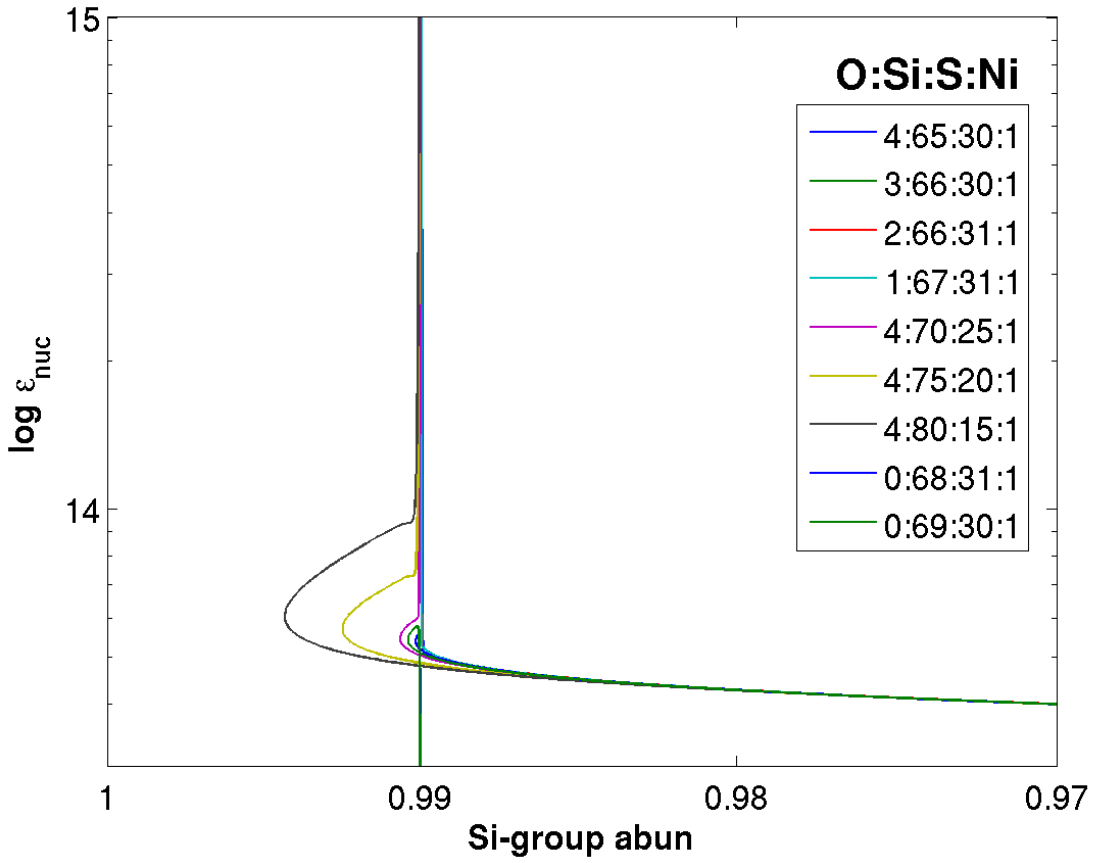

Figure 2.5: Energy generation rate during silicon burning for different initial composition. The nickel abundance is 1% for each case. Different colors correspond to different initial abundances of oxygen, silicon and sulphur. The constant thermodynamical conditions are $T = 3.5 \times 10^9$ K, $\rho = 10^8$ g cm^{-3}.

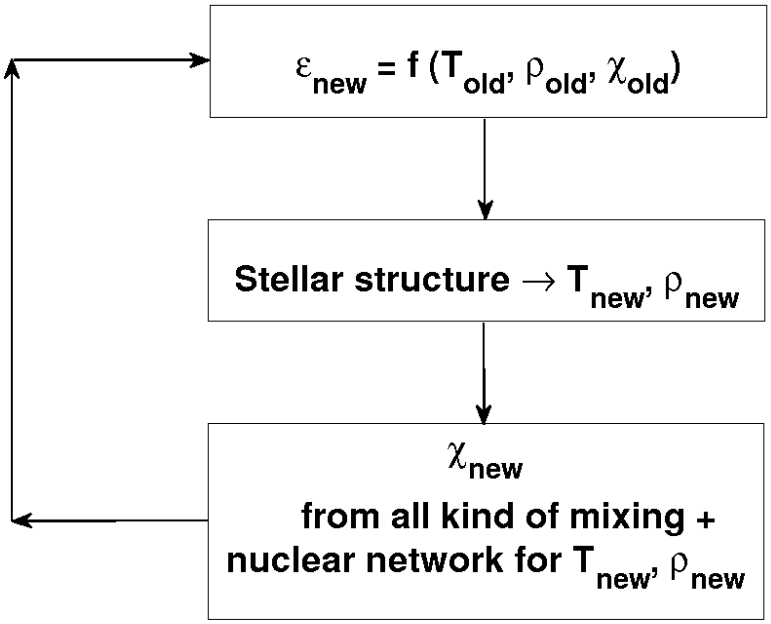

Figure 2.6: Schematic flow chart of the BEC code. The symbol χ represents the chemical composition, T and ρ are temperature and density, correspondingly.

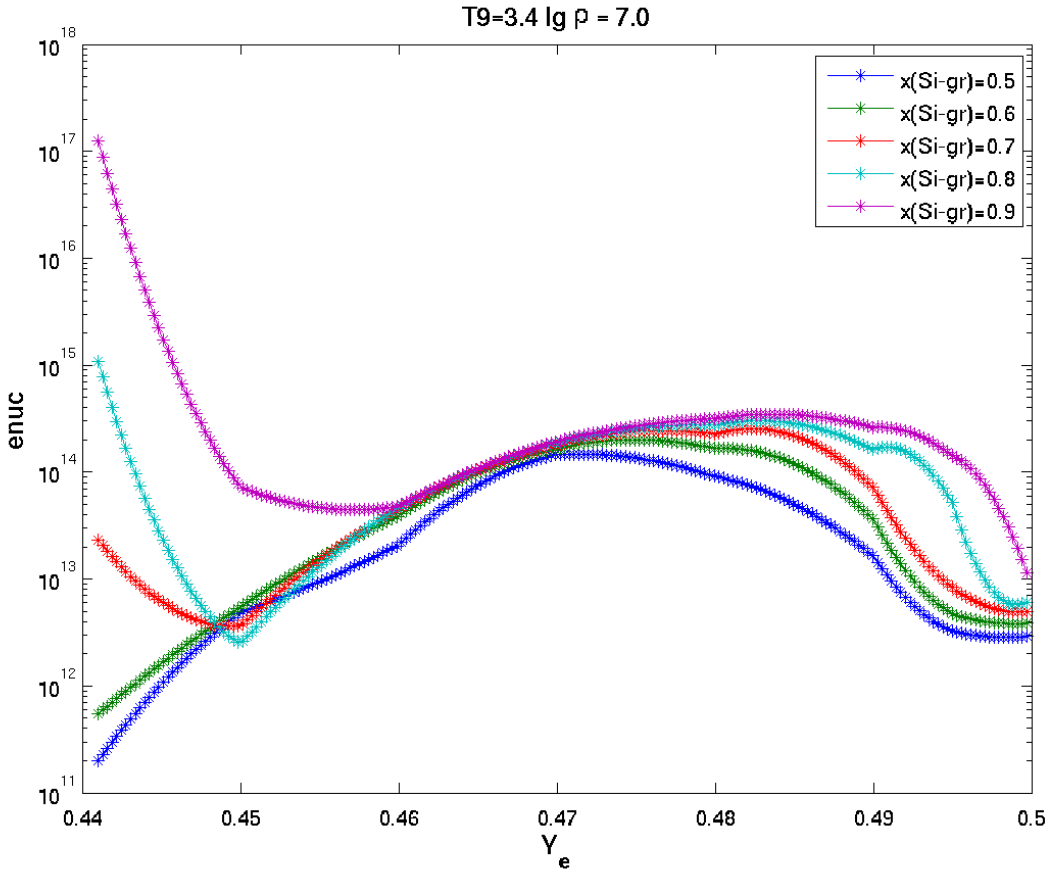

Figure 2.7: Dependence of the nuclear energy generation rate on the electron number Y_e. This composite plot of the energy generation rate during silicon burning is based on the energy generation table. The constant thermodynamical conditions are $T = 3.4 \times 10^9$ K, $\rho = 10^7$ g cm^{-3}.

Table 2.5: Radioactive decay

Daughter isotope		Decay product	Daughter isotope		Decay product
^{9}B(11%)	→	^{1}H	^{42}K,^{42}Sc	→	^{42}Ca
^{8}B,^{9}B(89%)	→	^{4}He	^{43}Sc	→	^{43}Ca
^{6}Li	→	^{7}Li	^{44}Sc,^{44}Ti	→	^{44}Ca
^{11}C	→	^{11}B	^{45}Ca,^{45}Ti,^{45}V	→	^{45}Sc
^{13}N	→	^{13}C	^{47}Ca,^{47}Sc,^{47}V	→	^{47}Ti
^{14}O	→	^{14}N	^{49}Ca,^{49}Sc,^{49}V,^{49}Cr	→	^{49}Ti
^{15}O	→	^{15}N	^{46}Sc,^{46}V	→	^{46}Ti
^{18}Ne	→	^{16}O	^{48}Sc,^{48}V,^{48}Cr	→	^{48}Ti
^{17}F	→	^{17}O	^{50}Sc	→	^{50}Ti
^{18}F	→	^{18}O	^{51}Ti,^{51}Cr,^{51}Mn	→	^{51}V
^{19}O,^{19}Ne	→	^{19}F	^{52}V,^{52}Mn,^{52}Fe	→	^{52}Cr
^{21}Na	→	^{21}Ne	^{53}Mn,^{53}Fe	→	^{53}Cr
^{22}Na,^{22}Mg	→	^{22}Ne	^{54}Mn	→	^{54}Cr
^{23}Ne,^{23}Mg	→	^{23}Na	^{55}Cr,^{55}Fe,^{55}Co	→	^{55}Mn
^{24}Na	→	^{24}Mg	^{56}Mn,^{56}Co,^{56}Ni	→	^{56}Fe
^{25}Al	→	^{25}Mg	^{57}Mn,^{57}Co,^{57}Ni,^{57}Cu	→	^{57}Fe
^{26}Al	→	^{26}Mg	^{58}Co	→	^{58}Fe
^{27}Mg,^{27}Si	→	^{27}Al	^{59}Fe,^{59}Ni,^{59}Cu	→	^{59}Co
^{28}Al	→	^{28}Si	^{60}Fe,^{60}Co,^{60}Cu,^{60}Zn	→	^{60}Ni
^{29}P	→	^{29}Si	^{61}Fe,^{61}Co,^{61}Cu,^{61}Zn,^{61}Ga	→	^{61}Ni
^{30}P	→	^{30}Si	^{62}Co,^{62}Cu,^{62}Zn,^{62}Ga	→	^{62}Ni
^{31}Si,^{31}S	→	^{31}P	^{58}Cu	→	^{58}Ni
^{32}Si,^{32}P	→	^{32}S	^{63}Ni,^{63}Zn,^{63}Ga	→	^{63}Cu
^{33}P,^{33}Cl	→	^{33}S	^{64}Cu(61.5%)	→	^{64}Ni
^{34}P,^{34}Cl	→	^{34}S	^{64}Cu(38.5%),^{64}Ga,^{64}Ge	→	^{64}Zn
^{35}S	→	^{35}Cl	^{65}Ni,^{65}Zn,^{65}Ga,^{65}Ge	→	^{65}Cu
^{37}Ar,^{37}K	→	^{37}Cl	^{66}Cu,^{66}Ga,^{66}Ge	→	^{66}Zn
^{38}Cl,^{38}K	→	^{38}Ar	^{67}Ga,^{67}Ge	→	^{67}Zn
^{36}Cl	→	^{36}Ar	^{68}Ga,^{68}Ge	→	^{68}Zn
^{39}Ar	→	^{39}K	^{69}Zn,^{69}Ge	→	^{69}Ga
^{41}Ar,^{41}Ca,^{41}sc41	→	^{41}K	^{70}Ga	→	^{70}Ge

Radioactive decay

We calculate the results of radioactive decay with a post-processing routine by adding the mass fraction of short living isotopes to the mass fraction of their decay products. Daughter isotopes decay through β^+, β^-–decay. We list the final decay results in Table 2.5.

2.3 Applications of the $\alpha-$chain network

Here we discuss the limits and applicability of our new $\alpha-$chain network. As mentioned above, this network was developed only for a pilot study of the thesis work, and is not used for the main topic of the thesis, namely the pair-instability explosions that are discussed in Chapter 3. For the calculation of the PISN nucleosynthesis, we used the Torch network with 200 isotopes, instead of the $\alpha-$chain network. However, the $\alpha-$chain network is computationally much less expensive than the Torch network, and can be particularly useful for some specific topics including the evolution of very massive stars, as discussed below.

2.3.1 Helium star models

With the new $\alpha-$chain network, we ran a set of single helium star models starting from the helium zero age main sequence. We used the latest version of BEC (Yoon et al. 2010) for evolving pure helium star models at solar metallicity ($Z = 0.02$). We present the results of the calculations in Figures 2.8 and 2.9. We continued the evolutionary calculations for some of our helium models until the end of core silicon burning. These results are shown separately in Figure 2.10.

We show that some of our models undergo rapid inflation of the envelope during the core carbon burning phase (Petrovic et al. 2006; Yoon et al. 2010). Those stars that lose their extended envelopes (more massive initially, $M > 5M_\odot$) remain very hot ($T_{\rm eff} > 50000$ K) and compact until the end of the evolution ($\sim R_\odot$). Stars with lower initial masses ($M < 5M_\odot$) have their envelopes more inflated and become relatively cool by the end of their lives. We applied the results of these calculations to predict the nature of type Ibc supernova progenitors in Yoon et al. (2012b).

In Figures 2.9 and 2.10 we show the evolutionary tracks of our helium star models in the central density–temperature diagram. Our models follow successive burning stages. Some calculations cover core helium and carbon burning (3 $M_\odot$, 3.5 $M_\odot$, 4 $M_\odot$). Other models evolve further through core neon and oxygen burning (4.5 $M_\odot$, 6 $M_\odot$). Models with 10 $M_\odot$ and 15 $M_\odot$ reach the end of core silicon burning.

In Figure 2.11, we plot the track of our 15 $M_\odot$ helium star model in the $\rho-T$-diagram, compared to the models with ZAMS masses of 25 $M_\odot$ and 40 $M_\odot$ by Chieffi & Limongi (2013). The 40 $M_\odot$ model has a helium core of 14.4 $M_\odot$ at the end of hydrogen burning, which is close to the initial mass of our 15 $M_\odot$ helium star model. However, our 15 $M_\odot$ helium star model and the 40 $M_\odot$ model evolve differently in the central density–temperature diagram. One of the crucial parameters governing the evolution in the $\rho - T$–diagram is

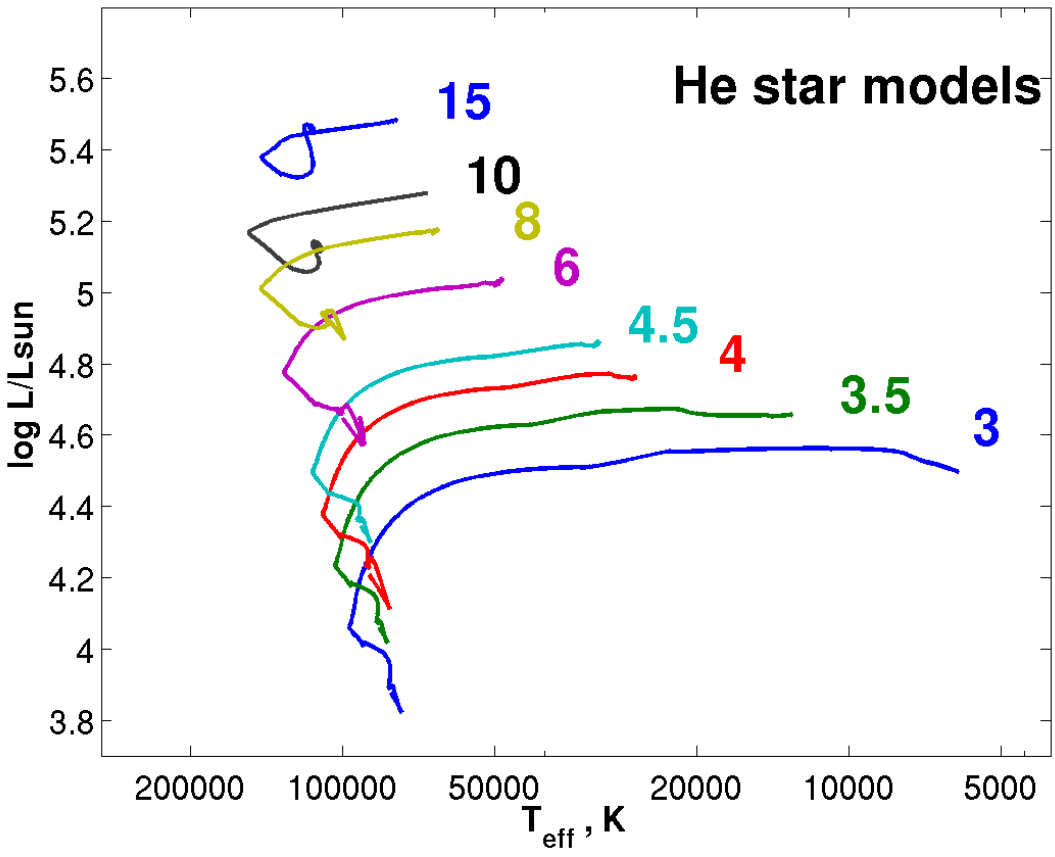

Figure 2.8: Evolutionary tracks of helium star models of solar metallicity in the Hertzsprung-Russel diagram. Labels correspond to initial mass of the helium star models.

the core mass. Our 15 $M_\odot$ helium star loses 5.4 $M_\odot$ during helium burning via Wolf-Rayet winds, while in the 40 $M_\odot$ model the helium core grows to about 16.6 $M_\odot$ because of the hydrogen burning shell during the core helium burning phase. This explains why the central temperature remains higher in the 40 $M_\odot$ model than in our 15 $M_\odot$ helium star model. The 25 $M_\odot$ star has a 9.8 $M_\odot$ helium core at the end of the evolution (Chieffi & Limongi 2013) and its evolutionary track looks compatible to that of our 15 $M_\odot$ helium star model, which has a final mass of about 9.4 $M_\odot$.

The iron core mass of our 15 $M_\odot$ helium star is 1.68 $M_\odot$ at the pre-supernova stage. Those of the 25 $M_\odot$ and 40 $M_\odot$ models (Chieffi & Limongi 2013) are 1.48 $M_\odot$ and 1.58 $M_\odot$, respectively. The main reason for the higher iron core mass in our helium star model is because our $\alpha-$chain network does not include weak interactions, resulting in no neutronization in the iron core (i.e, $Y_e = 0.5$). Given that the Chandrasekhar limit is proportional to ${Y_e}^2$, it is a natural consequence of higher electron-degenerate pressure in the core that our helium star model has a higher iron core mass at the pre-supernova stage than the

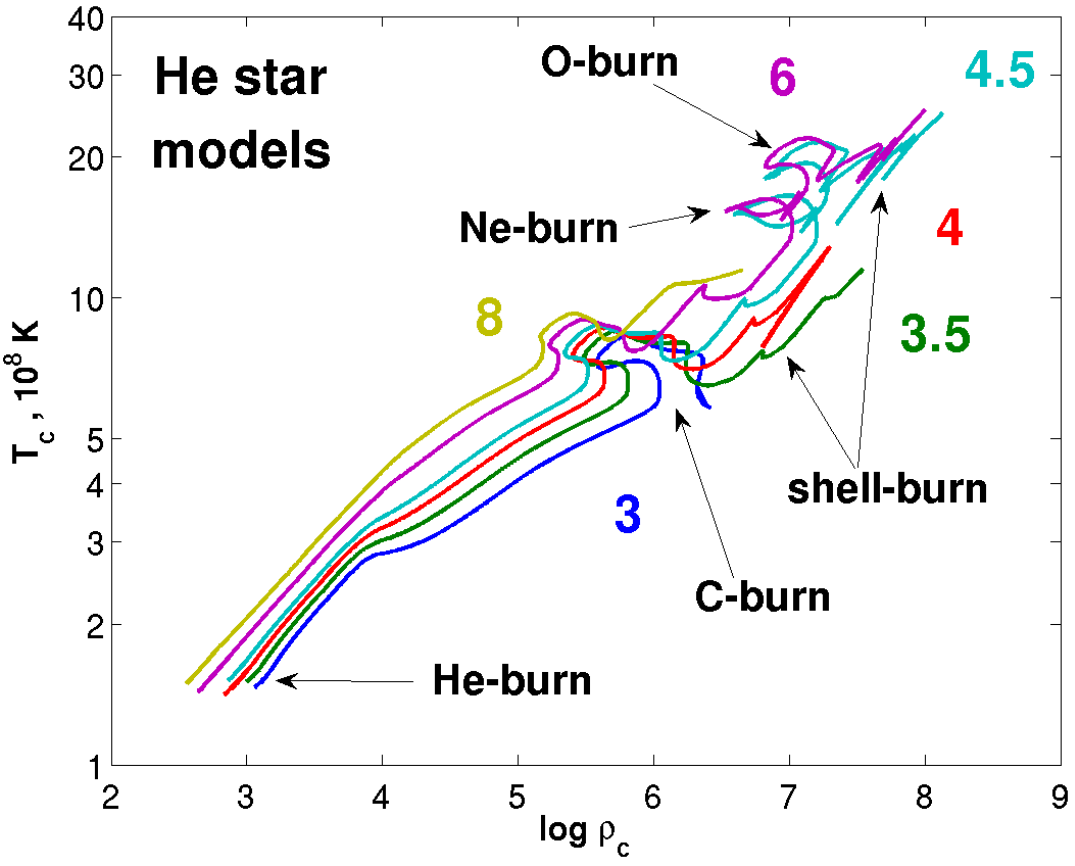

Figure 2.9: Evolutionary tracks of helium star models of solar metallicity in the central density – central temperature diagram. Labels correspond to initial masses of the helium star models and the indicated core burning stages.

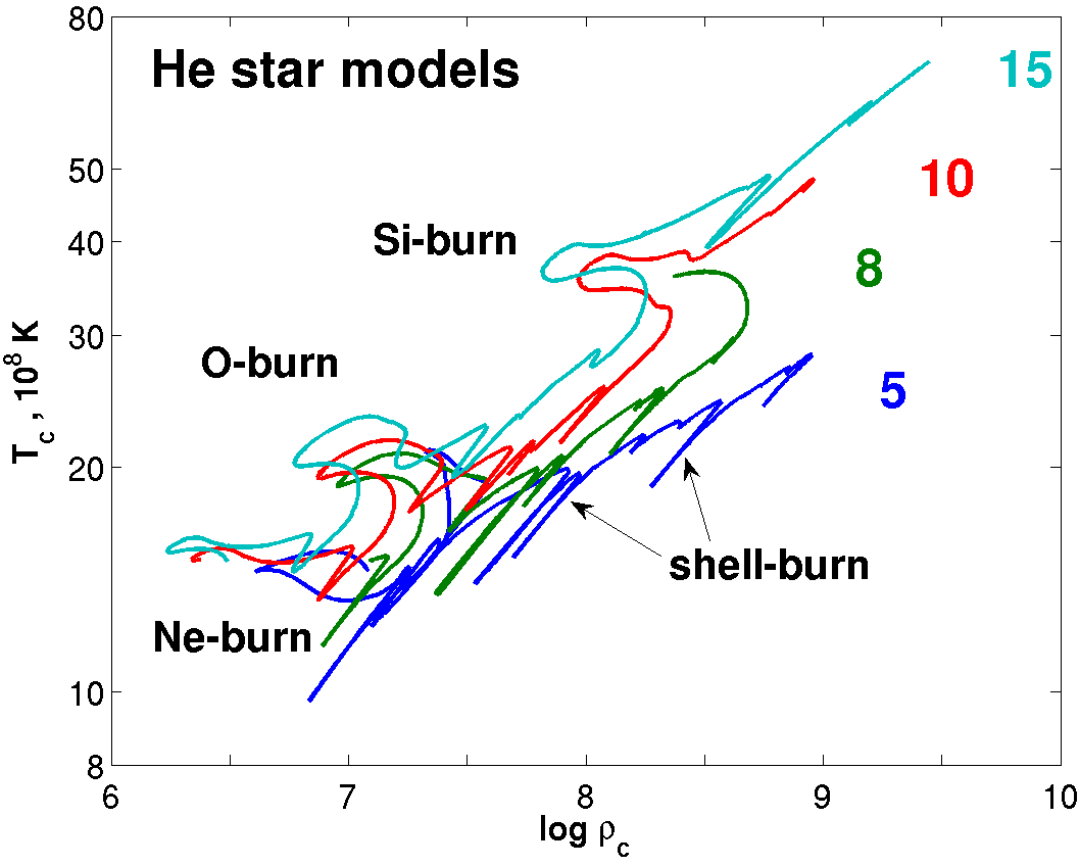

Figure 2.10: Evolutionary tracks of helium star models at solar metallicity during core oxygen and silicon burning in the central density – central temperature diagram. Labels correspond to initial masses of the helium star models and the indicated core burning stages.

models having comparable helium core masses where weak interactions are fully considered as in Chieffi & Limongi (2013).

This comparison indicates that our $\alpha-$chain network can describe the inner structure of core-collapse supernova progenitors during the final stage only in an approximate way. However, this network can still be employed for modelings of core-collapse progenitors with some specific purposes. For example, Hirschi et al. (2004) used a similar $\alpha-$chain network to investigate the angular momentum evolution at the pre-supernova stage in massive stars, which does not necessarily require a precise description of the iron core structure.

In principle, the Torch network can be used to construct core-collapse supernova progenitors, given that it includes all the necessary weak interactions and that our energy generation table for silicon burning covers a wide range of thermodynamic conditions that can be applied to silicon burning in core-collapse supernova progenitors, as explained above.

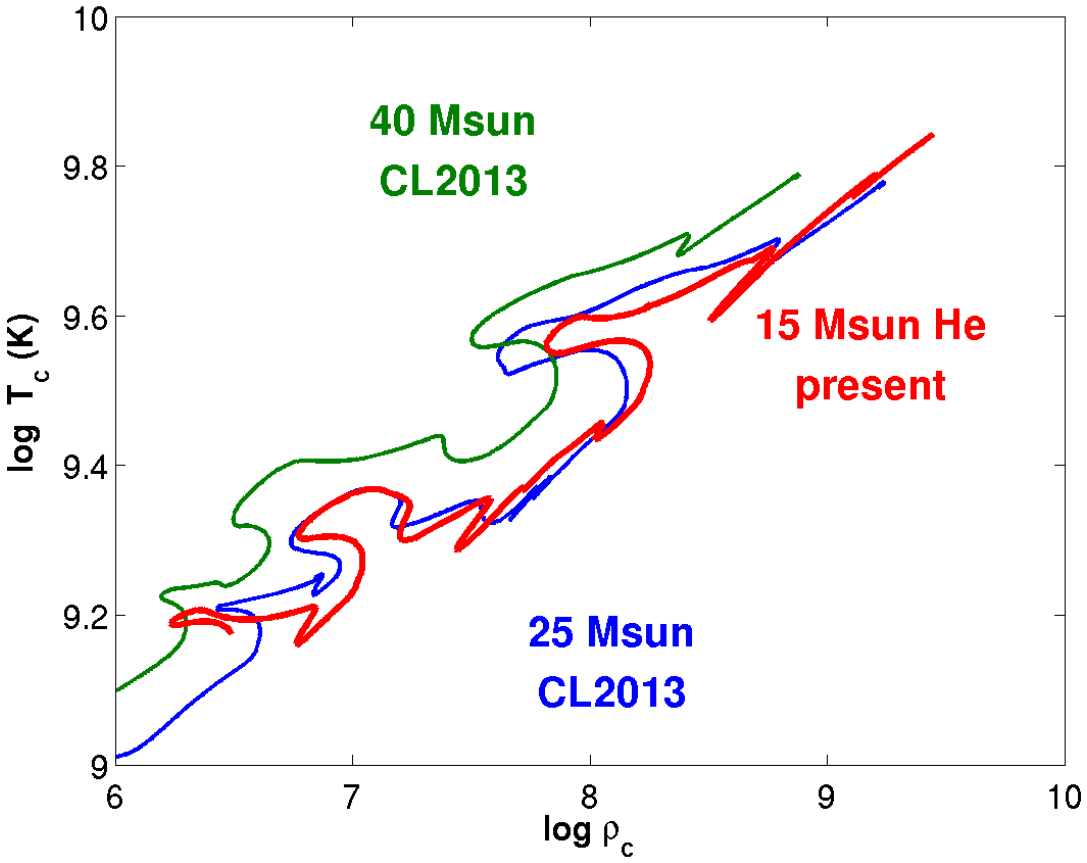

Figure 2.11: Evolutionary tracks of 15 $M_{\odot}$ helium star model of solar metallicity during core oxygen and silicon burning in the central density – central temperature diagram, compared to models with initial mass of 25 $M_{\odot}$ and 40 $M_{\odot}$ of solar metallicity from Chieffi & Limongi (2013).

However, applying the Torch network for this case is a time consuming task and beyond the scope of the thesis.

2.3.2 Supercollapsar progenitors

Although the effect of weak interactions is crucial for the iron-core structure in core-collapse supernova progenitors, it does not play an important role for very massive stars that undergo the pair-instability during the late stages in the cores because the central density in these stars remains very low throughout all the nuclear burning stages, especially if we consider stars above 260 $M_{\odot}$ which end in black hole formation after the pair instability phase. Therefore, our $\alpha-$chain network can properly describe the final core structure of such a very massive star.

One such science case is the angular momentum evolution in very massive stars with

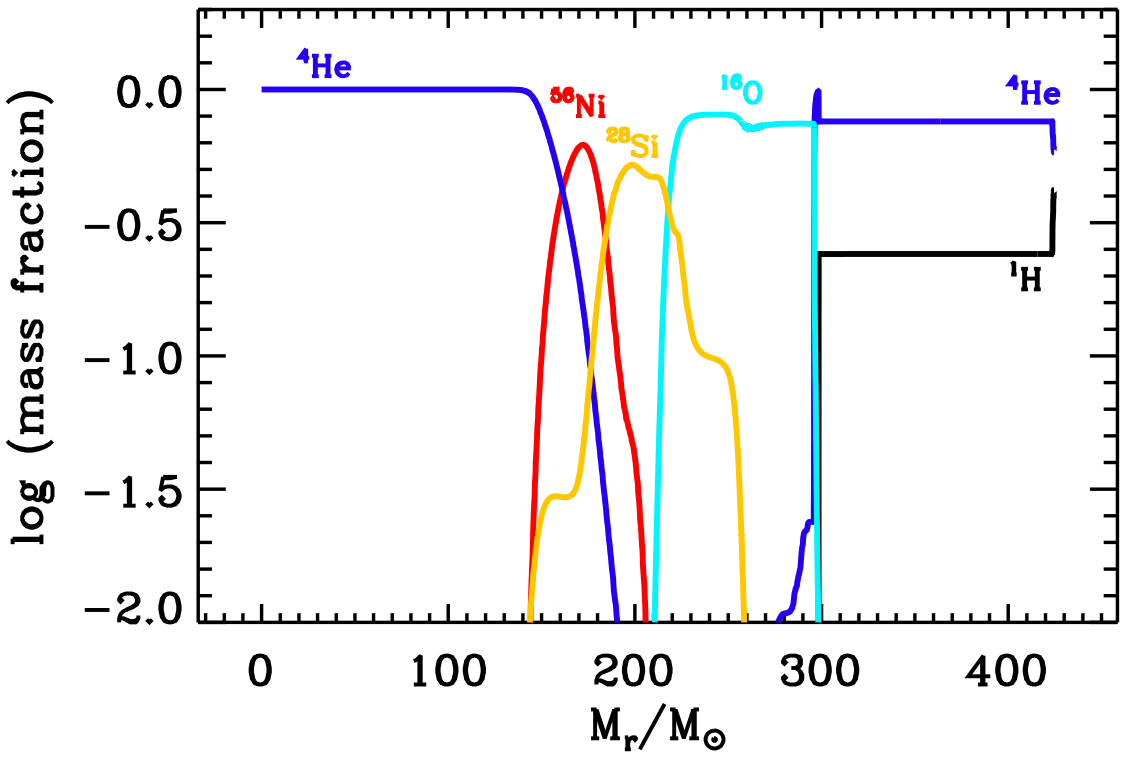

Figure 2.12: Chemical structure at the pre-collapse stage in the rotating 500 $M_{\odot}$ star model with an initial rotational velocity of 30% of the Keplerian value at the equatorial surface.

initial masses of 260 $M_\odot$ – 1000 $M_\odot$. Retention of a large amount of angular momentum around the iron core at the pre-collapse stage in such an object may lead to the formation of relativistic jets followed by an X-ray or gamma-ray burst, when the iron core collapses into a black hole. This is the so-called supercollapsar scenario in which short lived jets are powered by the Blandford-Znajek magnetic mechanism (Komissarov & Barkov 2009, 2010; Mészáros & Rees 2010). The structure of supercollapsar progenitors including rotation can be accurately obtained with our $\alpha-$chain network as it does not require any more detailed nucleosynthesis.

As an example, we evolved a 500 $M_\odot$ model at zero-metallicity with an initial rotational velocity of 30% of the Keplerian value at the equatorial surface from the zero-age main sequence to the pre-collapse stage, using the $\alpha-$chain network. In this calculation, the transport of angular momentum via hydrodynamical instabilities is considered, but a magnetic torque is not included (see Yoon et al. 2012a). This star undergoes the pair-instability after central carbon exhaustion, but continues to collapse because the released nuclear energy during the oxygen and silicon burning phases is not large enough to reverse it. The final model reaches a central density of 6.1×10^6 g cm^{-3} and a central temperature of 1.3×10^{10} K, where the maximum infall velocity of the core reaches 25000 km s^{-1}. Figure 2.12 shows the final chemical structure which is qualitatively similar to a model of 300 $M_\odot$ by Fryer et al. (2001). The innermost 140 $M_\odot$ is completely photo-dissociated into helium, and about 17 $M_\odot$ of ^{56}Ni is produced in the layer above. Figure 2.13 shows the angular momentum distribution at this stage. The specific angular momentum (j_r) in the innermost 300 $M_\odot$ is lower than the critical value $j_{\rm Kerr}$ that is needed to form an accretion disk around a rotating black hole. Right above this region, the material of about 8 $M_\odot$ in the outermost layer of the oxygen core is rotating with $j_r > j_{\rm Kerr}$.

Therefore, it is expected that a 300 $M_\odot$ black hole forms as a result of the collapse, which is surrounded by an accretion disk of about 8 $M_\odot$. The expected accretion rate is about 1.6 $M_\odot$ s^{-1}, which is derived from the free fall time of the matter in this layer, and the consequent accretion time is only about 5 seconds. The radius of our 500 $M_\odot$ star at the final stage is 6491 $R_\odot$ and the corresponding jet crossing time is about 4 hours. Therefore, even if a jet is produced via the accretion of the rapidly rotating material in the outermost layer of the oxygen core into the black hole, it would not be able to break out from the star. The outermost layers in the hydrogen envelope are also rotating rapidly with $j_r > j_{\rm Kerr}$, but the hydrogen envelope is very loosely bound and not likely to form an accretion disk to make a powerful jet. The presence of a magnetic torque would provide a higher degree of angular momentum loss, therefore, a lower angular momentum distribution inside the star. In short, our calculations indicate that a supercollapsar from a very massive Population III star is not likely to produce a jet-powered burst, in agreement with Fryer et al. (2001).

More details on this issue will be presented in a forthcoming paper.

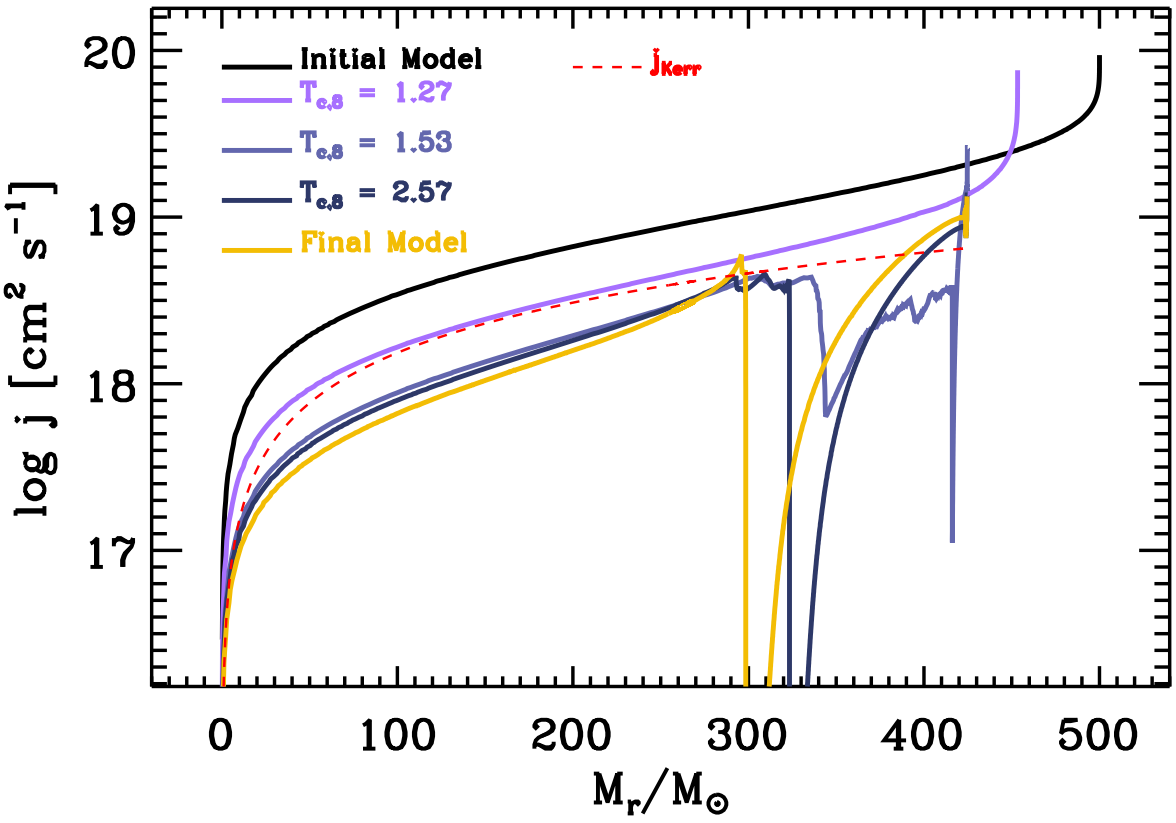

Figure 2.13: Specific angular momentum as a function of the mass-coordinate for different evolutionary stages ($T_c = 1.27, 1.53, 2.57,$ and 12.6×10^8 K) in the rotating 500 $M_\odot$ model. The red dashed line denotes the critical specific angular momentum above which the collapsing material can form an accretion disk around a rotating black hole of the given mass.

Chapter 3

Explosion and nucleosynthesis of low redshift pair instability supernovae

This chapter describes the self-consistent evolutionary calculations of 150 $M_\odot$ and 250 $M_\odot$ stellar models of metallicity 0.001 from the zero-age main sequence up to the collapse due to pair creation and subsequent explosion. The chapter performs the first detailed nucleosynthetic yields of finite metallicity pair instability supernovae and briefly discusses the imprint of the pair instability supernovae on the chemical evolution of the local Universe.

3.1 Overview

Both recent observations and stellar evolution models suggest that pair-instability supernovae (PISNe) could occur in the local Universe, at metallicities below $\lesssim Z_\odot/3$. Previous PISN models were mostly produced at very low metallicities in the context of the early Universe.

We present new PISNe models at a metallicity of $Z = 0.001$, which are relevant for the local Universe.

We take the self-consistent stellar evolutionary models of pair-instability progenitors with initial masses of 150 $M_\odot$ and 250 $M_\odot$ at metallicity of $Z = 0.001$ by Langer et al. (2007) and follow the evolution of these models through the supernova explosions, using a hydrodynamics stellar evolution code with an extensive nuclear network including 200 isotopes.

Both models explode as PISNe without leaving a compact stellar remnant. Our models produce a nucleosynthetic pattern that is generally similar to that of Population III PISN models, which is mainly characterized by the production of large amounts of $\alpha-$elements and a strong deficiency of the odd-charged elements. However, the odd-even effect in our models is significantly weaker than that found in Population III models. The comparison with the nucleosynthetic yields from core-collapse supernovae at a similar metallicity ($Z =$

0.002) indicates that PISNe could have strongly influenced the chemical evolution below $Z \approx 0.002$, assuming a standard initial mass function. The odd-even effect is predicted to be most prominent for the intermediate mass elements between silicon and calcium.

With future observations of chemical abundances in Population II stars, our result can be used to constrain the number of PISNe that occurred during the past evolution of our Galaxy.

3.2 Introduction

The pair instability mechanism for supernova explosions was first suggested in 1960s (Fowler & Hoyle 1964; Bisnovatyi-Kogan & Kazhdan 1967; Rakavy & Shaviv 1967; Barkat et al. 1967; Fraley 1968; Zeldovich & Novikov 1971). The cores of very massive stars with initial masses higher than about 100 $M_\odot$ (Bond et al. 1982; Heger et al. 2003) have relatively low densities and high temperatures for which radiation pressure is dominant over gas pressure. When the core temperature approaches 10^9 K, the creation of electron-positron pairs out of gamma-ray photons from the high energy tail of the black body spectrum becomes important and makes the adiabatic index Γ drop below 4/3. This causes gravitational collapse of the core if a significant fraction of the core has $\Gamma < 4/3$. The consequent oxygen burning induces a thermonuclear explosion that completely disrupts the star if the released energy exceeds its binding energy. This happens for oxygen core masses above approximately 45 $M_\odot$.

For a pair instability supernova to occur, its progenitor needs to retain its mass high enough to keep its helium core mass above about $\sim$ 65 $M_\odot$. This condition cannot be easily fulfilled at high metallicity for which the evolution of very massive stars are dominated by stellar wind mass-loss (e.g. Vink et al. 2011). This is the reason why most theoretical studies of pair instability supernovae (PISNe) have focused on zero or extremely metal poor stars in the early Universe (El Eid et al. 1983; Umeda & Nomoto 2002; Heger & Woosley 2002; Scannapieco et al. 2005; Kasen et al. 2011; Pan et al. 2012a; Whalen et al. 2013a; Dessart et al. 2013). However, Langer et al. (2007) recently pointed out that the metallicity threshold for PISNe can be as high as $Z_\odot/3$ within the current theoretical uncertainty of stellar wind mass-loss rates, implying one PISN per one thousand supernovae in the local Universe.

PISNe would be marked by broad light curves given their high progenitor masses. They would also appear extremely luminous if their progenitors have large radii and/or if a large amount of nickel is produced as a result of the pair creation instability (e.g., Scannapieco et al. 2005; Kasen et al. 2011). This raises the question whether some of the super-luminous SNe of various types like SN 2006gy and SN 2007bi discovered in the nearby Universe have a pair instability origin (see Gal-Yam 2012a, for a review). For example, the light curve of SN 2007bi implies the radioactive decay of more than 3 $M_\odot$ of nickel, for which a pair instability explosion gives one of the best explanations (Gal-Yam et al. 2009). Alternative possibilities are supernova powered by a young magnetar as suggested by various authors (Kasen & Bildsten 2010; Dessart et al. 2012b) and interaction-driven supernova (Moriya

et al. 2010). If local PISNe would exist, one would have to wonder how they would have impacted on the chemical evolution of the local Universe.

Addressing these questions requires PISN models that are relevant to the environment of the local Universe. The first studies of local PISN models were performed by Langer & El Eid (1986), El Eid & Langer (1986) and Herzig et al. (1990) who calculated evolutionary models with an initial mass of 100 $M_\odot$ and a metallicity of $Z = 0.03$. More recently, Langer et al. (2007) calculated 150 $M_\odot$ and 250 $M_\odot$ models at a metallicity of $Z = 0.001$ as PISN progenitors, adopting the most up-to-date prescriptions for stellar wind mass-loss rates. These models provide self-consistent progenitor models for PISNe in the local Universe together with more recent models by Yusof et al. (2013). In the present study we follow the evolution of two models from Langer et al. (2007) through the explosive oxygen and silicon burning stages to verify that they explode via the pair instability mechanism, and to discuss implications for nucleosynthesis in the local Universe. Their shock-breakout signatures and light curves will be discussed in a separate paper (Kozyreva et al. 2014a).

This paper is organized as follows. We describe the numerical method adopted in the present study in Section 3.3. The results of our calculations are reported in Section 3.4, where we also discuss the nucleosynthesis yields of our PISN models. We discuss the implications of our results for the chemical evolution of the local Universe in Section 3.5, and conclude our study in the final section.

3.3 Numerical method and input physics

We use an implicit Lagrangian hydrodynamics code which solves the difference equations for the stellar structure iteratively by the Henyey relaxation method (Henyey et al. 1964; Heger et al. 2000; Yoon & Langer 2005; Yoon et al. 2006). We list the relevant stellar structure equations in the Appendix A. The equation of state is based on Blinnikov et al. (1996) and includes ions, electrons and positrons, radiation, degeneracy effects and ionization contributions. The opacity is computed from the OPAL tables (Iglesias & Rogers 1996) and Alexander & Ferguson (1994).

We compute the nucleosynthesis and the corresponding energy generation rate in the following way. For temperatures less than 4.5×10^8 K, a small nuclear network (39 isotopes) is utilized. For higher temperatures we use the "Torch" nuclear network developed by Timmes (1998, 1999) with 200 isotopes. In this network, the weak interactions are followed using the data provided by Fuller et al. (1982). For a temperature range where silicon burning is well described in terms of quasi-statistical equilibrium (QSE, Bodansky et al. 1968; Hix & Thielemann 1996), energy generation rates can be given as a function of temperature T, density ρ, total mass fraction of the silicon QSE-group[1] elements $X_{\rm Si}$ and electron abundance Y_e. For calculating energy generation rates during silicon burning, therefore, we use an energy generation rate table for a number of combinations of different physical parameters ($T = (2.4 - 5) \times 10^9$ K, $\log_{10}(\rho \ / \ (\mathrm{g\ cm^{-3}})) = 5 - 10$, $X_{\rm Si} = 0 \ - \ 1$,

[1]QSE-groups are the groups of isotopes formed in the condition of quasi-statistical equilibrium (Wallerstein et al. 1997).

$Y_e = 0.44 - 0.5$), following Nomoto & Hashimoto (1988). For very high temperatures ($T > 5 \times 10^9$ K), the nuclear statistical equilibrium routine by Timmes (1998) is employed.

Our starting models are taken from the stellar evolutionary calculations with an initial masses of 150 $M_\odot$ and 250 $M_\odot$ and initial rotational velocity of 10 km s^{-1} at $Z = 0.001$ by Langer et al. (2007, the model Sequences 3 and 4). These models were calculated from the zero-age main sequence until the onset of the pair instability in the core, with the stellar wind mass-loss prescription described in Yoon et al. (2006). The starting point of our calculations is core carbon exhaustion, after which these stars quickly enter the pair instability phase. The stellar masses at this point are 94 $M_\odot$ and 169 $M_\odot$ for the 150 $M_\odot$ and 250 $M_\odot$ stars, respectively. We summarize some model properties in Table 3.1 along with those of zero metallicity models by Heger & Woosley (2002) for comparison.

The stellar evolutionary models from Langer et al. (2007) were calculated using the Ledoux criterion for convection, with the assumption of semi-convection (Langer et al. 1983) using a large semi-convective mixing parameter ($\alpha_{\rm SEM} = 1$, Langer (1991)), and without convective core overshooting. The mixing length parameter was chosen to be 1.5 of pressure scale height (Yoon et al. 2006). We neglected the convective mixing during the explosive oxygen and silicon burning phases in our calculations because the convection timescale is two orders of magnitude larger than the hydrodynamical timescale on which the collapse induced by the pair instability develops.

Note that the recent PISN progenitor models at higher metallicity (0.002 and 0.006) by Yusof et al. (2013) are computed using the Schwarzschild criterion for convection and with core overshooting with a moderate overshooting parameter ($\alpha_{\rm over} = 0.1$). The convection in the outer layers is calculated with mixing-length parameter scaled to the density scale height ($\alpha_{\rm MLT} = l/H_\rho = 1$) to avoid density inversions (see also Ekström et al. 2012). The consequences of this treatment are more compact stellar models, a lesser degree of mass loss, and larger carbon-oxygen cores. Those models from Yusof et al. (2013) which are supposed/declared to produce PISNe are evolved until the end of helium/oxygen burning. Electron-positron pair creation is not included in the equation of state of the employed evolutionary code. The statement about the PISN fate is based on the size of the carbon-oxygen core. In more recent study the PISN models from Yusof et al. (2013) (at the end of core helium burning) were mapped into the KEPLER code (Heger & Woosley 2010). With these calculations the models were evolved through pair instability and eventually exploded (Whalen et al. 2013c).

Rotation is not included during the present calculations because these models retain very small amounts of angular momentum.

Table 3.1: Properties of our PISN progenitor models and of comparable Population III helium star models from Heger & Woosley (2002). $T_{\rm c}^{\rm max}$ and $\rho_{\rm c}^{\rm max}$ are the maximum values of central temperature and central density, respectively, that are achieved during the calculations. The last two columns give the values of the central neutron excess initially and at maximum temperature.

Initial mass	Final mass $[M_\odot]$	He-core $[M_\odot]$	O-core $[M_\odot]$	$T_{\rm c}^{\rm max}$ $[10^9$ K]	$\log \rho_{\rm c}^{\rm max}$ [g cm^{-3}]	$\eta_{\rm c}^{\rm init}$	$\eta_{\rm c}^{\rm max}$
150 $M_\odot$	94	72	64	3.45	6.25	1.0×10^{-4}	2.5×10^{-4}
70 $M_\odot$ He	70	70	60	3.57	6.30	1.9×10^{-7}	2.8×10^{-4}
250 $M_\odot$	169	121	110	5.12	6.69	1.0×10^{-4}	1.6×10^{-3}
115 $M_\odot$ He	115	115	90	5.14	6.67	1.9×10^{-7}	7.3×10^{-4}

3.4 Results

3.4.1 Explosion

Through the hydrodynamics terms included in the BEC code (see the Appendix A) we could follow the dynamical phase of the evolution of our PISN models. Usually hydrodynamic stellar evolution codes are not able to describe dynamical processes in stars because of the implicit nature of the adopted numerical solvers (causing strong numerical damping) and the large time steps which are required to follow the evolution time scale (Appenzeller 1970; Woosley & Weaver 1982). Pulsations and shock waves however can be resolved if the time step becomes comparable to the dynamical characteristic time (possible during late stages of stellar evolution), and if the growth rate of a hydrodynamical phenomenon is sufficiently large (El Eid & Langer 1986; Heger et al. 1997; Yoon & Cantiello 2010).

We find that both models explode as a result of explosive nuclear burning during the pair instability phase, which confirms the prediction by Langer et al. (2007).

In Figure 3.1, the evolutionary tracks of the central density and temperature are shown. Both quantities increase rapidly during the dynamical contraction of the core induced by the pair instability. The maximum temperature and density achieved during this phase are $T_{\rm c} = 3.45 \times 10^9$ K and $\rho_{\rm c} = 1.8 \times 10^6$ g cm^{-3} for the 150 $M_\odot$ star, and $T_{\rm c} = 5.1 \times 10^9$ K and $\rho_{\rm c} = 4.9 \times 10^6$ g cm^{-3} for the 250 $M_\odot$ star, respectively. As shown in Table 3.1, these values are comparable to those found in Population III star models by Heger & Woosley (2002) for similar helium core masses. Beyond this point, the contraction is reversed, and the star explodes.

In Figure 3.2, the fact that our models explode by the nuclear energy release is illustrated. Initially our models have a negative binding energy ($E_{\rm bind} = E_{\rm grav} + E_{\rm thermal}$). The pair creation triggers the collapse which is visible as a minor increase of the kinetic energy around $t = 0$ for Model 150M and around $t = 0 - 10$ s for Model 250M. The consequent

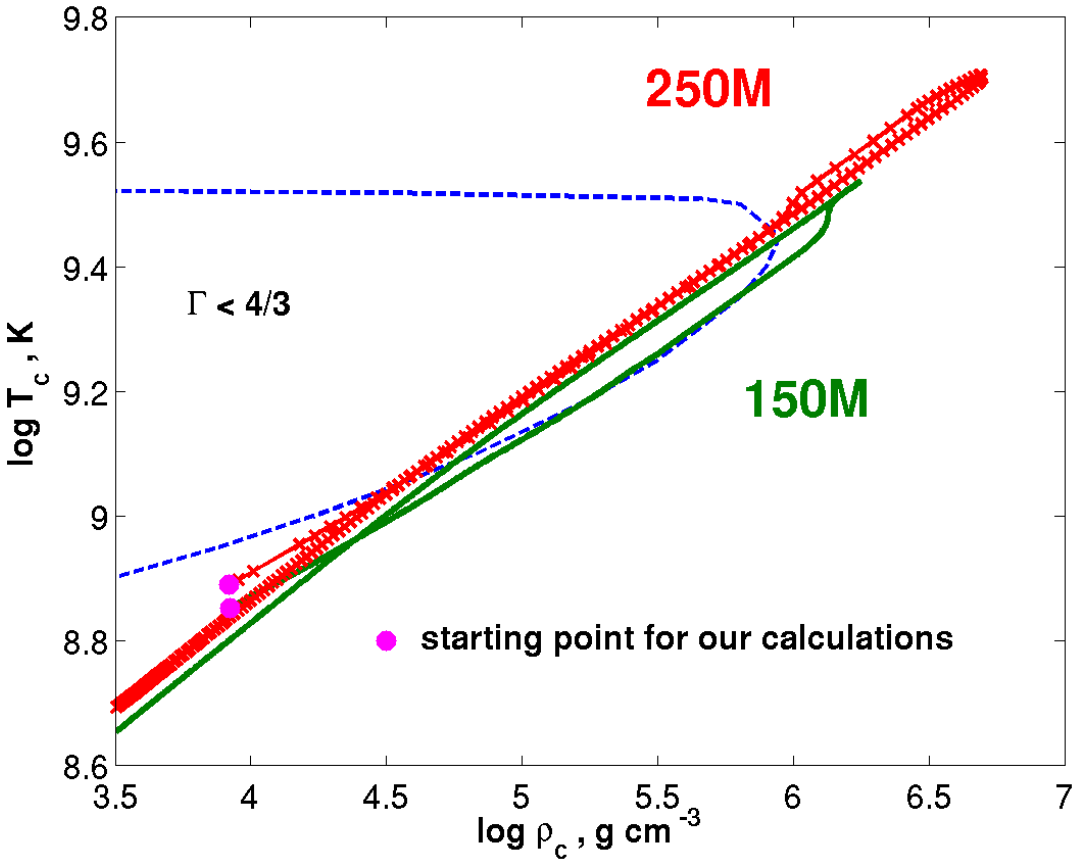

Figure 3.1: Evolutionary tracks of our 150 $M_{\odot}$ (labeled '150M', solid line) and 250 $M_{\odot}$ (labeled '250M', line with times signs) models in central density – temperature diagram. The area enclosed with the dashed line indicates the pair instability regime where $\Gamma < 4/3$. The filled circles mark the starting points for each model sequence.

oxygen and silicon burning occur with a sharp decrease of the nuclear binding energy.

The nuclear binding energy is defined the following way:

$$E_{\rm bind} = \sum_k \sum_i X_i \, e_i \, \frac{\Delta M_k}{m_i} \, , \tag{3.1}$$

where X_i represents the mass fractions of the isotopes, e_i and m_i are the nuclear binding energy and nuclear mass of the isotope i, and ΔM is the mass of the mass shell of the numerical stellar model. The sum is made over all mass shells and over all isotopes. Figure 3.2 shows the difference of nuclear binding energy at a given time to that at the end of carbon burning, i.e. the first time point in the figures. The drop in the nuclear binding energy shows the amount of energy released by nuclear burning during the pair instability explosion.

The released nuclear energy from oxygen and silicon burning is converted into thermal and kinetic energy, resulting in a positive binding energy. A positive binding energy means that the system becomes unbound. Eventually, most of the released nuclear energy is converted into the kinetic energy, which is strong evidence for the explosion of the star. The final kinetic energy is 8 foe[2] for Model 150M and 44 foe for Model 250M. This corresponds to an asymptotic velocity of the ejecta at the infinity of 2.9×10^3 km s^{-1} for Model 150M and 5.1×10^3 km s^{-1} for Model 250M.

The BEC code has no provision for treating shocks. However, due to the strong density contrast at the base of the hydrogen-rich envelope, a shock wave develops at this point due to the explosion of the carbon-oxygen core. Its Mach number is about 2 for both our models. As a consequence, energy is not perfectly conserved in our models at the time when the shock enters the stellar envelope (see Figure3.3). Still the total energy is conserved to better than 5% in our 150 $M_\odot$model, and to better than 20% in our 250 $M_\odot$model. We note that the velocities scale with $\sqrt{E_{\rm kin}}$, and that we expect our velocities to be precise to 3% and 10%, respectively. The comparison of Figures 3.2 and 3.3 shows that energy conservation during the nuclear burning phase is very good, such that our nucleosynthesis results are not affected by this issue.

3.4.2 Nucleosynthesis

Figure 3.4 shows the final chemical structure of our models. The total amounts of produced ^{56}Ni are 0.04 $M_\odot$ and 19.3 $M_\odot$ for the 150 $M_\odot$ and 250 $M_\odot$ star, respectively. As shown in Table 3.2, the overall nucleosynthetic results are in good agreement with that of the 70 $M_\odot$ and 115 $M_\odot$ Population III helium star models by Heger & Woosley (2002) of which the masses are comparable to the He core masses of our models.

We summarize the chemical yields and the production factors of each isotope from our explosion models in Table 3.3. Here the production factor of a given isotope is defined as

$$p_{\rm iso} = \frac{m_{\rm iso}}{X^\odot_{\rm iso} \times M_{\rm tot}} \, , \tag{3.2}$$

[2] 1 foe = 10^{51}erg (from 'fifty-one-erg')

Table 3.2: Total nucleosynthetic yields for selected isotopes in solar masses for our 150 $M_\odot$ and 250 $M_\odot$ models (including matter lost by stellar wind and decay products) in comparison with 70 $M_\odot$ and 115 $M_\odot$ zero metallicity helium star yields (Heger & Woosley 2002), respectively. Yields for hydrogen and helium neglecting the wind matter are given after the slash sign.

	^{1}H	^{4}He	^{12}C	^{16}O	^{20}Ne	^{24}Mg	^{28}Si
150 $M_\odot$	36.6/4.9	49.2/24.4	2.2	46.9	2.6	2.3	6.2
He 70 $M_\odot$	–	1.5	4.5	45.8	4.0	3.0	8.0
250 $M_\odot$	57.1/10.3	81.5/47.5	0.9	42.	1.8	2.5	23.1
He 115 $M_\odot$	–	1.8	3.7	40.	3.8	4.5	25.7
	^{32}S	^{36}Ar	^{40}Ca	^{46}Ti	^{50}Cr	^{56}Fe	
150 $M_\odot$	2.8	0.5	0.5	10^{-4}	10^{-4}	0.04	
He 70 $M_\odot$	2.4	0.3	0.2	10^{-4}	10^{-4}	0.01	
250 $M_\odot$	14.3	2.9	2.8	10^{-4}	10^{-4}	19.4	
He 115 $M_\odot$	11.8	1.9	1.6	10^{-5}	10^{-4}	19.0	

where $m_{\rm iso}$ is the total yield of a given isotope in solar masses, $X^{\odot}_{\rm iso}$ is the mass fraction of the isotope according to the solar metallicity pattern, and $M_{\rm tot}$ is the initial mass of the star (150 $M_\odot$ or 250 $M_\odot$ in the present study). The effect of radioactive decays is fully considered in the final set of the isotope yields that consists only of stable nuclei.

We use the solar abundances taken from Woosley & Weaver (1995) which were adopted from Anders & Grevesse (1989) to be consistent in our comparison to other PISN and CCSN nucleosynthetic yields. A more recent study of solar abundances (Asplund et al. 2009) shows somewhat different solar abundances. The overall fraction of heavy elements differs by a factor of 0.7 mostly due to a reduced oxygen abundance. $Z = 0.0134$ in Asplund et al. (2009) and $Z = 0.0201$ in Anders & Grevesse (1989). However, the solar abundances serve as a denominator for our qualitative comparison. Generally, the relative scatter of the elemental/isotopic production factor (i.e. odd-even effect) remains the same. We plot all production factors in Figures 3.6, 3.7, and 3.9 in logarithmic scale. Therefore, using the lower metal fraction will shift all data (except hydrogen and helium) by $|\log 0.7| \simeq 0.15$ dex.

The pair instability explosion in our models is mostly driven by oxygen burning because oxygen is the most abundant element at core carbon exhaustion. Our models 150M and 250M contain 64 $M_\odot$ and 110 $M_\odot$ oxygen cores, correspondingly, and a large fraction of the oxygen core remains unburnt: more than 40 $M_\odot$ of oxygen enrich the circumstellar medium, making oxygen the third most abundant element after hydrogen and helium. Note that only about 3 $M_\odot$ of oxygen are produced in an ordinary core-collapse SN (Woosley & Weaver 1995) and even less (about 0.1 $M_\odot$) is left after a SN Ia (Iwamoto et al. 1999; Travaglio et al. 2004).

Table 3.3: Total nucleosynthetic yields in solar masses and production factors for 150 $M_\odot$ and 250 $M_\odot$ models at metallicity $Z = 0.001$. Yields include matter lost by the stellar wind and decay products.

	Yields		Prod.factor	
	150 $M_\odot$	250 $M_\odot$	150 $M_\odot$	250 $M_\odot$
^{1}H	36.56	57.10	0.34	0.32
^{2}H	7.10(-11)	1.63(-10)	1.71(-8)	2.36(-8)
^{3}He	5.01(-5)	5.47(-5)	9.80(-3)	6.42(-3)
^{4}He	49.16	81.53	1.20	1.19
^{6}Li	4.93(-12)	2.10(-11)	4.45(-5)	1.14(-4)
^{7}Li	7.17(-10)	4.57(-8)	4.55(-4)	1.74(-2)
^{9}Be	8.77(-12)	1.88(-11)	3.01(-4)	3.88(-4)
^{10}B	2.14(-10)	4.25(-10)	1.43(-3)	1.70(-3)
^{11}B	7.17(-10)	4.58(-9)	1.07(-3)	4.10(-3)
^{12}C	2.22	0.90	6.04	1.46
^{13}C	3.58(-4)	5.60(-4)	8.00(-2)	7.52(-2)
^{14}N	4.10(-2)	7.27(-2)	0.34	0.37
^{15}N	1.17(-4)	3.37(-5)	0.25	4.31(-2)
^{16}O	46.86	41.96	47.33	25.43
^{17}O	1.10(-4)	1.54(-4)	0.28	0.24
^{18}O	1.24(-4)	4.94(-5)	5.57	1.33(-2)
^{19}F	3.76(-7)	4.03(-7)	5.36	3.45(-3)
^{20}Ne	2.58	1.85	14.69	6.32
^{21}Ne	4.17(-4)	8.79(-5)	0.95	0.12
^{22}Ne	1.19(-3)	1.17(-3)	8.42(-2)	4.94(-2)
^{23}Na	1.39(-2)	8.67(-3)	2.39	0.90
^{24}Mg	2.30	2.52	27.12	17.83
^{25}Mg	1.34(-2)	5.37(-3)	1.20	0.29
^{26}Mg	2.68(-2)	1.11(-2)	2.09	0.52
^{27}Al	1.14(-2)	4.20(-2)	1.15	2.53
^{28}Si	6.17	23.08	54.52	122.29
^{29}Si	4.62(-2)	3.24(-2)	7.76	3.26
^{30}Si	2.52(-2)	1.35(-2)	6.19	2.00
^{31}P	2.96(-3)	8.16(-3)	2.60	4.30
^{32}S	2.82	14.32	47.47	144.69
^{33}S	3.83(-3)	8.14(-3)	7.93	10.11
^{34}S	8.17(-3)	1.12(-2)	2.93	2.41
^{36}S	2.36(-8)	5.23(-8)	1.96(-3)	2.62(-3)
^{35}Cl	7.24(-4)	1.09(-2)	1.19	10.70
^{37}Cl	6.68(-4)	1.37(-3)	3.25	4.01
^{36}Ar	0.51	2.93	37.28	128.15

continuing at the next page

	Yields		Prod.factor	
	150 $M_\odot$	250 $M_\odot$	150 $M_\odot$	250 $M_\odot$
^{38}Ar	6.75(-3)	7.92(-3)	2.57	1.81
^{40}Ar	1.37(-10)	3.11(-9)	3.26(-5)	4.42(-4)
^{39}K	1.23(-3)	1.16(-2)	2.09	11.82
^{40}K	3.71(-8)	1.68(-6)	3.95(-2)	1.07
^{41}K	1.63(-4)	3.15(-4)	3.63	4.22
^{40}Ca	0.49	2.80	45.99	156.82
^{42}Ca	1.87(-4)	2.09(-4)	2.50	1.67
^{43}Ca	6.48(-8)	2.07(-5)	4.30(-3)	0.78
^{44}Ca	1.14(-4)	9.65(-4)	0.45	2.28
^{46}Ca	0	0	0	0
^{48}Ca	8.71(-20)	3.92(-17)	3.50(-15)	9.45(-13)
^{45}Sc	4.32(-6)	1.18(-5)	0.64	1.05
^{46}Ti	9.23(-5)	1.14(-4)	2.29	1.69
^{47}Ti	3.87(-7)	2.42(-6)	1.04(-2)	3.92(-2)
^{48}Ti	2.02(-4)	1.69(-2)	0.54	26.96
^{49}Ti	1.91(-5)	4.61(-4)	0.68	9.81
^{50}Ti	4.23(-12)	3.35(-12)	1.53(-7)	7.29(-8)
^{50}V	1.63(-10)	1.65(-10)	1.04(-3)	6.28(-4)
^{51}V	1.93(-5)	6.42(-4)	0.30	5.98
^{50}Cr	2.43(-4)	1.02(-3)	1.98	4.99
^{52}Cr	1.62(-3)	0.38	0.66	91.77
^{53}Cr	1.79(-4)	1.40(-2)	0.63	29.60
^{54}Cr	1.09(-8)	2.02(-8)	1.51(-4)	1.69(-4)
^{55}Mn	1.00(-3)	5.73(-2)	0.45	15.59
^{54}Fe	2.12(-2)	0.21	1.82	11.07
^{56}Fe	4.62(-2)	19.33	0.24	61.36
^{57}Fe	4.41(-4)	0.21	9.93(-2)	28.38
^{58}Fe	4.09(-6)	5.44(-5)	6.81(-3)	5.44(-2)
^{59}Co	3.99(-5)	5.11(-3)	6.63(-2)	5.10
^{58}Ni	1.83(-3)	0.37	0.22	26.73
^{60}Ni	1.24(-4)	7.35(-2)	3.75(-2)	13.36
^{61}Ni	2.57(-7)	3.75(-3)	1.76(-3)	15.44
^{62}Ni	9.40(-7)	2.59(-2)	1.99(-3)	32.86
^{64}Ni	7.44(-12)	4.46(-9)	6.00(-8)	2.16(-5)
^{63}Cu	3.95(-9)	2.40(-5)	3.92(-5)	0.14
^{65}Cu	1.76(-11)	9.92(-6)	3.80(-7)	0.13
^{64}Zn	1.98(-9)	1.20(-4)	1.18(-5)	0.43
^{66}Zn	6.34(-11)	2.24(-4)	6.40(-7)	1.36
^{67}Zn	5.63(-15)	1.56(-7)	3.81(-10)	6.34(-3)
^{68}Zn	8.90(-15)	4.64(-8)	1.30(-10)	4.06(-4)

continuing at the next page

	Yields		Prod.factor	
	150 $M_\odot$	250 $M_\odot$	150 $M_\odot$	250 $M_\odot$
^{70}Zn	0	0	0	0
^{69}Ga	4.22(-16)	4.47(-13)	6.45(-11)	4.10(-8)
^{71}Ga	0	0	0	0
^{70}Ge	6.93(-16)	9.16(-15)	8.82(-11)	7.00(-10)

The highest yields in Model 150M are those of intermediate even-charged isotopes between oxygen and sulphur (2.6 $M_\odot$ of ^{20}Ne, 2.3 $M_\odot$ of ^{24}Mg, 6.2 $M_\odot$ of ^{28}Si, 2.8 $M_\odot$ of ^{32}S) because only a small fraction of silicon is burnt in this PISN (see Table 3.3). The yields of iron-group isotopes are fairly low compared to intermediate mass isotopes. At the same time the ejecta of Model 250M contains large amounts of intermediate mass isotopes similar to the Model 150M (1.85 $M_\odot$ of ^{20}Ne, 2.5 $M_\odot$ of ^{24}Mg, 23.1 $M_\odot$ of ^{28}Si, 14.3 $M_\odot$ of ^{32}S, 2.9 $M_\odot$ of ^{36}Ar, 2.8 $M_\odot$ of ^{40}Ca), significant amounts of iron-group isotopes (0.4 $M_\odot$ of ^{52}Cr, 0.2 $M_\odot$ of ^{54}Fe, 0.2 $M_\odot$ of ^{57}Fe, 0.4 $M_\odot$ of ^{58}Ni) and a very large iron-56 yield (19.3 $M_\odot$). There is a gap around the titanium isotopes since these are the bottle-neck isotopes between QSE-groups (Hix & Thielemann 1996).

Large amounts of silicon (6 $M_\odot$ and 23 $M_\odot$, respectively) are left after incomplete silicon burning in both models, which are 10 – 100 times higher than silicon yields resulting from core-collapse SNe and SNe Ia. The average yield of silicon in core-collapse SNe and SNe Ia is 0.4 $M_\odot$ and 0.6 $M_\odot$, respectively. A large amount of radioactive nickel produced in our higher mass Model 250M (19.3 $M_\odot$) will result in a very bright and broad supernova light curve (Scannapieco et al. 2005; Kasen et al. 2011; Kozyreva et al. 2014a). This amount is much larger than the average iron yield of 0.04 – 0.2 $M_\odot$ in core-collapse SNe and 0.5 $M_\odot$ in SNe Ia (Patat et al. 1994; Smartt 2009).

We emphasize here that both our PISN models do not produce pronounced amounts of isotopes beyond the iron-group: the mass fractions of copper, zinc gallium and germanium isotopes are well below 10^{-4}. The lack of r- and s-isotopes is explained mostly by the neutron deficiency that is explained below[3].

PISNe occur since the cores of their progenitors remain much less dense than those of core-collapse SN progenitors (c.f. Langer 2012). This makes neutronization during the final evolutionary stages much less significant than in core-collapse progenitors. Heger & Woosley (2002) showed that this results in a remarkable deficiency of odd-charged nuclei compared to even-charged nuclei in the nucleosynthesis of Population III PISNe. Table 3.1 shows that our starting models have much larger neutron excesses ($\eta_\mathrm{i} \sim 10^{-4}$) than the initial Population III star models of Heger & Woosley ($\eta_\mathrm{i} \sim 10^{-7}$). However, the neutron excess in the central region (η_c) where silicon burning occurs does not increase much. The maximum neutron excess achieved at the center ($\eta_\mathrm{c}^\mathrm{max}$) in the 150 $M_\odot$ and 250 $M_\odot$ models is only 2×10^{-4} and 1.6×10^{-3}, respectively. In the comparable Population III helium star models of Heger & Woosley (2002) (i.e. their 70 $M_\odot$ and 115 $M_\odot$ models; see Figure 3.2), the values of $\eta_\mathrm{c}^\mathrm{max}$ are 2.8×10^{-4} and 7.3×10^{-4}, respectively (Table 3.1), which is a factor

[3]Note that in the nuclear network used in our study no element heavier than germanium is included.

of 3. . .5 lower.

This indicates that the neutron excess in PISNe during the explosion phase does not increase by much more than about 10^{-3} over the values at core helium exhaustion. Interestingly, this implies that even if the initial metallicity of a PISN progenitor was as high as $Z_{\odot}$, the neutron excess in the core would not become much higher than about 10^{-3}, which is the typical value of the neutron excess in the innermost layers of solar metallicity massive stars at core helium exhaustion. This value is much smaller than the neutron excess achieved in the silicon shell of a typical core-collapse progenitor ($\eta \cong 10^{-2}$), where explosive nuclear burning occurs during the supernova explosion. We conclude that the odd-even effect is expected to be significant even in metal-rich PISNe.

Heger & Woosley (2005) argued that an unusually strong mixing of nitrogen into the helium core of a PISN progenitor may make the odd-even effect as weak as in the nucleosynthesis of a core-collapse supernova. However, to increase the neutron excess to $\eta \cong 10^{-2}$ by such mixing is very difficult to achieve in massive stars, as discussed in Yoon et al. (2012a). It requires abundant production of primary nitrogen in the first place, which in turn requires efficient chemical mixing of carbon and oxygen into hydrogen shell burning during the post-main sequence phases. Then, the primary nitrogen has to be mixed into the core of the star to increase the neutron excess, via the $^{14}\mathrm{N}\,(\alpha,\gamma)^{18}\mathrm{F}\,(e^{+},\nu)^{18}\mathrm{O}$ reaction. One possibility for such mixing is the penetration of the helium-burning convective core into the hydrogen burning shell source, which is often observed in massive Population III star models (Heger & Woosley 2010; Yoon et al. 2012a). Such mixing of nitrogen into the stellar core by convection is not observed in our PISN progenitor models as shown in Figure 3.5. Even if it occurred, it would be difficult to enhance the neutron excess to more than about 10^{-3} (Yoon et al. 2012a). Another possibility is rotationally induced mixing. Our models are initially slow rotators and lost most of their initial angular momentum via mass loss, rendering the role of rotation unimportant. Yoon et al. (2012a) concluded that mixing of nitrogen resulting from rotation may not enhance the neutron excess by more than about 10^{-5} even for the extreme case of the so-called chemically homogeneous evolution. Furthermore, PISNe through chemically homogeneous evolution are expected only at extremely low metallicity of $Z \lesssim 10^{-5}$ (Yoon et al. 2006; Langer et al. 2007). We conclude that the neutron excess does not exceed $\sim 10^{-3}$ in most PISN progenitors.

As expected from the above discussion, the odd-even effect in our models also appears to be strong (Figures 3.6, 3.7, and 3.9). The ratio of the even- to odd-charged isotope mass fractions reaches $10^{2} - 10^{5}$, which is far from the observed values in the solar system and in metal-poor stars (Cayrel et al. 2004; Christlieb et al. 2004; Frebel et al. 2005). However, this effect is significantly weakened, compared to the case of the corresponding Population III star models, for relatively light nuclei (i.e., lighter than silicon for the 150 $M_{\odot}$ model and calcium for the 250 $M_{\odot}$ model respectively). This is because these elements are produced in the upper layers of the star where neutronization during the explosive phase does not occur and the degree of the odd-even effect is largely determined by the initial metallicity of the star. For example, the production factors of magnesium and sodium differ by 1.2 dex in our 250 $M_{\odot}$ model, while this difference increases to 2.1 dex in the corresponding Population III model.

Note also that the overall production factors of our models are smaller than those of the corresponding Population III star models, despite the fact that the total yields of heavy elements are similar as shown in Table 3.2. For example, the production factors of iron from our 250 $M_\odot$ model and a Population III 115 $M_\odot$ helium star model are 59 and 125, respectively, while both models give the same total amount of iron (about 19 $M_\odot$). The reason for this difference is simply that the presence of a hydrogen envelope is ignored in the case of the Population III helium star models (i.e., the helium core masses correspond to the initial masses), while in our models the helium core masses are only certain fractions of the initial masses.

In the next section, we discuss the implications of this result for the chemical evolution of galaxies.

3.5 Implications for chemical evolution

As mentioned above, very massive stars at relatively high metallicity are supposed to lose too much mass to produce PISNe, and metal-poor environments are preferred for PISN progenitors. Langer et al. (2007) argued that the metallicity threshold for PISNe ($Z_{\rm PISN}$) may be about $Z_\odot/10 \ldots Z_\odot/3$. This conclusion is in an agreement with the recent result of another detailed numerical study by Yusof et al. (2013).

Therefore, it is an important question how PISNe contributed to the chemical evolution of galaxies in environments with $Z \lesssim Z_{\rm PISN}$. This critically depends on how many PISN progenitors form as a function of time. There are several possibilities for the formation mechanism of very massive stars (cf. Zinnecker & Yorke 2007), including very rapid mass accretion (e.g. Hosokawa & Omukai 2009), mergers in close binary systems and stellar collisions (e.g., Yungelson et al. 2008; Pan et al. 2012b). Recent observations indicate that the upper stellar mass limit ($M_{\rm UP}$) may be as high as 180 $M_\odot$ in our Galaxy and 300 $M_\odot$ in Large Magellanic Cloud (Crowther et al. 2010; Schneider et al. 2014). Because of the paucity of very massive stars discovered in the local Universe, these observations still do not give a good constraint on the initial mass function for potential progenitors of PISNe. If we simply assume the Salpeter-like IMF ($\Gamma = -2.3$), about 2% of all supernova progenitors ($M \gtrsim 12$ $M_\odot$) have initial masses high enough ($M \gtrsim 140$ $M_\odot$) to produce a PISN.

To evaluate the contribution of PISNe to chemical evolution compared to that of core-collapse SNe, we calculated the production factor of major nuclei in the following way. The production factor integrated over an IMF ($\Phi(M) \propto M^\Gamma$) relative to solar abundances for a given isotope is given by

$$P^{\rm int} = \frac{\int_{12}^{260} m_{\rm iso}\, \Phi(M)\, dM}{\int_{12}^{260} X_{\rm iso}^\odot\, M\, \Phi(M)\, dM} = \frac{\int_{12}^{260} m_{\rm iso}\, M^\Gamma\, dM}{\int_{12}^{260} X_{\rm iso}^\odot\, M^{\Gamma+1}\, dM} \ . \tag{3.3}$$

Here, the minimum and the maximum masses for supernova progenitors are assumed to be 12 $M_\odot$ and 260 $M_\odot$, respectively. We adopt the core-collapse SN yields from Woosley &

Weaver (1995). Since we have only two models at 150 $M_\odot$ and 250 $M_\odot$, we interpolate and extrapolate our results to cover the full PISN regime (140 – 260 $M_\odot$) for this calculation, as shown in Figure 3.8. From the qualitative analysis of metal-free helium PISN models (Heger & Woosley 2002) we find that linear interpolation gives about 20% effect on weighted bulk yields, which correspond to 0.1 – 0.2 dex differences for final bulk production factors.

This figure illustrates the contributions of core-collapse SNe and PISNe to the chemical enrichment. We assume that yields from core-collapse SNe come from the explosions of massive stars in the mass range from 12 $M_\odot$ to 40 $M_\odot$. These values are taken from the low energy explosion models of massive stars at a metallicity of $Z = 0.002$ by Woosley & Weaver (1995). The integration over the hatched regions in the figure denotes the IMF-weighted total amount of heavy elements (all elements heavier than helium) ejected by the stars from one generation. Note that even though the number of stars in the PISN range is significantly smaller than the number of core-collapse progenitors, the total amount of heavy elements ejected from PISNe appears comparable to the integrated CCSN yield.

Here we assume that stars with initial masses between 40 $M_\odot$ and 140 $M_\odot$, and also above 260 $M_\odot$ do not considerably contribute to the enrichment of surrounding medium with heavy elements. We should mention that massive stars lose mass through winds, which may be enhanced in metals (e.g. carbon) and they contribute to the galactic enrichment even though they form black holes in the end. However, the stellar winds, also those of the carbon-rich Wolf-Rayet stars, are reduced for lower initial iron abundances (Vink & de Koter 2005), such that their effect at the considered metallicities will be small.

Figure 3.9 clearly indicates that the inclusion of PISN yields has a strong impact on the total production factors even at finite metallicity: the production factor of the even-charged nuclei is enhanced by a factor of 2 – 3 for most of the $\alpha-$elements with PISNe, while it is mostly negligible for the odd-charged nuclei. Note that this odd-even effect becomes strongest for the elements between Al and Sc. However, the odd-even effect is much weaker in our models compared to the Population III models. The Population III yields give almost 10 times higher production factors of even-charged nuclei with the inclusion of PISNe. This difference is mainly because the overall core-collapse SN yields at a metallicity of $Z = 0.002$ are significantly larger than those of Population III core-collapse SNe, and partly because our PISN models give a somewhat weaker odd-even effect than the Population III models as discussed above.

As discussed in Section 3.2, the event rate of PISNe is expected to decrease to zero for metallicities higher than about $Z = Z_\odot/3$. The nucleosynthetic signature of PISNe should be washed out by contribution of core-collapse SNe as the metallicity reaches the solar value, and the effect of PISNe on chemical evolution might not be found in Population I stars. However, from our study we conclude that the impact of PISNe in the environment of $Z = 0.001 - 0.002$ may be still significant depending on the IMF, and should be tested in future observations of Population II stars with metallicities well below $Z = Z_\odot/3$.

3.6 Conclusions

In the frame of this study we calculated the evolution of two very massive stellar models at a metallicity of $Z = 0.001$. These two models have initial zero age main sequence masses of 150 $M_\odot$ and 250 $M_\odot$. The models were evolved through the core hydrogen, helium and carbon burning (Langer et al. 2007) with the Binary Evolution Code BEC of the Bonn stellar physics group (Yoon et al. 2006). Here, we continued the evolution using the same evolutionary code with an extended nuclear network where 200 isotopes are considered. We evolved these models through the electron-positron pair creation phase and the consequent collapse and explosive oxygen and silicon burning. The 150 $M_\odot$ and 250 $M_\odot$ models eject a total amount of 64 $M_\odot$ and 111 $M_\odot$ of metals, respectively.

We find that an excess production of even-charged elements compared to odd-charged elements is still found in our models as in Population III PISNe. However, the odd-even effect is smaller for most of the $\alpha-$elements compared to the case of Population III stars because of the initially higher metallicity. The nucleosynthetic pattern of the iron-group elements is critically determined by the neutronization during the explosive burning and therefore less affected by the initial metallicity.

Given that our 150 $M_\odot$ and 250 $M_\odot$ models represent the low-mass and high-mass ends of PISN regime respectively, this study allowed us to compare the PISN nucleosynthesis with that of core-collapse supernovae at a similar metallicity. We find that the impact of PISNe on the overall nucleosynthetic pattern is expected to be weaker at $Z = 0.001 - 0.002$ than in the metal-free environment (Figure 3.9). This is mainly because of the higher initial neutron excess of our models set by higher initial metallicity.

However, the total nucleosynthetic yields from both core-collapse SNe and PISNe at $Z = 0.001 - 0.002$, assuming a Salpeter IMF, would result in the enhancement of $\alpha-$elements by factors of 2 – 3 compared to the case without PISN contribution (Figures 3.8 and 3.9). This analysis shows that PISNe at a metallicity of $Z = 0.001$ can contribute to the enrichment of the interstellar medium with heavy elements in a similar way as Population III PISNe: the odd-even effect is still expected in metal-poor stars at metallicities of about $0.001 - 0.002$, although its degree would be reduced by factors of 3 – 4 compared to the prediction from Population III stars, as shown in Figure 3.9. Therefore, our models may be a useful guide for interpreting future observations of the chemical abundances in Population II stars at $Z \approx 0.001 - 0.002$ to constrain the number of PISNe that might have occurred in our Galaxy.

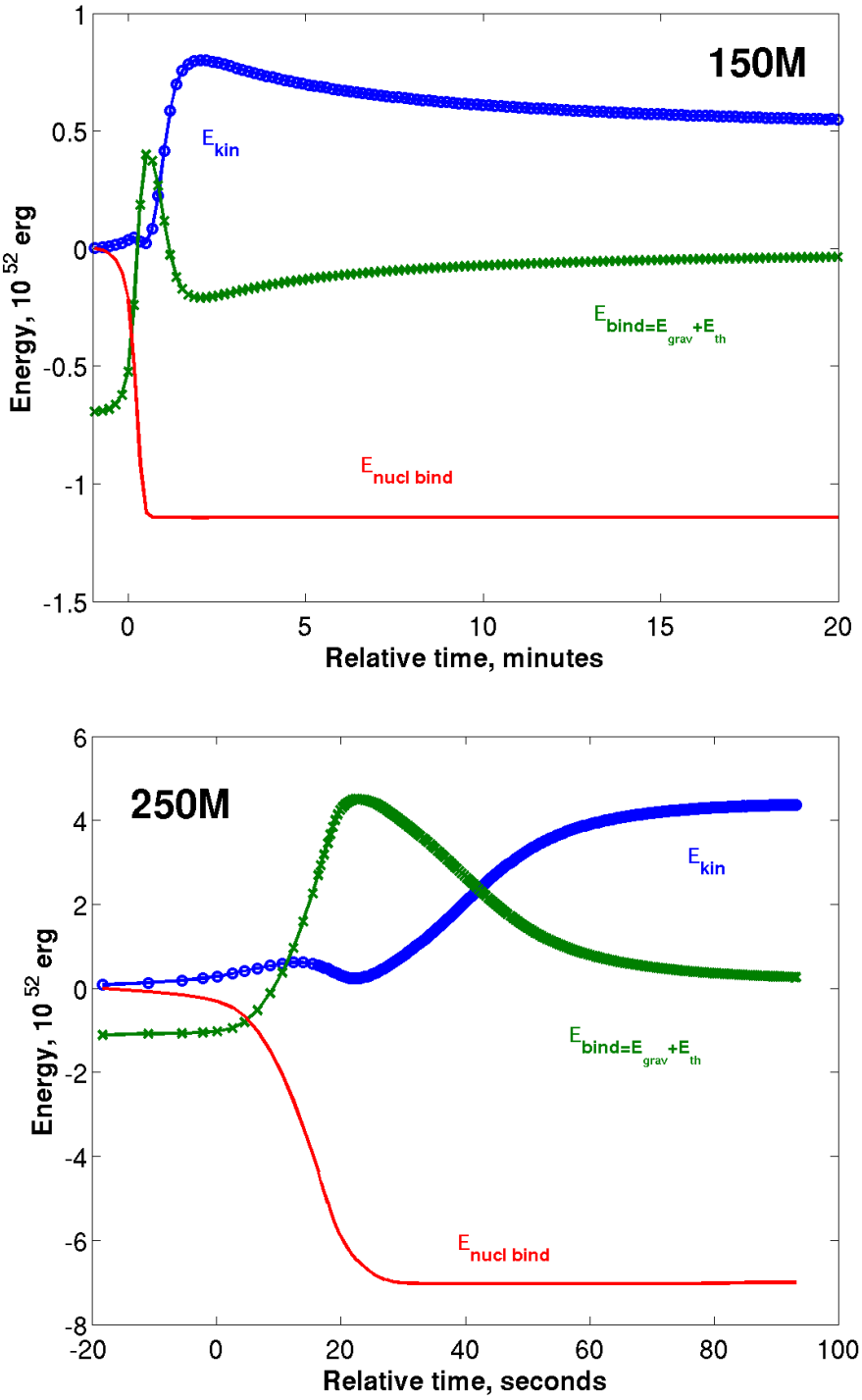

Figure 3.2: Evolution of the energetics for our 150 $M_{\odot}$ and 250 $M_{\odot}$ models. The kinetic energy (blue, circles), the binding energy (green, times) that is the sum of gravitational and thermal energies, and the nuclear binding energy (red) of the stars are shown. Here, the nuclear binding energy is defined by the difference between the total nuclear binding energy of all nuclei at the end of carbon burning and that of a given evolutionary epoch (see description in the text). The zero point in time is defined as the time of the beginning of pair instability explosion.

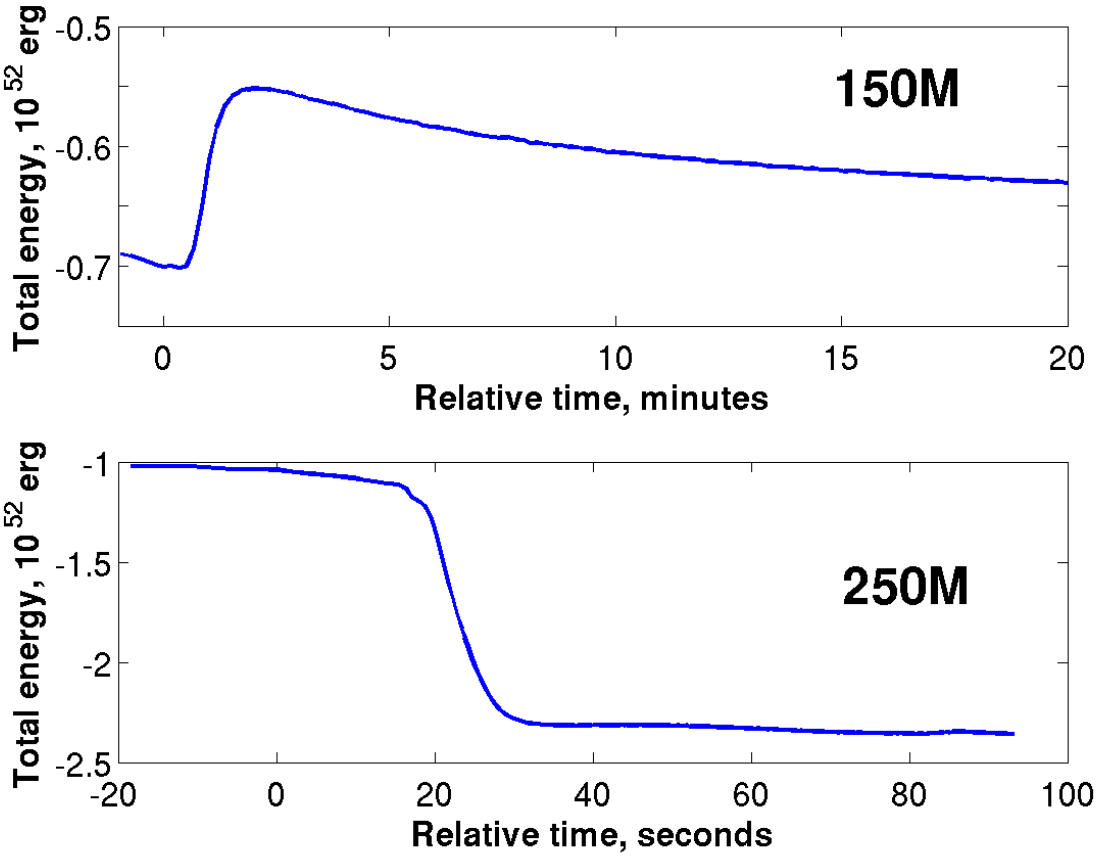

Figure 3.3: Total energy evolution for our 1500 $M_{\odot}$ (upper) and 250 $M_{\odot}$ (bottom) models.

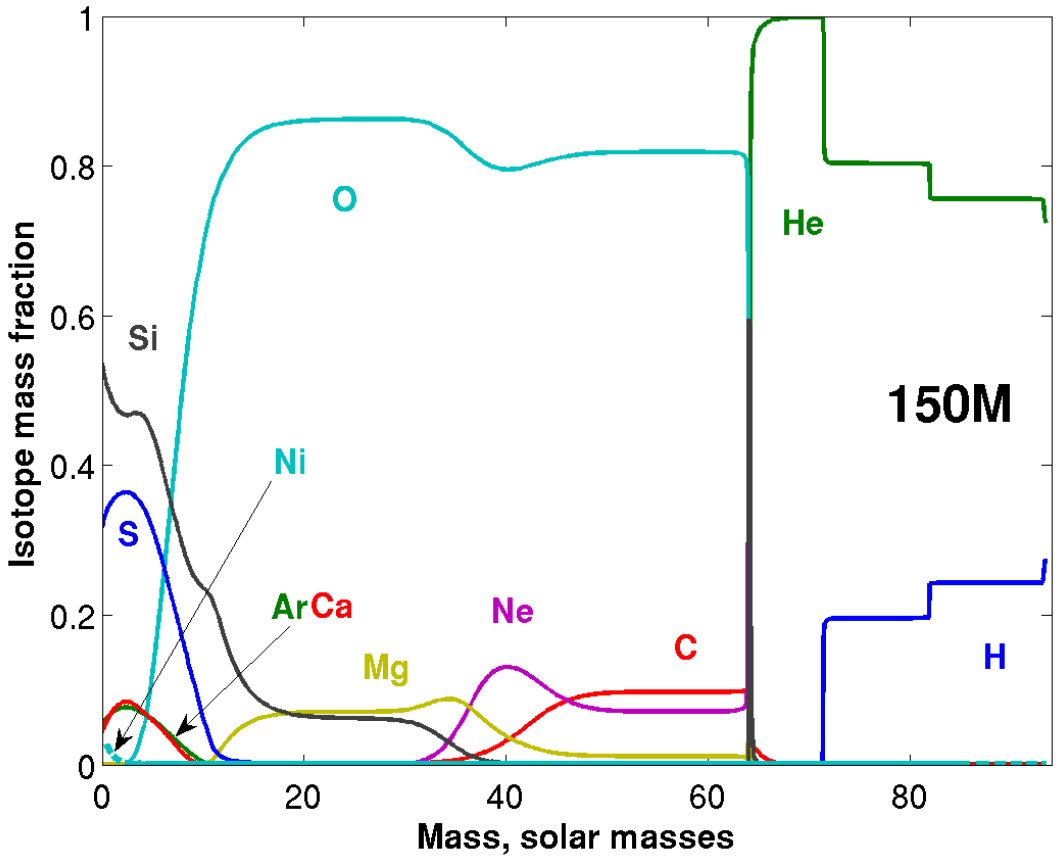

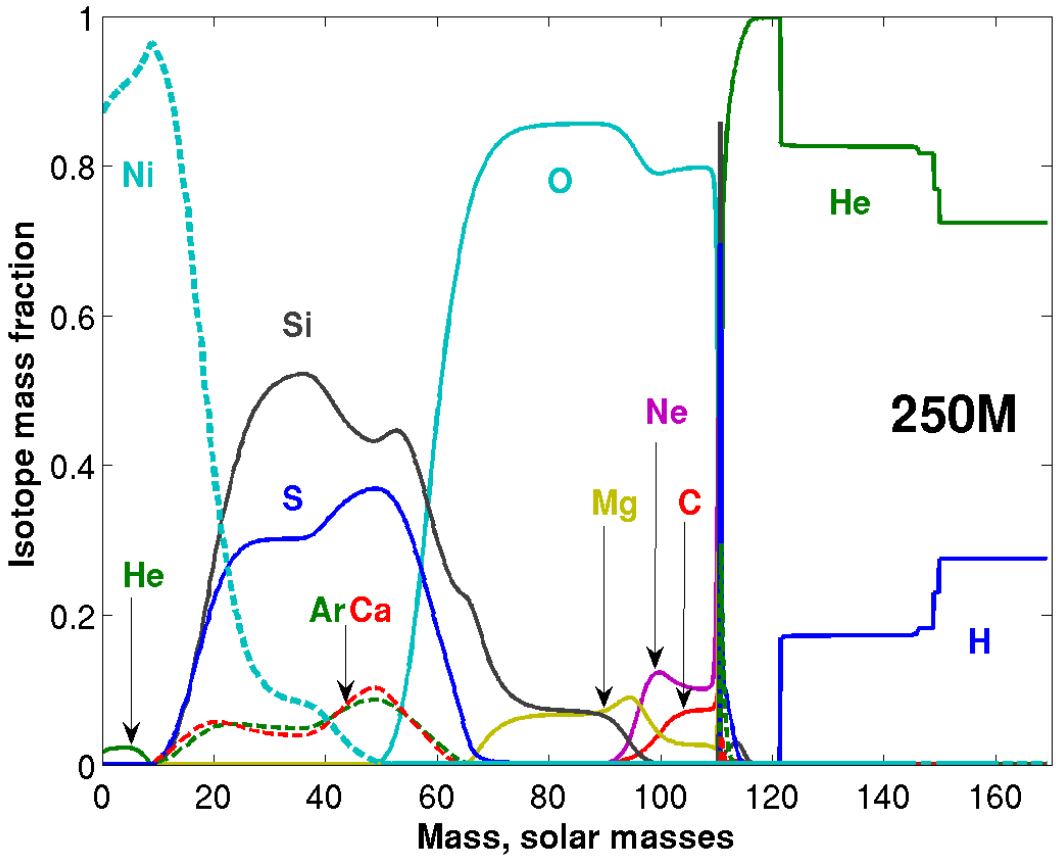

Figure 3.4: The final chemical structure of our models.

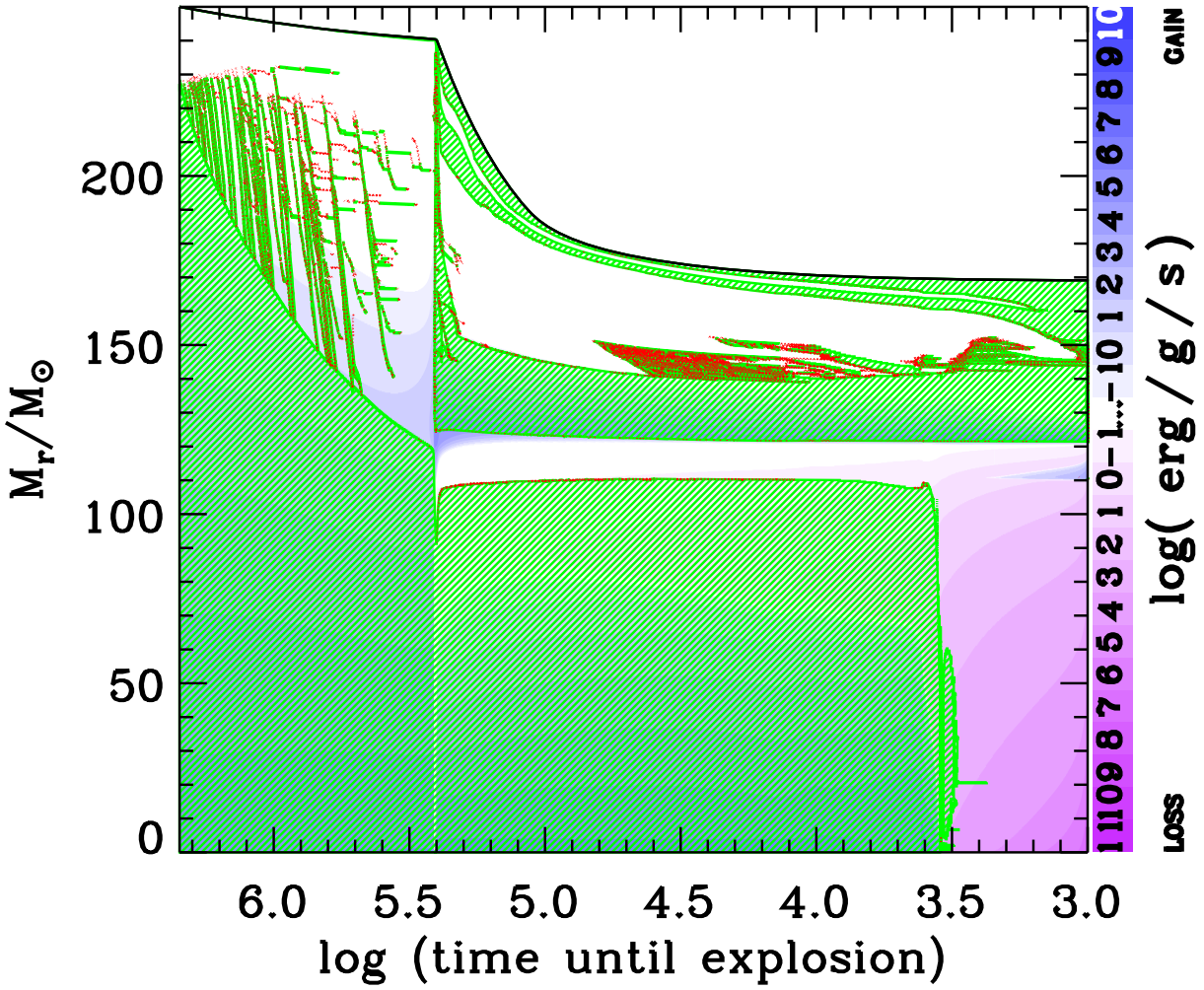

Figure 3.5: Kippenhahn diagram for the 250 $M_\odot$ PISN model. Convective and semi-convective layers are marked by green hatched lines and red dots, respectively. The net amount of local energy loss and production is indicated by colar shading. The surface of the star is marked by the black solid line.

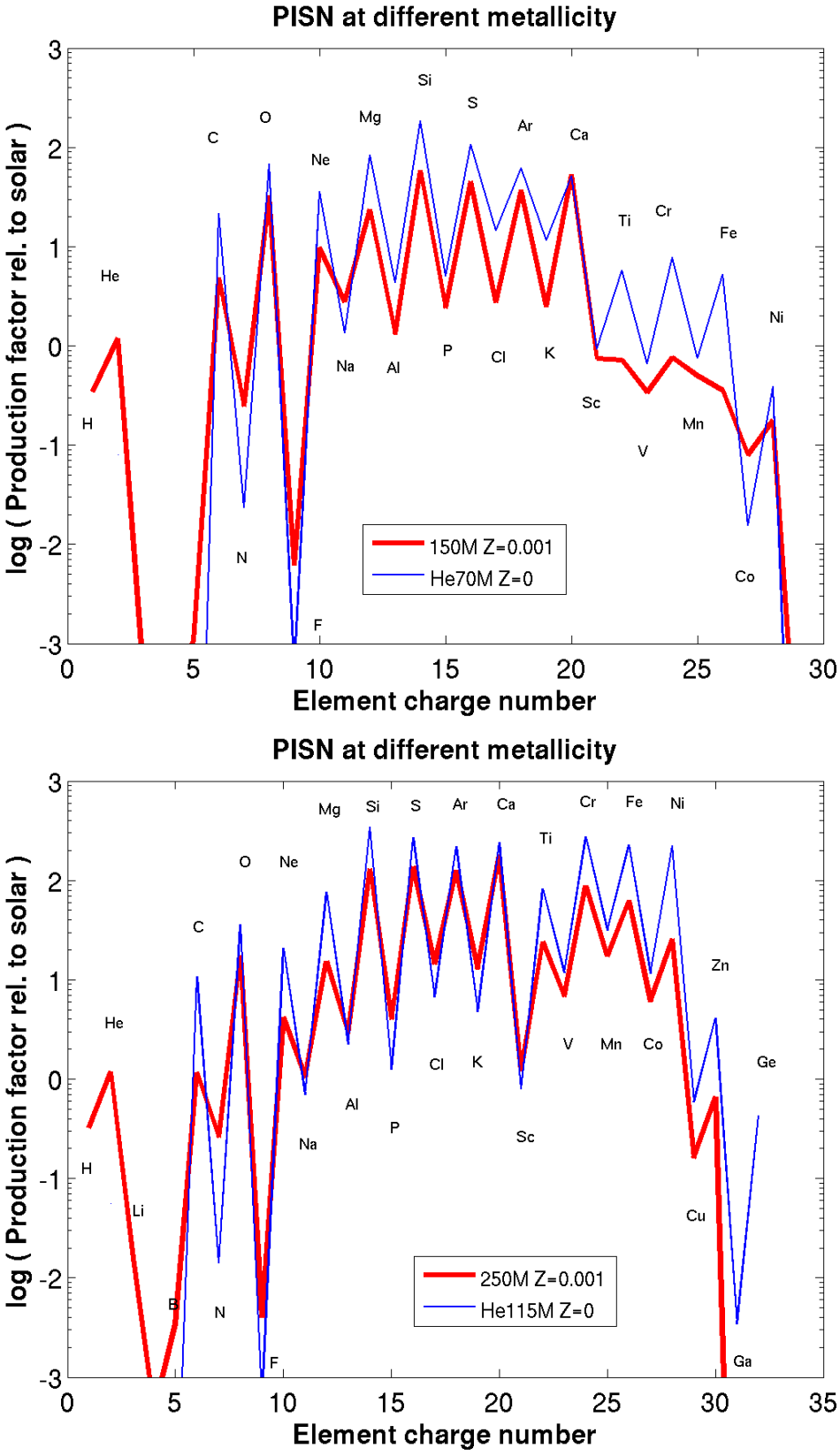

Figure 3.6: Production factors of major elements from our 150 $M_{\odot}$(upper panel) and 250 $M_{\odot}$(lower panel) PISN models (red thick lines) compared with those of comparable 70 $M_{\odot}$ (upper panel) and 115 $M_{\odot}$ (lower panel) Population III helium star model by Heger & Woosley (2002) (blue thin lines).

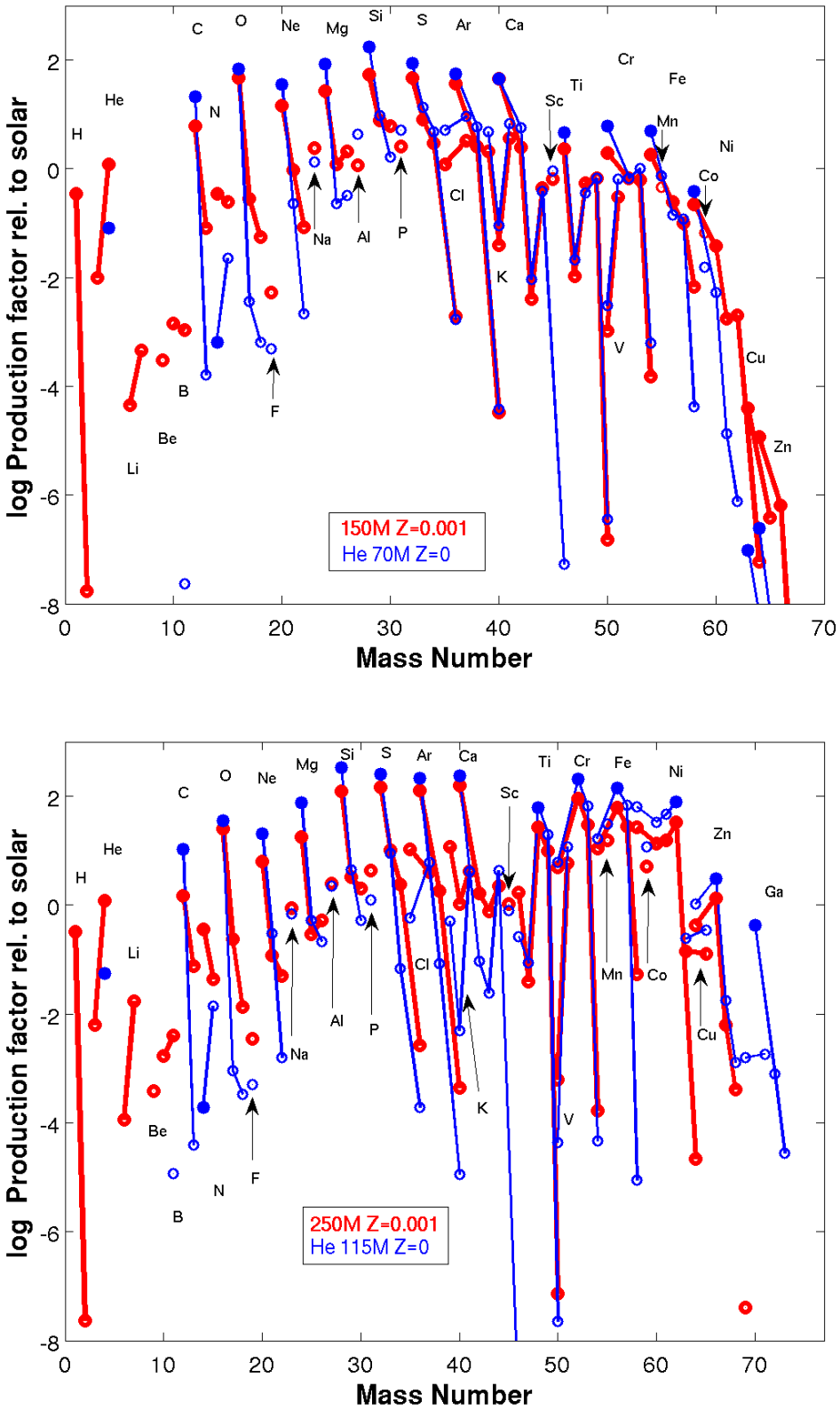

Figure 3.7: Isotopic production factors for the indicated nuclei. The isotopes of a given element are connected by solid lines. The filled circles indicates the most abundant isotope for each element, while the open circles denote the other isotopes. Our 150 $M_{\odot}$(upper panel) and 250 $M_{\odot}$(lower panel) PISN models (red thick) are compared with those of comparable 70 $M_{\odot}$ (upper panel) and 115 $M_{\odot}$ (lower panel) Population III helium star model by Heger & Woosley (2002) (blue thin).

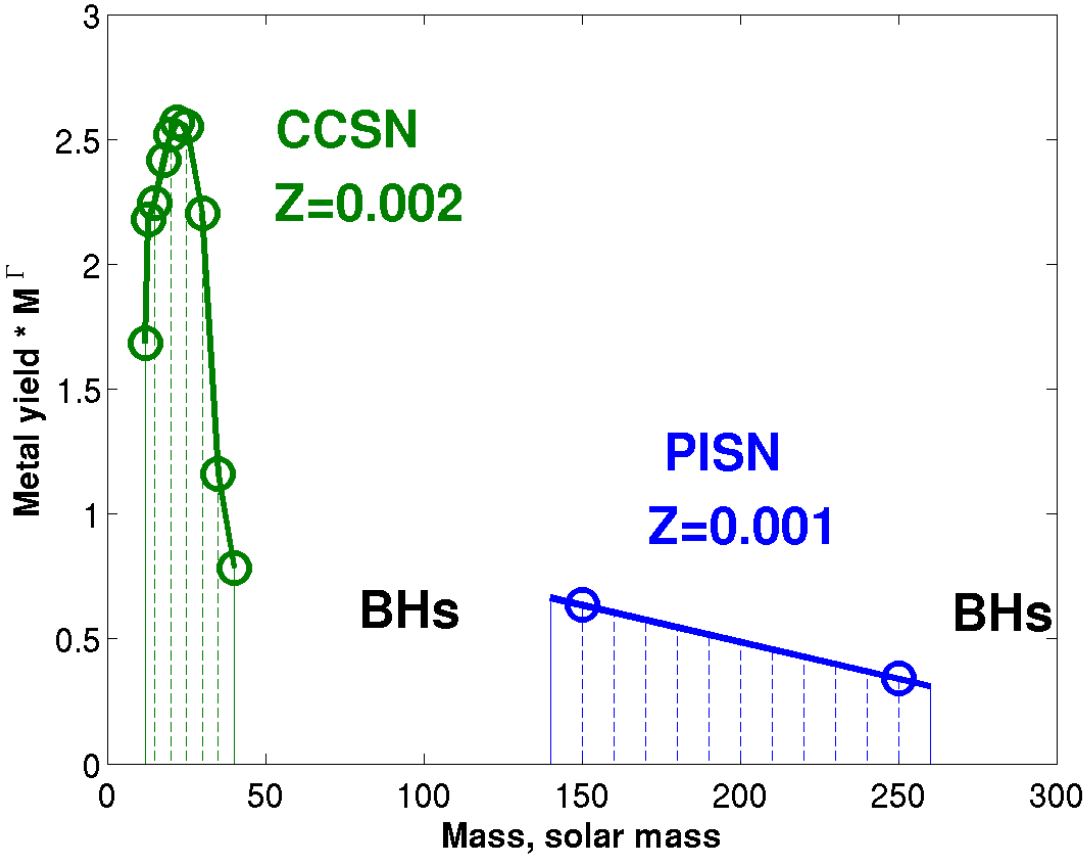

Figure 3.8: The total metal yields of core-collapse SN models at $Z = 0.002$ provided by Woosley & Weaver (1995) (the A-series SNe models; green line) and of PISNe at $Z = 0.001$ (blue line), multiplied by the initial mass function probability ($\Phi(M) \propto M^{\Gamma}$), as a function of the initial mass. The y-axis is given in arbitrary units. Here, the PISN yields in the range 140 $M_{\odot}$ – 260 $M_{\odot}$ are given by the extrapolation and interpolation of our 150 $M_{\odot}$ and 250 $M_{\odot}$ model results. We assumed a negligible metal yield for 40 $M_{\odot} < M < 140 M_{\odot}$ and above 260 $M_{\odot}$.

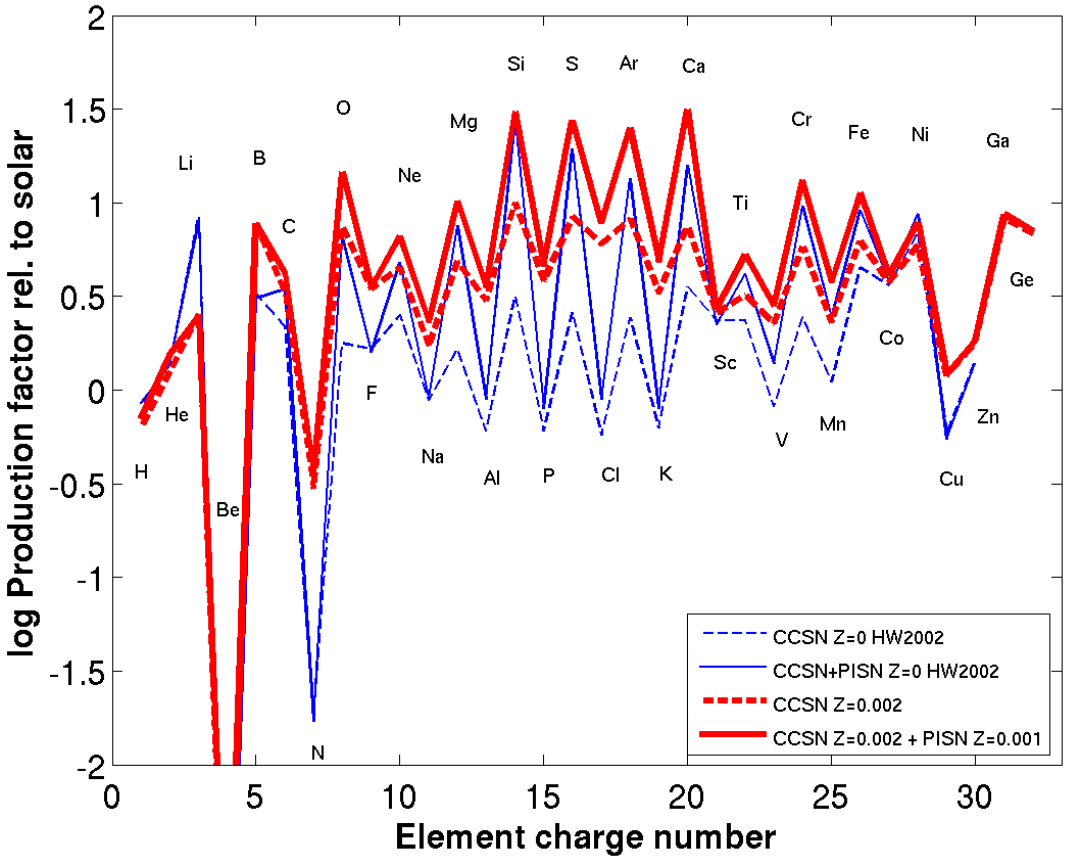

Figure 3.9: Production factors relative to solar abundances of major elements from core-collapse SNe (dotted lines), and from both core-collapse and pair-instability SNe (solid lines). The blue thin lines are the results using the Population III star models by Woosley & Weaver (1995) and Heger & Woosley (2002). The red thick lines correspond to the production factors using the values from Woosley & Weaver (1995) and present study (shown in Figure 3.8).

Chapter 4

Observational properties of low redshift pair instability supernovae

This chapter includes the description of carried out simulations of the explosion of very massive stars. It contains the results of calculations for two evolutionary models of 150 $M_{\odot}$ and 250 $M_{\odot}$ exploded as pair instability supernovae. The chapter illustrates similarities and differencies to other pair instability supernova simulations and also the comparison to discovered bright and luminous supernovae type IIP and type Ic.

4.1 Overview

So-called superluminous supernovae have been recently discovered in the local Universe. It appears possible that some of them originate from stellar explosions induced by the pair instability mechanism. Recent stellar evolution models also predict pair instability supernovae from very massive stars at fairly high metallicities (i.e., $Z \sim 0.004$).

We provide supernova models and synthetic light curves for two progenitor models, a 150 $M_{\odot}$ red supergiant and a 250 $M_{\odot}$ yellow supergiant at a metallicity of $Z = 0.001$, for which the evolution from the main sequence to collapse and the initiation of the pair instability supernova (PISN) itself has been previously computed in a realistic and self-consistent way.

We use the radiation hydrodynamics code STELLA to describe the supernova evolution of both models over a time frame of about 500 days.

We describe the shock-breakout phases of both supernovae, which are characterized by a higher luminosity, a longer duration and a lower effective temperature than those of ordinary Type IIP supernovae. We derive the bolometric, as well as the U, B, V, R, and I, light curves of our pair instability supernova models, which show a long-lasting plateau phase with maxima at $M_{\rm bol} \simeq -19.3$ mag and -21.3 mag for our lower and higher mass

models, respectively. While we do not produce synthetic spectra, we also describe the photospheric composition and velocity as a function of time.

We conclude that the light curve of the explosion of our initially 150 $M_\odot$ star resembles those of relatively bright type IIP supernovae, whereas its photospheric velocity at early times is somewhat lower. Its ^{56}Ni mass of 0.04 $M_\odot$ also falls well into the range found in ordinary core collapse supernovae. The light curve and photospheric velocity of our 250 $M_\odot$ models has a striking resemblance to that of the superluminous SN 2007bi, strengthening its interpretation as pair instability supernova. We conclude that pair instability supernovae may occur more frequently in the local universe than previously assumed.

4.2 Introduction

The final fate of very massive stars with initial masses between approximately 140 $M_\odot$ and 260 $M_\odot$ has been studied in many papers (Fowler & Hoyle 1964; Bisnovatyi-Kogan & Kazhdan 1967; Rakavy & Shaviv 1967; Barkat et al. 1967; Fraley 1968; El Eid & Langer 1986; Heger et al. 2003). Such massive stars undergo the dynamical instability caused by the creation of electron-positron pairs in oxygen cores, if they can keep their oxygen core masses high enough ($\gtrsim 60$ $M_\odot$) until carbon exhaustion at the center (Heger et al. 2003). This leads to explosive oxygen burning that eventually causes complete disruption of the star without leaving a compact remnant behind.

Theoretical models predict that these pair instability supernovae (PISNe) can be much more energetic and luminous than ordinary SNe. Explosion energies of up to 10^{53} erg and masses of radioactive nickel up to 40 $M_\odot$ (e.g., Heger & Woosley 2002) are found to be achieved depending on the progenitor mass. The corresponding light curves are characterized by a long-duration of several hundreds of days and luminosities of up to $10^{43} - 10^{44}$ erg s^{-1} (Scannapieco et al. 2005; Kasen et al. 2011; Dessart et al. 2013; Whalen et al. 2013a,d).

It is believed that PISNe are particularly relevant to the first generations of stars in the early Universe. Theoretical studies indicate that a significant fraction of the first stars would be massive enough to be potential progenitors of PISNe, mainly because of the lack of efficient coolants in the star-forming regions in the early Universe (e.g., Bromm et al. 1999; Nakamura & Umemura 2001; Abel et al. 2002; Omukai & Palla 2003; O'Shea & Norman 2006; Ohkubo et al. 2009). Such very massive stars in the early Universe would not lose much mass during the pre-supernova evolutionary stages in favor of PISN production, because metal-free massive stars are not supposed to have strong line-driven winds (Krtička & Kubát 2006) and because they are expected to be stable against pulsations (Baraffe et al. 2001). Several numerical studies have been therefore presented to discuss the nature and detectability of PISNe in the early Universe (Scannapieco et al. 2005; Kasen et al. 2011; Dessart et al. 2013; Whalen et al. 2013a). These studies considered a variety of PISN progenitors including red supergiants (RSG), blue supergiants (BSG) and pure helium stars, but the considered metallicities of these progenitor models were limited to zero or very small values ($Z \leq 10^{-4}$).

However, several recent studies indicate that PISNe are likely to occur not only in the early Universe, but also in the local Universe where metallicity is systematically higher than in the environments with high redshift. Crowther et al. (2010) found several very massive stars (VMS) with initial masses of 150 $M_\odot \lesssim M \lesssim 320\ M_\odot$ in the Large Magellanic Clouds (LMC), which are potential PISN progenitors. The final fate of such VMS stars is critically determined by mass loss (e.g., Vink et al. 2011). Given the strong metallicity dependence of the stellar winds mass loss rate (e.g., Mokiem et al. 2007), it is generally believed that VMSs cannot retain enough mass to produce PISNe for high metallicity. However, Langer et al. (2007) point out that the production of PISNe does not necessarily require extremely metal-poor environments, although low metallicity is still preferred. Using stellar evolution models, they argue that the metallicity threshold below which PISNe may occur ($Z_{\rm PISN}$) can be as high as $Z_\odot/3$ (Langer 2009). More recently Yusof et al. (2013) drew a similar conclusion.

The recent discovery of several superluminous SNe (SLSNe) that cannot be easily explained by usual core-collapse and/or interaction supernovae (see Gal-Yam 2012a, for a recent review) also provides evidence for PISN in the local Universe. In particular, the observed properties of SN 2007bi and SN 2213-1745 seem to imply a large amount of radioactive nickel in these supernovae (i.e, more than 3 $M_\odot$ of ^{56}Ni), for which PISN explosion gives one of the best explanations (Gal-Yam et al. 2009; Young et al. 2010; Cooke et al. 2012). Given that some other possibilities like very energetic core-collapse explosion or magnetar-driven SN have also been suggested to explain SLSNe (Moriya et al. 2010; Woosley 2010; Kasen & Bildsten 2010) and that future observational SN surveys will discover more diverse SLSN events in nearby galaxies, detailed studies on the observable properties of PISNe in the local Universe are still needed to have a solid conclusion on the association of SLSNe and PISNe (e.g., Dessart et al. 2012b).

Langer et al. (2007) presented PISN progenitor models with initial masses of 150 $M_\odot$ and 250 $M_\odot$, which roughly represent the low- and high-mass ends of PISN progenitors, at a metallicity of Z=0.001 to discuss the possible event rate of PISNe in the local Universe. Kozyreva et al. (2014b) investigated the explosions and consequent nucleosynthesis of these models to discuss the implications of PISNe for the chemical evolution. In this paper, we explore these models further to investigate their observable properties using the radiation hydrodynamics code STELLA (Blinnikov et al. 2006). These models together with those from Herzig et al. (1990) and Whalen et al. (2013c) are among the highest metallicity PISN light curve models available in the literature, and therefore useful to identify PISN events at low redshift.

We explain the method of calculations in Section 4.3 and discuss the produced light curves in Section 4.4. In Section 4.5, we compare our results with other synthetic light curves for PISNe and with observational light curves of usual and unusual core collapse SNe (CCSNe). We conclude our work in Section 4.6.

4.3 Evolutionary models and light curves modeling

4.3.1 Description of the evolutionary models

For simulating the light curves of PISNe we use the results of evolutionary calculations produced with the Binary Evolution Code (BEC, Langer et al. 2007; Kozyreva et al. 2014b). These are initially 150 $M_\odot$ and 250 $M_\odot$ models at a metallicity of $Z = 10^{-3}$, with an initial rotation velocity of 10 km s^{-1}. The evolution of the stars was calculated all the way from the zero age main sequence to the thermonuclear explosion caused by the pair instability. To follow the nucleosynthesis, Kozyreva et al. (2014b) used the Torch nuclear network developed by Timmes (1998, 1999) using 200 isotopes. Our progenitor models are red and yellow supergiants for the 150 $M_\odot$ and 250 $M_\odot$ models, respectively (Langer et al. 2007; Kozyreva et al. 2014b). The main characteristics of the models are summarized in Table 4.1. We also list PISN models from Dessart et al. (2013) (labeled '.D') and Kasen et al. (2011) (labeled '.K') for comparison. 'R' and 'B' indicate red and blue supergiant progenitors.

Our stellar models lose a large fraction of their initial mass during core hydrogen and core helium burning due to line-driven winds (Langer et al. see 2007, for details and Kudritzki et al. 1989; Vink et al. 2001; Vink & de Koter 2005; Yoon et al. 2010). The average mass-loss rate is about 2×10^{-5} $M_\odot$ yr^{-1}. By the onset of the pair instability our 150 $M_\odot$ star has lost 56 $M_\odot$ and our 250 $M_\odot$ star 81 $M_\odot$. We show the pre-supernova evolution of stellar mass in Figure 4.3.

The stellar evolutionary models were calculated with the assumption of semi-convection using a large semi-convective mixing parameter ($\alpha_{\rm SEM} = 1$), and without convective core overshooting. The mixing length parameter was chosen to be 1.5 (Yoon et al. 2006). Note that we neglected any convective mixing during the pair instability phase (Kozyreva et al. 2014b).

The input models for the STELLA calculations already contain the shock wave generated at the boundary between the oxygen and helium shells emerging from the interaction between the rapidly expanding inner core and the nearly static outer helium-hydrogen envelope (Kozyreva et al. 2014b). The physics of the pair instability explosion mechanism is well understood and smoothly reproduced by evolutionary simulations without the need of invoking artificial assumptions. This is contrasted to other SN types that often need free parameters for supernova modeling, such as the critical density for the transition from deflagration to detonation for type Ia supernovae and the mass cut, degree of chemical mixing, and explosion energy for core-collapse supernovae.

In Figures 4.1 and 4.2, we show the density and the chemical structure of our progenitor models at the onset of the STELLA calculations. At this moment the matter below the helium shell expands nearly homologously ($v \propto r$). In Figure 4.2, we truncated the outer hydrogen-helium envelope which moves at very low velocity compared to the fast moving inner ejecta. We also do not show in this figure the bottom of the hydrogen-helium envelope where the shock is located and causes a strong discontinuities.

The ejecta in the 150 $M_\odot$ model contain 0.04 $M_\odot$ of ^{56}Ni in the innermost region,

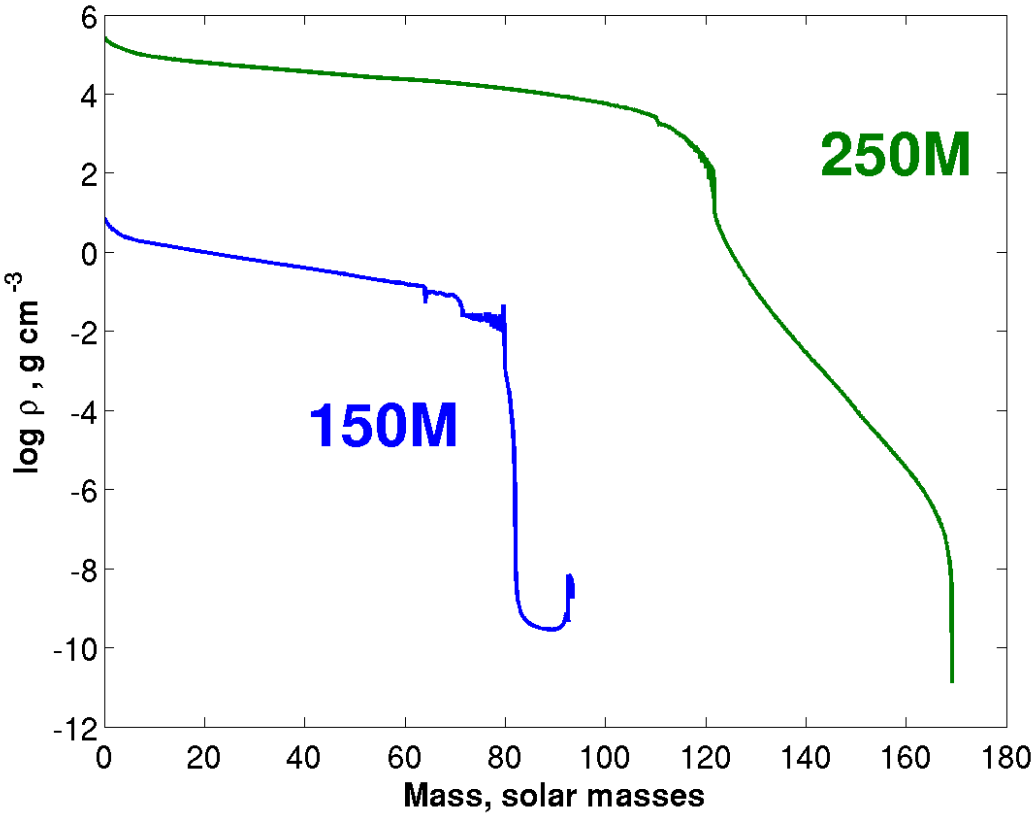

Figure 4.1: Density structure of the 150 $M_{\odot}$ and 250 $M_{\odot}$ PISN progenitor models at the onset of the STELLA calculations.

moving at a velocity of less than 500 km s^{-1}. The 250 $M_\odot$ model contains 19 $M_\odot$ of nickel over an extended region with 0 km $s^{-1} \leq v \leq$ 5000 km s^{-1}, which corresponds to 0 $M_\odot \leq M_r \leq$ 50 $M_\odot$. We do not apply any mixing in our models. Later we discuss the impact of this chemical structure on light curves. There is a small amount of helium in the innermost region of the 250 $M_\odot$ star as seen in Figure 4.2. This helium was produced by photo-disintegration of heavy elements during the explosive burning. We summarize the main properties of the PISNe in Table 4.1 along with other PISN models that we use for comparison.

4.3.2 Simulation of theoretical light curves and SEDs[1]

For simulating the hydrodynamic evolution during the pair instability explosion we use the one-dimensional (1D) multigroup radiation Lagrangian implicit hydrodynamics code STELLA (Blinnikov et al. 2006 and references therein). The code solves the hydrodynamic equations coupled with the radiative transfer equations without assuming radiative equilibrium. The STELLA code uses one temperature for the matter and has no specific temperature for radiation. The non-steady radiative transfer is solved for each of the one hundred frequency groups in all radial zones. The energy groups are uniformly distributed in logarithmic scale (i.e. in geometric progression) between the maximum wavelength of 50,000 Å and the minimum wavelength of 1 Å. The light curves are computed by integration of fluxes calculated with the STELLA code with *UBVRI* Bessel filter function using logarithmic interpolation.

The opacity is calculated for each frequency group taking about 160000 spectral lines into account according to Kurucz data (Kurucz 1991). The opacity also includes photoionization, free-free absorption and electron scattering assuming local thermodynamical equilibrium. Because of the large velocity gradient the opacity is calculated accounting for the effect of an expanding medium following Friend & Castor (1983) and Eastman & Pinto (1993). Local thermodynamic equilibrium is assumed in the plasma allow the use of the Boltzmann-Saha's distribution for ionization and level populations. This is needed for determining absorption, scattering and emission coefficients. Gamma-ray transfer is calculated using the one-group approximation for the non-local deposition of energy from the radioactive decay (Ambwani & Sutherland 1988). The code treats strong discontinuities (shock propagation) with an artificial viscosity term. The STELLA code does not follow any nuclear reactions.

To map the BEC models into the STELLA code we remeshed the models. The original number of zones was reduced from 1931 BEC zones to 242 STELLA zones for the 150 $M_\odot$ model and from 2202 BEC zones to 276 STELLA zones for the 250 $M_\odot$ model. We reduce the number of isotopes from 200 (from hydrogen to germanium) to 16 (H, He, C, N, O, Ne, Na, Mg, Al, Si, S, Ar, Ca, Fe, Co, Ni).

The envelopes of the progenitor models are optically thick and photons are not able to leave them on a short time scale. Therefore, STELLA radiation transport calculations

[1]SED — spectral energy distribution.

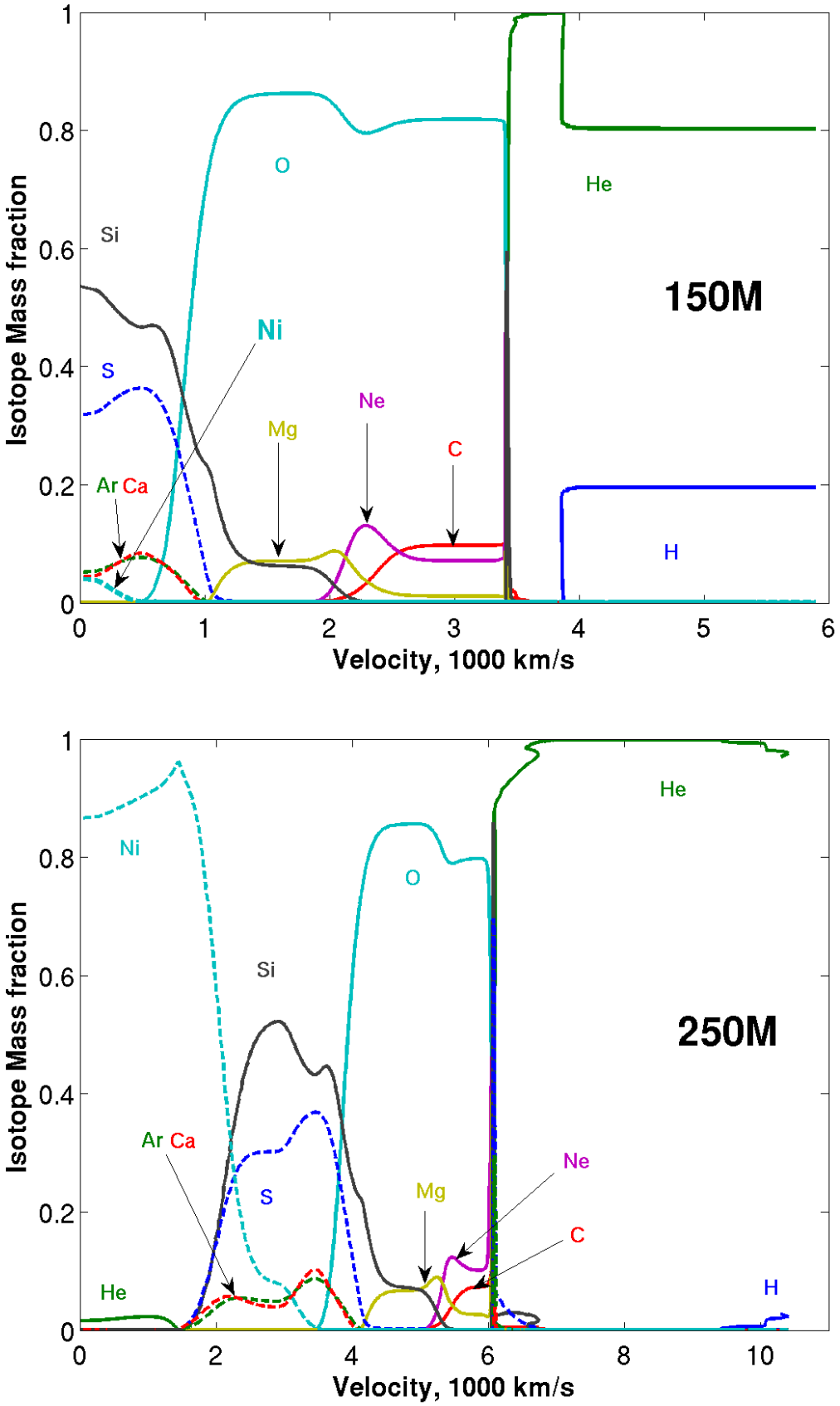

Figure 4.2: Chemical structure of the exploding 150 $M_\odot$ and 250 $M_\odot$ stars at metallicity $Z = 10^{-3}$ at the onset of the STELLA calculations.

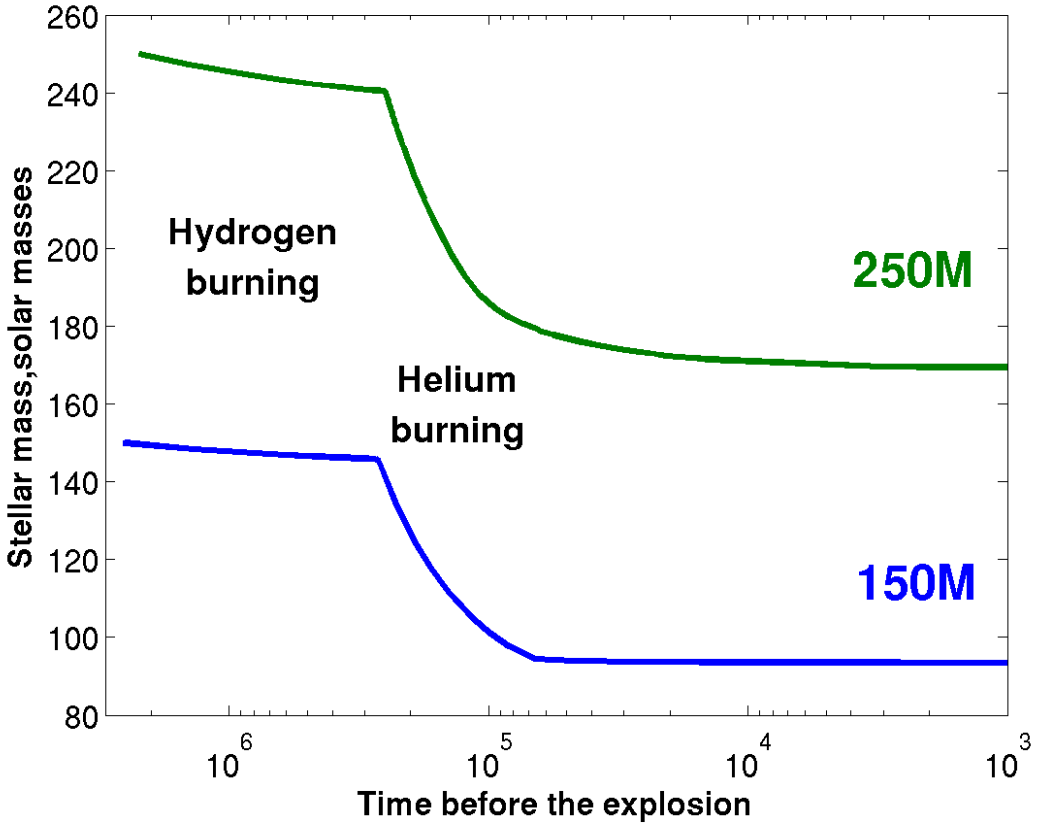

Figure 4.3: Pre-supernova evolution of the stellar mass of our models due to stellar wind mass loss.

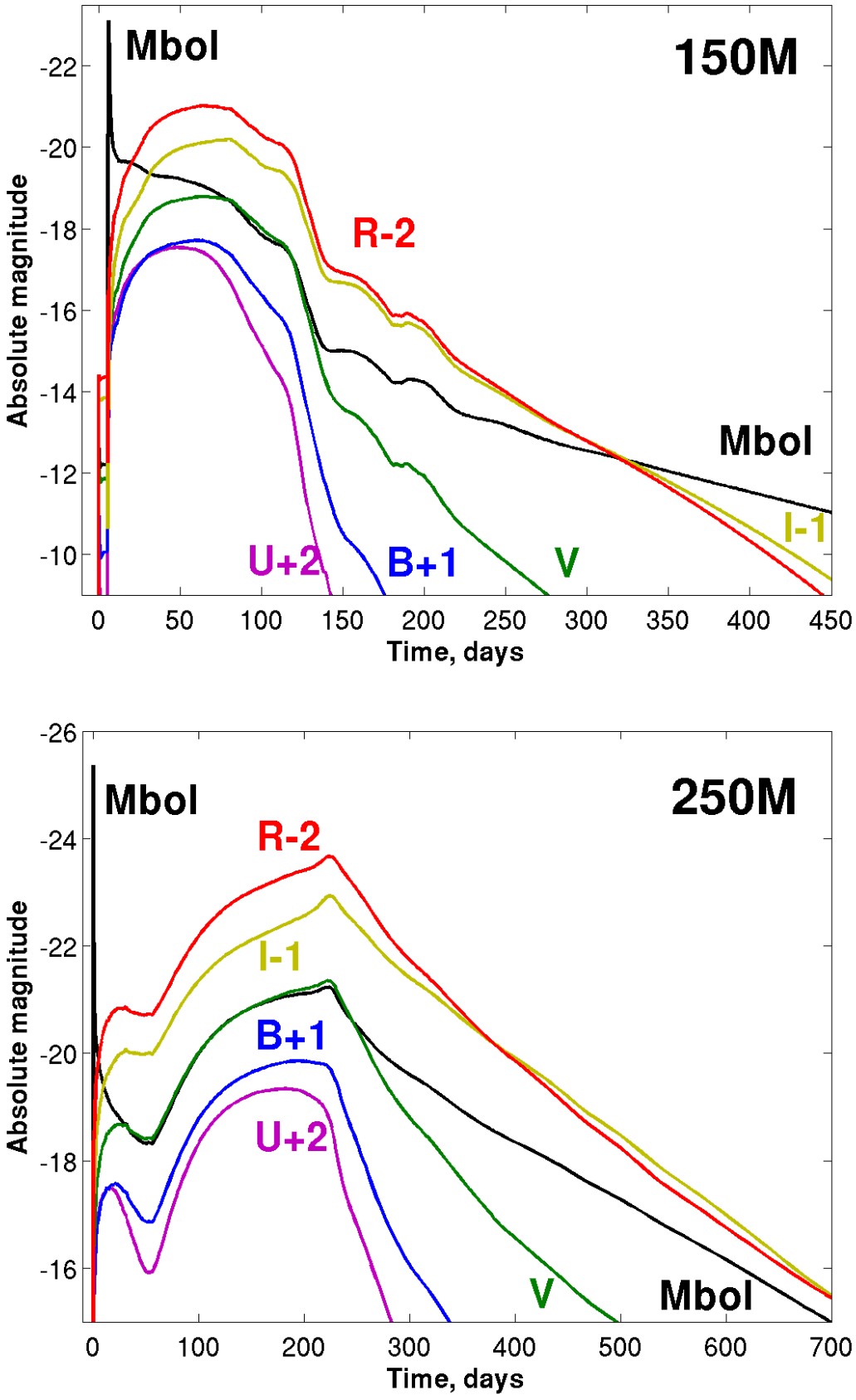

Figure 4.4: Bolometric and multiband (U, B, V, I, R) light curves for 150 $M_\odot$ and 250 $M_\odot$ PISNe at metallicity $Z = 10^{-3}$. U, B, V, I, R magnitudes are plotted with a shift of +2, +1, 0, -1, -2 magnitudes, respectively.

are computationally very expensive for an input model in which a shock is located far from the photosphere. On the other hand, using a more evolved input model in which the shock front is closer to the photosphere causes more numerical instabilities just behind the shock because the BEC code does not include artificial viscosity. We therefore compared two different cases to test how the choice of the starting model affects the final outcome: one in which the shock front is located at the bottom of the helium shell and the other in which the shock is propagating in the middle of the helium envelope. We find that the final solutions differ only by less than 10% in the terms of bolometric luminosity. In the following we use the model in which the shock reached the bottom of hydrogen-helium envelope. This defines the point $t = 0$ for all the figures.

Note that the zero point in time ($t = 0$) is not the same as the time of the explosion. Nevertheless, the time between the onset of the pair instability explosion (namely the highest central density) and the beginning of the light curve calculations is 1 hour for 150 $M_\odot$ model and 44 seconds for 250 $M_\odot$ model. These are the time intervals that the shock takes to propagate through the shallow pure helium layer to reach the bottom of hydrogen-helium envelope. These intervals are relatively small compared to the light curve evolution (months), therefore, one can consider the time in all figures as approximate time since the onset of the pair instability explosion.

4.4 Results

In Figure 4.4, we plot the bolometric and U, B, V, R, I band light curves for the 150 $M_\odot$ and 250 $M_\odot$ models. Hereafter, in figures and tables we designate the models as Model 150M and Model 250M respectively. The U, B, V, R, I magnitudes are plotted with a shift of +2, +1, 0, -1, -2 magnitudes, respectively. The bolometric curves follow closely the V-band light curves, except for early time where it needs ultraviolet bolometric corrections, and for late time where it needs infrared bolometric corrections (Bersten & Hamuy 2009). We summarize the details about shock breakout events (duration, maximum luminosity, effective and color temperatures, spectral wavelength peak, spectral energy peak) and light curves in comparison to other radiative simulations of PISN explosion (Kasen et al. 2011; Dessart et al. 2013) in Table 4.2.

For the discussion on the light curves below, we also show the evolution of the chemical composition at the photosphere which recedes along the decreasing Lagrangian mass coordinate, in Figure 4.5. The photosphere is defined as the mass zone where the electron-scattering optical depth in B-band turns above 2/3. This consideration is valid while matter and radiation temperatures are comparable at an accuracy better than 10%. The estimated period during which such conditions are present is approximately the first 350 days for Model 150M and 250 days for Model 250M. At later times, the opacity is dominated by line opacity and non-local thermodynamical equilibrium consideration is required.

Soon after the explosion, the shock wave forms when the fast expanding inner part of the star encounters the slowly moving helium layer and the hydrogen-helium envelope. Because the whole envelope is optically thick it takes a long time for photons generated during the

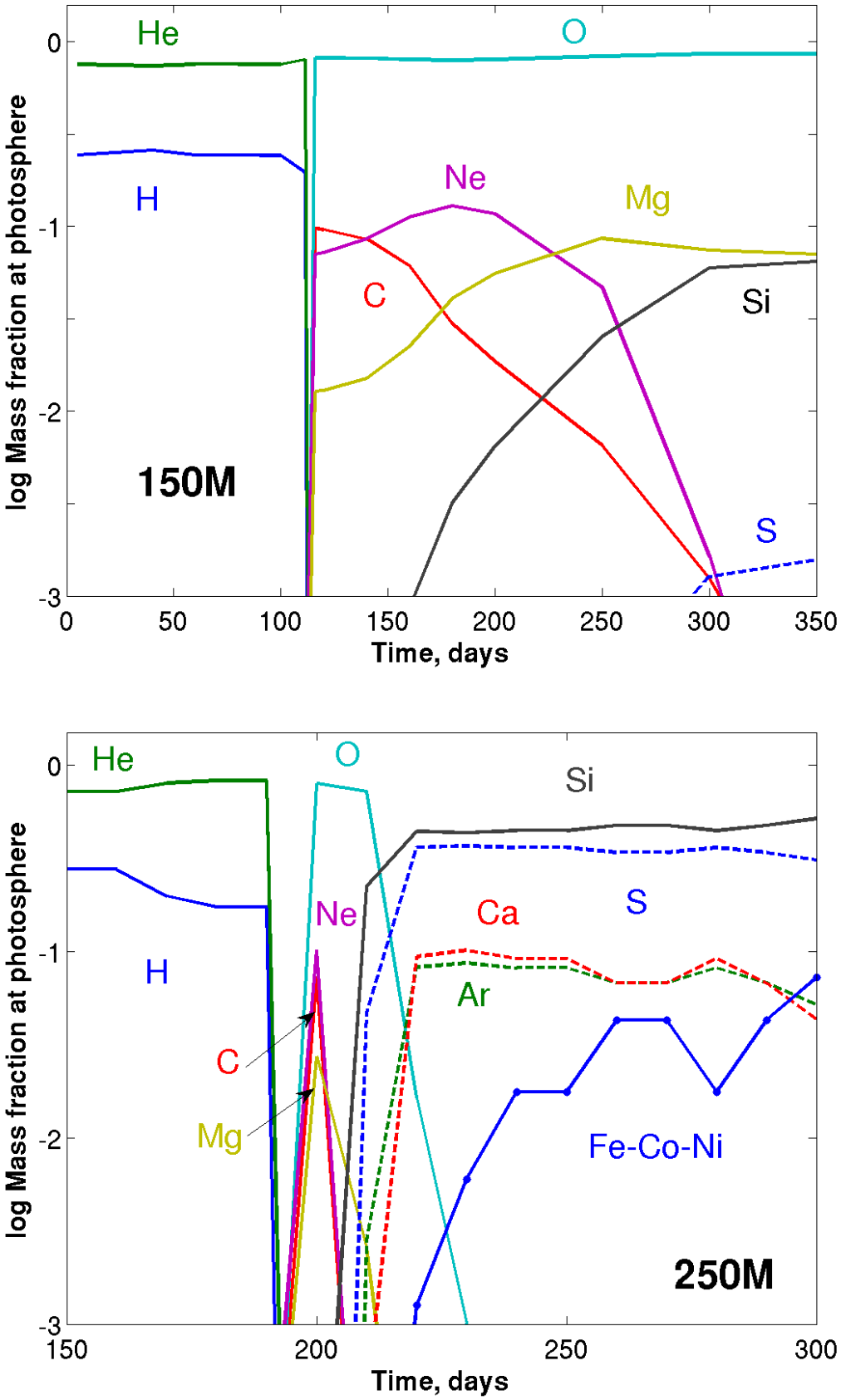

Figure 4.5: Evolution of the composition at the receding electron-scattering photosphere for the 150 $M_\odot$ and 250 $M_\odot$ PISN models.

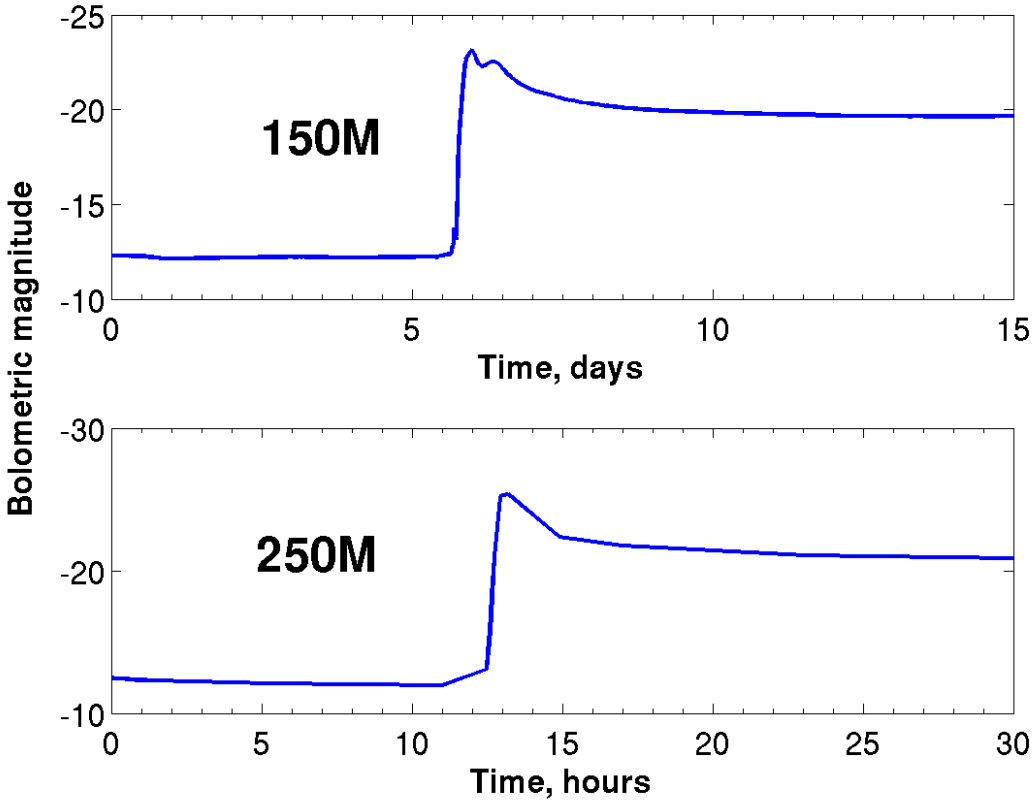

Figure 4.6: Shock breakout events for 150 $M_{\odot}$ and 250 $M_{\odot}$ PISN explosions.

explosive burning to reach the surface (optically transparent medium). Therefore, firstly, during about 6 days for Model 150M and 12 hours for Model 250M the shock passes through the entire envelope (see e.g., Shigeyama et al. 1987; Blinnikov et al. 2000). The shock wave reaches the surface, and the envelope matter behind the shock is heated and ionized. When the shock emerges at the surface the energetic shock breakout flash of ultraviolet and X-ray emission appears with a duration of a few hours. The shock breakout is shown in the Figure 4.6. We draw some important conclusions about the shock breakout in Section 4.5.

4.4.1 The 150 $M_\odot$ model

Soon after the shock breakout, the temperature drops rapidly due to adiabatic cooling. Later the recombination losses become comparable to adiabatic cooling (Grasberg et al. 1971). The recession of the photosphere along the Lagrangian mass coordinate is compensated by an overall expansion of the envelope. The combination of expansion and cooling provides the condition for only slight variations of the luminosity for some time (Grasberg & Nadezhin 1976; Imshennik & Nadezhin 1989). This emerges as a plateau phase in the light curve. The plateau phase lasts for about 100 days for Model 150M. The light curve shape of Model 150M looks similar to that of ordinary type IIP supernovae. This fact is also noticed by Scannapieco et al. (2005) and Kasen et al. (2011). The absolute V-band magnitude becomes about $M_V = -19$ mag at the visual maximum, which is about 10 times brighter than an average SN IIP. However, the peak luminosities of type IIP SNe vary by a factor of 100, and that of our model is still contained in this range. Its high luminosity results from the relatively high supernova energy (about 10 foe) and the large radius (3394 $R_\odot$) of the progenitor. Once the photosphere recedes to the region below the hydrogen-rich envelope, the luminosity decreases rapidly and then becomes governed by the radioactive decay of ^{56}Co.

It is interesting to consider the effective temperature evolution which we present in Figure 4.7. Note that the recombination effectively slows the adiabatic cooling during the expansion. The recombination starts playing a role when recombination radiation becomes comparable to adiabatic cooling. This happens when the effective temperature is approximately 10000 K (Imshenik & Nadezhin 1965), i.e. well before the establishment of a recombination cooling wave. The effective temperature of an ordinary SN II remains nearly constant ($\sim$ 5500 K) after the establishment of a recombination cooling wave. This phase begins about 20 days after the explosion for an ordinary SN II (Bersten & Hamuy 2009; Dessart & Hillier 2011). This delay of 20 days depends mostly on the progenitor radius (Grasberg et al. 1971; Imshennik & Utrobin 1977).

Due to the very large progenitor radius of 150 $M_\odot$ PISN (3400 $R_\odot$) the onset of the recombination cooling wave is delayed up to day 100 in this case. For about 20 days thereafter, when the photosphere is still inside the hydrogen-helium layer (Figure 4.5), the recombination cooling wave is established for a while and the effective temperature is kept at the hydrogen recombination level. Although the mass fraction ratio between hydrogen and helium is 4:1, the number of hydrogen atoms is about equal to the number of helium atoms and the relative contribution to the electron density from hydrogen stays high. The

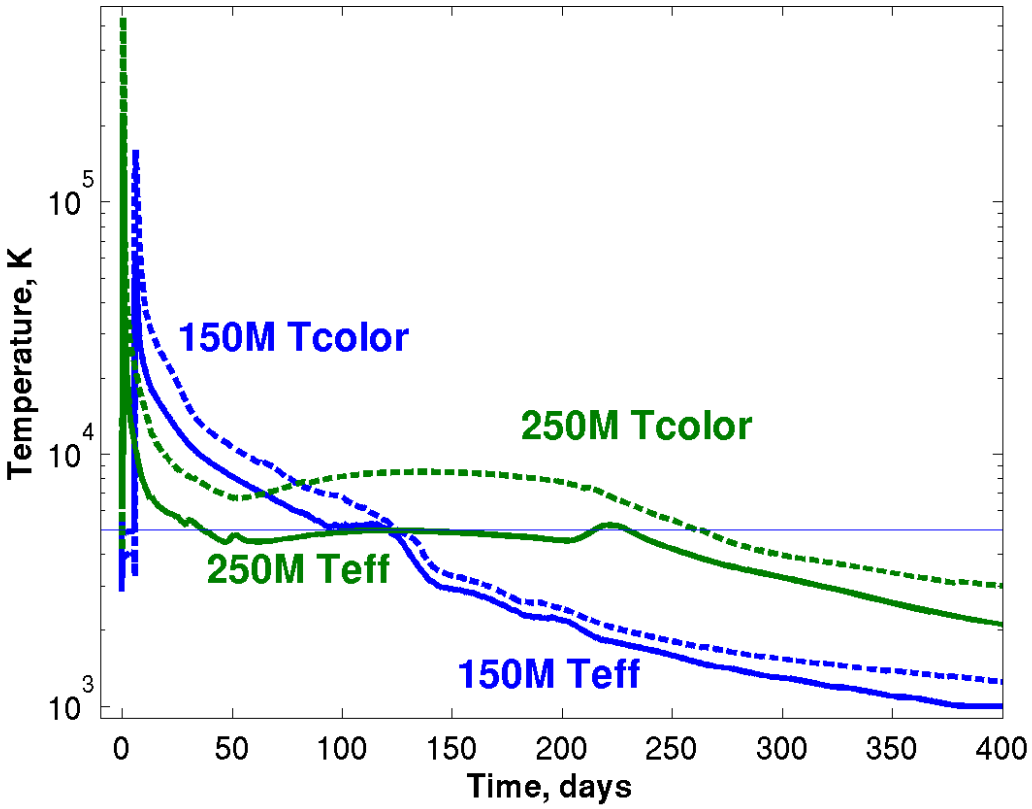

Figure 4.7: Evolution of the effective and color temperature of 150 $M_{\odot}$ (blue) and 250 $M_{\odot}$ (green) PISN models. Solid curves correspond to color temperatures. The dashed and dashed-dotted curves represent effective temperature of the 150 $M_{\odot}$ and the 250 $M_{\odot}$ models, respectively. The thin line is located at 5000 K and approximately corresponds to hydrogen recombination temperature.

plateau phase of this model mostly corresponds to the phase of rapidly evolving photospheric temperature. This is different from the case of ordinary SN IIP (see e.g., Bersten & Hamuy 2009). In Section 4.5.3 we provide the comparison of the color temperature with those of typical and bright SNe IIP, and with SN 2009kf which was bright in the near-ultraviolet (NUV) range at early time.

4.4.2 The 250 $M_\odot$ model

The light curve looks very different for our Model 250M (Figure 4.4). After the shock breakout, the bolometric magnitude drops to about $M \simeq -18$ mag during the first 50 days. The luminosity decreases due to the adiabatic expansion more rapidly than in Model 150M, because the progenitor of Model 250M is more compact (i.e., $R = 745\ R_\odot$, compared to 3394 $R_\odot$ in Model 150M). A precursor-like event happens at around day 20 in U, B, V-bands at magnitude $M \simeq -18.5$ mag. Such precursor could be perceived as a separate hydrogen-rich SN being discovered long before reaching the maximum luminosity.

A re-brightening occurs thereafter, as the energy from the radioactive decay of nickel and cobalt in the ejecta diffuses out (Dessart et al. 2010). The photosphere recedes below the hydrogen-rich envelope starting at about day 175 (Figure 4.5), but unlike in the case of Model 150M, the luminosity keeps increasing until about 220 days, reaching $M_V = -21$ mag at the visual maximum. At later times, the light curve is largely governed by the radioactive decay of ^{56}Co. A hump-like feature on top of the main maximum phase is shown around day 220. At this time the photosphere leaves the oxygen-rich layer and moves down to the silicon-rich layers. The receding front gradually encounters a bubble of diffusing photons generated by the radioactive decay.

It is interesting to note that the photosphere is located in the inner layers where there is no hydrogen and helium well before the luminosity reaches its peak, as mentioned above (Figures 4.4 and 4.5). Based on our results we cannot predict whether hydrogen and helium lines are expected in the spectrum at the time of maximum luminosity due to excitation by radiation above the photosphere. However, Dessart & Hillier (2011) showed that the Balmer lines disappear after the photosphere leaves the hydrogen-rich shell of ejecta in the case of type II plateau SN and there are no Balmer-continuum photons at later time. The spectral models for PISNe by Dessart et al. (2013) also indicate that hydrogen lines do not appear once the photosphere moves down to the hydrogen-free core. Non-thermal excitation of hydrogen can happen if there is some degree of mixing of cobalt and nickel into layers containing hydrogen (Li et al. 2012). However it is expected that PISNe do not experience such mixing during the explosion according to the recent numerical simulations of Joggerst & Whalen (2011). Therefore, we expect that PISNe like Model 250M will not have any hydrogen lines once the photosphere recedes to the hydrogen-free core. For the same reason, we do not expect helium lines in the optical bands either, because strong mixing of helium and radioactive nickel is needed to excite helium lines as shown in Dessart et al. (2012a). This means that the Model 250M would appear as a type II SN initially but look like a SN Ic from about day 175, well before the luminosity reaches its peak value.

4.5 Discussion

4.5.1 Comparison with other theoretical PISN light curves

In this section we compare our results with other PISN models from red or blue supergiant progenitors. These include PISN models carried out with the Monte Carlo radiation transport code SEDONA (labeled '.K' in figures, tables; Kasen et al. 2006, 2011) and with the non-LTE radiative-transfer code CMFGEN (labeled '.D'; Dessart et al. 2013). Light curves from the SEDONA simulations are integrated from spectra provided by D. Kasen and artificially smoothed. The noisy appearance is a consequence of the statistical approach of Monte Carlo transport calculations. The advantage of the STELLA calculations over the SEDONA and the non-LTE CMFGEN codes is the capability to simulate the radiation-hydrodynamical evolution from the onset of the explosion. Hence we reproduce the emergence of the shock breakout event and the hydrodynamical evolution during the pair instability explosion. Both, SEDONA and CMFGEN, carry out the radiative transfer calculations once the homologous expansion is reached. The codes have their advantages for spectral computations well described in a number of papers (Kasen et al. 2006; Woosley et al. 2007b; Dessart & Hillier 2010, 2011).

Red supergiants

Red supergiant (RSG) progenitors are common for producing SNe IIP (Grasberg et al. 1971; Smartt 2009). Typically the light curve from the explosion of a red supergiant is characterized by a pronounced plateau phase lasting for about 100 days, followed by a radioactive tail (Barbon et al. 1979). In this section we compare our lower mass PISN Model 150M with other PISNe produced by RSG progenitors.

In Figure 4.8, we plot the theoretical light curves for different RSG PISN models: Model 150M, Model R150.K, Model R150.D, and Model R250.K (see Table 4.1 for details). As already discussed by Kasen et al. (2011) and Dessart et al. (2013), more massive progenitors result in higher luminosities and broader light curves. In particular, heating due to radioactive decay of nickel and cobalt leads to an increase in luminosity in Model R190.D and Model R250.K which produced large amounts of ^{56}Ni (2.63 $M_{\odot}$ and 37.9 $M_{\odot}$, respectively), while it is not seen in Model R150.K and Model 150M which have only 0.07 $M_{\odot}$ and 0.04 $M_{\odot}$ of ^{56}Ni, respectively. The tail of each light curve is powered by cobalt decay and its luminosity is directly proportional to the amount of radioactive nickel generated during the explosion. This dependence is clearly visible in Figure 4.8.

Our Model 150M is directly comparable to Model R150.K, because it has the same initial progenitor mass, a similar explosion energy and a similar nickel mass (Table 4.1). Compared to Model 150M, Model R150.K has a 500 times lower metallicity, which results in several important differences in the progenitor properties:

1. The ejecta mass is much lower for Model 150M (94 $M_{\odot}$) than that of Model R150.K (143 $M_{\odot}$).

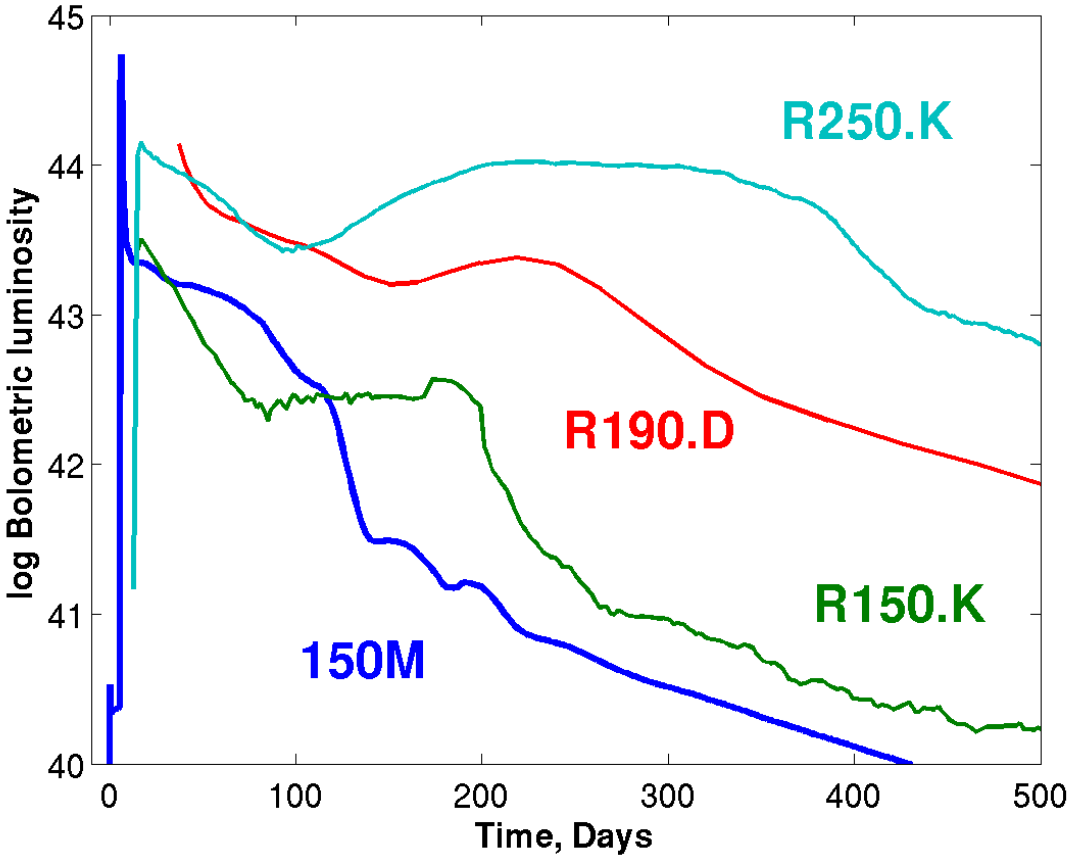

Figure 4.8: Bolometric luminosity for the red supergiant models 150M (blue thick solid curve), R150.K (green thin solid curve), R190.D (red dashed curve), and R250.K (cyan dashed-dotted curve).

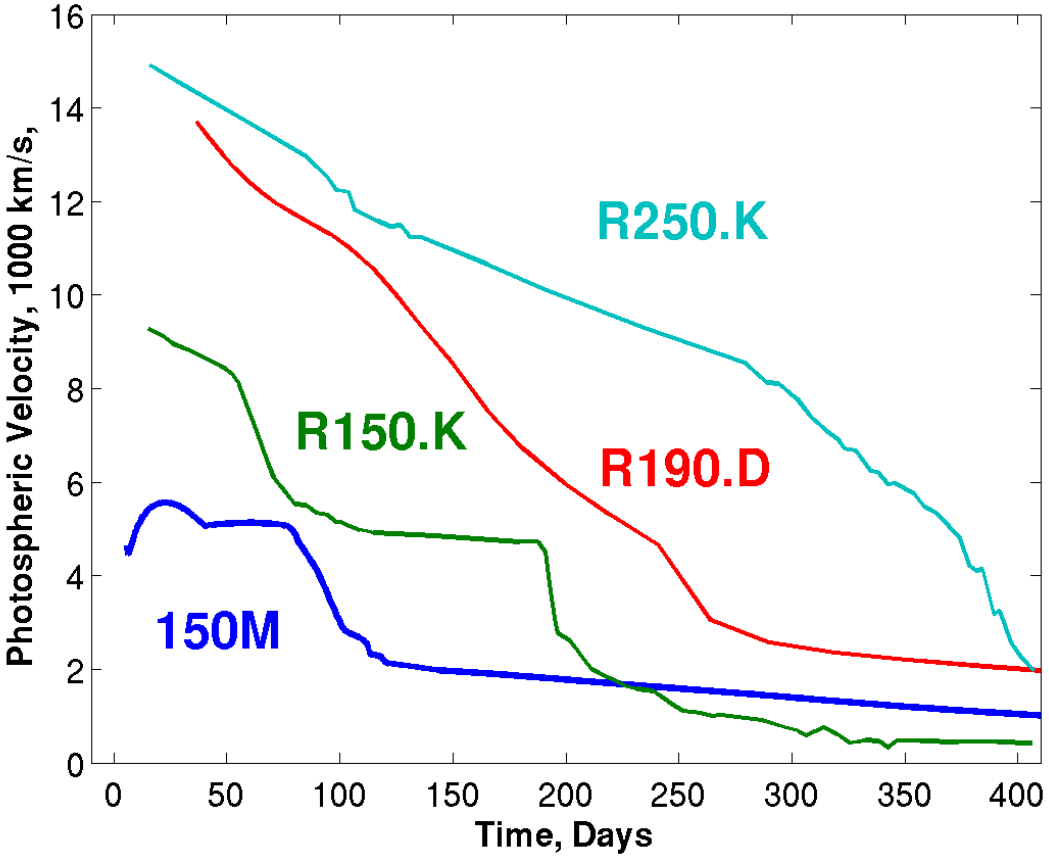

Figure 4.9: Photospheric velocities for the same models as shown in Figure 4.8. Labels, line styles and colours have identical meanings.

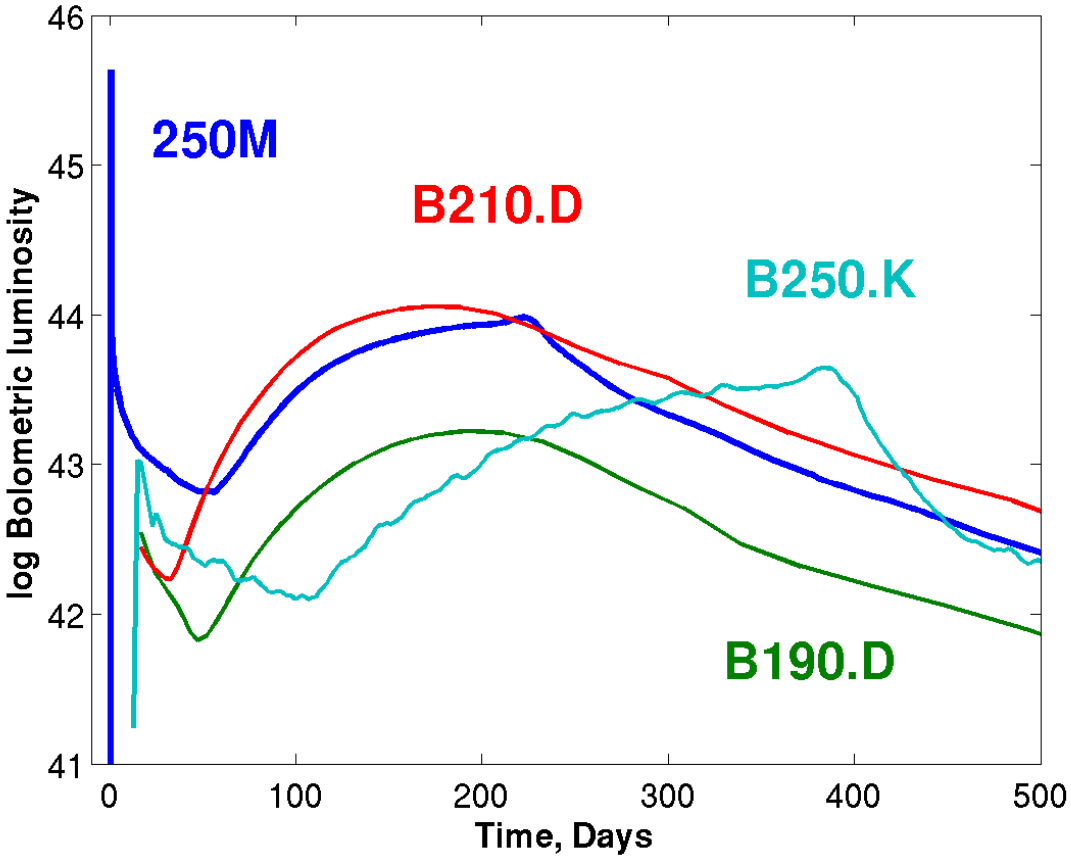

Figure 4.10: Bolometric luminosity for the Model 250M (blue thick solid curve), Model B190.D (green thin solid curve), Model B210.D (red dashed-dotted curve), and Model B250.K (cyan dashed curve).

2. The hydrogen-helium envelope masses are 29 $M_\odot$ in Model 150M and 71 $M_\odot$ in Model R150.K, respectively.

3. Because of stronger mass loss, the hydrogen mass fraction in the envelope of Model 150M is much lower ($X_\mathrm{H} \approx 0.2$) than that of Model R150.K ($X_\mathrm{H} \approx 0.7$).

4. The radius at the pre-supernova stage is significantly larger for Model 150M ($R = 3394\ R_\odot$) than for Model R150.K ($R = 2314\ R_\odot$).

As a consequence the overall plateau duration is shorter in Model 150M than in Model R150.K, because of the lower hydrogen envelope mass and lower mass fraction of hydrogen in the envelope. Moreover, nickel was additionally mixed into outer layers in Model R150.K which in turn caused extra nickel heating during plateau phase.

Figure 4.9 plots the photospheric velocities of the RSG models. The Model 150M and Model R150.K have a phase where the photospheric velocity remains nearly constant, which results from the interplay between the recession of the photospheric front and the expansion of the ejecta. For the models with higher E/M ratio, i.e. Model R190.D and Model R250.K, the photospheric velocities stay at a high level for a longer time. This is the result of a stronger explosion and hence a more powerful shock. More energetic photons keep the medium ionised for longer and the photosphere remains in hydrogen-rich regions (larger Lagrangian mass coordinate) for a longer time (up to around day 250 and day 300 for Model R190.D and Model R250.K, respectively).

The photospheric velocity in Model 150M is very low at the moment of shock breakout (4000 km/s) because the shock spends a large fraction of its energy on ionizing the medium while traveling along the extremely extended envelope. As showed in Grasberg et al. (1971), Falk & Arnett (1977), Blinnikov & Tolstov (2011) and Tolstov et al. (2013), extended progenitors result in lower photospheric velocities than more compact ones.

Yellow and blue supergiants

In Figure 4.10, we plot light curves for PISNe from more compact progenitors than RSGs: Model 250M, Model B190.D[2], Model B210.D, and Model B250.K. These PISNe produce light curves reminiscent to that of SN 1987A: the luminosity decreases rapidly in the beginning, but the supernova re-brightenes again as the thermalized photons from the radioactive decay of nickel and cobalt diffuse out. The bolometric luminosity of our yellow supergiant Model 250M is higher than that of the other blue supergiant models during the initial phase ($t \lesssim 50$ days), because of the larger radius of the progenitor (e.g. Popov 1993).

In Figure 4.11, we show the evolution of the photospheric velocity for the compact progenitor models. In all of these models, the photosphere recedes very rapidly through the outer hydrogen-helium layer after shock breakout. In Model 250M, Model B210.D

[2]Blue supergiant B190.D is the same evolutionary model as red supergiant R190.D but with truncated hydrogen atmosphere (about 30 $M_\odot$ of outer hydrogen layer is cut; Dessart et al. 2013).

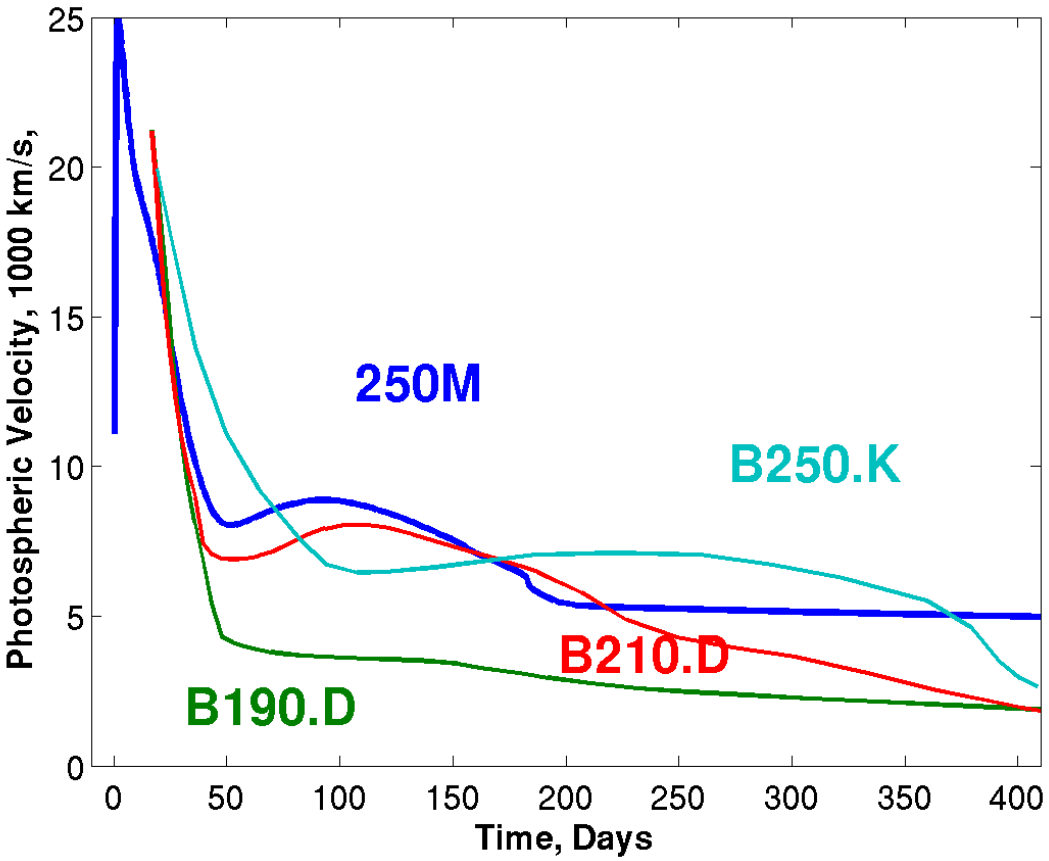

Figure 4.11: Photospheric velocities for the same models as shown in Figure 4.10. Labels, line styles and colours have identical meanings.

and Model B250.K, where the amounts of nickel exceed 19 $M_{\odot}$, the reversion of the photospheric velocity occurs when the recombination and cooling wave encounters the expanding "bubble" of diffusing photons generated by nickel radioactive decay. These photons ionize the just recombined medium and push the photospheric front to outer shells. A higher envelope mass leads to a broader phase of this reverse photosphere motion.

The sudden drop in the velocity of Model 250M occurs around day 175. At this time the photosphere leaves the hydrogen-helium envelope (Figure 4.5) and moves rapidly through hotter layers of oxygen, neon, carbon and magnesium heated by diffusing nickel photons. There is a lack of such a sharp drop in other calculations because their input chemical structure was smeared (Kasen et al. 2011; Dessart et al. 2013) to mimic hydrodynamical mixing happened during the explosion. However, it was shown by a number of studies that the degree of mixing for the inner regions containing radioactive nickel is not so prominent (Joggerst & Whalen 2011; Chen et al. 2012; Chatzopoulos et al. 2013; Chen et al. 2014). Mixing is more efficient in the oxygen layer where the shock emerges and above it due to the propagation of the reverse shock. Red supergiants exhibit a higher degree of mixing compared to more compact blue supergiants, similar to red and blue supergiant core collapse SNe (Joggerst et al. 2009).

4.5.2 The chemical structure during the coasting phase

Figure 4.12 shows the ejecta structure of Model 150M and Model 250M at coasting phase. In fact, the coasting phase begins around day 10 for both our models. In Figure 4.12, we plot the chemical composition of the ejecta at day 950 and day 1200, respectively. The plots demonstrate what would be the degree of Doppler broadening for the spectral lines of the given elements 10 days after the explosion and later.

The oxygen shell in Model 150M, which contains small amounts of carbon, neon, magnesium and silicon, expands at a velocity of 1000 – 2200 km s^{-1}. The inner silicon-sulfur shell moves at velocities below 2000 km s^{-1}. Model 250M shows systematically higher velocities. The oxygen-rich layers travel at 4000 – 5000 km s^{-1}, the silicon-sulfur shell — at about 4000 km s^{-1}, and the nickel-rich layer moves at 0 – 3900 km s^{-1}.

In the Model 250M the structure has some peculiarity at the sulfur-silicon layer moving at velocity around 4000 km s^{-1}. The reason is the hydrodynamical effect of nickel heating (Arnett 1988; Woosley 1988; Arnett et al. 1989a; Pinto & Eastman 2000; Woosley et al. 2007b). The additional radiation pressure produced by nickel heating provides an acceleration of the innermost 30 $M_{\odot}$ of ejecta. The effect increases the velocity field in the inner part of the ejecta by a few hundred km s^{-1} and decreases the density. The overall changes in density and velocity do not exceed 10% on a relative scale. This effect has no influence on the light curve shape around the luminosity peak (Woosley et al. 2007b) because the photosphere retains far from the innermost region at this time.

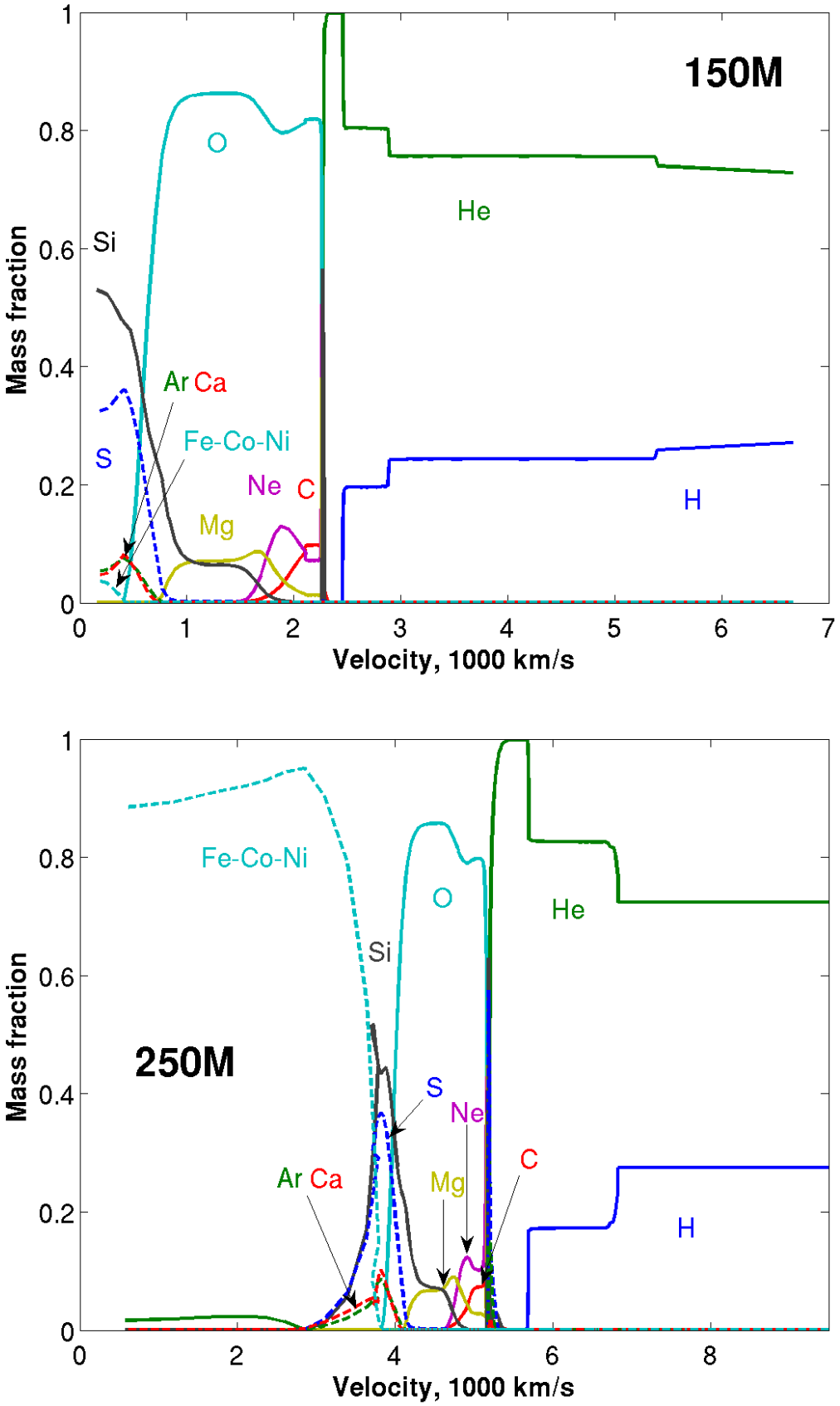

Figure 4.12: Chemical structure of ejecta of 150 $M_\odot$ and 250 $M_\odot$ PISNe at day 950 and day 1200 correspondingly.

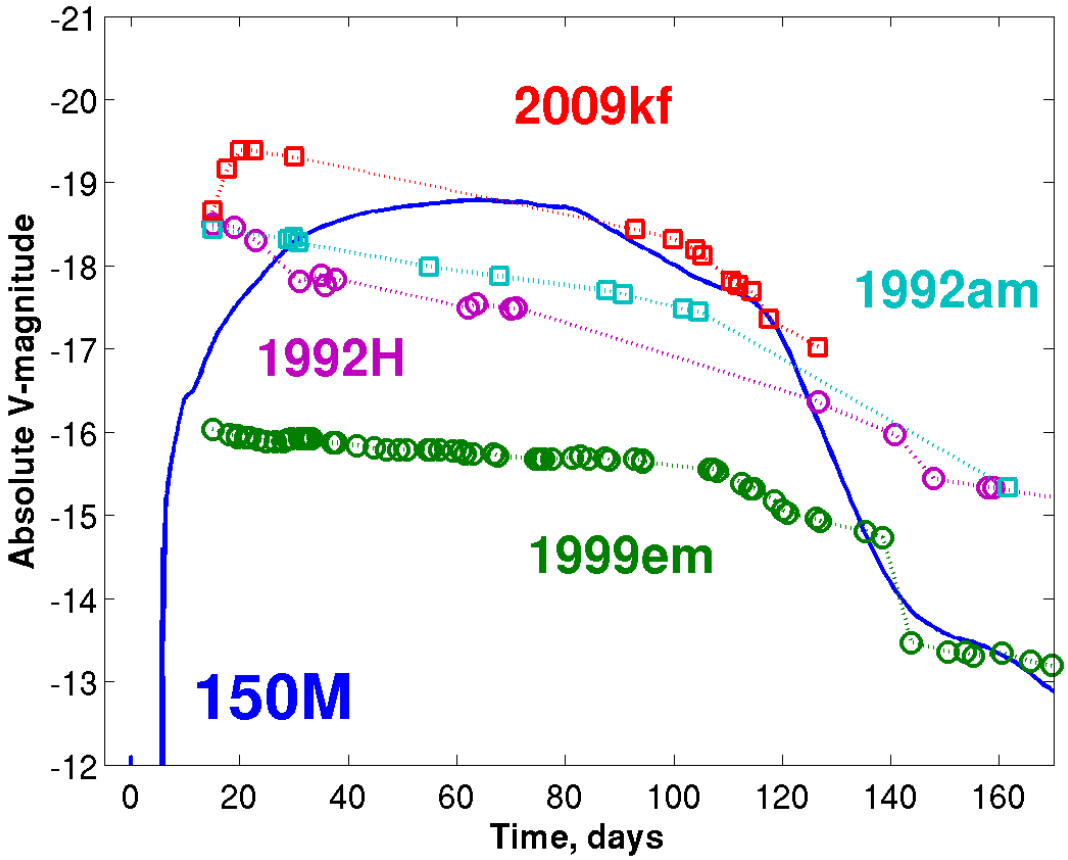

Figure 4.13: Absolute V-band light curve for 150 $M_{\odot}$ PISN (blue solid line) and absolute V-band magnitudes for typical plateau SN 1999em (green circles) and three bright plateau SNe 1992H (magenta circles), 1992am (cyan squares), 2009kf (red squares).

4.5.3 Comparison with observed SNe

Relatively low-mass PISNe and type IIP SNe

Our Model 150M is particularly relevant for the identification of PISNe in the local Universe. This is because SNe from the low-mass end of the PISN regime like Model 150M are expected to be more abundant than those from the high-mass end like our Model 250M. In Figure 4.13, therefore, we show the first 170 days of light curves for our synthetic PISN models and compare it to several observed plateau SNe. The data for these particular SNe are taken from the Sternberg Astronomical Institute Supernova Light Curve Catalogue (Tsvetkov et al. 2010; Tsvetkov & Pavlyuk 2013) and are compiled from the original data (Tsvetkov 1994; Clocchiatti et al. 1996; Hamuy 2001; Botticella et al. 2010).

Model 150M has a plateau phase during the first 115 days which is not unusual for SNe IIP. Although this model has a higher envelope mass (29 $M_{\odot}$) than those of typical

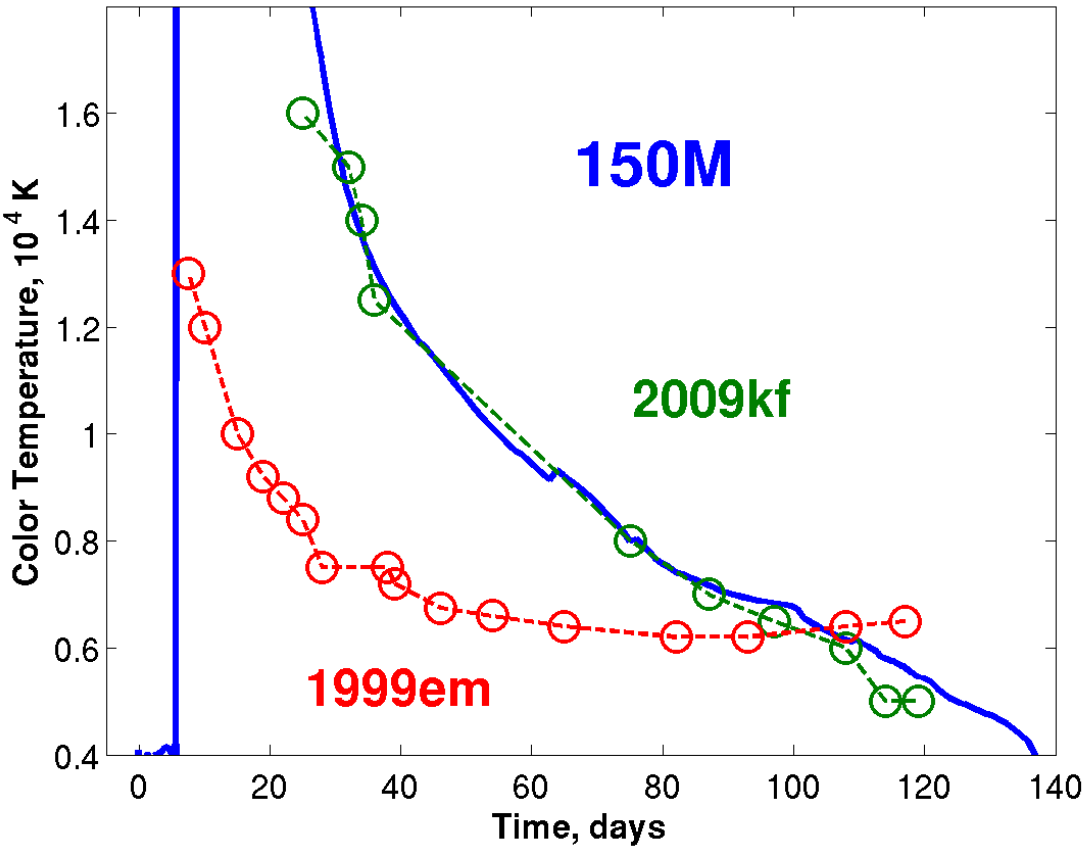

Figure 4.14: Color temperature evolution of 150 $M_{\odot}$ PISN (solid line) and of typical SN IIP SN 1999em (squares) and of NUV-bright SN 2009kf (circles) Bersten & Hamuy (2009); Botticella et al. (2010). SN 2009kf data are shifted in time by 15 days.

SNe IIP progenitors ($< 10\ M_\odot$), the helium mass fraction is very high (about 80%). At the same time it is expected that the envelopes of typical SN IIP progenitors have helium mass fractions of 35% – 50% depending on their initial masses (Woosley et al. 2002; Langer 2012). Helium recombines at higher temperatures to reduce the electron scattering opacity and the hydrogen recombination front recedes more rapidly with a higher fraction of helium in the envelope (Kasen & Woosley 2009). This makes our Model 150M to have a fairly short duration of the plateau phase compared to high redshift RSG PISN models (cf. Figure 4.8). The plateau duration of the light curve for our Model 150M is comparable to those of typical SNe IIP, despite the relatively high envelope mass.

During the plateau phase, the V-band magnitude varies by 1-2 magnitudes (Barbon et al. 1979; Hamuy 2003a). Compared to the typical plateau supernova SN 1999em, the plateau luminosity of the Model 150M is higher by 2-3 magnitudes, but comparable to those of the three bright SNe IIP (SN 1992H, 1992am and 2009kf, cf. Figure 4.13). The estimated nickel masses for these SNe IIP are comparable or higher than that in Model 150M: $M_{\rm Ni} = 0.058\ M_\odot$, $0.075 M_\odot$, $0.36 M_\odot$ for 1999em, 1992H, 1992am (Clocchiatti et al. 1996; Hamuy 2003a; Nadyozhin 2003; Bersten et al. 2011), respectively, and limited by $0.4\ M_\odot$ for 2009kf (Botticella et al. 2010).

Our Model 150M has a very large initial radius of 3394 $R_\odot$ (see Table 4.1), while those of ordinary SNe IIP progenitors have radii of less than 1000 $R_\odot$. Due to this difference our PISN explosion and SN IIP explosions have a different appearance of the shock breakout event. The shock breakout duration is longer for a larger progenitor (Tominaga et al. 2011). The color temperature is higher for a SN IIP shock breakout than that for our PISN ($T_{\rm col} \sim R^{-1/2}$) while the peak luminosity is similar depending mostly on the explosion energy (Tolstov et al. 2013). Since our PISN shock breakout is redder the spectral maximum occurs at a longer wavelength (see Table 4.2). Unfortunately the shock breakout of local SNe II is very difficult to detect because it appears as a ultraviolet/X-ray burst lasting only minutes to hours (Calzavara & Matzner 2004).

The large progenitor radius of our 150 $M_\odot$ PISN model has consequences for the photospheric temperature evolution. In Figure 4.14, we compare the color temperature of our 150 $M_\odot$ PISN with those of the typical SN IIP SN 1999em and the near UV-bright SN 2009kf. The color temperature evolution of our model is very different to that of SN IIP 1999em, but similar to that of SN IIP SN 2009kf, which had a high NUV excess at early time. Nevertheless, the NUV light curve of our model does not show such a high luminosity as SN 2009kf. The maximum NUV luminosity reaches -20.5 mag and -22 mag for our 150 $M_\odot$ PISN model and for SN 2009kf, respectively (Botticella et al. 2010). The high NUV luminosity of 2009kf is explained by the interaction of the SN shock with a dense stellar wind preceding the SN explosion (Moriya et al. 2011). The higher temperature is the direct consequence of the ultraviolet excess. However, in case of our low mass PISN model the shock breakout event occurs and the high temperature is related to the relaxation of the highly excited medium. Any interaction of the SN ejecta with the progenitor wind is neglected in our model.

Another possible way to distinguish a SN IIP from a PISN explosion is to check the photospheric velocities. In Figure 4.15 we show the photospheric velocity for our 150 $M_\odot$

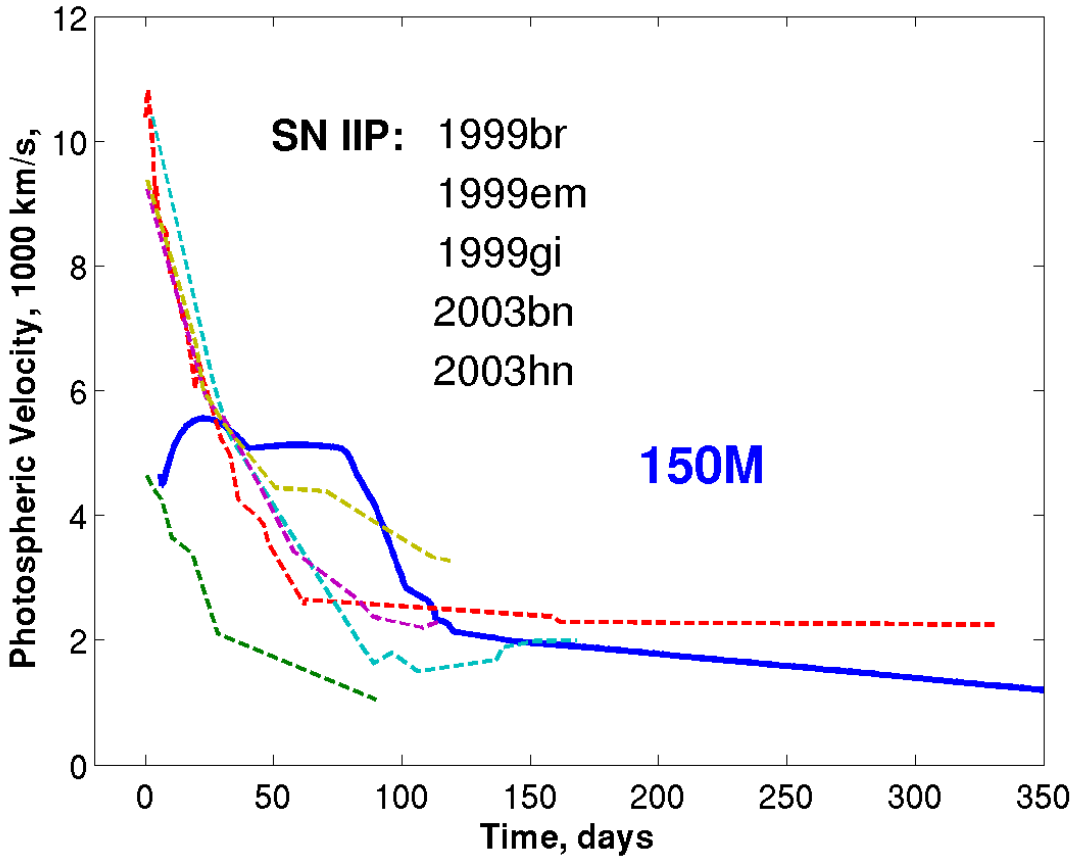

Figure 4.15: Photospheric velocity for our 150 $M_\odot$ PISN model (blue solid line) and observational data for several SNe IIP (Jones 2008). The zero point for the observed data is the first spectroscopic observation.

PISN model along with those of a few ordinary plateau SNe taken from Jones (2008). The estimate for the photospheric velocity is based on the H_β absorption line (Jones et al. 2009). The distinct property of our model is the low photospheric velocity at earlier time compared to the maximum photospheric velocities of SNe IIP (cf., Grasberg et al. 1971; Young 2004). The photospheric velocities at later time are similar for both SNe IIP and our low mass PISN model.

SLSNe linked to type Ic SNe

As discussed in Section 4.4 the photosphere of our 250 $M_\odot$ PISN model during its peak luminosity phase recedes to the bottom of the hydrogen-rich envelope (see also Kasen et al. 2011; Dessart et al. 2013). Therefore, one could classify it as a SN Ic, like SN 2007bi, if it was discovered during the maximum or post-maximum phase. In Figures 4.16 and 4.17, therefore, we compare the synthetic bolometric light curve of our 250 $M_\odot$ model with the

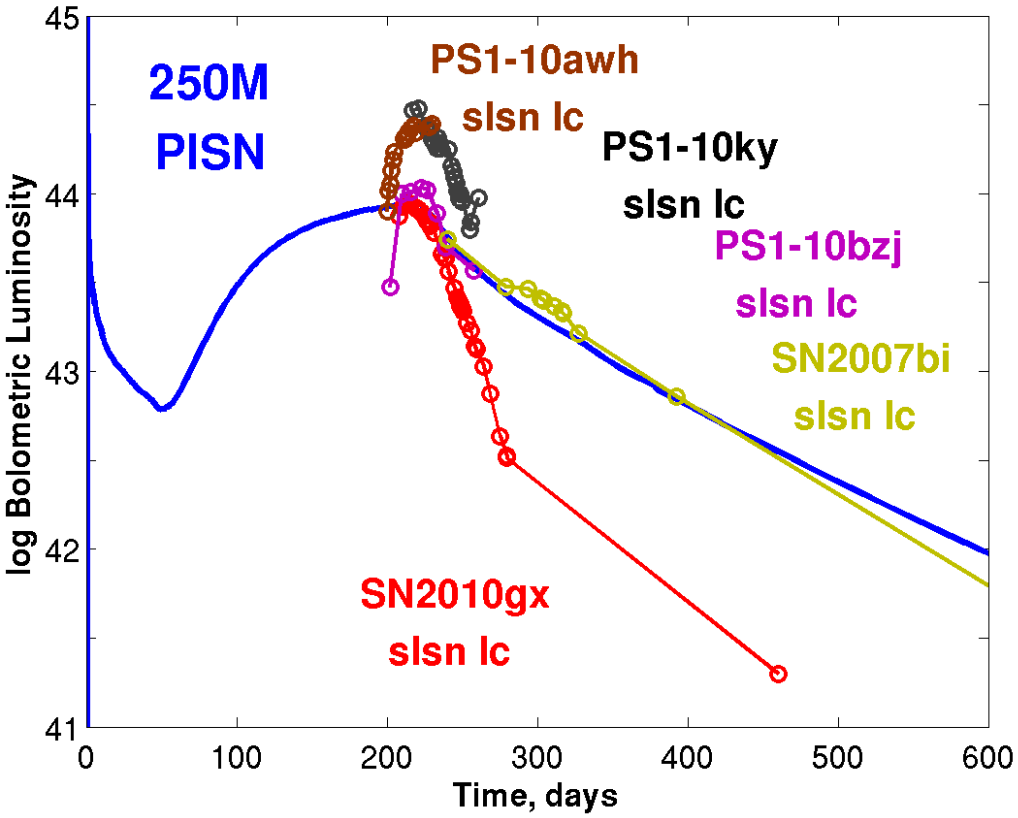

Figure 4.16: Absolute bolometric light curve for our 250 $M_{\odot}$ PISN model (blue solid curve) and quasi-bolometric and bolometric light curves of superluminous type Ic SN 2010gx (red circles, Inserra et al. 2013), PS1-10awh and PS1-10ky (green and black triangles, Chomiuk et al. 2011) PS1-10bzj (magenta squares, Lunnan et al. 2013), and SN 2007bi (yellow diamonds, Young et al. 2010).
The observed curves are shifted in time by 200 days to coincide with the maximum phase of the theoretical curve.

quasi-bolometric light curves of some superluminous type Ic SNe: SN 2010gx, PS1-10awh, PS1-10ky PS1-10bzj, SN 2007bi, and PTF10nmn.

From Figure 4.16 it is clear that Model 250M cannot explain several of the unusually luminous SNe Ic, because of the very broad light curve of our model. Unambiguous evidence for a pair instability explosion of an initially high mass progenitor would be the observation of an extremely long rise to the maximum phase (Benetti et al. 2013). Therefore, some attempts are made to complete the light curves with retrospective detection of data points before the maximum phase(Nicholl et al. 2013). The synthetic light curve of our 250 $M_{\odot}$ PISN model shows 200 days of rise while many SNe Ibc and SLSNe demonstrate significantly shorter rise time less than 40 days (see e.g. Modjaz et al. 2009; Drout et al. 2011; Chomiuk et al. 2011). A good example of a SLSN with a reliable long-lasting rise is PTF10nmn. The data for this particular SLSN and for SN 2007bi are shown in Figure 4.17. Our Model 250M agrees well with the broad light curves of PTF10nmn and SN 2007bi.

The photospheric velocity of our high mass PISN model around the luminosity peak is lower than typical velocities of luminous SNe Ibc (Figure 4.18). The reason for the low velocity is the high ejecta mass of our model. This may be another criterion for distinguishing luminous PISNe powered by large amounts of nickel from superluminous CCSNe. However, the photospheric velocities measured for SN 2007bi demonstrate that the ejecta of this particular SLSN moves at a lower velocity than those of other SLSNe, which is in good agreement with our model. This renders precise spectroscopic observations important to shed light on this question.

Being discovered around or after its maximum, SN 2007bi resembles some other SLSNe which show a short rise to their peak luminosity (Nicholl et al. 2013). Particularly, this rules out the pair instability origin of these SNe. Nevertheless, we conclude that our Model 250M agrees with observed properties (light curve, photospheric velocity) of SLSN 2007bi well. Therefore, SN 2007bi might emerge from pair instability explosion of very massive star with initial mass above 200 $M_{\odot}$.

4.6 Conclusions

We carried out simulations of shock breakouts and light curves of pair instability supernovae using two evolutionary models of 150 $M_{\odot}$ and 250 $M_{\odot}$ at metallicity $Z = 10^{-3}$ (Langer et al. 2007; Kozyreva et al. 2014b). We used the radiation hydrodynamics code STELLA for this purpose (Blinnikov et al. 2006). The considered metallicity ($Z = 10^{-3}$) is among the highest of PISN models that have been so far presented in the literature (Herzig et al. 1990; Whalen et al. 2013c). Therefore, our models may serve as useful references for future studies on PISNe observed in the local Universe, as well as in the early Universe.

From our qualitative comparison to ordinary core collapse SNe we conclude that it is difficult to distinguish low mass pair instability explosions from hydrogen-rich core collapse explosions. The photometric and spectroscopic observations, including X-ray and ultraviolet (for detection of shock breakout events), should be very detailed from the earliest

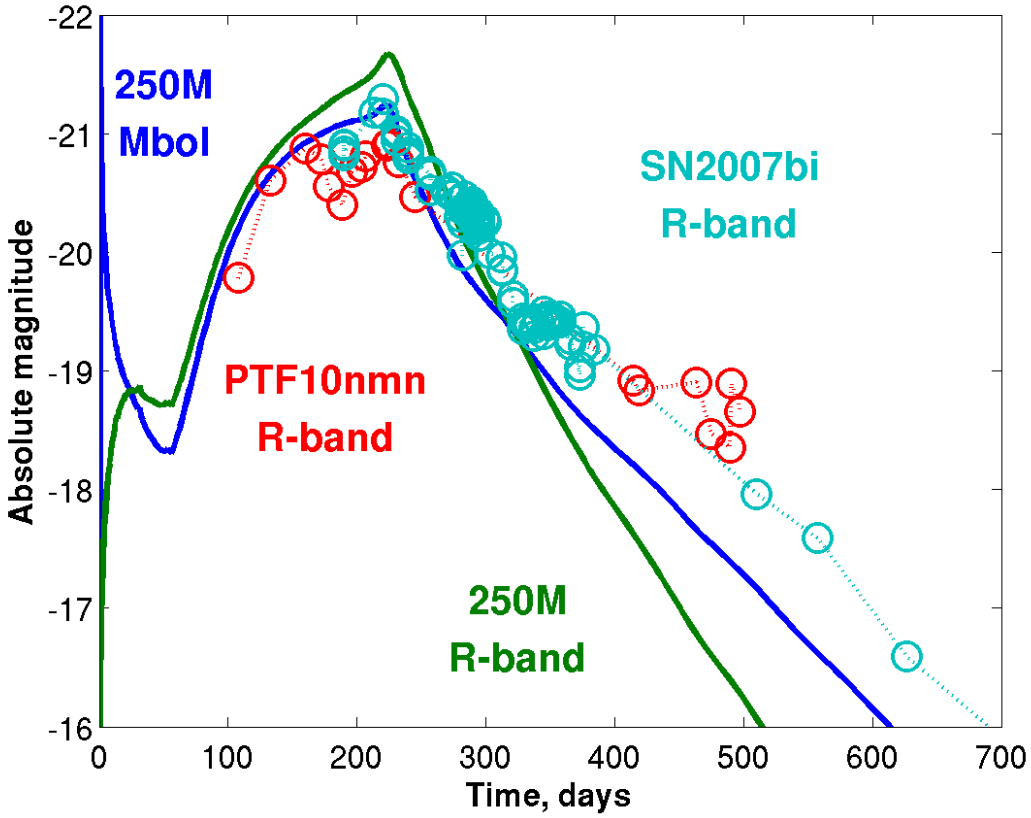

Figure 4.17: Absolute R-band (thin green line) and bolometric (thick blue line) light curve for our 250 $M_{\odot}$ PISN model, and R-band data for SLSN 2007bi (cyan circles) and PTF-10nmn (red circles) Gal-Yam (2012b).
The observed curves are shifted in time by 200 days to coincide with the maximum phase of the theoretical curve.

epoch to help shed light on this. The increasing number of SN surveys will increase the number of discovered SNe, as well as providing detailed data from the very early epoch after explosion, especially from those missions which have the short cadences (e.g., PTF).

Given the low-mass preference of the stellar initial mass function, a large fraction of PISNe that will be observed in the local Universe could resemble our 150 $M_{\odot}$ model, which represents PISNe from the low-mass end of the PISN regime. These PISNe are predicted to have the following characteristics:

1. The progenitors are likely to be red supergiants having very extended envelopes ($R \sim 3000$ R$_{\odot}$), if they can retain some fraction of the hydrogen envelopes by the time of explosion. Our 150 $M_{\odot}$ model has the final mass of 94 $M_{\odot}$ and the envelope mass is 29 $M_{\odot}$, which is significantly lower than in the corresponding case of zero or extremely low metallicity (~ 70 $M_{\odot}$). The hydrogen mass fraction in the envelope is only about 0.25.

2. The resulting PISN would appear to be a bright type IIP supernova like SN 2009kf. Its luminosity at the visual maximum would be typically higher by 2-3 magnitudes than average SNe IIP, although the total amount of radioactive nickel would be more or less similar to those from usual hydrogen-rich core-collapse supernovae ($\sim$ 0.05 $M_{\odot}$), depending on the final mass of the progenitor.

3. The plateau duration would be similar to those of ordinary SNe IIP, but much shorter than in the corresponding case at extremely low metallicity because of the relatively low mass of the envelope and the low hydrogen mass fraction.

4. The shock breakout duration would be somewhat longer ($\sim$ 6 hrs) and redder (0.07 keV) than those of ordinary SNe IIP.

5. The photospheric color temperature would be systematically higher than those of ordinary SNe IIP, and its evolution would look quite similar to that of SN 2009kf, which is an unusually bright SN IIP with a NUV-excess.

6. Because of the very large radius of the progenitor, the photospheric velocity at early times would be systematically lower than those of ordinary SNe IIP (Figure 4.15).

We also conclude that some observed luminous SNe Ic could have emerged from a pair instability explosion. Careful and deep photometric and spectroscopic observations would help to differentiate a pair instability explosion from SN Ic, in particular for the rise epoch and the tail. A general property of PISN explosions from the high mass regime is a slow light curve evolution due to massive ejecta. This causes a long rise to the peak luminosity and a long transition to the radioactive tail.

It was previously noted (Scannapieco et al. 2005; Kasen et al. 2011; Whalen et al. 2013a; Dessart et al. 2013) that a PISN from the high mass end of the PISN regime does not resemble any of the observed supernovae so far. However, we demonstrated that SLSNe 2007bi and PTF10mnm may fit well to our high mass PISN Model 250M. This

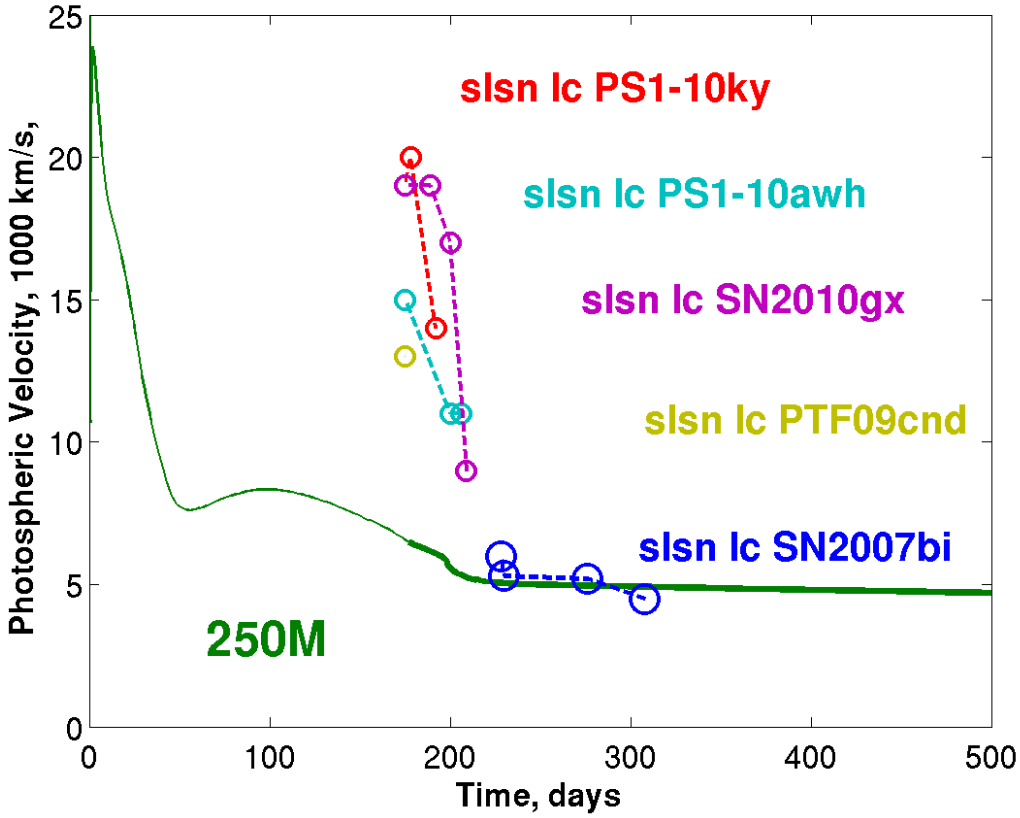

Figure 4.18: Photospheric velocity of our 250 $M_{\odot}$ PISN model and of several SLSN Ic. The observed data are taken from Young et al. (2010); Chomiuk et al. (2011). SN 2007bi points show the lower velocity limit measured from O I λ 7774 which we use as a best estimate for the photospheric velocity. The observed data are shifted to the maximum phase of the theoretical curve (day 175). The bold part of the theoretical curve (green) covers the maximum phase (from day 175) and the successive decline phase.

concerns the light curve shape, the peak luminosity, the photospheric velocity and the bulk ejecta masses.

We suggest the following criteria to distinguish high mass PISN from CCSN:

1. A short precursor in U, B, V-bands at about -19 mag lasting less than 40 days which can appear itself as a SN long before (e.g., half a year – a year before) the main maximum.

2. The pronounced rise time is larger than 200 days, which is significantly longer than for ordinary SN Ic.

3. A PISN may evolve from hydrogen-rich to hydrogen-poor type.

4. The nebular luminosity is powered by radioactive nickel decay and determined by the amount of produced nickel. Large amounts of radioactive nickel, tens of solar masses, produced in PISN significantly exceed typical 0.05 – 0.5 $M_{\odot}$ of nickel left by ordinary SNe Ic.

5. The photospheric velocity is lower than the velocities of SNe Ic during the whole evolution. On top of that the PISN photospheric velocity has a peculiar evolution during the rise to maximum light.

Increasing SN statistics will discover the brightest SNe together with others (Kaiser et al. 2002; Ivezic et al. 2008; Law et al. 2009). According to Langer et al. (2007) one pair instability explosion in the local Universe occurs among one thousand core collapse SNe. At present the number of discovered SNe per year surpasses one thousand, therefore, we expect several PISNe among the large number of discovered SNe. However, their unambiguous identification may be challenging, which we hope to facilitate with our present study.

Table 4.1: Characteristics of the PISN models: name of the model, initial metallicity Z, initial/final mass ($M_{\rm ini}/M_{\rm f}$) in solar masses, radius of the star at the onset of the radiative calculation R in solar radii, explosion ($E_{\rm expl}$) and kinetic ($E_{\rm kin}$) energy in foe (= 10^{51} erg), specific energy (E/M) in units [10^{50} erg/$M_\odot$], the velocity at the outer edge of the ^{56}Ni-rich layer in km s^{-1} ($v_{\rm ni,max}$), bulk yields of the isotopes in the ejecta in solar masses (hydrogen ^{1}H, helium ^{4}He, carbon ^{12}C, oxygen ^{16}O, silicon ^{28}Si, nickel ^{56}Ni). The names of the models starting with 'R' indicate red supergiants. The names starting with 'B' are blue supergiants. Models labeled '.D' (Dessart et al. 2013) and labeled '.K' (Kasen et al. 2011) are given for comparison.

Name	Z	$M_{\rm in}/M_{\rm f}$ ($M_\odot$)	R ($R_\odot$)	$E_{\rm expl}$ (foe)	$E_{\rm kin}$ (foe)	E/M	$v_{\rm ni,max}$ (km/s)	^{1}H ($M_\odot$)	^{4}He ($M_\odot$)	^{12}C ($M_\odot$)	^{16}O ($M_\odot$)	^{28}Si ($M_\odot$)	^{56}Ni ($M_\odot$)
150M	10^{-3}	150/94	3394	12	8	1.3	500	5	24	2	47	6	0.04
R150.K	2×10^{-6}	150/143	2314	9		0.6	no data	50	21				0.07
R190.D	2×10^{-6}	190/164	4044	44	33	2.7	1800	24	46	5	78	0.05	2.63
R250.K	2×10^{-6}	250/236	3214	69		2.9	5000	73	39				37.9
B190.D	2×10^{-6}	190/134	186	∼44	34	3.3	1200	6	34	5	78	0.05	2.99
B210.D	2×10^{-6}	210/147	146	75	66	5.1	4400	4	31	6	93	0.06	21.3
250M	10^{-3}	250/169	745	70	44	4.1	5000	10	48	1	42	23	19.3
B250.K	0	250/250	187	63		2.5	3200	86	40				23.1

Table 4.2: Shock breakout and plateau-maximum phase characteristics. Shock breakout duration (defined as a full width at half-maximum), bolometric peak luminosity, effective and color temperature, spectral wavelength peak in $\mathring{A}$, spectral energy peak in keV. The photospheric phase begins after relaxation from the shock breakout and is limited by the transition to the radioactive decay tail. Model 150M and Model 250M are those of 150 $M_\odot$ and 250 $M_\odot$ PISNe simulated in the frame of present study. Labeled 'R190.D', 'B190.D' and 'B210.D' are models from (Dessart et al. 2013) and 'R150.K' and 'R250.K' are models simulated by (Kasen et al. 2011).

	shock breakout					**photospheric phase**	
	duration, (hours)	L, (erg/s)	$T_{\rm eff}/T_{\rm color}$, ($10^3$ K)	$\lambda_{\rm max}$, ($\mathring{A}$)	E_p, (keV)	duration, (days)	L, (erg/s)
150M	6	5.4×10^{44}	60/160	170	0.07	110	1.6×10^{43}
R150.K	2	1.2×10^{45}	90/170	169	0.07	200	$3 \times 10^{42} - 10^{43}$
R190.D	—	—	—	—	—	260	3×10^{43}
R250.K	1.6	9.6×10^{45}	130/350	83	0.15	410	$6 \times 10^{43} - 10^{44}$
B190.D	—	—	—	—	—	300	1.6×10^{43}
B210.D	—	—	—	—	—	280	$2 \times 10^{42} - 10^{44}$
250M	1.4	6.2×10^{45}	230/570	51	0.24	280	$10^{43} - 6 \times 10^{43}$
B250.K	0.3	1.4×10^{45}	330/630	46	0.27	440	$2 \times 10^{42} - 5 \times 10^{43}$

Chapter 5

Summary and concluding remarks

This chapter summarises the work done, the obtained results and the overall achievements of the thesis.

The role of supernova explosions in the Universe is very significant. Firstly, most of them are the result of the relatively quick evolution of massive star. Therefore, they are the first contributors to the enrichment of the medium with heavy elements. Secondly, the appearance of supernova explosion serves as an excellent probe for the stellar evolution. This is especially important nowadays when the number of discovered supernovae exceeds one thousand every year.

In this thesis, we provide some of the first models of very massive stars exploding through the pair instability mechanism in the local Universe. While the pre-supernova evolution of our models has been published earlier (Langer et al. 2007), we have calculated the supernova explosions with the hydrodynamics stellar evolution code BEC (Yoon et al. 2010), and the subsequent supernova expansion phase with the radiation hydrodynamics code STELLA (Blinnikov et al. 2006).

5.1 Improvement of the nuclear network

Before this work, the BEC code was able to simulate the hydrostatic evolution of massive stars though hydrogen, helium, carbon, neon and oxygen burning. However, silicon burning as well as any explosive burning stages could not be calculated reliably due to limitations in the nuclear network of the BEC code.

To remedy this, a simplified $\alpha-$chain network was implemented as a first attempt of extending the existing nuclear network until the end of silicon burning. One of the main reasons why the $\alpha-$chain network is appropriate for the stellar evolutionary calculations is that it produces a reliable energy generation rate during the silicon burning phase. This is important for realistic stellar structure calculations. Being computationally inexpensive, the $\alpha-$chain network is valuable for extensive stellar evolutionary simulations.

Firstly, we revised the list of reactions relevant for oxygen burning and added the main

chain of reactions from silicon to nickel involving capture and production of $\alpha-$particles and implicitly included protons. The numerical recipe, which solves the system of differential equations, was improved by adding the "corrector" loop. Secondly, we extended the nuclear network to include 204 isotopes from hydrogen until germanium and 2134 reactions. Since the reactions involve capture and production of neutrons and protons the network fairly deals with weak interactions which are responsible for altering the electron fraction. The value of the electron fraction (and in turn neutron excess) strongly influences the nucleosynthetic yields which describes the nucleosynthesis of pair instability supernovae as we show in Chapter 3. We also implemented a table for energy generation rate calculations to optimize stellar evolutionary computations during the silicon burning phase.

For test purposes ,we successfully calculated a set of helium star models at solar metallicity starting from the helium zero-age main sequence. In particular, 10 $M_{\odot}$ and 15 $M_{\odot}$ helium star models were evolved until the pre-supernova stage, i.e., until the formation of an iron-nickel core. We found an overall agreement of our helium star evolution models with simulations provided by other evolutionary codes. This means that the code can now be used for calculations of the approximate structure of pre-supernova models which can be used further to simulate supernova explosions.

5.2 Pair instability supernovae in the local Universe

The recent discovery of superluminous supernovae initiated great interest in evolutionary models of pair instability supernova (PISN) progenitors. Moreover, as the observed superluminous supernovae exploded in the local Universe, whereas previous modeling efforts of PISNe focused on the early Universe, the special challenge was to construct the self-consistent evolution of very massive star at metallicities suitable for the local Universe.

One on the main result of the thesis is our successful calculations of the evolution of very massive stars exploding as PISNe. We calculated two models of PISNe, with initial masses of 150 $M_{\odot}$ and 250 $M_{\odot}$ and with an initial metallicity of $Z = 0.001$ (Kozyreva et al. 2014b). For this task we used the BEC code with the newly implemented large nuclear network including 204 isotopes (Timmes 1998). Both models were evolved through the pair creation, collapse, and explosive burning phases (explosive oxygen and explosive silicon burning) and eventually exploded. The final kinetic energy of our models is 1.2×10^{52} erg for the 150 $M_{\odot}$ and 7×10^{52} erg for the 250 $M_{\odot}$ model.

PISNe are completely disrupted during the explosion and eject a large mass (the entire stellar mass) of processed stellar matter enriched with heavy elements into the circumstellar medium. We calculated nucleosynthetic yields for both our PISN models. We show that PISNe produce very large amounts of oxygen. Either, the low-mass and the high-mass model, eject about 40 $M_{\odot}$ of oxygen which remains unburnt after the explosive burning stage. For the 150 $M_{\odot}$ model the highest yields are those of intermediate mass elements between oxygen and silicon. The production of heavier elements is fairly reduced because only a small fraction of silicon is burnt in this model. The 250 $M_{\odot}$ model yields large amounts of intermediate mass elements similarly to the 150 $M_{\odot}$ model, and considerable

amounts of iron-group isotopes. We draw special attention to the production of radioactive nickel-56. Our low mass model produces only 0.04 $M_{\odot}$ of this isotope which is comparable to an average amount of nickel in core-collapse supernovae. The consequences of this relate to the emerging shape of the supernova light curve. The ejecta of our 250 $M_{\odot}$ model contains about 20 $M_{\odot}$ of radioactive nickel which is far beyond any possible value generated in core-collapse supernovae or in SNe Ia. Such a high nickel mass results in a high peak luminosity and a long-lasting light curve of the PISN.

We provide an extensive nucleosynthesis analysis of our models in comparison to metal-free PISN models (Heger & Woosley 2002; Umeda & Nomoto 2002). We calculated the final isotopic yields and nucleosynthetic production efficiency of our models. We demonstrated that the PISN contribution to the yields produced by one generation of stars is less pronounced for the local Universe (a so-called "odd-even effect") compared to metal-free PISN models. We conclude that although the PISN progenitors contribute only 2% to the total number of stars in one generation, the signature of PISNe is noticeable and can be visible in the abundances of long-lived low-mass stars at a similar metallicity.

5.3 Observational properties of low redshift pair instability supernovae

One of the main interests in PISN explosions is related to the recently discovered superluminous supernovae. In order to be able to compare our models with the observed properties of these supernovae, a simulation of expanding supernova ejecta on the timescale of years is required.

For this purpose, both our evolutionary PISN models were mapped into the radiation hydrodynamics code STELLA (Blinnikov et al. 2006) about 30 seconds after the end of the explosive nuclear burning. We then simulated the further explosion through the shock breakout phase (when the shock emerges on the stellar surface) and the successive photospheric evolution (Kozyreva et al. 2014a). Our calculations differ from simulations made with other radiative transfer codes (SEDONA and CMFGEN, Kasen et al. 2011; Dessart et al. 2013) which were mostly used for simulation of metal-free and very metal-poor PISNe. Among others, the main advantage of the STELLA code is the coupled hydrodynamical and radiation field evolution, which provides self-consistent calculations of the propagation of radiation dominated supernova shocks.

Although our 150 $M_{\odot}$ PISN model does not appear as superluminous, its bolometric magnitude reaches -19 mag during the so-called "plateau" phase (the corresponding bolometric luminosity is about 2×10^{43} erg s^{-1}). We emphasize that even though the initial metallicity of our model is relatively high (0.001), the PISN progenitor retains a massive hydrogen envelope (29 $M_{\odot}$), i.e. our 150 $M_{\odot}$ PISN model explodes as very extended red supergiant. The overall shape of the light curve (a plateau phase of 100 days and a successive radioactive tail) and the photospheric evolution are similar to those of bright type II plateau supernovae (SNe IIP) which are thought to originate from iron-core collapse.

We demonstrated that it is difficult to distinguish low mass pair instability explosions from hydrogen-rich core collapse explosions. However, we suggested that detailed photometric and spectroscopic observations from the earliest epoch can help to differentiate PISN from core-collapse supernova (CCSN). PISNe have a longer and redder shock breakout, a lower photospheric velocity, and a higher color temperature compared to SNe IIP.

The peak bolometric magnitude of our 250 $M_\odot$ PISN explosion model reaches -21 mag (i.e. about 10^{44} erg s^{-1} in terms of luminosity) and hence competes with superluminous supernovae, which occur with peak magnitudes above -21 mag. The light curve of this high-mass PISN model appears very broad because the ejecta mass is sufficiently large ($\sim 170\,M_\odot$). The rise time to the main maximum is about 200 days. Due to the same reason the photospheric velocity is relatively low. We also show that during the maximum phase the photosphere in this PISN model is located in hydrogen/helium-deficient layers, which means that during the maximum phase it might be classified as hydrogen-free type Ic supernova. Although most superluminous type Ic supernovae possess narrower light curves, some of them (the best candidates for PISNe are SN 2007bi and PTF10nmn) might rise and decline slowly. We showed that the photospheric evolution of our 250 $M_\odot$ PISN model agrees well with the observable characteristics of SN 2007bi. Moreover, the nucleosynthetic yields of our model are surprisingly comparable to elemental yields provided by spectral observations of SN 2007bi. Therefore, based on our comparison we claim that SN 2007bi is not unlikely to originate from pair instability explosion.

The expected rate of PISNe among usual type II CCSNe (which are the most numerous ones in unbiased supernova samples) is one PISN explosion per one thousand CCSNe, assuming they occur in galaxies with a metallicity of less than about one-third of the solar metallicity. According to the progress in observational astronomy the number of discovered supernovae surpasses one thousand every year. Given the low-mass preference of the stellar mass function, relatively low-mass PISNe are supposed to occur more frequently than high-mass ones. Therefore, we believe that possibly several PISN events have already been observed. An observational confirmation of PISNe would verify their theoretical predictions from half a century ago. It would emphasize the nucleosynthetic impact of this type of supernova explosions to the chemical evolution of the Universe.

Appendix A

Basic stellar structure equations

The structure and evolution of stars are goverened by a set of partial differential equations. The following are *hydrodynamic* equations which include inertia term. However, they can be easily be converted into *hydrostatic* version while equating the inertia term with zero.

The set contains the equations of (1) continuity of mass, (2) momentum and (3) energy. Written in the vector form they are:

$$\frac{\partial \rho}{\partial t} + \nabla \cdot (\rho \mathbf{u}) = 0 \tag{A.1}$$

$$\frac{\partial \rho \mathbf{u}}{\partial t} + \nabla \cdot (\mathbf{u} \otimes \rho \mathbf{u}) + \nabla p_g = 0 \tag{A.2}$$

$$\frac{\partial E}{\partial t} + \nabla \cdot [\mathbf{u}\,(E + p_g)] = 0\,, \tag{A.3}$$

where ρ is the gas density, $\mathbf{u}$ its velocity, p_g the gas pressure, and E the total gas energy per unit volume, $E = \rho e_{\rm int} + \frac{1}{2}\rho u^2$, where $e_{\rm int}$ is the internal energy per unit mass. $\otimes$ denotes the outer product of two vectors giving a 3×3 tensor.

In case of a non-rotating spherically symmetric star it is appropriate to use comoving Lagrangian coordinates bound with the matter. Therefore, the above-written set of equations can be replaced by the following set:

$$\left(\frac{\partial r}{\partial m}\right)_t = \frac{1}{4\pi r^2 \rho} \tag{A.4}$$

$$\left(\frac{\partial r}{\partial t}\right)_m = u \tag{A.5}$$

$$\left(\frac{\partial P}{\partial m}\right)_t = \frac{Gm}{4\pi r^4} - \frac{1}{4\pi r^2}\left(\frac{\partial u}{\partial t}\right)_m \tag{A.6}$$

$$\left(\frac{\partial l}{\partial m}\right)_t = \varepsilon_{\rm nuc} + \varepsilon_\nu + \frac{P}{\rho^2}\left(\frac{\partial \rho}{\partial t}\right)_m - \left(\frac{\partial \varepsilon}{\partial t}\right)_m \tag{A.7}$$

$$\left(\frac{\partial T}{\partial m}\right)_t = -\nabla \frac{GmT}{4\pi r^4 P}\left[1 + \frac{r^2}{Gm}\left(\frac{\partial u}{\partial t}\right)_m\right], \tag{A.8}$$

where r is the radial distance of the shell to the centre of the star, m is the mass contained – serves as mass coordinate of the shell $m(r) = \int_0^r 4\pi r^2 \rho dr$, ρ is the density in the shell, u is the radial velocity, P is the pressure, G is the gravitational constant, l is the local luminosity, T is the temperature, ε is the internal energy per unit mass, $\varepsilon_{\rm nuc}$ corresponds to the energy release due to thermonuclear burning, ε_ν represents the local heat losses due to neutrino flux.

The details about this set of equations can be found, e.g., in Kippenhahn & Weigert (1990); Heger (1998).

The temperature gradient in radiative mass shells

$$\nabla \equiv \left(\frac{\partial \ln T}{\partial \ln P}\right)_t \tag{A.9}$$

is given by radiative temperature gradient

$$\nabla_{\rm rad} = \frac{3}{16\pi acG}\frac{\varkappa l P}{m T^4}\left[1 + \frac{r^2}{Gm}\left(\frac{\partial u}{\partial t}\right)_m\right]^{-1}, \tag{A.10}$$

where a is the radiation constant, c is the speed of light, and $\varkappa$ is the Rosseland mean opacity. The opacities are based on Alexander & Ferguson (1994) and Iglesias & Rogers (1996).

The temperature gradient in convective shells is calculated using the mixing-length theory (see e.g. Kippenhahn & Weigert 1990, and references therein).

The equation of state should be added to this set of equations, which binds the pressure P with the temperature T.

The set of equations is the system of non-linear partial differential equations. The evolution code solves it using the Newton-Raphson iteration method. The details about the numerical method can be found in Henyey et al. (1959, 1964).

Appendix B

Integration SN yields over the IMF

B.1 Integration over the IMF

B.1.1 Isotopic production factor

The production factor $P_{\rm iso}$ of a given isotope for the star with the mass M is defined as:

$$P_{\rm iso}(M) = \frac{\int X_{\rm iso}^{\rm zones} dm_{\rm zones}}{X_{\rm iso}^{\odot} \cdot M} = \frac{m_{\rm iso}(M)}{X_{\rm iso}^{\odot} M}\,, \tag{B.1}$$

where $X_{\rm iso}^{\rm zones}$ is mass fraction of the given isotope in zones, $X_{\rm iso}^{\odot}$ is solar mass fraction of the isotope, M is the total mass of the star, $m_{\rm iso}(M)$ is the total yield of the isotope in the ejecta.

The production factor $P_{\rm iso}^{\rm int}$ averaged over the IMF is

$$P_{\rm iso}^{\rm int} = \frac{\int m_{\rm iso}(M)\,\Phi(M) dM}{\int X_{\rm iso}^{\odot} M \Phi(M) dM}\,, \tag{B.2}$$

where $m_{\rm iso}(M)$ is the set of total yields of the isotopes (see Equation B.1), $\Phi(M) \propto M^{\Gamma}$ is IMF ($\Gamma = -1.6; -2.3$). Note that yield $m_{\rm iso}(M)$ is an additive variable, and production factor $P_{\rm iso}(M)$ is not an additive variable.

In other words production factor $P_{\rm iso}^{\rm int}$ is:

$$P_{\rm iso}^{\rm int} = \frac{\int m_{\rm iso}(M)\, M^{\Gamma} dM}{\int X_{\rm iso}^{\odot} M M^{\Gamma} dM} = \frac{\int \left(\frac{m_{\rm iso}}{X_{\rm iso}^{\odot} M}\right) M^{\Gamma+1} dM}{\int M^{\Gamma+1} dM} = \frac{\int P_{\rm iso}(M)\, M^{\Gamma+1} dM}{\int M^{\Gamma+1} dM}\,. \tag{B.3}$$

Direct integration of the production factor gives:

$$P_{\rm iso}^{\rm int} = \frac{\int P_{\rm iso}(M)\, M^{\Gamma} dM}{\int M^{\Gamma} dM}\,, \tag{B.4}$$

which means to be not correct (since production factor $P_{\rm iso}(M)$ is not an additive variable) but give almost the same result. It is obvious that difference between Equation (B.3) and Equation (B.4) consists in the different IMF slopes. But as it is shown in Heger & Woosley (2002) the IMF exponent has a weak effect on the integrated values.

B.2 Elemental production factor

All written above is related to isotopic production factor. If we consider elemental production factor $P^{\rm int}_{\rm ele}$ the expresion is:

$$P^{\rm int}_{\rm ele} = \frac{m^{\rm int}_{\rm ele}}{X^{\odot}_{\rm ele}\, M^{\rm int}}\,, \tag{B.5}$$

where $m^{\rm int}_{\rm ele}$ is the yield of the element integrated over the IMF, $X^{\odot}_{\rm ele}$ is the solar mass fraction of the element ($\equiv$ sum of mass fractions of the isotopes along the given element), $M^{\rm int}$ is an integrated mass.

The integrated yield of the element $m^{\rm int}_{\rm ele}$ is defined as:

$$m^{\rm int}_{\rm ele} = \int m_{\rm ele}(M)\, M^{\Gamma} dM = \int \left[\sum_{\rm iso} m_{\rm iso}(M)\right] \cdot M^{\Gamma} dM\,. \tag{B.6}$$

Substituting $m_{\rm iso}$ defined in Equation (B.1) (in the case of CCSN data $M \equiv M_{\rm ejecta}$) the expression for production factor could be rewritten as:

$$P^{\rm int}_{\rm ele} = \frac{\int \left[\sum_{\rm iso} P_{\rm iso}(M) \left(\frac{X^{\odot}_{\rm iso}}{X^{\odot}_{\rm ele}}\right)\right] M_{\rm ejecta} \cdot M^{\Gamma} dM}{\int M_x \cdot M^{\Gamma} dM}\,, \tag{B.7}$$

where M_x in denominator could be considered as $M_{\rm ejecta}$ or $M(\equiv M_{\rm initial})$.

If $M_x = M_{\rm ejecta}$ the normalization includes integration of $M_{\rm ejecta}$ over the IMF. This is correct for the average yield integrated over ejecta mass. The integration in Heger & Woosley (2002) (concerning CCSN data) is done according to above-mentioned recipe. From Equation (B.5), $M^{\rm int}$ should be the initial stellar mass integrated over the IMF (weighted mass). This is correct to set $M_x = M = M_{\rm initial}$.

B.2.1 The sum details

Following the results from the previous section B.2 we rewrite the integral for the elemental production factor Equation (B.7) as the sum:

$$P^{\rm int}_{\rm ele} = \frac{\sum_i \left(P_{\rm ele}(M_i) \cdot M_i^{\rm ej} \cdot M_i^{\Gamma} + P_{\rm ele}(M_{i+1}) \cdot M_i^{\rm ej} \cdot M_{i+1}^{\Gamma}\right) \Delta M_i}{\sum_i \left(M_i^{\Gamma+1} + M_{i+1}^{\Gamma+1}\right) \Delta M_i}\,, \tag{B.8}$$

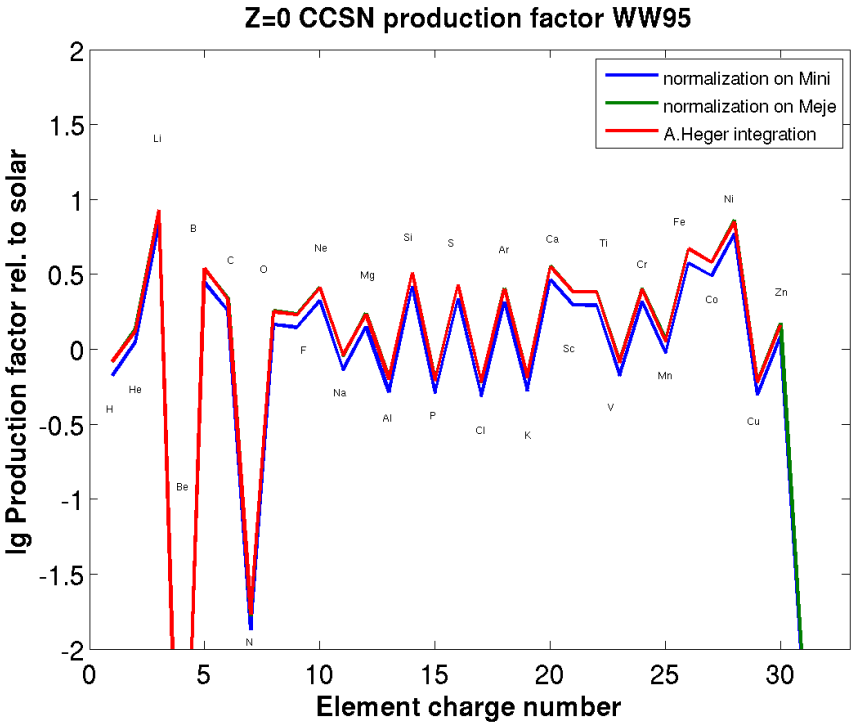

Figure B.1: Average elemental production factor for CCSN at zero metallicity. The integration is done for stars $12-40\ M_\odot$ over the IMF with the slope $\Gamma = -2.5$ (-1.5 in Heger & Woosley (2002)). Blue line represents result normalized on integrated initial mass. Green line represents result normalized on integrated ejecta mass. (The green line is almost under the red one). Red line is the dotted line in the Figure 4 Heger & Woosley (2002). CCSN data are taken from Woosley & Weaver (1995).

where $M_i = \{$ 12, 13, 15, 18, 20, 22, 25, 30, 35, 40, 150, 250 $\}$ — initial masses of the stellar models in solar masses (from Woosley & Weaver (1995) and our study), $M_i^{\rm ej} = \{$ 10.7, 11.8, 13.6, 16.4, 18.1, 20.0, 23.1, 27.4, 28.5, 31.1, 150, 250 $\}$ — ejecta masses in solar masses (given numbers are taken from Tables 10A, 10B (Woosley & Weaver 1995) for models at metallicity $Z = 0.1Z_\odot$; ejecta masses for metal free models are in Tables 16A, 16B), $\Delta M_i = M_{i+1} - M_i = \{$ 1, 2, 3, 2, 2, 3, 5, 5, 5, 110, 100$\}$ solar masses, $\Gamma = -2.5$ is the IMF slope.

Then the elemental production factor $P_{\rm ele}(M_i)$ for a particular stellar model is defined as:

$$P_{\rm ele}(M_i) = \sum_{\rm iso} P_{\rm iso}(M_i) \left(\frac{X^\odot_{\rm iso}}{X^\odot_{\rm ele}} \right) , \tag{B.9}$$

where $P_{\rm iso}(M_i)$ is isotopic production factor for the model, and the sum is done over isotopes for a given element. The production factor in Woosley & Weaver (1995) as:

$$P_{\rm iso}(M_i) = \frac{m_{\rm iso}(M_i)}{X^\odot_{\rm iso} M_{\rm ej}} , \tag{B.10}$$

where $m_{\rm iso}$ is the total isotopic yield in the ejecta.

Both in numerator and denominator we do not include the term involving $M_i = 40$ and $M_{i+1} = 150$, i.e. we do not take into consideration the range of initial masses between 40 $M_\odot$ and 150 $M_\odot$, because we assume no considerable contribution from these stars.

B.2.2 The imprint of pair instability supernovae on the yield from one generation of stars

In this section we briefly descuss the imprint of pair instability supernovae (PISN). The main conclusions are done in Chapter 3. Let us consider the ratio of the production factor for one generation of stars (P(CCSN + PISN)) to production factor for massive stars which result in core-collapse supernovae (CCSN, P(CCSN)). The ratio for a given isotope for zero metallicity models is:

$$R_0 = \frac{P(\mathrm{CCSN} + \mathrm{PISN})_0}{P(\mathrm{CCSN})_0} = \frac{M_{\rm CC} Y(\mathrm{CCSN} + \mathrm{PISN})_0}{M_{\rm CCPISN} Y(\mathrm{CCSN})_0}\,, \tag{B.11}$$

where P(CCSN + PISN) is an average production factor for one generation of massive and very massive stars, and P(CCSN) is the average production factor for one generation of massive stars (the contribution to metals from CCSN). $\log(R_0)$ is the difference between blue solid line and blue dotted line. Y values are corresponding yields. M_{CC} is a weighted mass $\int M\, M^{\Gamma} dM$ over CCSN range (12-40 $M_\odot$) and $M_{\rm CCPI}$ is a weighted mass over the whole mass range (12 – 260 $M_\odot$).

$$R_0 = \frac{M_{\rm CC}}{M_{\rm CCPI}} \frac{Y(\mathrm{CCSN})_0 + Y(\mathrm{PISN})_0}{Y(\mathrm{CCSN})_0} = \frac{M_{\rm CC}}{M_{\rm CCPI}} \left[1 + \frac{Y(\mathrm{PISN})_0}{Y(\mathrm{CCSN})_0}\right] \tag{B.12}$$

The similar expression can be written for the production factors for models at metallicity $Z = 0.002$:

$$R_{0002} = \frac{M_{\rm CC}}{M_{\rm CCPI}} \left[1 + \frac{Y(\mathrm{PISN})_{0002}}{Y(\mathrm{CCSN})_{0002}}\right]\,. \tag{B.13}$$

The bulk yields of even-charged elements: ^{16}O, ^{20}Ne..., ^{28}Si for PISN at different metallicity are similar. Therefore, $Y(\mathrm{PISN})_{0002} \approx Y(\mathrm{PISN})_0 = Y(\mathrm{PISN})$. The yields ratio f is defined as: $f = Y(\mathrm{CCSN})_{0002}/Y(\mathrm{CCSN})_0$. A factor f is different for different isotopes. The final expression for the ratio between production factor R_{0002} is:

$$R_{0002} = A + \frac{1}{f} \cdot R_0\,, \tag{B.14}$$

where $A = \frac{M_{\rm CC}}{M_{\rm CCPI}} \left[1 - \frac{1}{f}\right]$

The value of f is above unity for many isotopes as it is seen in the Figure B.2 (red dotted line is above blue dotted line in many nodes). In mathematical point of view this means that R_{0002} is always less than R_0. In the Figure B.2 this is seen as smaller difference

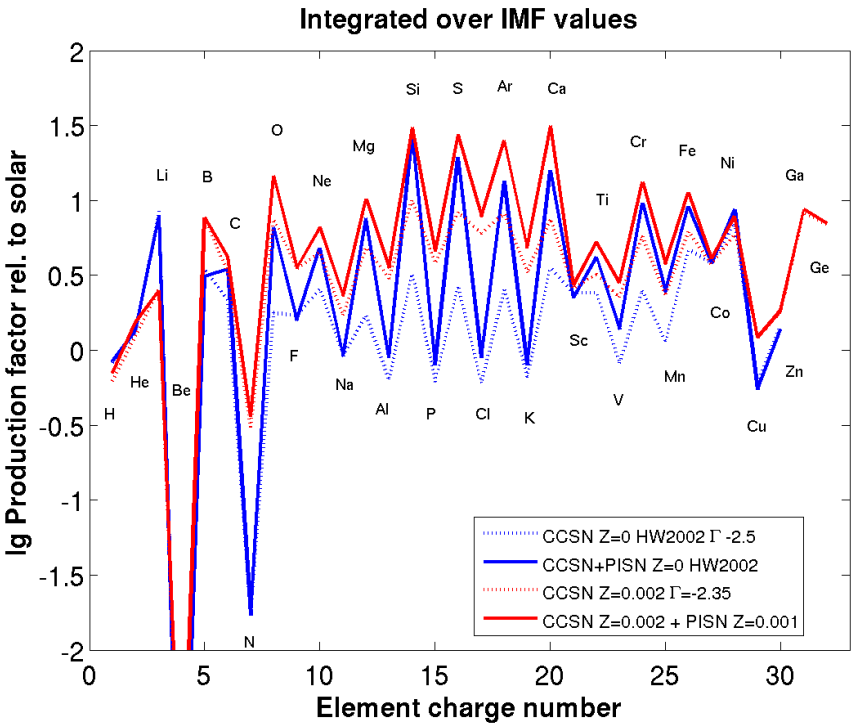

Figure B.2: Average elemental production factor for one generation of massive and very massive stars at different metallicities.
Dotted lines: an average elemental production factor for one generation of massive stars 12-40 $M_\odot$ over the IMF with the slope $\Gamma = -2.5$ (– 1.5 in Heger & Woosley (2002)) at metallicity $Z = 0$ (blue) and $Z = 0.002$.
Solid lines: the same integration is done with taking into account PISN yields at mass range 150-250 $M_\odot$. Blue line corresponds to metallicity $Z = 0$ and red line corresponds to metallicity $Z = 0.002$ (CCSN at $Z = 0.002$ + PISN at $Z = 0.001$). CCSN data are taken from Woosley & Weaver (1995). Zero metallicity results are taken from Heger & Woosley (2002).

between red solid and red dotted lines comparing to the same difference between blue solid and blue dotted lines.

Larger value of f means the larger contribution of non-zero metallicity CCSN compared to zero metallicity CCSN. The consequence of larger f is the smaller ratio R_{0002} and so the smaller imprint of PISN to the total yield from one generation of stars.

We conclude that in the local Universe the contribution from PISN is strongly washed out by the large impact from CCSN. However, the PISN signature is still noticable since PISNe change averaged elemental production factor by about 0.5 dex.

Bibliography

Abel, T., Bryan, G. L., & Norman, M. L. 2002, Science, 295, 93 18, 30, 90

Agnoletto, I., Benetti, S., Cappellaro, E., et al. 2009, ApJ, 691, 1348 33

Alexander, D. R. & Ferguson, J. W. 1994, ApJ, 437, 879 67, 130

Ambwani, K. & Sutherland, P. 1988, ApJ, 325, 820 94

Anders, E. & Grevesse, N. 1989, Geochimica et Cosmochimica Acta, 53, 197 72

Appenzeller, I. 1970, A&A, 9, 216 69

Arcavi, I., Gal-Yam, A., Kasliwal, M. M., et al. 2010, ApJ, 721, 777 18

Arnett, D., Fryxell, B., & Mueller, E. 1989a, ApJ, 341, L63 110

Arnett, W. D. 1969, Ap&SS, 5, 180 19

Arnett, W. D. 1988, ApJ, 331, 377 110

Arnett, W. D., Bahcall, J. N., Kirshner, R. P., & Woosley, S. E. 1989b, ARA&A, 27, 629 22

Asplund, M., Grevesse, N., Sauval, A. J., & Scott, P. 2009, ARA&A, 47, 481 72

Baraffe, I., Heger, A., & Woosley, S. E. 2001, ApJ, 550, 890 90

Barbon, R., Ciatti, F., & Rosino, L. 1979, A&A, 72, 287 21, 104, 114

Barkat, Z., Rakavy, G., & Sack, N. 1967, Physical Review Letters, 18, 379 24, 66, 90

Barkov, M. V. & Komissarov, S. S. 2011, MNRAS, 415, 944 35

Barniske, A., Oskinova, L. M., & Hamann, W.-R. 2008, A&A, 486, 971 15

Benetti, S., Nicholl, M., Cappellaro, E., et al. 2013, ArXiv e-prints, 1310.1311, submitted to MNRAS 117

Bersten, M. C., Benvenuto, O., & Hamuy, M. 2011, ApJ, 729, 61 114

Bersten, M. C. & Hamuy, M. 2009, ApJ, 701, 200 98, 101, 103, 113

Bestenlehner, J. M., Vink, J. S., Gräfener, G., et al. 2011, A&A, 530, L14 15

Bethe, H. A. 1939, Physical Review, 55, 103 39

Bisnovatyi-Kogan, G. S. 1968, Sov. Astr., 12, 58 30

Bisnovatyi-Kogan, G. S. & Kazhdan, Y. M. 1967, Sov. Astr., 10, 604 24, 66, 90

Blinnikov, S., Lundqvist, P., Bartunov, O., Nomoto, K., & Iwamoto, K. 2000, ApJ, 532, 1132 101

Blinnikov, S. I. & Bartunov, O. S. 1993, A&A, 273, 106 34

Blinnikov, S. I., Dunina-Barkovskaya, N. V., & Nadyozhin, D. K. 1996, ApJS, 106, 171 26, 67

Blinnikov, S. I., Röpke, F. K., Sorokina, E. I., et al. 2006, A&A, 453, 229 91, 94, 117, 125, 127

Blinnikov, S. I. & Sorokina, E. I. 2010, ArXiv e-prints, 1009.4353 34

Blinnikov, S. I. & Tolstov, A. G. 2011, Astronomy Letters, 37, 194 36, 108

Bodansky, D., Clayton, D. D., & Fowler, W. A. 1968, ApJS, 16, 299 49, 67

Bond, J. R., Arnett, W. D., & Carr, B. J. 1982, in NATO ASIC Proc. 90: Supernovae: A Survey of Current Research, ed. M. J. Rees & R. J. Stoneham, 303–311 28, 66

Bond, J. R., Arnett, W. D., & Carr, B. J. 1984, ApJ, 280, 825 28

Botticella, M. T., Riello, M., Cappellaro, E., et al. 2008, A&A, 479, 49 19

Botticella, M. T., Trundle, C., Pastorello, A., et al. 2010, ApJ, 717, L52 33, 112, 113, 114

Bromm, V., Coppi, P. S., & Larson, R. B. 1999, ApJ, 527, L5 18, 90

Bruenn, S. W., Mezzacappa, A., Hix, W. R., et al. 2009, Journal of Physics Conference Series, 180, 012018 19

Bruenn, S. W., Mezzacappa, A., Hix, W. R., et al. 2013, ApJ, 767, L6 19

Burbidge, E. M., Burbidge, G. R., Fowler, W. A., & Hoyle, F. 1957, Reviews of Modern Physics, 29, 547 39

Burrows, A. 2013, Reviews of Modern Physics, 85, 245 19

Calzavara, A. J. & Matzner, C. D. 2004, MNRAS, 351, 694 20, 114

Cameron, A. G. W. 1959a, ApJ, 130, 429 46

Cameron, A. G. W. 1959b, ApJ, 130, 895 46

Carr, B. J., Bond, J. R., & Arnett, W. D. 1984, ApJ, 277, 445 30, 31

Carr, B. J. & Glatzel, W. 1986, in NATO ASIC Proc. 163: Nucleosynthesis and its Implications on Nuclear and Particle Physics, ed. J. Audouze & N. Mathieu, 87–94 28

Caughlan, G. R. & Fowler, W. A. 1988, Atomic Data and Nuclear Data Tables, 40, 283 40, 46

Caughlan, G. R., Fowler, W. A., Harris, M. J., & Zimmerman, B. A. 1985, Atomic Data and Nuclear Data Tables, 32, 197 46

Cayrel, R., Depagne, E., Spite, M., et al. 2004, A&A, 416, 1117 76

Chatzopoulos, E. & Wheeler, J. C. 2012, ApJ, 748, 42 28

Chatzopoulos, E., Wheeler, J. C., & Couch, S. M. 2013, ApJ, 776, 129 110

Chen, K. J., Heger, A., & Almgren, A. 2012, in Astronomical Society of the Pacific Conference Series, Vol. 453, Advances in Computational Astrophysics: Methods, Tools, and Outcome, ed. R. Capuzzo-Dolcetta, M. Limongi, & Tornambe 110

Chen, K.-J., Heger, A., Woosley, S., Almgren, A., & Whalen, D. 2014, ArXiv e-prints, 1402.5960, submitted to ApJ 30, 110

Chevalier, R. A. 1981, ApJ, 251, 259 33

Chevalier, R. A. 1982, ApJ, 258, 790 33

Chevalier, R. A. 2012, ApJ, 752, L2 34

Chevalier, R. A. & Irwin, C. M. 2011, ApJ, 729, L6 34

Chieffi, A. & Limongi, M. 2013, ApJ, 764, 21 18, 41, 56, 57, 59, 60

Chieffi, A., Limongi, M., & Straniero, O. 1998, ApJ, 502, 737 18

Chomiuk, L., Chornock, R., Soderberg, A. M., et al. 2011, ApJ, 743, 114 31, 116, 117, 120

Christlieb, N., Gustafsson, B., Korn, A. J., et al. 2004, ApJ, 603, 708 76

Clocchiatti, A., Benetti, S., Wheeler, J. C., et al. 1996, AJ, 111, 1286 112, 114

Cooke, J., Sullivan, M., Gal-Yam, A., et al. 2012, Nature, 491, 228 91

Couch, S. M. 2013, ApJ, 775, 35 19

Crowther, P. A., Schnurr, O., Hirschi, R., et al. 2010, MNRAS, 408, 731 15, 16, 35, 77, 91

Davidson, K. 1999, in Astronomical Society of the Pacific Conference Series, Vol. 179, Eta Carinae at The Millennium, ed. J. A. Morse, R. M. Humphreys, & A. Damineli, 6 15

Denissenkov, P. A. & Hartwick, F. D. A. 2014, MNRAS, 437, L21 30

Dessart, L. & Hillier, D. J. 2010, MNRAS, 405, 2141 104

Dessart, L. & Hillier, D. J. 2011, MNRAS, 410, 1739 101, 103, 104

Dessart, L., Hillier, D. J., Li, C., & Woosley, S. 2012a, MNRAS, 424, 2139 23, 103

Dessart, L., Hillier, D. J., Livne, E., et al. 2011, MNRAS, 414, 2985 29

Dessart, L., Hillier, D. J., Waldman, R., Livne, E., & Blondin, S. 2012b, MNRAS, 426, L76 33, 34, 35, 66, 91

Dessart, L., Livne, E., & Waldman, R. 2010, MNRAS, 405, 2113 103

Dessart, L., Waldman, R., Livne, E., Hillier, D. J., & Blondin, S. 2013, MNRAS, 428, 3227 66, 90, 92, 98, 103, 104, 108, 110, 115, 119, 122, 123, 127

Dolence, J. C., Burrows, A., Murphy, J. W., & Nordhaus, J. 2013, ApJ, 765, 110 19

Drake, A. J., Djorgovski, S. G., Prieto, J. L., et al. 2010, ApJ, 718, L127 33

Drout, M. R., Soderberg, A. M., Gal-Yam, A., et al. 2011, ApJ, 741, 97 33, 117

Eastman, R. G. & Pinto, P. A. 1993, ApJ, 412, 731 94

Eddington, A. S. 1926, The Internal Constitution of the Stars, 416 pp. 25

Ekström, S., Georgy, C., Eggenberger, P., et al. 2012, A&A, 537, A146 36, 68

El Eid, M. F., Fricke, K. J., & Ober, W. W. 1983, A&A, 119, 54 35, 66

El Eid, M. F. & Langer, N. 1986, A&A, 167, 274 36, 67, 69, 90

Eldridge, J. J., Fraser, M., Smartt, S. J., Maund, J. R., & Crockett, R. M. 2013, MNRAS, 436, 774 18, 24

Elmhamdi, A., Danziger, I. J., Chugai, N., et al. 2003, MNRAS, 338, 939 39

Ensman, L. & Burrows, A. 1992, ApJ, 393, 742 20

Fadeyev, Y. A. 2011, Astronomy Letters, 37, 11 34

Fadeyev, Y. A. 2012, Astronomy Letters, 38, 260 34

Falk, S. W. & Arnett, W. D. 1977, ApJS, 33, 515 20, 108

Ferrario, L. & Wickramasinghe, D. 2008, MNRAS, 389, L66 34

Filippenko, A. V. 1997, ARA&A, 35, 309 23, 39

Filippone, B. W. 1985, in American Institute of Physics Conference Series, Vol. 126, Solar Neutrinos and Neutrino Astronomy, ed. M. L. Cherry, K. Lande, & W. A. Fowler, 100–108 46

Filippone, B. W. 1986, Annual Review of Nuclear and Particle Science, 36, 717 46

Fowler, W. A. 1954, Memoires of the Societe Royale des Sciences de Liege, 1, 88 39

Fowler, W. A. 1966a, Transactions of the International Astronomical Union, Series B, 12, 581 31

Fowler, W. A. 1966b, ApJ, 144, 180 31

Fowler, W. A., Caughlan, G. R., & Zimmerman, B. A. 1975, ARA&A, 13, 69 46

Fowler, W. A. & Hoyle, F. 1964, ApJS, 9, 201 24, 66, 90

Fraley, G. S. 1968, Ap&SS, 2, 96 24, 66, 90

Frebel, A., Aoki, W., Christlieb, N., et al. 2005, Nature, 434, 871 36, 76

Fricke, K. J. 1973, ApJ, 183, 941 40

Fricke, K. J. 1974, ApJ, 189, 535 31

Friend, D. B. & Castor, J. I. 1983, ApJ, 272, 259 94

Fryer, C. L. 1999, ApJ, 522, 413 20

Fryer, C. L., Woosley, S. E., & Heger, A. 2001, ApJ, 550, 372 62

Fuller, G. M., Fowler, W. A., & Newman, M. J. 1982, ApJS, 48, 279 67

Fuller, G. M., Woosley, S. E., & Weaver, T. A. 1986, ApJ, 307, 675 30, 31

Gal-Yam, A. 2012a, Science, 337, 927 31, 33, 66, 91

Gal-Yam, A. 2012b, in IAU Symposium, Vol. 279, Death of Massive Stars: Supernovae and Gamma-Ray Bursts, 253–260 29, 118

Gal-Yam, A., Mazzali, P., Ofek, E. O., et al. 2009, Nature, 462, 624 31, 33, 35, 66, 91

Gal-Yam, A., Mazzali, P. A., Manulis, I., & Bishop, D. 2013, PASP, 125, 749 19

Georgy, C., Ekström, S., Eggenberger, P., et al. 2013, A&A, 558, A103 18

Glatzel, W., Fricke, K. J., & El Eid, M. F. 1985, A&A, 149, 413 28

Graboske, H. C., Dewitt, H. E., Grossman, A. S., & Cooper, M. S. 1973, ApJ, 181, 457 46

Grasberg, E. K., Imshenik, V. S., & Nadyozhin, D. K. 1971, Ap&SS, 10, 3 23, 101, 104, 108, 115

Grasberg, E. K. & Nadezhin, D. K. 1976, Ap&SS, 44, 409 21, 101

Hamuy, M. 2001, PhD thesis, The University of Arizona 112

Hamuy, M. 2003a, ApJ, 582, 905 114

Hamuy, M. 2003b, ArXiv e-prints, 0301006 22, 29

Harris, M. J., Fowler, W. A., Caughlan, G. R., & Zimmerman, B. A. 1983, ARA&A, 21, 165 46

Heger, A. 1998, PhD thesis, Ph.D. Dissertation, Max-Planck-Institut für Astrophysik, unpublished (1998) 130

Heger, A., Fryer, C. L., Woosley, S. E., Langer, N., & Hartmann, D. H. 2003, ApJ, 591, 288 20, 39, 66, 90

Heger, A., Jeannin, L., Langer, N., & Baraffe, I. 1997, A&A, 327, 224 22, 69

Heger, A., Langer, N., & Woosley, S. E. 2000, ApJ, 528, 368 18, 28, 67

Heger, A. & Woosley, S. 2005, in IAU Symposium, Vol. 228, From Lithium to Uranium: Elemental Tracers of Early Cosmic Evolution, ed. V. Hill, P. Francois, & F. Primas, 297–302 76

Heger, A. & Woosley, S. E. 2002, ApJ, 567, 532 24, 27, 28, 29, 35, 36, 66, 68, 69, 71, 72, 75, 78, 84, 85, 87, 90, 127, 132, 133, 135

Heger, A. & Woosley, S. E. 2010, ApJ, 724, 341 19, 29, 68, 76

Henyey, L. G., Forbes, J. E., & Gould, N. L. 1964, ApJ, 139, 306 67, 130

Henyey, L. G., Wilets, L., Böhm, K. H., Lelevier, R., & Levee, R. D. 1959, ApJ, 129, 628 130

Heras, R. 2012, in Astronomical Society of the Pacific Conference Series, Vol. 466, Electromagnetic Radiation from Pulsars and Magnetars, ed. W. Lewandowski, O. Maron, & J. Kijak, 253 34

Herzig, K., El Eid, M. F., Fricke, K. J., & Langer, N. 1990, A&A, 233, 462 67, 91, 117

Hillebrandt, W., Thielemann, F.-K., & Langer, N. 1987, ApJ, 321, 761 31

Hirschi, R., Meynet, G., & Maeder, A. 2004, A&A, 425, 649 18, 28, 41, 59

Hix, W. R., Khokhlov, A. M., Wheeler, J. C., & Thielemann, F.-K. 1998, ApJ, 503, 332 49

Hix, W. R. & Meyer, B. S. 2006, Nuclear Physics A, 777, 188 49

Hix, W. R. & Thielemann, F.-K. 1996, ApJ, 460, 869 49, 50, 67, 75

Hosokawa, T. & Omukai, K. 2009, ApJ, 703, 1810 30, 77

Hosokawa, T., Yorke, H. W., Inayoshi, K., Omukai, K., & Yoshida, N. 2013, ApJ, 778, 178 30

Humphreys, R. M. & Davidson, K. 1994, PASP, 106, 1025 34

Iben, Jr., I. & Tutukov, A. V. 1984, ApJS, 54, 335 40

Iglesias, C. A. & Rogers, F. J. 1996, ApJ, 464, 943 67, 130

Imshenik, V. S. & Nadezhin, D. K. 1965, Sov. Astr., 8, 664 101

Imshennik, V. S. & Nadezhin, D. K. 1989, Astrophysics and Space Physics Reviews, 8, 1 22, 101

Imshennik, V. S. & Utrobin, V. P. 1977, Soviet Astronomy Letters, 3, 34 101

Inserra, C., Smartt, S. J., Jerkstrand, A., et al. 2013, ApJ, 770, 128 31, 33, 34, 35, 116

Ivezic, Z., Tyson, J. A., Acosta, E., et al. 2008, ArXiv e-prints 121

Iwamoto, K., Brachwitz, F., Nomoto, K., et al. 1999, ApJS, 125, 439 29, 72

Iwamoto, K., Mazzali, P. A., Nomoto, K., et al. 1998, Nature, 395, 672 29

Janka, H.-T. 2012, Annual Review of Nuclear and Particle Science, 62, 407 19

Joggerst, C. C. & Whalen, D. J. 2011, ApJ, 728, 129 103, 110

Joggerst, C. C., Woosley, S. E., & Heger, A. 2009, ApJ, 693, 1780 40, 110

Johnson, J. L., Whalen, D. J., Even, W., et al. 2013, ApJ, 775, 107 31

Jones, M. I. 2008, PhD Thesis, ArXiv e-prints, 0810.5538, 104 pp. 115

Jones, M. I., Hamuy, M., Lira, P., et al. 2009, ApJ, 696, 1176 115

Kaiser, N., Aussel, H., Burke, B. E., et al. 2002, in Society of Photo-Optical Instrumentation Engineers (SPIE) Conference Series, Vol. 4836, Survey and Other Telescope Technologies and Discoveries, ed. J. A. Tyson & S. Wolff, 154–164 121

Kasen, D. & Bildsten, L. 2010, ApJ, 717, 245 33, 34, 35, 66, 91

Kasen, D., Thomas, R. C., & Nugent, P. 2006, ApJ, 651, 366 104

Kasen, D. & Woosley, S. E. 2009, ApJ, 703, 2205 29, 114

Kasen, D., Woosley, S. E., & Heger, A. 2011, ApJ, 734, 102 66, 75, 90, 92, 98, 101, 104, 110, 115, 119, 122, 123, 127

Kippenhahn, R. & Weigert, A. 1990, Stellar Structure and Evolution (Springer-Verlag Berlin Heidelberg New York. Also Astronomy and Astrophysics Library), 468 pp. 24, 27, 130

Kippenhahn, R. & Weigert, A. 1994, Stellar Structure and Evolution, 468 pp. 25, 26

Kolmogorov, A. 1941, Akademiia Nauk SSSR Doklady, 30, 301 14

Komissarov, S. S. & Barkov, M. V. 2009, MNRAS, 397, 1153 62

Komissarov, S. S. & Barkov, M. V. 2010, MNRAS, 402, L25 62

Kosenko, D., Helder, E. A., & Vink, J. 2010, A&A, 519, A11 40

Kotake, K., Sumiyoshi, K., Yamada, S., et al. 2012, Progress of Theoretical and Experimental Physics, 2012, 010000 19

Kozyreva, A., Blinnikov, S., Langer, N., & Yoon, S.-C. 2014a, ArXiv e-prints, 1403.5212, accepted by A & A 67, 75, 127

Kozyreva, A., Yoon, S.-C., & Langer, N. 2014b, submitted to A & A 29, 91, 92, 117, 126

Krtička, J. & Kubát, J. 2006, A&A, 446, 1039 90

Kudritzki, R. P., Pauldrach, A., Puls, J., & Abbott, D. C. 1989, A&A, 219, 205 92

Kuroda, T., Kotake, K., & Takiwaki, T. 2012, ApJ, 755, 11 19

Kurucz, R. L. 1991, in NATO ASIC Proc. 341: Stellar Atmospheres - Beyond Classical Models, ed. L. Crivellari, I. Hubeny, & D. G. Hummer, 441 94

Langer, N. 1991, A&A, 252, 669 68

Langer, N. 2009, Nature, 462, 579 35, 91

Langer, N. 2012, ARA&A, 50, 107 23, 75, 114

Langer, N. & El Eid, M. F. 1986, A&A, 167, 265 22, 28, 36, 67

Langer, N., Fricke, K. J., & Sugimoto, D. 1983, A&A, 126, 207 68

Langer, N., Norman, C. A., de Koter, A., et al. 2007, A&A, 475, L19 35, 36, 37, 66, 67, 68, 69, 76, 77, 79, 91, 92, 117, 121, 125

Law, N. M., Kulkarni, S. R., Dekany, R. G., et al. 2009, PASP, 121, 1395 121

Lewis, K. T., Burrows, D. N., Hughes, J. P., et al. 2003, ApJ, 582, 770 40

Li, C., Hillier, D. J., & Dessart, L. 2012, MNRAS, 426, 1671 103

Li, W., Chornock, R., Leaman, J., et al. 2011, MNRAS, 412, 1473 18

Limongi, M. & Chieffi, A. 2003, ApJ, 592, 404 29

Limongi, M., Straniero, O., & Chieffi, A. 2000, ApJS, 129, 625 18

Litvinova, I. Y. & Nadezhin, D. K. 1985, Soviet Astronomy Letters, 11, 145 23

Lopez, L. A., Ramirez-Ruiz, E., Huppenkothen, D., Badenes, C., & Pooley, D. A. 2011, ApJ, 732, 114 40

Lunnan, R., Chornock, R., Berger, E., et al. 2013, ApJ, 771, 97 31, 116

Mackey, J., Bromm, V., & Hernquist, L. 2003, ApJ, 586, 1 18

Maeder, A. & Meynet, G. 1987, A&A, 182, 243 28

Mannucci, F., Della Valle, M., & Panagia, N. 2007, MNRAS, 377, 1229 19

Marek, A. & Janka, H.-T. 2009, ApJ, 694, 664 19

Martins, F., Hillier, D. J., Paumard, T., et al. 2008, A&A, 478, 219 15

Mattila, S., Dahlen, T., Efstathiou, A., et al. 2012, ApJ, 756, 111 19

McCracken, D. D. & Dorn, W. S. 1965, Numerical methods and FORTRAN programming with applications in engineering and science, 583 pp. 48

Mészáros, P. & Rees, M. J. 2010, ApJ, 715, 967 62

Meyer, B. S. 1994, ARA&A, 32, 153 17

Meyer, B. S., Krishnan, T. D., & Clayton, D. D. 1998, ApJ, 498, 808 17

Meynet, G. & Maeder, A. 1987, in Lecture Notes in Physics, Berlin Springer Verlag, Vol. 287, Nuclear Astrophysics, ed. W. Hillebrandt, R. Kuhfuss, E. Mueller, & J. W. Truran, 195–203 28

Minkowski, R. 1941, PASP, 53, 224 22

Modjaz, M., Li, W., Butler, N., et al. 2009, ApJ, 702, 226 117

Mokiem, M. R., de Koter, A., Vink, J. S., et al. 2007, A&A, 473, 603 91

Moll, R. & Woosley, S. E. 2013, ApJ, 774, 137 50

Moriya, T., Tominaga, N., Blinnikov, S. I., Baklanov, P. V., & Sorokina, E. I. 2011, MNRAS, 415, 199 23, 34, 114

Moriya, T., Tominaga, N., Tanaka, M., Maeda, K., & Nomoto, K. 2010, ApJ, 717, L83 19, 29, 33, 66, 91

Moriya, T. J., Blinnikov, S. I., Baklanov, P. V., Sorokina, E. I., & Dolgov, A. D. 2013, MNRAS, 430, 1402 34

Müller, B., Janka, H.-T., & Heger, A. 2012, ApJ, 761, 72 19

Nadyozhin, D. K. 2003, MNRAS, 346, 97 114

Nakamura, F. & Umemura, M. 2001, ApJ, 548, 19 18, 90

Neill, J. D., Sullivan, M., Gal-Yam, A., et al. 2011, ApJ, 727, 15 36

Nicholl, M., Smartt, S. J., Jerkstrand, A., et al. 2013, Nature, 502, 346 34, 35, 117

Nomoto, K. 1982, ApJ, 253, 798 19

Nomoto, K. & Hashimoto, M. 1988, Physics Reports, 163, 13 50, 68

Nomoto, K., Sugimoto, D., & Neo, S. 1976, Ap&SS, 39, L37 19

Nordin, J., Rubin, D., Richard, J., et al. 2014, MNRAS, 440, 2742 31

Ohkubo, T., Nomoto, K., Umeda, H., Yoshida, N., & Tsuruta, S. 2009, ApJ, 706, 1184 18, 90

Omukai, K. & Palla, F. 2003, ApJ, 589, 677 18, 90

Oppenheimer, J. R. & Snyder, H. 1939, Physical Review, 56, 455 20

Oppenheimer, J. R. & Volkoff, G. M. 1939, Physical Review, 55, 374 20

O'Shea, B. W. & Norman, M. L. 2006, ApJ, 648, 31 18, 90

Paczyński, B. 1971, ARA&A, 9, 183 23

Pan, T., Kasen, D., & Loeb, A. 2012a, MNRAS, 422, 2701 66

Pan, T., Loeb, A., & Kasen, D. 2012b, MNRAS, 423, 2203 77

Panov, I. V., Blinnikov, S. I., & Thielemann, F.-K. 2001, Astronomy Letters, 27, 239 49

Papish, O., Nordhaus, J., & Soker, N. 2014, ArXiv e-prints 19

Pastorello, A., Smartt, S. J., Botticella, M. T., et al. 2010, ApJ, 724, L16 29

Patat, F., Barbon, R., Cappellaro, E., & Turatto, M. 1994, A&A, 282, 731 24, 29, 75

Patel, B., McCully, C., Jha, S. W., et al. 2013, ArXiv e-prints, 1312.0943 31

Petrovic, J., Pols, O., & Langer, N. 2006, A&A, 450, 219 56

Pinto, P. A. & Eastman, R. G. 2000, ApJ, 530, 744 110

Podsiadlowski, P., Joss, P. C., & Hsu, J. J. L. 1992, ApJ, 391, 246 23

Popov, D. V. 1993, ApJ, 414, 712 23, 108

Prantzos, N., Arnould, M., & Arcoragi, J.-P. 1987, ApJ, 315, 209 48

Quimby, R. M., Kulkarni, S. R., Kasliwal, M. M., et al. 2011, Nature, 474, 487 31, 33

Rakavy, G. & Shaviv, G. 1967, ApJ, 148, 803 24, 27, 66, 90

Richardson, D., Jenkins, III, R. L., Wright, J., & Maddox, L. 2014, AJ, 147, 118 29, 31

Richter, P., Paerels, F. B. S., & Kaastra, J. S. 2008, Space Science Reviews, 134, 25 31

Ride, S. K. & Walker, Jr., A. B. C. 1977, A&A, 61, 339 31

Salpeter, E. E. 1955, ApJ, 121, 161 14, 18

Scannapieco, E., Madau, P., Woosley, S., Heger, A., & Ferrara, A. 2005, ApJ, 633, 1031 66, 75, 90, 101, 119

Schneider, F. R. N., Izzard, R. G., de Mink, S. E., et al. 2014, ApJ, 780, 117 14, 15, 16, 35, 77

Schnurr, O., Casoli, J., Chené, A.-N., Moffat, A. F. J., & St-Louis, N. 2008, MNRAS, 389, L38 15, 16

Seitenzahl, I. R., Townsley, D. M., Peng, F., & Truran, J. W. 2009, Atomic Data and Nuclear Data Tables, 95, 96 17

Shapiro, S. L. & Teukolsky, S. A. 1983, Black holes, white dwarfs, and neutron stars: The physics of compact objects, 663 pp. 31

Shigeyama, T. & Nomoto, K. 1990, ApJ, 360, 242 29

Shigeyama, T., Nomoto, K., Hashimoto, M., & Sugimoto, D. 1987, Nature, 328, 320 20, 101

Shklovskii, I. S. 1960, Sov. Astr., 4, 355 23

Shklovskii, I. S. 1966, Sverkhnovye zvezdy (Supernovae), 398 pp. 22

Smartt, S. J. 2009, ARA&A, 47, 63 18, 75, 104

Smith, N. 2014, ArXiv e-prints 33

Smith, N., Li, W., Filippenko, A. V., & Chornock, R. 2011, MNRAS, 412, 1522 18, 23

Sonoi, T. & Umeda, H. 2012, MNRAS, 421, L34 30

Taam, R. E. 1980, ApJ, 237, 142 40

Taddia, F., Stritzinger, M. D., Sollerman, J., et al. 2013, A&A, 555, A10 34

Takiwaki, T., Kotake, K., & Suwa, Y. 2013, ArXiv e-prints, 1308.5755 19

Thielemann, F.-K., Fröhlich, C., Hirschi, R., et al. 2007, Progress in Particle and Nuclear Physics, 59, 74 17

Timmes, F. X. 1998, http://cococubed.asu.edu/code_pages/net_torch.shtml 37, 40, 46, 47, 49, 67, 68, 92, 126

Timmes, F. X. 1999, ApJS, 124, 241 37, 41, 42, 67, 92

Timmes, F. X., Hoffman, R. D., & Woosley, S. E. 2000, ApJS, 129, 377 40, 42, 46, 48, 49

Timmes, F. X., Woosley, S. E., & Weaver, T. A. 1995, ApJS, 98, 617 17

Tolstov, A. G., Blinnikov, S. I., & Nadyozhin, D. K. 2013, MNRAS, 429, 3181 20, 108, 114

Tominaga, N., Morokuma, T., Blinnikov, S. I., et al. 2011, ApJS, 193, 20 114

Travaglio, C., Hillebrandt, W., Reinecke, M., & Thielemann, F.-K. 2004, A&A, 425, 1029 29, 72

Tsvetkov, D. Y. 1994, Astronomy Letters, 20, 374 112

Tsvetkov, D. Y. & Pavlyuk, N. N. 2013, http://dau.itep.ru/sn/node/72 112

Tsvetkov, D. Y., Pavlyuk, N. N., Bartunov, O. S., & Pskovskii, Yu, P. 2010, http://stella.sai.msu.su/~pavlyuk/snlcurve/ 112

Turatto, M. 2003, in Lecture Notes in Physics, Berlin Springer Verlag, Vol. 598, Supernovae and Gamma-Ray Bursters, ed. K. Weiler, 21–36 23

Ugliano, M., Janka, H.-T., Marek, A., & Arcones, A. 2012, ApJ, 757, 69 20

Umeda, H. & Nomoto, K. 2002, ApJ, 565, 385 29, 35, 36, 66, 127

Umeda, H. & Nomoto, K. 2003, Nature, 422, 871 19, 36

Umeda, H. & Nomoto, K. 2008, ApJ, 673, 1014 29

Utrobin, V. 1993, A&A, 270, 249 19

Vink, J. S. 2012, in Astrophysics and Space Science Library, Vol. 384, Astrophysics and Space Science Library, ed. K. Davidson & R. M. Humphreys, 221 34

Vink, J. S. & de Koter, A. 2005, A&A, 442, 587 78, 92

Vink, J. S., de Koter, A., & Lamers, H. J. G. L. M. 2001, A&A, 369, 574 23, 35, 92

Vink, J. S., Muijres, L. E., Anthonisse, B., et al. 2011, A&A, 531, A132 35, 66, 91

Wagoner, R. V. 1969a, ARA&A, 7, 553 25, 30

Wagoner, R. V. 1969b, ApJS, 18, 247 47

Walborn, N. R., Morrell, N. I., Howarth, I. D., et al. 2004, ApJ, 608, 1028 15

Wallerstein, G., Iben, Jr., I., Parker, P., et al. 1997, Reviews of Modern Physics, 69, 995 17, 20, 39, 43, 49, 67

Weaver, T. A. & Woosley, S. E. 1993, Phys. Rep., 227, 65 40

Weaver, T. A., Zimmerman, G. B., & Woosley, S. E. 1978, ApJ, 225, 1021 41

Whalen, D. J., Even, W., Frey, L. H., et al. 2013a, ApJ, 777, 110 66, 90, 119

Whalen, D. J., Even, W., Smidt, J., et al. 2013b, ApJ, 778, 17 30

Whalen, D. J., Even, W., Smidt, J., et al. 2013c, ArXiv e-prints, 1312.5360, submitted to ApJ 68, 91, 117

Whalen, D. J., Fryer, C. L., Holz, D. E., et al. 2013d, ApJ, 762, L6 90

Whalen, D. J., Johnson, J. L., Smidt, J., et al. 2013e, ApJ, 777, 99 31

Willingale, R., Starling, R. L. C., Beardmore, A. P., Tanvir, N. R., & O'Brien, P. T. 2013, MNRAS, 431, 394 31

Wilms, J., Allen, A., & McCray, R. 2000, ApJ, 542, 914 31

Woosley, S. E. 1988, ApJ, 330, 218 110

Woosley, S. E. 2010, ApJ, 719, L204 34, 35, 91

Woosley, S. E., Blinnikov, S., & Heger, A. 2007a, Nature, 450, 390 27, 34

Woosley, S. E., Heger, A., & Weaver, T. A. 2002, Reviews of Modern Physics, 74, 1015 17, 41, 43, 46, 114

Woosley, S. E., Kasen, D., Blinnikov, S., & Sorokina, E. 2007b, ApJ, 662, 487 104, 110

Woosley, S. E., Langer, N., & Weaver, T. A. 1993, ApJ, 411, 823 22

Woosley, S. E. & Weaver, T. A. 1982, in NATO ASIC Proc. 90: Supernovae: A Survey of Current Research, ed. M. J. Rees & R. J. Stoneham, 79–122 69

Woosley, S. E. & Weaver, T. A. 1995, ApJS, 101, 181 18, 19, 29, 72, 77, 78, 86, 87, 133, 135

Yoon, S.-C. & Cantiello, M. 2010, ApJ, 717, L62 23, 69

Yoon, S.-C., Dierks, A., & Langer, N. 2012a, A&A, 542, A113 28, 62, 76

Yoon, S.-C., Gräfener, G., Vink, J. S., Kozyreva, A., & Izzard, R. G. 2012b, A&A, 544, L11 56

Yoon, S.-C. & Langer, N. 2005, A&A, 443, 643 28, 67

Yoon, S.-C., Langer, N., & Norman, C. 2006, A&A, 460, 199 40, 67, 68, 76, 79, 92

Yoon, S.-C., Woosley, S. E., & Langer, N. 2010, ApJ, 725, 940 24, 36, 40, 56, 92, 125

Young, D. R., Smartt, S. J., Mattila, S., et al. 2008, A&A, 489, 359 19

Young, D. R., Smartt, S. J., Valenti, S., et al. 2010, A&A, 512, A70 36, 91, 116, 120

Young, T. R. 2004, ApJ, 617, 1233 115

Young, T. R., Smith, D., & Johnson, T. A. 2005, ApJ, 625, L87 34

Yungelson, L. R., van den Heuvel, E. P. J., Vink, J. S., Portegies Zwart, S. F., & de Koter, A. 2008, A&A, 477, 223 77

Yusof, N., Hirschi, R., Meynet, G., et al. 2013, MNRAS, 433, 1114 28, 35, 36, 67, 68, 77, 91

Zel'dovich, Y. B., Blinnikov, S. I., & Shakura, N. I. 1981, Physical principles of structure and evolution of stars, 159 pp. 25, 27

Zeldovich, Y. B. & Novikov, I. D. 1971, Relativistic astrophysics. Vol.1: Stars and relativity (Chicago: University of Chicago Press, Translated by Eli Arlock, Ed. by K.S. Thorne and W.D. Arnett), 522 pp. 66

Zel'dovich, Y. B. & Novikov, I. D. 1971, Theory of gravitation and the evolution of stars (Moskva: Nauka), 484 pp. 31

Zinnecker, H. & Yorke, H. W. 2007, ARA&A, 45, 481 77

Remark: The small numbers after the references indicate the page numbers where the citations occur.

List of abbreviations:

ARA&A	:	Annual Review of Astron and Astrophys
AJ	:	Astronomical Journal
A&A	:	Astronomy and Astrophysics
ApJ	:	Astrophysical Journal
ApJS	:	Astrophysical Journal, Supplement
Ap&SS	:	Astrophysics and Space Science
MNRAS	:	Monthly Notices of the Royal Astronomical Society
PASP	:	Publications of the Astronomical Society of of the Pacific
Sov. Astr.	:	Soviet Astronomy

Acknowledgments

First of all, I would like to thank my supervisors, **Professor Dr. Norbert Langer**, and **Professor Dr. Sung-Chul Yoon**, who made this Ph.D. thesis and my work in Bonn possible. You spent a lot of energy and time on work with me and discussions. Thank you for suggesting such an interesting topic for my Ph.D.

My very special gratitude goes to **Dr. Sergey I. Blinnikov** who supervised my term, bachelor and graduate thesis at the Lomonosov Moscow State University. He conveyed to me the feeling of being in love with astronomy and inspired me to be involved into astrophysics for the whole life. He has been my mentor during the last 20 years. I thank him for the many hours he spent on teaching and discussing many theoretical astrophysical topics, numerics, and physics.

I thank all my teachers and lecturers at the Lomonosov Moscow State University who inspired me by their knowledge and yearning for astronomy. They are Dr. Konstantin V. Kuimov, Professor Dr. Anatoly V. Zasov, Professor Dr. Vladimir M. Lipunov, Professor Dr. Konstantin A. Postnov, Dr. Sergey A. Lamzin, Dr. Vadim K. Milyukov and many other astronomers from the Sternberg Astronomical Institute of the Lomonosov Moscow State University who dedicated their lives to astronomy.

I am grateful that I worked at the scientific library of the Nuclear University just before my Ph.D. time. Coming back to scientific work was re-initiated by checking the nuclear physics journals, differentiating the articles, and releasing that I cannot just read the abstract of the article. The members of the library Valentina I. Zolotareva, Tatiana N. Stukalova, Irina P. Kapochkina and many others, who respected me for the knowledge I have got, the highest degree of responsibility. They felt the comfort working with me, and saw in me a very promising researcher.

I would like to thank Dr. Nikolay Pavlyuk and Dr. Dmitriy Tsvetkov for providing observational light curves from the SAI SN catalogue, Dr. Daniel Kasen and Dr. Luc Dessart who provided the data from their simulations, Professor Dr. Alexander Heger, Matt Nicholl, Dr. Morgan Fraser for fruitful discussions, Matías Jones, Katsutoshi Takaki, Dr. Cosimo Inserra, Dr. Melina Bersten, Dr. Maria-Teresa Botticella for providing the observational data.

I am grateful to be involved in the work at Argelander-Institut für Astronomy of Bonn University, namely to work at Stellar Physics group. The members of the group, namely Professor Dr. Robert Izzard, Dr. Takashi Moriya, Sutirtha Sengupta, Dr. Jonathan Mackey, Dr. Shazrene Mohamed, Dr. Enrique Moreno Méndez, Dr. Hilding Neilson, Dr. Luca Fos-

sati, Debasish Sanyal, Dr. Ilka Petermann, Fabian Schneider were always ready to help in scientific questions and personal difficulties. Thanks to many members of other groups of the institute, especially, Dr. Tim Schrabback, Dr. Kaustuv moni Basu and their nice families, Professor Dr. Frank Bertoldi, and Dr. Soroush Nasoudi-Shoar.

I am very grateful to all secretaries, Elisabeth Danne, Elisabeth Kramer, Christina Stein-Schmitz, Kristina Biehl for the invaluable help in many bureaucratic questions and to Dr. Ole Marggraf for any kind of computer support.

I thank my sister Anastasia Lukina and her family, and my friends Dr. Anton Biryukov, Dr. Kirill Sokolovsky, Marina Berezina for their belief and support. Especially, thanks to Elena Sviridova, Anna Koch, Irina Enns, Swetlana Ganswind, Natalia Dziedzioch, Kristina Taran, Isabelle Rosa-Heinrichs and their families who believed in me and helped to survive and go through many difficulties I and my daughter encountered in the foreign country. Guys, you helped me not to give up at the most critical times.

I thank my landlady Dr. Christel Vedder and her large family, my neighbours Nina and Ulli Rosenzweig, Maria Peters for very warm, friendly and calm atmosphere in our house.

I also would like to thank my doctors Vassili Gorbachev, Viktoria Viprinski and Konstantin Yakovlev who helped me to deal with the health problems.

This work was not possible without encouragement and support from my parents, merely my father Dr. Vitaliy S. Kozyrev who has been working the whole his life (more than 50 years) on applied geophysics.

My muse, the base, the reason, the goal of all my work and life is **my daughter Galina**. She has been keeping my vigour during last 7 years and especially during Ph.D. time in Bonn. **I dedicate the thesis to her**.

Publication list

1. Kozyreva, A.; Blinnikov, S.; Langer, N.; Yoon, S.-C. **Observational properties of low redshift pair instability supernovae** // A & A, 2014, Vol. 565, A70 (arXiv:1403.5212).

2. Kozyreva, A.; Yoon, S.-C.; Langer, N. **Explosion and nucleosynthesis of low redshift pair instability supernovae** // 2014, submitted to A & A.

3. Kozyreva, A.; Blinnikov, S. I.; Langer, N.; Yoon, S.-C. **Synthetic light curves for local pair instability supernovae** // in Abstract book of Russian Conference 'High energy astrophysics today and tomorrow', 23-26 December 2013, Moscow. 2013, p. 9-10 (in Russian).

4. Kozyreva, A.; Yoon, S.-C.; Langer, N.; Blinnikov, S. I. **Evolutionary models of pair instability supernovae at non-zero metallicity** // in Abstract book of Russian Conference 'High energy astrophysics today and tomorrow', 24-27 December 2012, Moscow. 2012, p. 9-10 (in Russian).

5. Yoon, S.-C.; Gräfener, G.; Vink, J. S.; Kozyreva, A.; Izzard, R. G. **On the nature and detectability of Type Ib/c supernova progenitors** // Astronomy & Astrophysics. 2012, Vol. 544, L11 (arXiv:1207.3683).

6. Tikhomirova, Y.; Stern, B. E.; Kozyreva, A.; Poutanen, J. **New soft gamma-ray bursts in the BATSE records and spectral properties of X-ray rich bursts** // MNRAS. 2006, Vol. 367, p. 1473-1477 (astro-ph/0510213).

7. Tikhomirova, Y.; Stern, B. E.; Kozyreva, A.; Poutanen, J. **New Soft BATSE GRBs and Spectra of X-ray Rich Bursts** // Proceedings of the The X-ray Universe 2005 (ESA SP-604). 26-30 September 2005, El Escorial, Madrid, Spain. Editor: A. Wilson. 2005, p. 891.

8. Tikhomirova, Y.; Stern, B. E.; Kozyreva, A.; Poutanen, J. **Soft Gamma-Ray Bursts in the BATSE data** // Proceedings of 'Rencontres de Moriond: Very

High Energy Phenomena in the Universe'. La Thuile, Italy. March 12-19, 2005 (astro-ph/0505490).

9. Blinnikov, S. I.; Baklanov, P. V.; Kozyreva, A. V.; Sorokina, E. I. **Light Curve Models of Supernovae and X-ray spectra of Supernova Remnants** // '1604-2004: Supernovae as Cosmological Lighthouses', Padua, June 16-19, 2004, ASP Conference Series. 2005, Vol. 342, p. 382 (astro-ph/0409396).

10. Kozyreva, A. V.; Milyukov V. K. **Estimation of resonant characteristics of volcano Elbrus magmatic center by strain measurements** // Moscow University Physics Bulletin. 2003, N 3, p. 62-67 (in Russian).

11. Kozyreva, A. V.; Milyukov V. K. **Earth Oscillations** // In book: Modern geological and geophysical monitoring methods of natural processes at Kabardino-Balkarian region. 2003. p. 189-199 (in Russian).

12. Kozyreva, A. V.; Milyukov V. K. **Long-term monitoring crustal deformations in the North Caucasus by the laser interferometer** // Geophysical research abstracts of the Joint Assembly of the European Geophysical Society, Nice, France, 7-11 April, 2003, Vol. 5, p. 357-358.

13. Kozyreva, A. V.; Milyukov V. K. **Geophysical Applications of Laser Interferomters: Long-Term Monitoring Crustal Deformations** // Proceedings of the 28th International Cosmic Ray Conference. July 31-August 7, 2003. Trukuba, Japan, p. 3157.

14. Kozyreva, A. V.; Milyukov V. K. **Spectral least-squares-method algorithm for measurement geophysical signal parameters** // Measurements technics. Fundamental problems in metrology. 2002, Vol. 45, N 5, p. 453-460.

15. Blinnikov, S. I.; Kozyreva, A. V.; Panchenko, I. E. **Gamma-ray bursts: When does a blackbody spectrum look non-thermal?** // Astronomy Reports. 1999, Vol. 43, Is. 11, p. 739-747 (astro-ph/9902378).

Curriculum vitae

Surname:	Kozyreva
First Name:	Alexandra
Date of birth:	4. August, 1977
Gender:	Female
City of Birth:	Moscow, Russia
Citizenship:	Russian

Academic history

2010-2014	Stellar Physics Group, Argelander-Institut für Astronomie, University of Bonn, Germany
Ph.D. thesis (2014)	*Pair instability supernovae: Evolution, explosion, nucleosynthesis* supervised by Prof. Dr. N. Langer and Prof. Dr. S.-C. Yoon
1994-2000	Faculty of Physics, M.V. Lomonosov Moscow State University, Moscow, Russia Chair of Astrophysics and Stellar Astronomy Major: Astronomy, Astrophysics
Graduation thesis (2000):	*Numerical relativistic hydrodynamics of strong explosion in application to gamma ray bursts* supervised by Dr. Sergey Blinnikov
Bachelor thesis (1998):	*Spectra of relativistic gamma sources* supervised by Dr. Sergey Blinnikov
Term thesis (1997):	*Corrections for absorption in spectra of supernovae at first maximum light* supervised by Dr. Sergey Blinnikov

Practical experience

2000-2006	Laser Interferometric Laboratory, P.K. Sternberg Astronomical Institute, M.V. Lomonosov Moscow State University, Moscow, Russia
2004-2005	Cosmology and Theoretical Astrophysics Laboratory, Astro-Space Center, P.N. Lebedev Physics Institute of Russian Academy of Sciences, Moscow, Russia

Additional

2009-2010	Scientific library of National Nuclear Research University (Moscow Engineering Physics Institute), Moscow, Russia
1998-2009	Scientific library of M.V. Lomonosov Moscow State University (Library Department at P.K. Sternberg Astronomical Institute), Moscow, Russia
2001-2006	Astronomical division of Faculty of Physics, M.V. Lomonosov Moscow State University, Moscow, Russia